REPORT DOCUMENTATION PAGE

AFRL-SR-BL-TR-00-0774

ewing
nation

1. AGENCY USE ONLY *(Leave blank)*	2. REPORT DATE	3. REPORT
	December, 1997	

4. TITLE AND SUBTITLE
1997 Summer Research Program (SRP), High School Apprenticeship Program (HSAP), Final Reports, Volume 15C, Wright Laboratory

5. FUNDING NUMBERS
F49620-93-C-0063

6. AUTHOR(S)
Gary Moore

7. PERFORMING ORGANIZATION NAME(S) AND ADDRESS(ES)
Research & Development Laboratories (RDL)
5800 Uplander Way
Culver City, CA 90230-6608

8. PERFORMING ORGANIZATION REPORT NUMBER

9. SPONSORING/MONITORING AGENCY NAME(S) AND ADDRESS(ES)
Air Force Office of Scientific Research (AFOSR)
801 N. Randolph St.
Arlington, VA 22203-1977

10. SPONSORING/MONITORING AGENCY REPORT NUMBER

11. SUPPLEMENTARY NOTES

12a. DISTRIBUTION AVAILABILITY STATEMENT
Approved for Public Release

12b. DISTRIBUTION CODE

13. ABSTRACT *(Maximum 200 words)*

The United States Air Force Summer Research Program (USAF-SRP) is designed to introduce university, college, and technical institute faculty members, graduate students, and high school students to Air Force research. This is accomplished by the faculty members (Summer Faculty Research Program, (SFRP)), graduate students (Graduate Student Research Program (GSRP)), and high school students (High School Apprenticeship Program (HSAP)) being selected on a nationally advertised competitive basis during the summer intersession period to perform research at Air Force Research Laboratory (AFRL) Technical Directorates, Air Force Air Logistics Centers (ALC), and other AF Laboratories. This volume consists of a program overview, program management statistics, and the final technical reports from the HSAP participants at the Wright Laboratory.

14. SUBJECT TERMS
Air Force Research, Air Force, Engineering, Laboratories, Reports, Summer, Universities, Faculty, Graduate Student, High School Student

15. NUMBER OF PAGES

16. PRICE CODE

17. SECURITY CLASSIFICATION OF REPORT	18. SECURITY CLASSIFICATION OF THIS PAGE	19. SECURITY CLASSIFICATION OF ABSTRACT	20. LIMITATION OF ABSTRACT
Unclassified	Unclassified	Unclassified	UL

UNITED STATES AIR FORCE

SUMMER RESEARCH PROGRAM -- 1997

HIGH SCHOOL APPRENTICESHIP PROGRAM FINAL REPORTS

VOLUME 15C

WRIGHT LABORATORY

RESEARCH & DEVELOPMENT LABORATORIES

5800 Uplander Way

Culver City, CA 90230-6608

Program Director, RDL
Gary Moore

Program Manager, AFOSR
Major Linda Steel-Goodwin

Program Manager, RDL
Scott Licoscos

Program Administrator, RDL
Johnetta Thompson

Program Administrator, RDL
Rebecca Kelly

Submitted to:

AIR FORCE OFFICE OF SCIENTIFIC RESEARCH

Bolling Air Force Base

Washington, D.C.

December 1997

PREFACE

Reports in this volume are numbered consecutively beginning with number 1. Each report is paginated with the report number followed by consecutive page numbers, e.g., 1-1, 1-2, 1-3; 2-1, 2-2, 2-3.

Due to its length, Volume 15 is bound in three parts, 15A, 15B and 15C. Volume 15A contains #1-20. Volume 15B contains reports #21-40 and Volume 15C contains reports 41-56. The Table of Contents for Volume 15 is included in all parts.

This document is one of a set of 16 volumes describing the 1997 AFOSR Summer Research Program. The following volumes comprise the set:

VOLUME	TITLE
1	Program Management Report
	Summer Faculty Research Program (SFRP) Reports
2A & 2B	Armstrong Laboratory
3A & 3B	Phillips Laboratory
4A & 4B	Rome Laboratory
5A , 5B & 5C	Wright Laboratory
6	Arnold Engineering Development Center, United States Air Force Academy and Air Logistics Centers
	Graduate Student Research Program (GSRP) Reports
7A & 7B	Armstrong Laboratory
8	Phillips Laboratory
9	Rome Laboratory
10A & 10B	Wright Laboratory
11	Arnold Engineering Development Center, Wilford Hall Medical Center and Air Logistics Centers
	High School Apprenticeship Program (HSAP) Reports
12A & 12B	Armstrong Laboratory
13	Phillips Laboratory
14	Rome Laboratory
15A, 15B & 15C	Wright Laboratory
16	Arnold Engineering Development Center

SRP Final Report Table of Contents

SRP Final Report Table of Contents

SRP Final Report Table of Contents

SRP Final Report Table of Contents

SRP Final Report Table of Contents

SRP Final Report Table of Contents

SRP Final Report Table of Contents

SRP Final Report Table of Contents

1. INTRODUCTION

The Summer Research Program (SRP), sponsored by the Air Force Office of Scientific Research (AFOSR), offers paid opportunities for university faculty, graduate students, and high school students to conduct research in U.S. Air Force research laboratories nationwide during the summer.

Introduced by AFOSR in 1978, this innovative program is based on the concept of teaming academic researchers with Air Force scientists in the same disciplines using laboratory facilities and equipment not often available at associates' institutions.

The Summer Faculty Research Program (SFRP) is open annually to approximately 150 faculty members with at least two years of teaching and/or research experience in accredited U.S. colleges, universities, or technical institutions. SFRP associates must be either U.S. citizens or permanent residents.

The Graduate Student Research Program (GSRP) is open annually to approximately 100 graduate students holding a bachelor's or a master's degree; GSRP associates must be U.S. citizens enrolled full time at an accredited institution.

The High School Apprentice Program (HSAP) annually selects about 125 high school students located within a twenty mile commuting distance of participating Air Force laboratories.

AFOSR also offers its research associates an opportunity, under the Summer Research Extension Program (SREP), to continue their AFOSR-sponsored research at their home institutions through the award of research grants. In 1994 the maximum amount of each grant was increased from $20,000 to $25,000, and the number of AFOSR-sponsored grants decreased from 75 to 60. A separate annual report is compiled on the SREP.

The numbers of projected summer research participants in each of the three categories and SREP "grants" are usually increased through direct sponsorship by participating laboratories.

AFOSR's SRP has well served its objectives of building critical links between Air Force research laboratories and the academic community. opening avenues of communications and forging new research relationships between Air Force and academic technical experts in areas of national interest, and strengthening the nation's efforts to sustain careers in science and engineering. The success of the SRP can be gauged from its growth from inception (see Table 1) and from the favorable responses the 1997 participants expressed in end-of-tour SRP evaluations (Appendix B).

AFOSR contracts for administration of the SRP by civilian contractors. The contract was first awarded to Research & Development Laboratories (RDL) in September 1990. After completion of the

1990 contract, RDL (in 1993) won the recompetition for the basic year and four 1-year options.

2. PARTICIPATION IN THE SUMMER RESEARCH PROGRAM

The SRP began with faculty associates in 1979; graduate students were added in 1982 and high school students in 1986. The following table shows the number of associates in the program each year.

YEAR	SRP Participation, by Year			TOTAL
	SFRP	GSRP	HSAP	
1979	70			70
1980	87			87
1981	87			87
1982	91	17		108
1983	101	53		154
1984	152	84		236
1985	154	92		246
1986	158	100	42	300
1987	159	101	73	333
1988	153	107	101	361
1989	168	102	103	373
1990	165	121	132	418
1991	170	142	132	444
1992	185	121	159	464
1993	187	117	136	440
1994	192	117	133	442
1995	190	115	137	442
1996	188	109	138	435
1997	148	98	140	427

Beginning in 1993, due to budget cuts, some of the laboratories weren't able to afford to fund as many associates as in previous years. Since then, the number of funded positions has remained fairly constant at a slightly lower level.

3. RECRUITING AND SELECTION

The SRP is conducted on a nationally advertised and competitive-selection basis. The advertising for faculty and graduate students consisted primarily of the mailing of 8,000 52-page SRP brochures to chairpersons of departments relevant to AFOSR research and to administrators of grants in accredited universities, colleges, and technical institutions. Historically Black Colleges and Universities (HBCUs) and Minority Institutions (MIs) were included. Brochures also went to all participating USAF laboratories, the previous year's participants, and numerous individual requesters (over 1000 annually).

RDL placed advertisements in the following publications: *Black Issues in Higher Education, Winds of Change,* and *IEEE Spectrum.* Because no participants list either *Physics Today* or *Chemical & Engineering News* as being their source of learning about the program for the past several years, advertisements in these magazines were dropped, and the funds were used to cover increases in brochure printing costs.

High school applicants can participate only in laboratories located no more than 20 miles from their residence. Tailored brochures on the HSAP were sent to the head counselors of 180 high schools in the vicinity of participating laboratories, with instructions for publicizing the program in their schools. High school students selected to serve at Wright Laboratory's Armament Directorate (Eglin Air Force Base, Florida) serve eleven weeks as opposed to the eight weeks normally worked by high school students at all other participating laboratories.

Each SFRP or GSRP applicant is given a first, second, and third choice of laboratory. High school students who have more than one laboratory or directorate near their homes are also given first, second, and third choices.

Laboratories make their selections and prioritize their nominees. AFOSR then determines the number to be funded at each laboratory and approves laboratories' selections.

Subsequently, laboratories use their own funds to sponsor additional candidates. Some selectees do not accept the appointment, so alternate candidates are chosen. This multi-step selection procedure results in some candidates being notified of their acceptance after scheduled deadlines. The total applicants and participants for 1997 are shown in this table.

1997 Applicants and Participants			
PARTICIPANT CATEGORY	TOTAL APPLICANTS	SELECTEES	DECLINING SELECTEES
SFRP	490	188	32
(HBCU/MI)	(0)	(0)	(0)
GSRP	202	98	9
(HBCU/MI)	(0)	(0)	(0)
HSAP	433	140	14
TOTAL	1125	426	55

4. SITE VISITS

During June and July of 1997, representatives of both AFOSR/NI and RDL visited each participating laboratory to provide briefings, answer questions, and resolve problems for both laboratory personnel and participants. The objective was to ensure that the SRP would be as constructive as possible for all participants. Both SRP participants and RDL representatives found these visits beneficial. At many of the laboratories, this was the only opportunity for all participants to meet at one time to share their experiences and exchange ideas.

5. HISTORICALLY BLACK COLLEGES AND UNIVERSITIES AND MINORITY INSTITUTIONS (HBCU/MIs)

Before 1993, an RDL program representative visited from seven to ten different HBCU/MIs annually to promote interest in the SRP among the faculty and graduate students. These efforts were marginally effective, yielding a doubling of HBCI/MI applicants. In an effort to achieve AFOSR's goal of 10% of all applicants and selectees being HBCU/MI qualified, the RDL team decided to try other avenues of approach to increase the number of qualified applicants. Through the combined efforts of the AFOSR Program Office at Bolling AFB and RDL, two very active minority groups were found, HACU (Hispanic American Colleges and Universities) and AISES (American Indian Science and Engineering Society). RDL is in communication with representatives of each of these organizations on a monthly basis to keep up with the their activities and special events. Both organizations have widely-distributed magazines/quarterlies in which RDL placed ads.

Since 1994 the number of both SFRP and GSRP HBCU/MI applicants and participants has increased ten-fold, from about two dozen SFRP applicants and a half dozen selectees to over 100 applicants and two dozen selectees, and a half-dozen GSRP applicants and two or three selectees to 18 applicants and 7 or 8 selectees. Since 1993, the SFRP had a two-fold applicant increase and a two-fold selectee increase. Since 1993, the GSRP had a three-fold applicant increase and a three to four-fold increase in selectees.

In addition to RDL's special recruiting efforts, AFOSR attempts each year to obtain additional funding or use leftover funding from cancellations the past year to fund HBCU/MI associates. This year, 5 HBCU/MI SFRPs declined after they were selected (and there was no one qualified to replace them with). The following table records HBCU/MI participation in this program.

SRP HBCU/MI Participation, By Year				
YEAR	SFRP		GSRP	
	Applicants	Participants	Applicants	Participants
1985	76	23	15	11
1986	70	18	20	10
1987	82	32	32	10
1988	53	17	23	14
1989	39	15	13	4
1990	43	14	17	3
1991	42	13	8	5
1992	70	13	9	5
1993	60	13	6	2
1994	90	16	11	6
1995	90	21	20	8
1996	119	27	18	7

6. SRP FUNDING SOURCES

Funding sources for the 1997 SRP were the AFOSR-provided slots for the basic contract and laboratory funds. Funding sources by category for the 1997 SRP selected participants are shown here.

1997 SRP FUNDING CATEGORY	SFRP	GSRP	HSAP
AFOSR Basic Allocation Funds	141	89	123
USAF Laboratory Funds	48	9	17
HBCU/MI By AFOSR (Using Procured Addn'l Funds)	0	0	N/A
TOTAL	9	98	140

SFRP - 188 were selected, but thirty two canceled too late to be replaced.
GSRP - 98 were selected, but nine canceled too late to be replaced.
HSAP - 140 were selected, but fourteen canceled too late to be replaced.

7. COMPENSATION FOR PARTICIPANTS

Compensation for SRP participants, per five-day work week, is shown in this table.

1997 SRP Associate Compensation

PARTICIPANT CATEGORY	1991	1992	1993	1994	1995	1996	1997
Faculty Members	$690	$718	$740	$740	$740	$770	$770
Graduate Student (Master's Degree)	$425	$442	$455	$455	$455	$470	$470
Graduate Student (Bachelor's Degree)	$365	$380	$391	$391	$391	$400	$400
High School Student (First Year)	$200	$200	$200	$200	$200	$200	$200
High School Student (Subsequent Years)	$240	$240	$240	$240	$240	$240	$240

The program also offered associates whose homes were more than 50 miles from the laboratory an expense allowance (seven days per week) of $50/day for faculty and $40/day for graduate students. Transportation to the laboratory at the beginning of their tour and back to their home destinations at the end was also reimbursed for these participants. Of the combined SFRP and GSRP associates, 65 % (194 out of 286) claimed travel reimbursements at an average round-trip cost of $776.

Faculty members were encouraged to visit their laboratories before their summer tour began. All costs of these orientation visits were reimbursed. Forty-three percent (85 out of 188) of faculty associates took orientation trips at an average cost of $388. By contrast, in 1993, 58 % of SFRP associates took

orientation visits at an average cost of $685; that was the highest percentage of associates opting to take an orientation trip since RDL has administered the SRP, and the highest average cost of an orientation trip. These 1993 numbers are included to show the fluctuation which can occur in these numbers for planning purposes.

Program participants submitted biweekly vouchers countersigned by their laboratory research focal point, and RDL issued paychecks so as to arrive in associates' hands two weeks later.

This is the second year of using direct deposit for the SFRP and GSRP associates. The process went much more smoothly with respect to obtaining required information from the associates, only 7% of the associates' information needed clarification in order for direct deposit to properly function as opposed to 10% from last year. The remaining associates received their stipend and expense payments via checks sent in the US mail.

HSAP program participants were considered actual RDL employees, and their respective state and federal income tax and Social Security were withheld from their paychecks. By the nature of their independent research, SFRP and GSRP program participants were considered to be consultants or independent contractors. As such, SFRP and GSRP associates were responsible for their own income taxes, Social Security, and insurance.

8. CONTENTS OF THE 1997 REPORT

The complete set of reports for the 1997 SRP includes this program management report (Volume 1) augmented by fifteen volumes of final research reports by the 1997 associates, as indicated below:

1997 SRP Final Report Volume Assignments

LABORATORY	SFRP	GSRP	HSAP
Armstrong	2	7	12
Phillips	3	8	13
Rome	4	9	14
Wright	5A, 5B	10	15
AEDC, ALCs, WHMC	6	11	16

APPENDIX A – PROGRAM STATISTICAL SUMMARY

A. Colleges/Universities Represented

Selected SFRP associates represented 169 different colleges, universities, and institutions, GSRP associates represented 95 different colleges, universities, and institutions.

B. States Represented

SFRP -Applicants came from 47 states plus Washington D.C. Selectees represent 44 states.

GSRP - Applicants came from 44 states. Selectees represent 32 states.

HSAP - Applicants came from thirteen states. Selectees represent nine states.

Total Number of Participants	
SFRP	189
GSRP	97
HSAP	140
TOTAL	426

Degrees Represented			
	SFRP	GSRP	TOTAL
Doctoral	184	0	184
Master's	2	41	43
Bachelor's	0	56	56
TOTAL	186	97	298

SFRP Academic Titles	
Assistant Professor	64
Associate Professor	70
Professor	40
Instructor	0
Chairman	1
Visiting Professor	1
Visiting Assoc. Prof.	1
Research Associate	9
TOTAL	186

Source of Learning About the SRP		
Category	Applicants	Selectees
Applied/participated in prior years	28%	34%
Colleague familiar with SRP	19%	16%
Brochure mailed to institution	23%	17%
Contact with Air Force laboratory	17%	23%
IEEE Spectrum	2%	1%
BIIHE	1%	1%
Other source	10%	8%
TOTAL	100%	100%

APPENDIX B – SRP EVALUATION RESPONSES

1. OVERVIEW

Evaluations were completed and returned to RDL by four groups at the completion of the SRP. The number of respondents in each group is shown below.

Table B-1. Total SRP Evaluations Received

Evaluation Group	Responses
SFRP & GSRPs	275
HSAPs	113
USAF Laboratory Focal Points	84
USAF Laboratory HSAP Mentors	6

All groups indicate unanimous enthusiasm for the SRP experience.

The summarized recommendations for program improvement from both associates and laboratory personnel are listed below:

A. Better preparation on the labs' part prior to associates' arrival (i.e., office space, computer assets, clearly defined scope of work).

B. Faculty Associates suggest higher stipends for SFRP associates.

C. Both HSAP Air Force laboratory mentors and associates would like the summer tour extended from the current 8 weeks to either 10 or 11 weeks; the groups state it takes 4-6 weeks just to get high school students up-to-speed on what's going on at laboratory. (Note: this same argument was used to raise the faculty and graduate student participation time a few years ago.)

2. 1997 USAF LABORATORY FOCAL POINT (LFP) EVALUATION RESPONSES

The summarized results listed below are from the 84 LFP evaluations received.

1. LFP evaluations received and associate preferences:

Table B-2. Air Force LFP Evaluation Responses (By Type)

		How Many Associates Would You Prefer To Get ? (% Response)											
		SFRP				GSRP (w/Univ Professor)				GSRP (w/o Univ Professor)			
Lab	Evals Recv'd	0	1	2	3+	0	1	2	3+	0	1	2	3+
AEDC	0	-	-	-	-	-	-	-	-	-	-	-	-
WHMC	0	-	-	-	-	-	-	-	-	-	-	-	-
AL	7	28	28	28	14	54	14	28	0	86	0	14	0
USAFA	1	0	100	0	0	100	0	0	0	0	100	0	0
PL	25	40	40	16	4	88	12	0	0	84	12	4	0
RL	5	60	40	0	0	80	10	0	0	100	0	0	0
WL	46	30	43	20	6	78	17	4	0	93	4	2	0
Total	84	32%	50%	13%	5%	80%	11%	6%	0%	73%	23%	4%	0%

LFP Evaluation Summary. The summarized responses, by laboratory, are listed on the following page. LFPs were asked to rate the following questions on a scale from 1 (below average) to 5 (above average).

2. LFPs involved in SRP associate application evaluation process:
   a. Time available for evaluation of applications:
   b. Adequacy of applications for selection process:
3. Value of orientation trips:
4. Length of research tour:
5. a. Benefits of associate's work to laboratory:
   b. Benefits of associate's work to Air Force:
6. a. Enhancement of research qualifications for LFP and staff:
   b. Enhancement of research qualifications for SFRP associate:
   c. Enhancement of research qualifications for GSRP associate:
7. a. Enhancement of knowledge for LFP and staff:
   b. Enhancement of knowledge for SFRP associate:
   c. Enhancement of knowledge for GSRP associate:
8. Value of Air Force and university links:
9. Potential for future collaboration:
10. a. Your working relationship with SFRP:
    b. Your working relationship with GSRP:
11. Expenditure of your time worthwhile:

(Continued on next page)

12. Quality of program literature for associate:
13. a. Quality of RDL's communications with you:
    b. Quality of RDL's communications with associates:
14. Overall assessment of SRP:

Table B-3. Laboratory Focal Point Reponses to above questions

	AEDC	*AL*	*USAFA*	*PL*	*RL*	*WHMC*	*WL*
# Evals Recv'd	0	7	1	14	5	0	46
Question #							
2	-	86 %	0 %	88 %	80 %	-	85 %
2a	-	4.3	n/a	3.8	4.0	-	3.6
2b	-	4.0	n/a	3.9	4.5	-	4.1
3	-	4.5	n/a	4.3	4.3	-	3.7
4	-	4.1	4.0	4.1	4.2	-	3.9
5a	-	4.3	5.0	4.3	4.6	-	4.4
5b	-	4.5	n/a	4.2	4.6	-	4.3
6a	-	4.5	5.0	4.0	4.4	-	4.3
6b	-	4.3	n/a	4.1	5.0	-	4.4
6c	-	3.7	5.0	3.5	5.0	-	4.3
7a	-	4.7	5.0	4.0	4.4	-	4.3
7b	-	4.3	n/a	4.2	5.0	-	4.4
7c	-	4.0	5.0	3.9	5.0	-	4.3
8	-	4.6	4.0	4.5	4.6	-	4.3
9	-	4.9	5.0	4.4	4.8	-	4.2
10a	-	5.0	n/a	4.6	4.6	-	4.6
10b	-	4.7	5.0	3.9	5.0	-	4.4
11	-	4.6	5.0	4.4	4.8	-	4.4
12	-	4.0	4.0	4.0	4.2	-	3.8
13a	-	3.2	4.0	3.5	3.8	-	3.4
13b	-	3.4	4.0	3.6	4.5	-	3.6
14	-	4.4	5.0	4.4	4.8	-	4.4

3. 1997 SFRP & GSRP EVALUATION RESPONSES

The summarized results listed below are from the 257 SFRP/GSRP evaluations received.

Associates were asked to rate the following questions on a scale from 1 (below average) to 5 (above average) - by Air Force base results and over-all results of the 1997 evaluations are listed after the questions.

1. The match between the laboratories research and your field:
2. Your working relationship with your LFP:
3. Enhancement of your academic qualifications:
4. Enhancement of your research qualifications:
5. Lab readiness for you: LFP, task, plan:
6. Lab readiness for you: equipment, supplies, facilities:
7. Lab resources:
8. Lab research and administrative support:
9. Adequacy of brochure and associate handbook:
10. RDL communications with you:
11. Overall payment procedures:
12. Overall assessment of the SRP:
13. a. Would you apply again?
    b. Will you continue this or related research?
14. Was length of your tour satisfactory?
15. Percentage of associates who experienced difficulties in finding housing:
16. Where did you stay during your SRP tour?
    a. At Home:
    b. With Friend:
    c. On Local Economy:
    d. Base Quarters:
17. Value of orientation visit:
    a. Essential:
    b. Convenient:
    c. Not Worth Cost:
    d. Not Used:

SFRP and GSRP associate's responses are listed in tabular format on the following page.

Table B-4. 1997 SFRP & GSRP Associate Responses to SRP Evaluation

	Arnold	Brooks	Edwards	Eglin	Griffis	Hanscom	Kelly	Kirtland	Lackland	Robins	Tyndall	WPAFB	average
# res	6	48	6	14	31	19	3	32	1	2	10	85	257
1	4.8	4.4	4.6	4.7	4.4	4.9	4.6	4.6	5.0	5.0	4.0	4.7	4.6
2	5.0	4.6	4.1	4.9	4.7	4.7	5.0	4.7	5.0	5.0	4.6	4.8	4.7
3	4.5	4.4	4.0	4.6	4.3	4.2	4.3	4.4	5.0	5.0	4.5	4.3	4.4
4	4.3	4.5	3.8	4.6	4.4	4.4	4.3	4.6	5.0	4.0	4.4	4.5	4.5
5	4.5	4.3	3.3	4.8	4.4	4.5	4.3	4.2	5.0	5.0	3.9	4.4	4.4
6	4.3	4.3	3.7	4.7	4.4	4.5	4.0	3.8	5.0	5.0	3.8	4.2	4.2
7	4.5	4.4	4.2	4.8	4.5	4.3	4.3	4.1	5.0	5.0	4.3	4.3	4.4
8	4.5	4.6	3.0	4.9	4.4	4.3	4.3	4.5	5.0	5.0	4.7	4.5	4.5
9	4.7	4.5	4.7	4.5	4.3	4.5	4.7	4.3	5.0	5.0	4.1	4.5	4.5
10	4.2	4.4	4.7	4.4	4.1	4.1	4.0	4.2	5.0	4.5	3.6	4.4	4.3
11	3.8	4.1	4.5	4.0	3.9	4.1	4.0	4.0	3.0	4.0	3.7	4.0	4.0
12	5.7	4.7	4.3	4.9	4.5	4.9	4.7	4.6	5.0	4.5	4.6	4.5	4.6
Numbers below are percentages													
13a	83	90	83	93	87	75	100	81	100	100	100	86	87
13b	100	89	83	100	94	98	100	94	100	100	100	94	93
14	83	96	100	90	87	80	100	92	100	100	70	84	88
15	17	6	0	33	20	76	33	25	0	100	20	8	39
16a	-	26	17	9	38	23	33	4	-	-	-	30	
16b	100	33	-	40	-	8	-	-	-	-	36	2	
16c	-	41	83	40	62	69	67	96	100	100	64	68	
16d	-	-	-	-	-	-	-	-	-	-	-	0	
17a	-	33	100	17	50	14	67	39	-	50	40	31	35
17b	-	21	-	17	10	14	-	24	-	50	20	16	16
17c	-	-	-	-	10	7	-	-	-	-	-	2	3
17d	100	46	-	66	30	69	33	37	100	-	40	51	46

4. 1997 USAF LABORATORY HSAP MENTOR EVALUATION RESPONSES

Not enough evaluations received (5 total) from Mentors to do useful summary.

5. 1997 HSAP EVALUATION RESPONSES

The summarized results listed below are from the 113 HSAP evaluations received.

HSAP apprentices were asked to rate the following questions on a scale from 1 (below average) to 5 (above average)

1. Your influence on selection of topic/type of work.
2. Working relationship with mentor, other lab scientists.
3. Enhancement of your academic qualifications.
4. Technically challenging work.
5. Lab readiness for you: mentor, task, work plan, equipment.
6. Influence on your career.
7. Increased interest in math/science.
8. Lab research & administrative support.
9. Adequacy of RDL's Apprentice Handbook and administrative materials.
10. Responsiveness of RDL communications.
11. Overall payment procedures.
12. Overall assessment of SRP value to you.
13. Would you apply again next year? Yes (92 %)
14. Will you pursue future studies related to this research? Yes (68 %)
15. Was Tour length satisfactory? Yes (82 %)

	Arnold	Brooks	Edwards	Eglin	Griffiss	Hanscom	Kirtland	Tyndall	WPAFB	Totals
# resp	5	19	7	15	13	2	7	5	40	113
1	2.8	3.3	3.4	3.5	3.4	4.0	3.2	3.6	3.6	3.4
2	4.4	4.6	4.5	4.8	4.6	4.0	4.4	4.0	4.6	4.6
3	4.0	4.2	4.1	4.3	4.5	5.0	4.3	4.6	4.4	4.4
4	3.6	3.9	4.0	4.5	4.2	5.0	4.6	3.8	4.3	4.2
5	4.4	4.1	3.7	4.5	4.1	3.0	3.9	3.6	3.9	4.0
6	3.2	3.6	3.6	4.1	3.8	5.0	3.3	3.8	3.6	3.7
7	2.8	4.1	4.0	3.9	3.9	5.0	3.6	4.0	4.0	3.9
8	3.8	4.1	4.0	4.3	4.0	4.0	4.3	3.8	4.3	4.2
9	4.4	3.6	4.1	4.1	3.5	4.0	3.9	4.0	3.7	3.8
10	4.0	3.8	4.1	3.7	4.1	4.0	3.9	2.4	3.8	3.8
11	4.2	4.2	3.7	3.9	3.8	3.0	3.7	2.6	3.7	3.8
12	4.0	4.5	4.9	4.6	4.6	5.0	4.6	4.2	4.3	4.5
Numbers below are percentages										
13	60%	95%	100%	100%	85%	100%	100%	100%	90%	92%
14	20%	80%	71%	80%	54%	100%	71%	80%	65%	68%
15	100%	70%	71%	100%	100%	50%	86%	60%	80%	82%

Josh Pressnell's report was not available at the time of publication.

INITIAL EXPERIMENTAL EVALUATION OF AXIAL GROOVE HEAT PIPE FOR AIRCRAFT APPLICATIONS

Stephanie M. Puterbaugh

Beavercreek High school
2660 Dayton Xenia Rd.
Beavercreek, Ohio 45434

Final Report for:
High School Apprentice Program
Wright Laboratory

Sponsored by:
Air Force Office of Scientific Research
Bolling Air Force Base, Washington, DC

And

Wright Laboratory

August 1997

42-1

Initial Experimental Evaluation of an Axial Groove Heat Pipe for Aircraft Applications

Stephanie M. Puterbaugh
Beavercreek High School

Abstract

The performance and efficiency of an axial groove heat pipe to be used in aircraft applications was studied. An axial groove heat pipe was mounted onto a centrifuge table in order to observe the effects of acceleration and heat. The purpose of the experiment was to determine the operational characteristics of an axial grooved heat pipe. The heat pipe withstood heat loads of up to 15 Watts, with dry out occurring at 20 Watts.

Initial Experimental Evaluation of an Axial Grooved Heat Pipe for Aircraft Applications

Stephanie M. Puterbaugh

Introduction

The management of waste heat is always a problem when dealing with mechanical and electrical equipment. A piece of equipment must be kept cool for survival and efficient operation. In order to reduce system cost and complexity, cooling methods must be simple and efficient. One such method is that of the heat pipe, a simple device which can quickly transfer heat from one point to another without the need of electrical energy (http://heatpipe.com/).

A heat pipe is a structure which consists of a hollow pipe with grooves or another type of wicking structure lining the interior. This pipe is sealed at both ends and contains a small amount of working fluid.

Almost any fluid can be used in a heat pipe, depending on its ability to wet the wick structure. The wick structure must be wet in order to create the capillary pressure necessary for the heat pipe to operate. The properties of the fluid affect the operating temperature range of the heat pipe. The working fluid must be chosen such that it can operate within the conditions in which the heat pipe will be placed. The heat pipe in this experiment is made of copper and contains methyl alcohol.

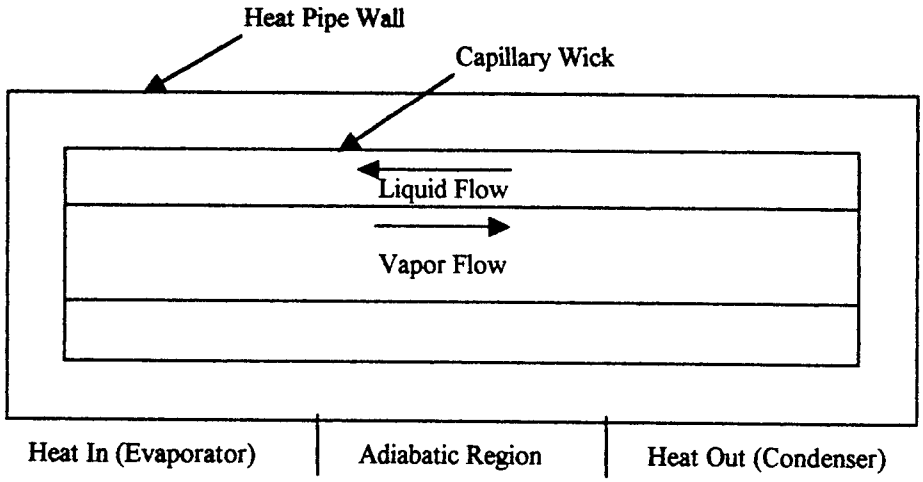

Figure 1 Basic Heat Pipe Elements of the liquid and the vapor

The heat pipe is separated into three sections: the evaporator region, the adiabatic region, and the condenser region (See Figure 1). At one end is located the evaporator region. In this region, the working fluid is heated until it becomes a vapor, creating a pressure which forces the vapor towards the other end of the pipe. The middle section of the pipe is the adiabatic region where no heat transfer takes place, just the movement. On the other end, the pipe is located the condenser region. The condenser section for our experiment consists of a pipe coiled around the heat pipe, through which a mixture of ethylene glycol and water is pumped. Through this process, the vapor is cooled and condensed into a liquid again. The liquid then works through the wicking structure, which in the case studied consisted of axial grooves cut into the interior of the pipe, back to the evaporator region of the pipe where the process begins again. In this way, the heat is moved from the heated end where it is released when the vapor is condensed into a liquid. Heat is released without a great temperature change which could inhibit the performance of the heat pipe.

The idea of the modern heat pipe was first thought of by R. S. Gaugler, an employee of the General Motors Corporation, Ohio, USA. He patented his idea but didn't develop it any further. Other technology which was currently available solved the problem for General Motors without the hassle of testing a new invention (Dunn, Reay, 8-9).

In 1964, Grover, Cotter, and Erickson of Los Alamos National Laboratory performed experiments dealing with heat transfer devices which they referred to as "heat pipes." These objects consisted of sealed tubes with an inner surface which was lined with a layer of porous material. The material was filled with

fluid, two with sodium and one with water. The interior of the heat pipes were filled with the vapor from the liquid filling the pores. Heat was added to each of the pipes and removed by natural convection and radiation. The temperature of the heat pipe remained generally constant, suggesting a way of moving heat without increasing the temperature of the device greatly (Silverstein, 1-3).

The heat pipe was not really needed until the arrival and development of the space program. The arrival of space projects brought about a need for a reliable, self-activating device which could remained at a relatively constant temperature and was able to function in the conditions of space. The heat pipe provided a solution for this need (Silverstein, 3).

For many years the heat pipe was used only for space programs. Complicated building procedures and high cost made it impractical for everyday use. However, in recent years the use of heat pipes has become more common. A company by the name of Thermacore is experimenting with applying the space applications to laptop computer cooling (http://www.thermacore.inter.net/techno.htm). Other companies are experimenting with the use of heat pipes in maintaining the temperature in railroad tracks in order to prevent ice buildup (http://www.eba.ca/arctic.html). The purpose of the current experiment is to evaluate heat pipes so they can be used to cool heat producing parts of airplanes, specifically electronics. Today, the uses for heat pipes have greatly expanded from its original space exploration applications.

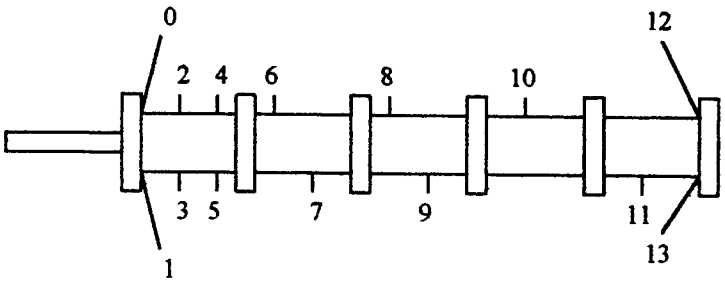

Figure 2 Heat pipe thermocouple positions

Methodology

The characteristics of the heat pipe mounted on the centrifuge (See Figure 3 - next page) were determined experimentally. In order to monitor the operation of the heat pipe during the experiment, it was necessary to keep track of the temperatures along the pipe. To accomplish this, sixteen thermocouples, numbered zero through fifteen, were mounted at different locations along the pipe (See Figure 2). These thermocouples monitored the temperature in all three regions of the pipe.

Thermocouples and Their Calibration

Thermocouples consist of two wires of dissimilar metals which are fused in two places. In this case, the wires are copper and constantan. One of the fused ends is attached to the object to measure its temperature. The other is kept at a known temperature, as a reference point. When one of the junctions is heated, a voltage is produced which is a function of the temperature of the heated end and the composition of the two metals (11, Z-9 - Z-10). Thermocouples can be made from different kinds of metals. The choice of the metals depends on the temperature range to be measured. For this experiment, the copper-constantan thermocouple has a range of -200°C to 350°C.

The analysis of the performance of the heat pipe depended greatly on the temperature readings of the thermocouples. In order to achieve accurate and dependable readings, the thermocouples had to be calibrated. For a calibration to be precise, a reliable source of accurate measurement was necessary. In

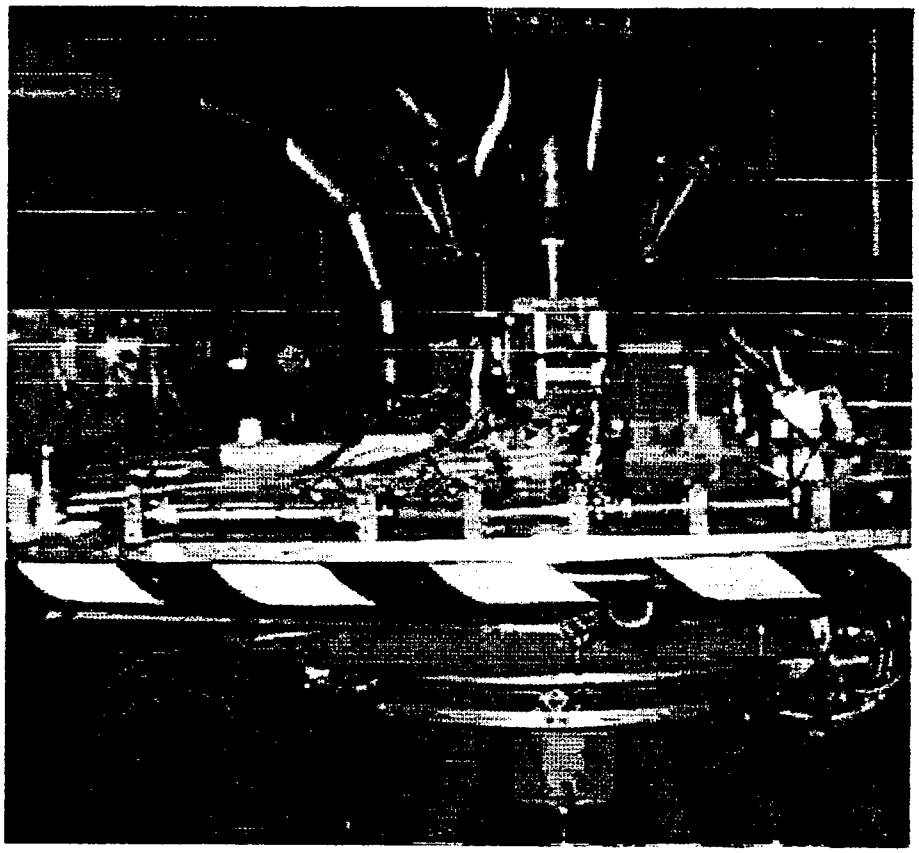

Figure 3 Heat pipe mounted to the centrifuge table

the case of the thermocouples, this was provided by a resistance-temperature detector, called an RTD. To calibrate the thermocouples, the following process was used.

A bath of oil was used which could be maintained at a set temperature. The thermocouples and the RTD were lowered into the oil and held at a constant level. After twenty minutes of suspension in the liquid, the temperature had stabilized and the readings of the thermocouples and the RTD were taken from the computer screen. At that time, the temperature of that bath was changed by ±10°C. The thermocouples and resistance-temperature detector were left for twenty minutes again, at which time the readings were taken. This process was repeated, starting at 0°C, until the final temperature of 100°C was reached. After the full range was complete, it was repeated backwards, starting at 100°C, decreasing to 0°C. This entire method was repeated until three complete trials were recorded. Following this, the data was entered into the computer and plotted onto graphs, one for each thermocouple (See Figure 4).

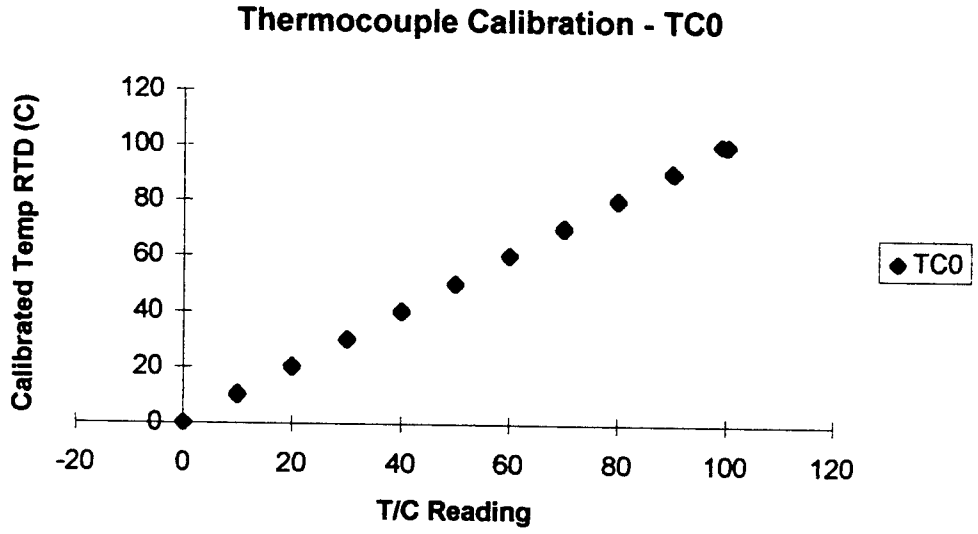

Figure 4 Sample graph of thermocouple calibration data

Each graph was fitted with a line of regression. The equation of these lines would compute the actual temperature when the thermocouple readings were entered. The error associated with the calculation of the

line of regression was calculated, comparing the calculated value and the actual reading. This error determined the quality of the fit of the line. Outliers were discarded for better results.

Calorimeters and Calibration of Flow Meter

Another method of analyzing the efficiency of a heat pipe is the calculation of the heat leaving the pipe with reference to the heat put into the pipe. In order to calculate the heat loss, it was necessary to set up a calorimeter. A calorimeter measures the heat change which occurs during a chemical reaction. The change of temperature in a known weight of liquid in an insulated container is measured by a very accurate device and is used to calculate the change of heat. In this case, the change in temperature is calculated from the readings of the calibrated thermocouples. The reading from thermocouple number fourteen is subtracted from the reading of thermocouple number fifteen. This provides the temperature change used to calculate heat out. To determine Heat Out, the mass, specific heat, and temperature change are multiplied together.

$$Q_{out} = M \cdot Cp \cdot (\Delta T)$$

Even small errors involved in this equation could cause a large error in the results.

A mixture of ethylene-glycol and water was used in the heat pipe in order to aid in the cooling process of the condenser. In order to know accurately the mass of liquid in the condenser pipe at any one time, it is necessary to know the flow rate of this liquid passing through the condenser. For this task, a calibrated flow meter was used. To calibrate the flow meter, a procedure of measuring the volumetric and mass flow of the fluid was followed. In this process, the cool bath was set to a certain temperature and maintained at that point throughout. The rate of flow according to the flow meter was varied. The liquid solution was collected in a large graduated cylinder through a tube exiting the condenser, for approximately one minute, as recorded by a stop watch. The volume was recorded by reading directly from the graduated cylinder. This reading contained an error of ±5mL. The mass of the cylinder was determined using a top load Mettler scale. The balance was adjusted to the mass of the cylinder and any excess liquid remaining after each test. This measurement contained an error of ±0.5 grams. These measurements signified the flow rate, as they were taken for a time span of one minute. In some cases the cylinder was too small for the

amount of liquid being removed from the pipe. In these cases, the stop watch was stopped short of one minute and the flow was determined by multiplying the mass and volume by sixty and then dividing them by the amount of time, as taken from the stop watch. This calculation provided the volumetric flow rate, in units of liters per minute (after dividing by one thousand), and the mass flow rate, in units of grams per minute.

This process was repeated. Five trials were run for each of six flow meter settings of 0.5 l/min., 0.37 l/min., 0.28 l/min., 1.44 l/min., 1.09 l/min., and 0.83 l/min. These trials were run at three different temperatures, 5°C, 20°C, and 35°C. After all of the data was collected, it was entered into the computer and fitted with a regression line (See Figure 5).

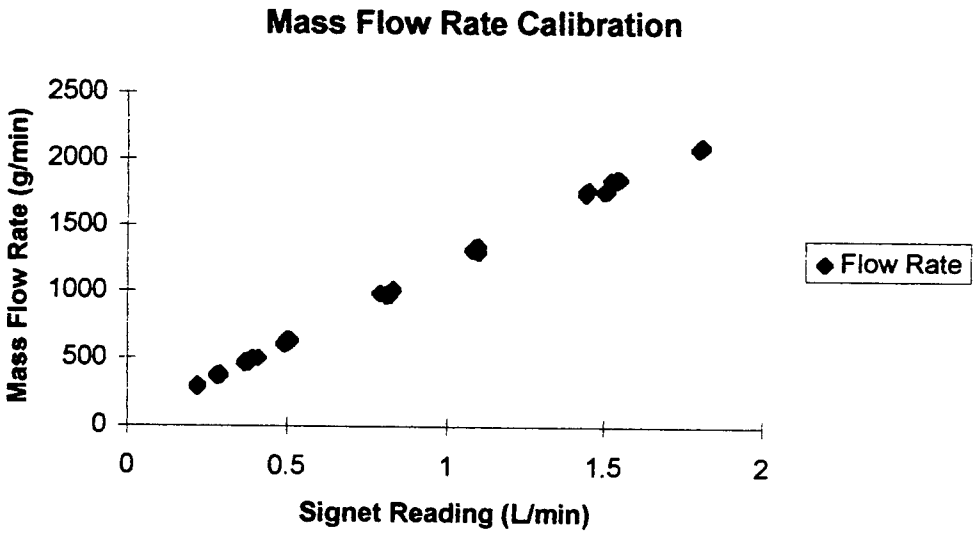

Figure 5 Sample graph of flow rate calibration data

The equation of the line was of great importance in that it made it possible to calculate the actual volumetric flow rate from the flow meter reading and the mass flow rate as well. After computing the mass flow rate, it was possible to determine the amount of solution in the condenser pipe. Thus the mass flow rate was known and the amount of heat leaving the pipe could be calculated.

Experiment

The initial testing involved a change of only the heat input. The acceleration remained at zero as the base line tests were run. Readings from the thermocouples on the evaporator and the evaporator end cap and the flow meter were taken by hand every ten minutes until the temperature stabilized for each setting of the heat input. Readings from all of the thermocouples and the accelerometer were taken every two seconds by the data acquisition system. These readings were copied to two large ASCII files. During the test, the temperatures recorded by the thermocouples began to rise drastically, suggesting dry out in the heat pipe. The system was shut down and the test stopped. After the completion of the experimental run, the files were copied to floppy disks, for the data to be analyzed. All of the data from the test was imported into a spreadsheet and graphing program. It was then converted to a usable format and plotted into separate graphs for the thermocouple readings and the accelerometer readings. Upon examination of the graphs, it was evident that there was a problem with the data. There was a great deal of fluctuation in the lines of data. This fluctuation was determined to be some sort of noise. The comparison of the data from the thermocouples to the data from the accelerometer showed a correlation in the behavior of this noise, suggesting it to be the fault of something in the data acquisition system. Because of this noise, the experiment was not run again for further results.

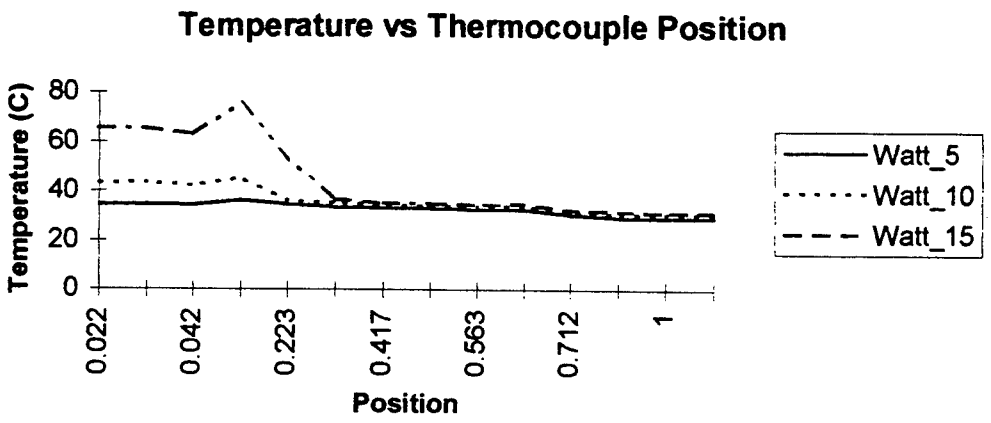

Figure 6 Graph of temperatures with reference to thermocouple position

Results

The data acquired from the experimental run suggested that the heat pipe was running properly, within a limit. The temperatures seemed to be distributed properly along the length of the heat pipe (See Figure 6). The highest temperatures occurred in the evaporator section and the coldest in the condenser section. The temperature change over the entire heat pipe was not very great, thus the heat pipe was constructed properly and functioned as it was intended. The operation of the heat pipe at 5W and 10W was nearly isothermal, as there was a small difference between the temperatures from the two ends (approximately 5.2°C for 5W and 12.5°C for 10 W). At fifteen Watts, the temperatures began to rise, with a difference of approximately 33.7°C, signifying the beginnings of dry out. A limit to the amount of heat able to be input was observed, as the temperatures read by the thermocouples shot up, above 100°C, showing dry out in the heat pipe. This limit occurred at a heat load of 20W.

Conclusions

Despite the inability to run the experiment for more than base line data, some conclusions were able to be made concerning the operation of the heat pipe. Upon examination of the temperatures with reference to the length of the pipe, it is possible to observe that the temperatures were distributed properly (see Figure 6). The highest temperatures occurred in the evaporator section with the coolest in the condenser section.

At 5W and 10 W heat load, the heat pipe was functioning properly, with a small change in temperature over the whole pipe. However, when the heat input was increased to 15W, the temperatures began to rise and the temperature change became greater as the heat pipe did not function as well. At 20W, dry out was observed as the temperatures rose sharply after a period of only a few minutes. Therefore, a limit was observed for this particular heat pipe under these conditions, it could not withstand a heat input of 20W.

NOMENCLATURE

Q_{out}	heat output
M	mass flow rate
Cp	specific heat
DT	temperature change

REFERENCES

1. Brennan, Patrick J., and Kroliczek, Edward J., Heat Pipe Design Handbook, B & K Engineering, Inc. Suite 825, One Investment Place Towson, Maryland 21204, 1979.

2. Bueche, Frederick, Introduction to Physics for Scientists and Engineers, McGraw-Hill Book Company, New York, St. Louis, San Francisco, London, Sydney, Toronto, Mexico, Panama, 1969.

3. Chi, S. W., Heat Pipe Theory and Practice, Hemisphere Publishing Corporation, New York, St. Louis, San Francisco, Aukland, Bogota, Düsseldorf, Johannesburg, London, Madrid, New Delhi, Panama, Paris, Sao Paulo, Singapore, Sydney, Tokyo, Toronto.

4. Dunn, P.D., Reay, D.A., Heat Pipes, Pergamon Press, 1976, Oxford, New York, Toronto, Sydney, Paris, Braunschweig.

5. Guillermin, Sean R., Thermal Efficiency of a Flexible Heat Pipe Subjected to Heat Flux and Transient Acceleration Environments, Air Force Office of Scientific Research, Bolling Air Force Base, Washington DC, 1995.

6. Lindenburg, Michael R., P.E., Mechanical Engineering Review Manual, Seventh Edition, Professional Publications, San Carlos, CA 94070, 1984.

7. Microsoft Internet Explorer

   http://www.thermacore.inter.net/techno.htm

   http://www.eba.ca/arctic.html

   http://www.aero.org/news/current/heatPipes.html

   http://heatpipe.com/

   http://eande.lbl.gov/CBS/Ateam/R-labDG/Help1268.htm

   http://www.thermacore.com/otherapp.htm

8. Nebergall, William H., Schmidt, Frederic C., Holtzclaw, Henry F. Jr., General Chemistry, Fifth Edition, D. C. Heath and Company, Lexington, Massachusetts, Toronto, 1976.

9. Silverstein, Calvin C., Design and Technology of Heat Pipes for Cooling and Heat Exchange, Hemisphere Publishing Company, 1992, Washington, Philadelphia, London.

10. "Thermal Characteristics of Conventional and Flat Miniature Axially Grooved Heat Pipes", Khrustalev, D., Faghri, D. Khrustalev, Journal of Heat Transfer, vol. 117 no. 4, The American Society of Mechanical Engineers, p. 1048.

11. "The Thermocouple", The Omega Complete Temperature Measurement Handbook and Encyclopedia, Omega Engineering, 1989.

12. "Transient Behavior of Axially Grooved Heat Pipes with Thermal Energy Storage", Chang, Ming-Jr, Chow, Louis C., Chang, Won Soon, Morgan, Michael J., Journal of Thermophysics and Heat Transfer, vol. 6 no. 2, American Institute on Aeronautics and Astronautics Incorporated, 1992.

13. Yerkes, Kirk L., and Beam, Jerry E., Arterial Heat Pipe Performance In a Transient Heat Flux and Body Force Environment, Wright-Patterson Air Force Base, Ohio 45433, USA.

Matthew Rabe's report was not available at the time of publication.

IMMERSION CORROSION TESTING OF TUNGSTEN HEAVY-METAL ALLOYS

Kristan Marie Nicole Raymond

Walton High School
555 Walton Road
DeFuniak Springs, Fl 32433

Final Report for:
High School Apprenticeship Program
Mentor: Richard Crews
WL/MNSE
Wright Laboratory
Eglin AFB

Sponsored by:
Air Force Office of Scientific Research
Bolling AFB, DC

and

Wright Laboratory
Eglin AFB

August 1997

IMMERSION CORROSION TESTING OF TUNGSTEN HEAVY-METAL ALLOYS

Kristan Raymond
Walton High School

Abstract

Wright Armament Directorate is considering the use of high-density tungsten alloys in kinetic energy penetrators and other munitions as a possible alternative to depleted uranium. Recently, some tungsten alloys were found to readily corrode under humid conditions. The discovery raised concerns about the ability of tungsten alloys to withstand long-term storage and the possible environmental effects of alloy corrosion in test environments. Until now, the corrosion of tungsten alloys was not seen as a problem. This experiment deals with the behavior of two liquid-sintered tungsten alloys in immersion corrosion tests.

One of the alloys (HD-17) contains significant amounts of tungsten, nickel, and copper, and the other alloy (WL-1) contains significant amounts of tungsten, nickel, and iron. Nine specimens of each of the two alloys were immersed for one year in various solutions. The nine solutions include: solutions with pH's of 2, 4, 7, 9, and 12; stream water; gulf (ocean) water; and two sea salt solutions with concentrations of 2.5% and 5% salt. The solutions were analyzed periodically for the presence of dissolved metals. Observation of corrosion products and mass loss analysis of the specimens were performed on Day 365 of the test.

The HD-17 alloy samples dissolved more tungsten into solution than the WL-1 alloy. The samples of both alloys in the pH 12 and pH 9 solutions dissolved more of the tungsten grain phase and less of the matrix metals into solution than the other samples of that alloy. The samples of both alloys in the pH 2 and pH 4 solutions dissolved high of matrix metals and low amounts of tungsten into solution.

The HD-17 samples had higher corrosion rates than the WL-1 samples; when exposed to salt water, the corrosion rates of both alloy were similar. The highest corrosion rate was 0.52 mils per year (HD-17 pH 4) and the lowest rate was 0.05 mils per year (WL-1 stream water). The corrosion rates are acceptable, but extensive pitting in the matrix phase of both alloys indicates possible loss of strength and ductility not indicated by the corrosion rate.

The HD-17 (copper-containing) alloy dissolved more of its main tungsten grain phase into solution than the WL-1 alloy samples did. The HD-17 alloy also had higher corrosion rates. The copper included in the matrix phase of the HD-17 alloy probably contributed to its poor corrosion resistance.

IMMERSION CORROSION TESTING OF TUNGSTEN HEAVY-METAL ALLOYS

Kristan Raymond

Introduction:

Wright Laboratory Armament Directorate is considering the use of high-density tungsten alloys as a possible alternative to the toxic and slightly radioactive depleted uranium that is currently used in kinetic energy penetrators and other munitions. The high density and strength of tungsten alloys make them ideal candidates for these and other purposes. Recently, however, it was discovered that certain tungsten alloys readily corrode in humid conditions. This discovery raises concerns about the ability of tungsten alloys to withstand long-term storage periods and about the possible environmental effects of alloy corrosion in test environments. The Department of Defense requires that munitions shall not corrode more than 10 mils per year (mpy) during either a 10 year storage period in an uncontrolled environment, or a 20 year storage period in a controlled environment. Corrosion of munition fragments could also adversely impact the environment around the test ranges. **Table 1** gives the toxic doses of some of the metals used in tungsten alloys. If an alloys' rate of corrosion is too rapid, a hazardous amount of toxic metals may be released into the environment. The purpose of this experiment is to gain more information on the corrosion rate of tungsten alloys in various solutions and the amount of metal that will dissolve into solution.

Methodology:

Immersion Testing:

Beaker Preparation:

Tall, 1000 ml glass beakers were used for the immersion tests. Before the test, the beakers were washed with a mild soap, rinsed with distilled water, rinsed with a 25% solution of hydrochloric acid, and again rinsed thoroughly with distilled water.

Sample Preparation:

Two different tungsten alloys were used in the experiment: HD-17, a commercial alloy that contains significant amounts of tungsten, nickel, copper and chromium, and WL-1, an alloy manufactured on Eglin AFB that contains significant amounts of tungsten, nickel, iron, and manganese. The content of the two alloys by percentage mass is given in **Table 2.** The alloys were fabricated using powder metallurgy techniques. This process involves a fine powder mix of alloyed metals that is pre-compacted and liquid-phase sintered at about 1500°C. The final alloy systems usually are of two phases: the rounded tungsten grains and the binder phase consisting of tungsten and the other alloyed elements.

Nine cylindrical samples of each alloy were selected for the experiment. The selected samples were chosen because their similar surface structure (crevices resulting from machine cutting), should have caused similar corrosion mechanisms to occur. The surface area of each sample is given in **Table 3**.

Before the immersion tests, the eighteen alloy samples were rinsed with distilled water, degreased in acetone, soaked briefly in ethanol, stored in a desiccator for a day, and then weighed individually. The mass in grams (accurate to 0.5 mg) of each sample, before and after the immersion test, is given in **Tables 4 and 5**. An explanation of the two values for mass after the test is given in the methodology for the mass analysis phase of the experiment.

Solution Preparation:

Nine different solutions were used in the experiment: solutions with pH's of 2, 4, 7, 9, and 12; stream water; sea water; and 2.5% and 5% solutions of sea salt. The solutions of pH 2 and 4 were prepared by adding a 25% solution of hydrochloric acid (HCl) to distilled water. The solutions of pH 9 and 12 were prepared by adding a 5M solution of sodium hydroxide (NaOH) to distilled water. These solutions were unbuffered. Distilled water was used for the pH 7 solution. Stream water from a stream on the Eglin AFB Reservation and sea water taken from the Gulf of Mexico near Eglin AFB (termed gulf water hereafter) were used for the two natural solutions. A commercial sea salt was used to mix a 2.5% and 5% solution of sea salt and distilled water. A list of the ion concentration of the sea salt is given in **Table 6**.

Each of the eighteen beakers was filled with 800 ml of the appropriate solution. The tungsten cylinders were placed on the bottom of the beakers so that one circular side was always in contact with the glass and the level of solution was marked on each beaker. The beakers were covered with film to retard evaporation and then placed in a darkened growth chamber. The temperature varied from 25 °C to 32 °C.

Pictures of each sample were taken on Day 12, Day 32, and Day 370.

Solution Analysis:

On Day 1 of the immersion tests, 50 ml samples of the following solutions were analyzed for targeted metals (tungsten, nickel, copper, iron, and chromium): pH 4, pH 7, pH 12, stream water, gulf water, and 5% sea salt solution. On Day 32, Day 90, Day 202, and Day 368, 50 ml samples of all eighteen solutions were tested for target metals and also for pH. (The samples taken on Day 202 replaced samples taken on Day 180 that were lost in shipment.)

Prior to sampling on Day 32 and Day 368, the level of solution in each beaker was brought up to the previously marked level with distilled water, and the new level of solution was marked after each sample was collected. Due to error, this procedure was not followed for samples collected on Day 90, Day 180, and Day 202.

To obtain more accurate results, the 50 ml sample was taken at different areas within the solution after the solution was stirred. The new level of solution was marked after each sampling.

Mass Loss Analysis:

Mass loss analysis can be used to determine the average corrosion rate for a material. The average corrosion rate may be obtained as follows:

Corrosion Rate = $(K \times W)/(A \times T \times D)$

where:

K = *constant determining units*

W = *mass loss in grams of the sample*

A = *surface area in* cm^2

T = *time of exposure in hours*

D = *density in* g/cm^3.

Before mass loss can be determined, the corrosion products must be removed from each alloy sample. To clean the samples, both mechanical and chemical cleaning methods were used. To allow for any mass lost during cleaning, an uncorroded specimen of each alloy was subjected to the same cleaning procedures as the other alloy specimens. The mass lost by the control specimens during cleaning was used to correct the mass loss for the other samples. In **Tables 4 and 5**, the second value for mass ("Mass of Sample After the Test, Uncorrected") is the actual physical mass of each specimen after the cleaning process; the third value for mass ("Mass of Sample After the Test, Corrected") was corrected to exclude any mass lost during cleaning.

Mass loss analysis was done after the Day 368 sampling. Each sample was taken out of solution, weighed, and observed prior to cleaning. After each step of the cleaning process, the samples were rinsed in distilled water, weighed, and observed using an optical microscope.

Cleaning Process for HD-17 Alloy Samples:

1. Ultrasonic cleaning for 45 minutes in distilled water.
2. Ten minute bath in a 24% by volume solution of HCl at room temperature.
3. Ten minute bath in a 30% by volume solution of NaOH at room temperature.
4. Oven drying for 18 hours at 75°C.
5. Ten minute bath in 30% by volume solution of ammonium hydroxide (NH_4OH) at room temperature.
6. Ultrasonic cleaning for 30 minutes in distilled water.
7. Ten minute bath in a 30% by volume solution of sulfuric acid (H_2SO_4) at 45°C.
8. Four minute bath in ethanol.
9. Oven drying for 18 hours at 75°C.
10. Ultrasonic cleaning for 30 minutes in distilled water and additional mechanical cleaning with a soft brush.

11. Oven drying for 60 hours at 75°C.

Cleaning Process for WL-1 Alloy Samples:

1. Ultrasonic cleaning for one hour in distilled water.
2. Three minute bath in a 30% by volume solution of HCl at room temperature.
3. Ultrasonic cleaning for thirty minutes and additional mechanical cleaning.
4. Oven drying for 16 hours at 75°C.
5. Three minute bath in a 30% by volume solution of NaOH at room temperature
6. Ultrasonic cleaning for thirty minutes in distilled water.
7. Three minute bath in a 30% by volume solution of H_2SO_4 at 45°C.
8. Ultrasonic cleaning for twenty minutes in distilled water.
9. Oven drying for 16 hours at 75°C.

**The cleaning processes for the two alloys differed because of dissimilar corrosion products on the two alloys. The samples were cleaned until no visible corrosion products remained or until mass measurements indicated that the cleaning process was removing base metal.*

Results:

Corrosion Products

Tables 7 and 8 give complete observations of corrosion products.Summary:

HD-17 alloy:

The alloy samples from the pH 2, pH 4, pH 7, pH 9, and stream water solutions had similar corrosion products. All five had yellow crystals, yellow precipitate, and all except the pH 9 solution had a yellow tinted solution. All had either green-black, black, or green-gold crystals in addition to the yellow. The sample in the pH 12 solution appeared a dull grey-brown and had crystals of many colors scattered on its surface. All of the samples were covered with small pits. The samples from the three salt solutions (gulf water, 2.5% sea salt, and 5% sea salt) had a few deeper pits in the matrix. The three samples in salt solutions also had aqua crystals, aqua precipitate, and blue-tinted solutions.

WL-1 alloy:

The alloy samples from the pH 2, pH 4, pH 7, pH 9, and stream water solutions had mostly orange, white, or yellow crystals and/or precipitate. All five also had several rings of different colored crystals around the bottom edge of the sample. The sample in the pH 12 solution had a red-gold appearance with scattered crystals and a little white precipitate. The tops of the samples in the three salt solutions were covered with a thick layer of crystals. All three samples in salt solutions had yellow or white precipitate and orange or multicolored rings around the bottom edge. The gulf water sample had more yellow, white, orange, and

brown crystals and a faintly yellow solution. The samples from the 2.5% and 5% sea salt solutions had mostly green crystals and a green-yellow solution.

Solution Analysis

Appendix I contains complete solution analysis results.

Summary:

HD-17 Alloy:

The solution with pH 12, followed by the pH 9 solution, had the lowest nickel and copper concentrations and highest tungsten concentration, while the pH 2 solution was just the opposite. The "neutral" solutions (pH 7 and stream water) and the pH 4 solution had average concentrations of tungsten, nickel, and copper. The solutions that contained salt had low tungsten, high nickel, and average copper concentrations.

WL-1 Alloy:

The solution with pH 12, followed by the pH 9 solution, had the lowest nickel and iron concentrations and highest tungsten concentration. The pH 2 solution had the highest nickel concentration, a low tungsten concentration, and an average iron concentration. The solutions that contained salt had a high iron concentration and an average nickel concentration. The gulf water and 5% sea salt solution had high tungsten concentrations, but the 2.5% sea salt solution had an average concentration. The "neutral" solutions (pH 7 and stream water) and the pH 4 solution had low tungsten and iron concentrations and an average nickel concentration.

Comparison:

All of the HD-17 alloy samples dissolved more tungsten into solution than all of the WL-1 samples except for the pH 12 solution of the WL-1 alloy, which contained more tungsten than some of the HD-17 solutions. All of the WL-1 alloy samples dissolved more nickel into solution than the same type of solution in the HD-17 alloy, except for the pH 12 and three salt solutions. Those four solutions had similar nickel concentrations for each alloy. All HD-17 alloy samples dissolved more tungsten than nickel. In the WL-1 alloy, pH 9, pH 12, gulf water, and 5% sea salt also dissolved more tungsten than nickel.

pH changes:

For the HD-17 alloy, the pH 2, pH 4, pH 7, pH 9 and stream water solutions ended the year-long test with a pH of around 3. The pH 12 solution and the three salt solutions ended with a pH of around 6.

For the WL-1 alloy, all solutions ended the year with a pH between 6 and 8.

Mass Loss Analysis

Appendix II contains complete mass loss and corrosion rate results.

Summary:

HD-17 Alloy:

The solutions of pH 4 and pH 7 and the stream water had higher corrosion rates than pH 2, pH 9, and pH 12 solutions. The three salt solutions had the lowest rates. The corrosion rates ranged from 0.52 mpy (pH 4 solution) to 0.08 mpy (2.5% sea salt solution).

WL-1 Alloy:

The corrosion rates ranged from 0.20 mpy (pH 2 solution) to 0.05 mpy (stream water). The pH 12 solution and the three salt solutions had similar corrosion rates, with all other solutions except pH 2 having slightly lower rates. The pH 2 solution had the highest corrosion rate.

Comparison:

In each solution, the corrosion rate of the HD-17 alloy specimen was higher than that of its WL-1 counterpart. Only the HD-17 alloy samples in the gulf water and 2.5% sea salt solution had lower corrosion rates than any of the nine WL-1 solutions.

Conclusions:

Effect of solution pH change:

In the HD-17 alloy, the pH 2, pH 4, pH 7, pH 9 and stream water solutions all had a pH of around 3 by the end of the test. They had similar corrosion products, but their metal dissolution and corrosion rates were not as similar. The metal dissolution varied more with the initial pH than with the final pH. The pH 12 solution of the HD-17 alloy had around the same final pH as the salt solutions, but there were no other significant similarities.

In the WL-1 alloy, all of the solutions had a final pH that was close to neutral. The corrosion products on the samples in all of the solutions were not any more alike than those in the HD-17 alloy. The amounts of metal dissolution in each solution and the corrosion rates for each sample of the WL-1 alloy were closer to one another than they were in the HD-17 alloy.

A similar final pH in the pH 2, pH 4, pH 7, pH 9 and stream water solutions of both alloys might have resulted in similar corrosion products on samples in those solutions. A neutral final pH in the solutions of the WL-1 alloy might have resulted in similar metal dissolution and corrosion rates.

Acid, Base, and Neutral:

The basic solutions (pH 9 and pH 12) had dissimilar corrosion products, but the amount of metal dissolution was similar. These two solutions dissolved more of the tungsten grain phase of both alloy types. The chemical NaOH in the two solutions probably had a greater effect on tungsten dissolution than the actual pH of the solutions because of the many changes in pH over the test period.

The acidic solutions (pH 2 and pH 4) had similar corrosion products, but the samples in the pH 7, pH 9, and stream water solutions were also similar. Since in both alloys these five solutions had a similar final pH, the pH of the solution probably had a greater effect on the corrosion products than the chemicals used to set pH. On the other hand, the HCl in the pH 2 and pH 4 solutions probably had an effect on metal dissolution. The pH 2 and pH 4 solutions had less of the main tungsten grain phase dissolve and more of the matrix phase (nickel, copper, and iron) dissolve than other solutions.

The neutral solutions (pH 7 and stream water) had similar corrosion products and ranged between the acids and bases in terms of metal dissolution. The corrosion rates of the neutral solutions were high for the HD-17 alloy but average for the WL-1 alloy.

Effect of Salt:

For each alloy, the three salt solutions had similar corrosion products, metal dissolution, and corrosion rates. The corrosion products of the samples in the salt solutions were distinctly different from the corrosion products of samples in the other solutions. The HD-17 alloy salt solutions had less tungsten and more nickel dissolved into solution than the pH 7 (distilled water) solution. The WL-1 alloy salt solutions had more iron dissolved into solution than the pH 7 solution. The salt apparently had an inhibiting effect on the corrosion rate of the HD-17 alloy, but not the WL-1 alloy when compared to the sample in the pH 7 solution.

Toxicity:

The solution with the most tungsten had 469 mg/L (HD-17 pH12). A 50 kg person would have to drink 53 liters or more of this solution for a lethal dose. The amount of tungsten in the pH 7 solution of the HD-17 alloy was 331 mg/L. A 50 kg person would have to drink 75 L or more of this solution for a lethal dose. The amount of tungsten in the pH 7 solution of the WL-1 alloy was 2.02 mg/L. A 50 kg person would have to drink 12500 L or more of this solution for a lethal dose.

The solution with the most nickel had 103 mg/L (WL-1 pH2) A 50 kg person would have to drink over 0.01 liters of this solution per day over a long period of time for a lethal dose. The amount of nickel in the pH 7 solution of the HD-17 alloy was 6.8 mg/L. A 50 kg person would have to drink 0.15 L or more of this solution per day over a long period of time for a lethal dose. The amount of nickel in the pH 7 solution of the WL-1 alloy was 17.4 mg/L. A 50 kg person would have to drink 0.06 L or more of this solution per day over a long period of time for a lethal dose.

The solution with the most copper had 30.6 mg/L (HD-17 pH2). A 50 kg person would have to drink 0.3 liters for a lethal dose. The amount of copper in the pH 7 solution of the HD-17 alloy was 2.3 mg/L. A 50 kg person would have to drink 2.6 liters for a lethal dose.

**The other elements did not have significant amounts in solution..*

From the dissolution data from this experiment, it appears that when placed in stagnant water the HD-17 alloy and the WL-1 alloy will release hazardous amounts of nickel and/or copper into solution. In

order to determine if tungsten alloys truly pose an environmental threat, however, more corrosion tests should be done on these or similar alloys using local environmental conditions as the parameters.

Corrosion Rates:

In their report, "Corrosion Behavior of High Density Tungsten Alloys," Levy and Chang reported that the tungsten alloys that they tested exhibited satisfactory corrosion rates (less than 10 mpy) for long storage periods. In another report, "Corrosion of High-Density Sintered Tungsten Alloys Part 1: Immersion Testing," by Batten, Mc Donald, Moore, and Silva, the tungsten alloys tested exhibited rates similar to those in the Levy and Chang report. The second report concluded that the corrosion rates were not acceptable. In both cases, however, the reports concluded that the evidence of pitting suggested that the tungsten alloys would lose more strength and ductility than was indicated by the corrosion rates.

Since the two alloys tested in this experiment exhibited corrosion rates similar to those in the mentioned reports and had extensive pitting, the conclusions are the same. The corrosion rates themselves are acceptable for the United States Department of Defense, but the alloys were penetrated deeper in some areas than the corrosion rate in mils per year indicates. The extensive attack of the matrix phase of the alloys and the resulting tungsten grain loss could result in a loss of strength and ductility.

Comparison of Alloys:

The HD-17 (copper-containing) alloy released more of the tungsten grain phase into solution and had higher corrosion rates than the WL-1 alloy. When exposed to salt solutions, both alloys had similar corrosion behavior.

References:

Batten, J., Mc Donald, I., Moore, B., and Silva, V. "Corrosion of High-Density Sintered Tungsten Alloys Part 1: Immersion Testing." Sponsored by the Australian Department of Defense. October 1988.

Gold, K. and Los, Michael. "Environmental Analysis of Tungsten Alloy Penetrators: Manufacturing and Testing Phases of the Life Cycle." Sponsored by US Army Armament Research. May 1996.

G 31 - 72 "Standard Practice for Laboratory Immersion Corrosion Testing of Metals." American Society for Testing and Materials Standard. Philadelphia, Pennsylvania. 1995.

G1 - 90 "Standard Practice for Preparing, Cleaning, and Evaluating Corrosion Test Specimens." American Society for Testing and Materials Standard. Philadelphia, Pennsylvania. 1994.

Lewis, Richard J. Sax's Dangerous Properties of Industrial Materials. Ninth Edition. Van Nostrand Reinhold. New York: 1996.

Levy, M., and Chang, F. "Corrosion Behavior of High Density Tungsten Alloys." Sponsored by US Army Materials Technology Laboratory. August 1987.

Meijer, A. "Environmental Effects of Tungsten and Tantalum Alloys." Sponsored by the Department of the Air Force. June 1996.

Table 1

Metal Toxicity

Alloyed Metal	Threshold Limit Values	Ingestion Limits
Tungsten	insoluble compounds: 5 mg/m^3 soluble compounds: 1 mg/m^3	Oral lethal dose to human: 0.5-5g/kg of body weight
Nickel	insoluble and soluble: 0.05 mg/m^3	Long term exposure safe at 0.02 mg/kg of body weight per day
Cobalt	insoluble and soluble: 0.1 mg/m^3	Dose for human not available
Iron	NA	NA
Copper	insoluble and soluble: 1 mg/m^3	Oral lethal dose to human: 0.12 mg/kg of body weight
Chromium	insoluble and soluble: 1 mg/m^3	Oral lethal dose to human: 71 mg/kg of body weight

Table 2

Alloyed Metals - % of Mass

HD- 17 Alloy	WL-1 Alloy
Tungsten - 77.59 %	Tungsten - 87.63%
Nickel - 14.29%	Nickel - 6.64%
Copper - 6.23%	Iron - 4.25%
Chromium - 1.89%	Manganese - 1.48%

Table 3

Surface Area

HD-17 Sample Number	Surface Area	WL-1 Sample Number	Surface Area
1	18.87679cm^2	10	22.8972cm^2
2	18.67579cm^2	11	22.80094cm^2
3	18.7106cm^2	12	22.88143cm^2
4	18.64689cm^2	13	22.62181cm^2
5	18.66094cm^2	14	22.7918cm^2
6	18.35503cm^2	15	22.77601cm^2
7	18.53458cm^2	16	22.8972cm^2
8	18.28821cm^2	17	22.6449cm^2
9	18.6881cm^2	18	22.72447cm^2

Table 4

HD-17 Alloy

Sample Number	Solution Type	Mass of sample Before the test	Mass of Sample After the test (Uncorrected)	Mass of sample After the test (Corrected)
1	pH 2	84.19185g	83.82875g	83.8314g
2	pH 4	83.76235g	83.24005g	83.2427g
3	pH 7	84.24500g	83.73075g	83.7334g
4	pH12	83.89015g	83.56385g	83.5665g
5	pH 9	83.11350g	82.7805g	82.78315g
6	Stream Water	79.45565g	79.0059g	79.00855g
7	Gulf Water	80.98605g	80.865g	80.86765g
8	2.5% salt	79.26440g	79.1836g	79.18625g
9	5% salt	84.34050g	84.1551g	84.15775g
19	Test sample for mass analysis	87.8892g	87.88655g	87.8892g

Table 5

WL-1 Alloy

Sample Number	Solution Type	Mass of sample Before the test	Mass of Sample After the test (Uncorrected)	Mass of sample After the test (Corrected)
10	pH 2	113.76605g	113.56375g	113.5678g
11	pH 4	112.47555g	112.3962g	112.40025g
12	pH 7	115.00020g	114.93495g	114.939g
13	pH12	111.19715g	111.075g	111.07905g
14	pH 9	113.57390g	113.49375g	113.4978g
15	Stream Water	114.41185g	114.35485g	114.3589g
16	Gulf Water	113.65990g	113.5515g	113.55555g
17	2.5% salt	112.01415g	111.9222g	111.92625g
18	5% salt	112.10725g	111.9982g	112.00225g
20	Test sample for mass analysis	109.50805g	109.504g	109.50805g

Table 6

Ion Concentration of Sea Salt

Ion	Concentration (mg/L)	Ion	Concentration (mg/L)
Chloride	19251	Sodium	10757
Sulfate	2659	Magnesium	1317
Potassium	402	Calcium	398
Carbonate/Bicarbonate	192	Strontium	8.6
Boron	5.6	Bromide	2.3
Iodide	0.22	Lithium	.18
Copper	Trace (<0.03)	Iron	Trace (<0.03)
Nickel	Trace (<0.04)	Zinc	Trace (<0.02)
Manganese	Trace (<0.01)	Molybdenum	Trace (<0.01)
Cobalt	Trace (<0.05)	Vanadium	Trace (<0.04)
Selenium	Trace	Fluorine	Trace (<0.05)
Lead	Trace (<0.005)	Arsenic	Trace (<0.0002)
Cadmium	Trace (<0.02)	Chromium	Trace (<0.0006)
Aluminum	Trace (<0.04)	Tin	Trace
Antimony	Trace	Rubidium	Trace
Barium	Trace (<0.05)	Mercury	None
Nitrate	None	Phosphate	None

Table 7

Corrosion Products of HD-17 Alloy: Day 365

Solution Type - HD-17 Alloy	Surface Corrosion	Crevice Corrosion and Pitting	Solution
pH 2	Covered with black and yellow crystals. Some white and green crystals. Yellow precipitate.	Small pits all over. More pits along bottom edge.	faint greenish yellow
pH 4	Same as above, with green-gold crystals on bottom and some red crystals.	Small pits all over.	greenish-yellow
pH 7	Same as above.	Small pits all over. More yellow crystals in crevices.	greenish-yellow
pH 9	Yellow crystal on top and green-black crystals on bottom. Yellow precipitate.	Small pits all over. Fewer pits on bottom. Most green-black crystals in crevices.	clear
pH 12	Appears grey-brown. Some crystals in different colors (gold, green, white,	Small pits all over. Most crystals in crevices.	clear

	and yellow).		
Stream Water	Green-black and some yellow crystals on top. Brown crystals on bottom. Yellow precipitate.	Small pits all over. Fewer pits on bottom.	yellow tint
Gulf Water	Silver and aqua crystals with some orange, white and yellow. Yellow-green and white crystals on bottom. Aqua precipitate.	Deep pits in matrix covering top. Black ring surrounded by an aqua ring around bottom. Most crystals on bottom in crevices.	light blue tint
2.5% Salinity	Aqua crystals. Some other colors. Aqua precipitate.	Deep pits in matrix covering top.	blue tint
5% Salinity	Same as above with more aqua precipitate and crystals.	Deep pits in matrix covering top. Shallow pits on bottom.	blue tint

Table 8

Corrosion Products of WL-1 Alloy: Day 365

Solution Type - WL-1 Alloy	Surface Corrosion	Crevice Corrosion and Pitting	Solution
pH 2	Orange film on surface. Aqua, brown, red and orange crystals. Orange precipitate.	Small pits and some deep pits all over. Ring on bottom with orange, yellow, red and purple crystals. Orange ring around bottom on beaker.	yellow-orange
pH 4	Covered with yellow crystals, with some orange and brown. Some yellow precipitate.	Small pits and some deep pits all over. Ring on bottom with orange, yellow, red and purple crystals. Orange ring around bottom on beaker.	fairly clear
pH 7	Same as above.	Same as above with fewer pits on bottom.	hazy
pH 9	Same as above with some black, red, and white crystals. White precipitate.	Small pits and some deep pits all over. Some evidence of shallow pits in the tungsten grain.	clear
pH 12	Surface appears red-gold. Few crystals of different colors. White precipitate (very little).	Shallow pits all over, probably in tungsten grain. A few deep pits in the matrix in bottom center. Orange ring on bottom.	clear
Stream Water	White-yellow crystals all over. Some white blobs and brown and orange crystals. Orange and yellow-white precipitate.	Small pits and some deep pits all over. Fewer pits on bottom. Ring on bottom with orange, yellow, red and purple crystals.	fairly clear
Gulf Water	Covered with yellow crystals, with	Small pits and some deep pits all over the	faintly

	some orange and brown. Some yellow-white and orange precipitate	bottom. None on top. More pitting along edge of bottom. Ring on bottom with orange, yellow, red and purple crystals.	yellow
2.5% Salinity	Mostly covered with green crystals. Some orange, white, yellow and brown-black. White and yellow precipitate.	Small pits and some deep pits all over the bottom. None on top. More pitting along edge of bottom. Small orange ring on bottom.	faintly greenish-yellow
5% Salinity	Same as above.	Same as above.	faintly greenish-yellow

Appendix I: Solution Analysis Results

Metal concentrations in tables are given in µg / L.

HD-17 pH 2

	DAY 1	*DAY 30*	*DAY 90*	*DAY 180*	*DAY 365*
Copper		6580	8280	13800	30600
Iron		112	122	125	126
Chromium		9.7	12.7	16.3	18.3
Nickel		9440	10900	17600	34900
Tungsten		44700	71400	128000	122000
pH	2	2.52	2.57	2.63	2.67

HD-17 pH 4

	DAY 1	*DAY 30*	*DAY 90*	*DAY 180*	*DAY 365*
Copper	6.4	673	871	2140	3680
Iron	11.1	71.2	79.9	58.2	40
Chromium	1.1	4.7	8.1	14.4	18.7
Nickel	8.9	2610	3020	5380	8400
Tungsten	1.1	64300	108000	216000	203000
pH	4	3.32	3.26	3.23	3.09

HD-17 pH 7

	DAY 1	*DAY 30*	*DAY 90*	*DAY 180*	*DAY 365*
Copper	.6	327	398	740	2290
Iron	11.1	46.7	61.7	64.2	27.8
Chromium	1.1	3.8	7.2	11.7	19.3
Nickel	1.1	1400	1690	2450	6840
Tungsten	1.1	79900	169000	304000	331000
pH	7	3.91	3.62	3.4	3.16

HD-17 pH 9

	DAY 1	*DAY 30*	*DAY 90*	*DAY 180*	*DAY 365*
Copper		28	30.9	60	886
Iron		37.5	51	63.40	74.4
Chromium		3.3	8.5	12.6	23.9
Nickel		1160	1460	1560	3820
Tungsten		85600	154000	281000	408000
pH	9	6.62	5.74	5.29	3.4

HD-17 pH 12

	DAY 1	*DAY 30*	*DAY 90*	*DAY 180*	*DAY 365*
Copper	2.5	6.1	4.3	6.6	122
Iron	11.1	11.1	11.1	11.1	37.7
Chromium	1.5	1.5	11.4	8.5	6.3
Nickel	1.1	20.1	256	724	2880
Tungsten	4.4	90500	166000	336000	469000
pH	12	7.17	8.11	7.81	6.24

HD-17 Stream Water

	DAY 1	*DAY 30*	*DAY 90*	*DAY 180*	*DAY 365*
Copper	0.6	251	290	906	1920
Iron	97.6	123	138	163	123
Chromium	1.1	3.3	6.8	14.9	22.1
Nickel	1.1	1070	1360	2470	4940
Tungsten	1.1	59000	127000	328000	373000
pH		4.17	3.78	3.37	3.08

HD-17 Gulf Water

	DAY 1	*DAY 30*	*DAY 90*	*DAY 180*	*DAY 365*
Copper	8.7	1330	1610	194	417
Iron	163	1570	1200	11.1	1890
Chromium	7.5	2.8	9.4	9.3	4
Nickel	25	480	6730	18800	19400
Tungsten	1.1	61900	114000	182000	154000
pH		6.41	7.56	7.6	5.89

HD-17 2.5% Sea Salt

	DAY 1	*DAY 30*	*DAY 90*	*DAY 180*	*DAY 365*
Copper		1220	746	1150	700
Iron		423	549	86.5	831
Chromium		3	7	5.3	3.8
Nickel		3880	10400	20700	24200
Tungsten		53800	111000	132000	75600
pH		6.55	7.46	7.26	6.01

HD-17 5% Sea Salt

	DAY 1	*DAY 30*	*DAY 90*	*DAY 180*	*DAY 365*
Copper	8.9	1300	327	2060	1520
Iron	11.1	1450	1310	32.8	2080
Chromium	7.7	4	18.8	12.4	5.4
Nickel	31.3	4670	8320	21100	18000
Tungsten	4.5	467007	102000	203000	147000
pH		7.08	7.83	7.82	6.64

WL-1 pH 2

	DAY 1	*DAY 30*	*DAY 90*	*DAY 180*	*DAY 365*
Copper		1.6	.6	.6	7.7
Iron		14800	24700	180	2760
Chromium		2.4	3.9	1.1	1.7
Nickel		34300	58900	89800	103000
Tungsten		12300	23200	3620	11000
pH	2	2.99	3.66	6.84	6.72

WL-1 pH 4

	DAY 1	*DAY 30*	*DAY 90*	*DAY 180*	*DAY 365*
Copper	6.4	.6	.6	.6	1.4
Iron	11.1	1370	473	74.8	1750
Chromium	1.1	1.1	1.1	1.5	1.3
Nickel	8.9	10800	14900	21500	22500
Tungsten	1.1	4130	4240	4270	1870
pH	4	5.15	7.10	7.33	7.02

WL-1 pH 7

	DAY 1	*DAY 30*	*DAY 90*	*DAY 180*	*DAY 365*
Copper	.6	.6	.6	.6	3.4
Iron	11.1	185	93.7	107	736
Chromium	1.1	1.1	1.1	2.1	1.4
Nickel	1.1	6160	10600	18300	17400
Tungsten	1.1	9500	8530	7160	2020
pH	7	6.71	7.31	7.54	7.07

WL-1 pH 9

	DAY 1	*DAY 30*	*DAY 90*	*DAY 180*	*DAY 365*
Copper		.7	.7	.6	1.1
Iron		210	49.4	67	163
Chromium		1.1	1.3	2.3	1.3
Nickel		5070	9440	15000	15800
Tungsten		20000	35700	33100	22800
pH	9	7.02	7.46	7.67	7.35

WL-1 pH 12

	DAY 1	*DAY 30*	*DAY 90*	*DAY 180*	*DAY 365*
Copper	2.5	.6	.6	.6	1.5
Iron	11.1	11.1	11.1	11.1	318
Chromium	1.5	1.7	13.2	16.6	4.4
Nickel	1.1	95.1	1600	327	1900
Tungsten	4.4	53500	104000	142000	176000
pH	12	8.02	8.32	8.45	7.82

WL-1 Stream Water

	DAY 1	*DAY 30*	*DAY 90*	*DAY 180*	*DAY 365*
Copper	.6	1.1	.8	.6	1.8
Iron	97.6	733	491	132	1260
Chromium	1.1	1.1	1.2	2.1	1.6
Nickel	1.1	5670	10200	15500	19000
Tungsten	1.1	5440	5200	3290	829
pH		6.88	7.40	7.56	7.28

WL-1 Gulf Water

	DAY 1	*DAY 30*	*DAY 90*	*DAY 180*	*DAY 365*
Copper	8.7	7.1	9.6	10.4	13.3
Iron	163	4220	3030	56.5	8330
Chromium	7.5	3.7	8.8	11.3	4.9
Nickel	25	16700	21000	22800	22600
Tungsten	1.1	11700	16000	17500	61200
pH		7.52	7.86	7.84	7.08

WL-1 2.5% Sea Salt

	DAY 1	*DAY 30*	*DAY 90*	*DAY 180*	*DAY 365*
Copper		5.3	7.5	6	6.5
Iron		2380	1620	99.8	1680
Chromium		4.4	7.3	9.8	4.1
Nickel		8620	13800	19200	11100
Tungsten		6080	7290	9840	8550
pH		7.78	7.89	7.86	7.42

WL-1 5% Sea Salt

	DAY 1	*DAY 30*	*DAY 90*	*DAY 180*	*DAY 365*
Copper	8.9	6.9	7	13.4	13.8
Iron	11.1	1610	1570	32.6	5120
Chromium	7.7	3.9	4.8	10.8	7
Nickel	31.3	8330	17100	19100	14700
Tungsten	4.5	10700	16600	18700	35900
pH		7.82	7.86	7.85	7.5

Appendix II: Mass Loss Analysis Results

HD-17 Alloy	Mass Loss	Corrosion Rate	WL-1 Alloy	Mass Loss	Corrosion Rate
pH 2	0.36045g	0.44643 mpy	**pH 2**	0.19825g	0.19493 mpy
pH 4	0.51965g	0.64427 mpy	**pH 4**	0.0753g	0.07442 mpy
pH 7	0.5116g	0.63018 mpy	**pH 7**	0.0612g	0.05967 mpy
pH 9	0.33035g	0.41012 mpy	**pH 9**	0.0761g	0.07494 mpy
pH 12	0.32365g	0.39901 mpy	**pH 12**	0.1181g	0.11708 mpy
Stream Water	0.4471g	0.56837 mpy	**Stream Water**	0.05295g	0.05188 mpy
Gulf Water	0.1184g	0.14942 mpy	**Gulf Water**	0.10435g	0.1027 mpy
2.5% salt	0.07815g	0.09906 mpy	**2.5% salt**	0.0879g	0.08664 mpy
5% salt	0.18275g	0.22478 mpy	**5% salt**	0.105g	0.1043 mpy

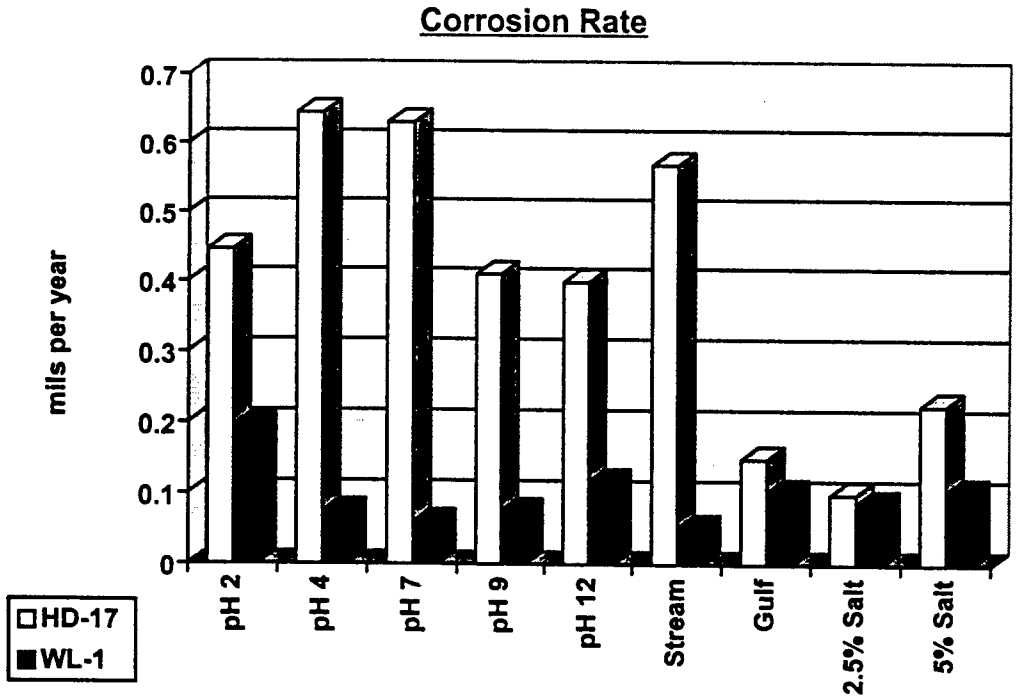

VERIFICATION OF THE STATE OF CHEMICAL EQUATIONS AND THE GENERATION OF TEXTURES FOR PHENOMENOLOGY MODELING

David S. Revill
WL/MNGA

Choctawhatchee High School
110 Racetrack Road
Ft. Walton Beach, FL 32548

Final Report for:
High School Apprentice Program
Wright Laboratory

Sponsored by:
Air Force Office of Scientific Research
Bolling Air Force Base, DC

and

Wright Laboratory

August 1997

VERIFICATION OF THE STATE OF CHEMICAL EQUATIONS AND THE GENERATION OF TEXTURES FOR PHENOMENOLOGY MODELING

David S. Revill
Choctawhatchee High School

Abstract

The first task in the project was to create a program which would be able to determine whether or not a chemical equation was balanced. This first task was performed primarily for the purpose of gaining knowledge of the programming language and capabilities of the C. In an effort to increase portability, the program was written in ANSI C.

The second task of the project was to generate textures for phenomenology modeling using Irma software. Irma software, created by Nichols Research Corporation of Shalimar, FL, models various scenes as they would be seen using either a passive infrared sensor, passive millimeter wave sensor, active millimeter wave sensor, or a Laser Radar (LADAR) sensor. The ability to generate these images provides an inexpensive way for the testing of sensors used in state of the art seeker systems. To generate the physical pieces of the image, (thus not including all of the data that goes along with every object incorporated into a scene, i.e. weather, temperature, reflectance properties, location, etc.) Irma uses facets and textures. Since it would be nonsensical to make a facet for every blade of grass, textures are used to simulate grass, sand, cement, or whatever the surface may be. In this project, texture files for grass, sand, and water were generated.

VERIFICATION OF THE STATE OF CHEMICAL EQUATIONS AND THE GENERATION OF TEXTURES FOR PHENOMENOLOGY MODELING

David S. Revill

Introduction To First Task

The first task at hand was to design a computer program using the C programming language. The program was designed to indicate whether or not chemical equations were balanced. The source code was developed over a period of three weeks. During this time span, the code was planned, written, tested, and then given to a chemist in the Fuzes Branch of Eglin Air Force Base for further testing. In the final stages of the testing, the executable program was given out to various chemists in the Laboratory for testing the extreme conditions of the program. The program will be made available to anyone at Wright Laboratory, Eglin Air Force Base whose work warrants the use of this program. A users guide is included in Appendix A and a structure chart is included in Appendix B.

Methodology

1. Planning

Planning took place throughout the writing of the code. The code was written in stages. Each module of the program was planned, written, debugged, and tested separately. The planning stage, obviously, did not take place all at once. During the planning stage, research of the appropriate style and syntax for each of the modules was conducted using the ANSI standard for C programming. Then, the program structure was designed via

handwritten pseudocode. The pseudocode was then studied and mentally checked before the next stage of the actual writing of the code was performed.

2. Writing

The source code was written following the model of the pseudocode which was developed in the planning stage. The writing of the code took place on a Sun Workstation, but was later moved to a personal computer with the Borland C++ Version 4.0 compiler. Appropriate comments were made throughout the program to make future updates as simple as possible. The comments would also serve to aid in any future debugging that may have to occur. Following the writing of each module of the program, debugging occurred.

3. Debugging

The debugging stage is always the most interesting stage of programming. It can also be the most frustrating. Due to certain oddities of the compiling of the code, sometimes extremely unexpected and unexplainable events occur. Some of the typical erroneous events that occurred in the debugging of the program included randomly repeating certain procedures within the program when the end of the program should have been reached, and certain infinite loops that occurred due to the fact that the input statement was never aware that a carriage return symbol should have been read when the equation was read from a file. All of these strange occurrences were overcome via trial and error of different methods. The primary manner in which the problems were corrected was through the tracing of the program to see where the problem was occurring. This method was extremely helpful in the correcting of infinite loops. To correct the first mistake of

randomly repeating different procedures when the end of the program was reached, the last function had to be taken out of function form and placed in the main program block. In order to allow the carriage return to be distinguished in the file, a different type of input statement had to be used. Other minor corrections of course had to be made, but no others were as interesting as the before mentioned examples. No complete redesigning of the code structure was necessary throughout the debugging stage. After each and along with each stage of debugging, testing of the program occurred over and over again.

4. Testing

Testing occurred in many phases of the project. Testing of each of the modules occurred throughout the writing of the source code. More extensive testing was also done after completion of the writing of the source code. No one part of the program tested perfect on the first try, but again, no part of the code had to be completely scratched and redesigned either. The tests were performed based on the compiling of the code with the Borland C++ Version 4.0 compiler. Further tests are planned using other compilers such as the SparCompiler C Version 2.0 for Sun Workstations. Tests on other machines would test the portability of the code. The hypothesis would be that the majority of the test would be successful because the conventions used in the writing of the source code were based on the ANSI standard, which is the definitive core of C programming.

The program works by inputting an equation in through a command line input, or multiple equations through an input file. The program then breaks them down into multiple reactants and products, which are then further broken down into the necessary components such as coefficients and subscripts. Those elements are stored in a

multidimensional array. The program will then check to determine if each side of the equation is equal and then sends the output to the screen and to an output file.

Future Upgrades

Many possible future upgrades to the program exist. The primary upgrade would of course be to perform the actual balancing of the chemical equations. This could be done simply by having the program check to see if the equation was balanced, then updating the coefficients, then repeating the process until the equation was balanced. Another possible upgrade would be to simply allow for a longer equation. The equation string, as of now, allows for 44 characters with up to fourteen reactants and fourteen products. The use of comments to form a variable dictionary makes the improving of this factor implicitly easy. Another possible upgrade to the program would be to allow for the use of parenthesis in the representation of the equation. Parenthesis are usually used to indicate polyatomic ions. Another upgrade would be to create a *Microsoft*® *Windows*™ GUI interface. A GUI interface is of course not necessary, but is always useful if the program were ever to be used by a novice computer user.

Skills Developed

The skills developed in the writing of this program go beyond simply learning C. Although that in itself was a large portion of the work that went into the writing of this program. Another result that came out of this project was the ability to use the UNIX operating system. Above all else in this project, the ability to come up with logical

algorithms, a firm grasp of fundamental program designs, and the strengthening of the ability to reason were the grander skills that were acquired in the development of this project.

Conclusions

The results of this project were quite successful. All program testing was successful. The program was also tested by a local chemists who gave the program top ratings. Future applications of this program could be for various professions. Pharmacists, chemists, chemical engineers, teachers, and almost anyone in the field of science could use this program to check to see whether or not their chemical equations are balanced. Although the span of time that was taken to complete the project may seem extensive, most of that time was spent learning C and UNIX, which were the real goals of the project.

Introduction To Second Task

Textures of grass, sand, and water were created for use with Irma software. The textures that were created are appropriate considering the landscape of the testing facilities of Eglin Air Force Base. The Irma software uses these textures in conjunction with facets and other objects to create realistic scenes as seen from the output of sensors from state of the art seekers. For example, Irma could render a scene with a faceted image of a tank and a tree. These facets could be placed on a square plate background that was painted with a grass texture.

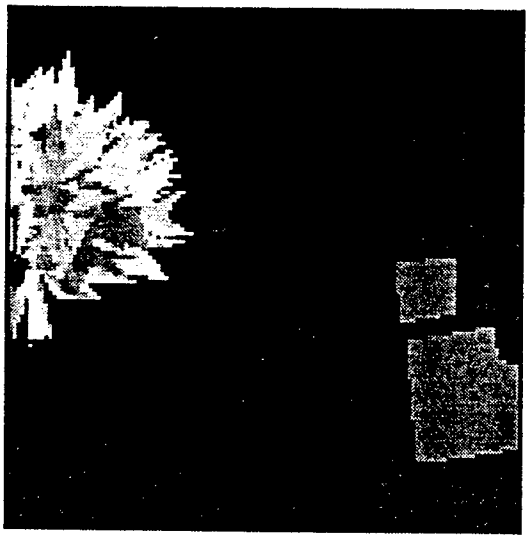

Figure 1 - Synthetic Image of brick tank and tree on a grass texture.

After rendering the passive infrared (IR) image, a radiance image of a brick tank and a tree would appear in a grassy field, analogous to one seen through an IR sensor. To receive an actual output from an IR sensor would be extremely expensive, but Irma allows the generation of the image extremely cost efficiently. All that is necessary to run Irma is the software and either a UNIX workstation or a PC.

An observation that should be noted in the report on textures is their relation to fractal images. While textures are not fractal images, there is a similar manner of thinking between the two fields. Both fractals and textures represent a mathematical approach to images and a manner of replicating nature. Fractal images and textures can be represented by a system of equations and thus both require respect in that manner of thinking.

Discussion of the Problem

The problem that was addressed in the project was to actually generate the textures by using only the text files associated with Irma. The texture files are in the format of table 1.

N	f_c	T_o	T_m	T_e	T_b
C_1	C_2	C_3	...	C_N	
P_1	P_2	P_3	...	P_N	
ϕ_{xy}	ϕ_z	R_{xy}	P_z	x_t	y_t
t_m	t_σ				
$d_\sigma^{\%}$	$T_\sigma^{\%}$				

Table 1

where

N	=	number of sine terms in the series.
f_c	=	cutoff frequency factor.
T_o	=	average offset for the sines and governs the texture contrast.
T_m	=	defines threshold of the function at the center of the quadric.
T_e	=	defines the threshold of the function at the edge of the quadric.
T_b	=	not used in this type of texture (must be set to a non-zero.
$C_1, C_2, C_3 \ldots C_N$	=	the sine coefficients.
$P_1, P_2, P_3 \ldots P_N$	=	the periods for each of the sine waves in summation.
ϕ_{xy}	=	controls the coupling strength of the x sines with y and the y sines with x.
ϕ_z	=	defines the vertical coupling strength.
R_{xy}	=	x-y period ratio parameter.
P_z	=	the period of phase shifting due to elevation.
x_t	=	the world x coordinate for the origin of the texture.
y_t	=	the world y coordinate for the origin of the texture.
t_m	=	mean value of the texture function.
t_σ	=	standard deviation of the texture function.
$d_\sigma^{\%}$	=	percentage of the reflectance that defines one standard deviation (1σ).
$T_\sigma^{\%}$	=	percentage of the temperature which defines one standard deviation (1σ).

Table 2

The equation which represents the texture images is shown below in figure 2.

$$t = \left(\frac{1}{a}\sum_{i=1}^{N}(C_i S_i^x + T_o)\right)\left(\frac{1}{a}\sum_{i=1}^{N}(C_i S_i^y + T_o)\right)$$

$$S_i^x = \sin\left(\frac{2\pi}{P_i}(x + x_t) + \phi_{xy} S_{i-1}^y + \Phi(z)\right) \qquad S_0^x = \sin\left(\frac{2}{P_1}(x + x_t)\right)$$

$$S_i^y = \sin\left(\frac{2\pi}{P_i}(y + y_t) + \phi_{xy} S_{i-1}^x + \Phi(z)\right) \qquad S_0^y = \sin\left(\frac{2}{P_1}(y + y_t)\right)$$

$$\Phi(z) = \phi_z \sin\left(\frac{2\pi z}{P_i}\frac{P_z}{P_1}\right)$$

$$a = \sum_{i=1}^{N}(C_i + T_o)$$

Figure 2 - Texture Equation

The textures were to be generated based on empirical methods due to the fact that all of the necessary statistical data had already been generated (e.g. temperature, reflectance properties, etc.). The textures were painted to a square plate for evaluation. The goal was to find textures with attributes similar to those of grass, sand, and water. True validation of the textures would come at a later date.

Methodology

Several methods were explored in the process of generating useful textures. There are very few limitations when it comes to the values that can be modified in the texture file. The two exceptions are the values for t_m and t_σ. The first method that was approached

was to create single term series textures. The simplest single term series texture would look something like table 3.

1.0	10.	0.0	0.0	0.0	1.0
1.0					
10.					
0.0	0.0	1.0	0.0	0.0	0.0
0.0	0.492				
10.0	0.0				

Table 3

The basis of the first method was to keep the coefficients and periods as simple as possible and to adjust the other values in order to create the desired effect. It was hypothesized that by keeping the coefficients and period simple, that this would be the most effective and efficient manner of creating textures. However, by keeping the coefficients and periods simple, almost all of the textures that were created were undesirable. Fortunately one desirable texture was created with this method. A sand texture was created by taking the repetitive nature of the texture to be very large scale. Thus, only having the texture repeat itself once in a very large area. The sand texture was created with table 4.

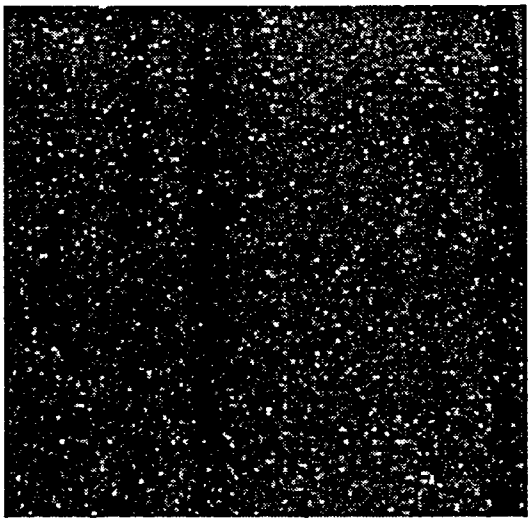

Figure 3 - Sand texture.

1.0	10.	0.0	5.0	0.3	1.0
0.06					
0.5					
50.0	10.0	0.001	66.1	0.0	0.0
0.0	0.786				
0.0	12.0				

Table 4

The problem with the single term method was that the textures became very uniform and repetitive. What was needed was textures that were more random and unpredictable in their design. The realization that a more random texture was needed led to the next method.

For the second method, all of the parameters were generally kept as simple as possible and different sequences of numbers with a strict mathematical approach were used for the coefficients and periods in the now seven term series. This approach definitely appeared more beneficial. It was through this method that the water texture was created. An example of one of the series that was used would be the y values of a sine wave at 30 degree intervals and a linear set of numbers for the coefficients (e.g. $P_N=\text{Sin}(30 * C_N)$ where C = 1, 2, 3, 4, 5, 6). The file for that example, and also the file for the water texture looks like table 5.

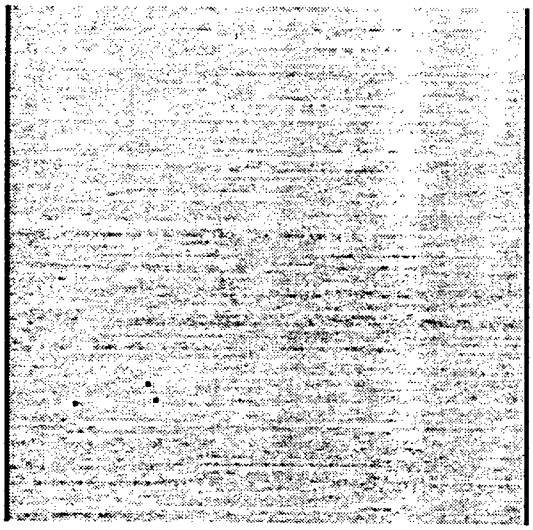

Figure 4 - Water texture.

6	10.0	0.76	0.0	0.0	1.0
1.0	2.0	3.0	4.0	5.0	6.0
0.5	0.866	1.0	0.866	0.5	0.0
5.0	0.0	100.0	1.0	0.0	0.0
0.0	1.0				
0.0	12.0				

Table 5

The mathematical series method was also unbeneficial in the fact that it too gave results that were extremely repetitive. Additionally, in many examples of this method, the texture appeared as a series of multiple sine waves. Obviously not what was needed.

In the third method, random numbers were used in the coefficients and periods and all other values were kept extremely simple. This method was taken because of the apparent need for a more random appearance in the textures. The origin of the numbers was a phone book. The phone book was chosen because it was an extremely accessible source of random numbers. An additional advantage of using a phone book for random numbers is that all of the phone numbers have seven digits and seven term series were desired. With the use of this method, several grass textures were created. Originally, in order to find values for the coefficients and periods, the sine of each digit of the phone number was taken and multiplied by 100. Table 6 represents the previous described algorithm and one of the grass textures.

Figure 5 - A grass texture.

7	10.0	0.76	0.0	0.0	1.0	
13.917	10.45	5.234	6.976	6.976	5.234	13.917
10.45	8.716	1.745	1.745	5.234	12.187	12.187
5.0	0.0	1.0	1.0	0.0	0.0	
0.0	1.0					
0.0	12.0					

Table 6

It was later found that simply using the digits of the phone number worked equally well. To ensure the highest degree of randomness, the first three digits of each of the two phone numbers used (one for the coefficients and one for the periods) should be different.

Results

The results of the project appear to be extremely worthwhile. The extensive validation of the textures will not come until a later time in the year. Some preliminary validation results, however, appeared encouraging. Textures were created for the three desired types: grass, water, sand. The water texture was created using the second method of mathematical series. The sand was created using the first method of single term series. Several different grass textures were created with the third, random number, method. The validation that was done on these textures was simply to compare the textures that were generated to actual pictures from an IR sensor. The IR images came from the dataset of the Smart Weapons Operability Enhancement Joint Test and Evaluation program (SWOE JT&E). Figure 7 came from a scene of Greyling, Michigan taken with an IR sensor. Only the grass texture could be checked in this manner because no IR

Figure 6 - synthetic grass texture

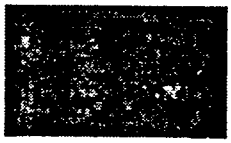

Figure 7 - actual grass from IR image

pictures of water and sand could be found. The results of the qualitative validation were extremely good. The grass textures appeared very similar to those of the actual IR images. There are multitudinous possibilities for additional grass textures because of the wide array of random seven digit series.

Conclusion

It was obvious that the most efficient and productive manner of creating textures was via the random number method. One possible improvement that could be made to the project later would be a random number generator that could generate two sets of seven numbers that could span a wider array that the digits in a phone book. Having the numbers in a wider array would definitely allow for more possibilities and perhaps more exacting textures.

References

"Data Analysis and Modeling: Irma 4.0 User's Guide." Nichols Research Corporation. Nov. 1995.

Kernighan, Brian W. and Dennis M. Ritchie. *The C Programming Language*. Prentice Hall PTR: Englewood Cliffs, New Jersey, 1988.

Mandelbrot, Benoit B. *The Fractal Geometry of Nature*. W. H. Freeman and Company: New York, 1977.

Vechinski, Douglas A. "Controlling Irma 3.2 Textures (Instructional Session)." Nichols Research Corporation.

Welsh, James P. "Smart Weapons Operablity Enhancement (SWOE) Joint Test and Evalutation (JT&E) Program: Final Report." Aug. 1994.

Acknowledgments

I would first like to thank my mentor, Lt. Vince Underwood, for his superior knowledge, assistance, and friendship. His ideas, insight, and tutelage shall follow me for years. Next, I would like to thank Mr. Mike Deiler for his UNIX proficiency and for helping me in my quest to learn the UNIX OS. I would also like to thank Mr. Don Harrison, Mrs. Jeanette Williams, and Mr. Mike Deiler for their support of the 1997 High School Apprentice Program. I would also like to thank Mr. Lee Prestwood for his assistance with the Irma software and for the loan of so many books. Another heartfelt thanks goes out to Mr. Tom Potowski for his cheery "Good Morning" every day that I came into the office. I would also like to thank all the apprentices who I ate lunch with for the delightful conversation and exchange of ideas: Chris Clark, Aaron Davis, Neil Harrison, Alex Lippert, Dan Murchison, Katie Pirog, and Kristan Raymond. I would also like to thank all the rest of the apprentices for their support. An added thanks is given for the support of everyone in MNGA. An acknowledgment must go to the Wright Laboratory Armament Directorate for sponsoring the High School Apprentice Program. Final thanks is given to Research & Development Laboratories (RDL) and the Air Force Office of Scientific Research (AFOSR).

APPENDIX A

Users Guide

- Run the executable file, "checker.exe"
- At the menu, enter either "A", "B", or "Q" depending on whether you would like to test your equation, view the list of balanced equations, or quit, respectively. Note: this program is *not* case-sensitive.
- If "A" was chosen, enter you equation in the form:

  "`Reactant + Reactant --> Product + Product;`"

  After pressing <ENTER>, then program will then tell you whether or not your equation was balanced and prompt you to go back to the main menu. You may quit the program from the main menu if you wish.
- If "B" was chosen, the program will print a list of all the balanced equations from the file "equation.txt". You may view these equations later by viewing the file, "balanced.txt". You may also modify the file "equation.txt" using a standard text editor to suit your needs.
- If "Q" was chosen, the program will end execution.

APPENDIX B

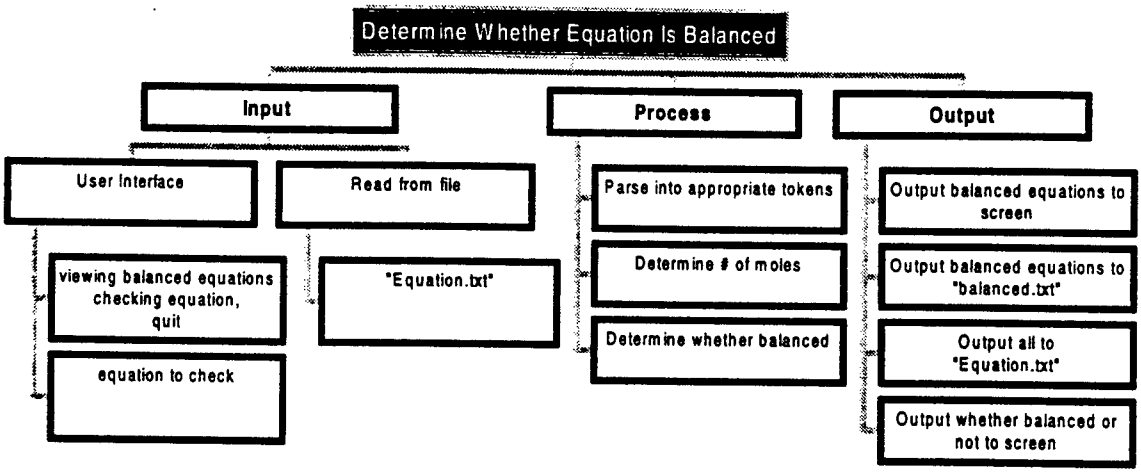
Determine Whether Equation Is Balanced
Input
Process
Output
User Interface
Read from file
Parse into appropriate tokens
Output balanced equations to screen
viewing balanced equations
checking equation,
quit
"Equation.txt"
Determine # of moles
Output balanced equations to "balanced.txt"
Determine whether balanced
Output all to "Equation.txt"
equation to check
Output whether balanced or not to screen

A STUDY OF THE CAPABILITIES OF COMPUTATIONAL FLUID DYNAMICS TECHNOLOGY TO SIMULATE THE FLIGHT PERFORMANCE OF A CRUCIFORM WING-BODY AT SUPERSONIC SPEEDS

Harris T. Schneiderman

The Miami Valley School
5151 Denise Drive
Dayton, OH 45429

Final Report for:
High School Apprentice Program
Wright Laboratories

Sponsored by:

Air Force Office of Scientific Research
Bolling Air Force Base, DC

and

Wright Laboratories

August 1997

A STUDY OF THE CAPABILITIES OF COMPUTATIONAL FLUID DYNAMICS TECHNOLOGY TO SIMULATE THE FLIGHT PERFORMANCE OF A CRUCIFORM WING-BODY AT SUPERSONIC SPEEDS

Harris T. Schneiderman
The Miami Valley School

Abstract

The performance of a cruciform wing-body missile at supersonic speeds was studied from wind tunnel data obtained in a previous experiment. A structured grid was generated around a computerized model of the missile's geometry and then analyzed using the General Aerodynamics Simulation Program (GASP). Both tests were given the objective of determining the coefficient of pressure (Cp) at various axial positions along the missile body. The results of each test were compared to determine the amount to which they agree. Experimental results indicate that readings for coefficients of pressure obtained in a wind tunnel can be effectively simulated strictly by a computer that utilizes computational fluid dynamics equations and techniques. Thus, computer simulation can be a viable alternative to wind tunnel testing for generating accurate and reliable performance data for a flying body.

A STUDY OF THE CAPABILITIES OF COMPUTATIONAL FLUID DYNAMICS TECHNOLOGY TO SIMULATE THE FLIGHT PERFORMANCE OF A CRUCIFORM WING-BODY AT SUPERSONIC SPEEDS

Harris T. Schneiderman

Introduction and Discussion of Problem

The ability to determine the capabilities of a flying body under specific conditions using practical and effective testing methods has always been a goal of aerodynamicists. Actual test flying is not always possible in the initial stages of development and often results in the destruction of the prototype, which can become quite costly. The discovery that accelerating air over a stationary body can produce the same effect as the body flying through the air was a giant leap forward for the field of aerodynamics. It led to the creation of wind tunnel testing facilities in order to simulate flight performance. This alternative method of testing was far more effective because it allowed greater flexibility in the manipulation of the environmental variables under which tests were conducted and it posed little danger to the prototype aircraft.

Another method of predicting the performance of a flying body is that of Computational Fluid Dynamics (CFD) which falls under the field of "Computational Aerodynamics." This technique relies upon mathematics, primarily the Navier-Stokes equations, to numerically simulate real-world behavior of aircraft. Computational Fluid Dynamics did not become a practical analytical technique until the last two decades. The reason is because the solutions to the Navier-Stokes equations are far too difficult to obtain without the assistance of a high-powered computer. Thus, CFD only became a viable alternative to wind tunnel testing with the advent of the rapid arithmetic capabilities of today's computers {1}.

Computational Fluid Dynamics can often be a more desirable analysis method than wind tunnel testing for a number of reasons. The first reason is the ease with which various flight conditions can be simulated with CFD as opposed to wind tunnel testing. For example, the majority of wind tunnels currently in use have limited setting capabilities for such variables as Mach number, Reynolds number, and other critical values. This often necessitates operating and maintaining multiple wind tunnels to obtain data over a broad range of values. With CFD, the same aerodynamics simulation program can be used over a much wider range of variables because the relevant equations are included in the same software package. Thus, CFD can be more advantageous because no physical restrictions exist in a computer simulated test. The most significant advantage of CFD over wind tunnel testing is the sizable difference in cost to the experimenter. While computer equipment and software can often be expensive, the overall cost

is far less when compared with that of maintaining and operating a wind tunnel facility. This can offer tremendous benefits to anyone in the field of aerodynamics research, especially during times of budget cutbacks which necessitate wind tunnel closings. The potential for savings to researchers, business owners, and consumers makes continued research in the field of CFD very critical for the near future.

The difficulty with using CFD lies in the question of reliability. It is a relatively new technique as compared to wind tunnel testing. There are many varieties of CFD software currently on the market and also different techniques for researchers to obtain computational solutions. As countless experiments have shown, experimental results in any field of study quite often do not coincide with those predicted by theory. Therefore, it is important for any researcher who uses CFD to have verification that the software and processes being used produce accurate data as compared to that of a wind tunnel. Only after this has been accomplished can such data be used with any confidence. Once this has been achieved, wind tunnel testing can be rejected in favor of more cost-effective CFD methods.

Symbols

A	body cross-sectional area,	$\pi*d^2/4$
Cp	pressure coefficient,	$(P - P_\infty)/Q$
d	body diameter, cm	
M	free-stream mach number	
P	measured surface pressure, kPa	
Q	free-stream dynamic pressure, kPa	
R	free-stream Reynolds number based on body diameter	
X/D	axial distance from wing leading edge nondimensionalized by body diameter	
α	angle of attack, degrees	
θ or T	angular location of pressure orifices, degrees	
	sign(y)*acos(2*z/d)*(180/π) + 180*(1-sign(y))	
ϕ	roll angle, degrees	

Facility Abbreviations:

HSWT	The Vought Corporation High Speed Wind Tunnel Facility
NYU	The Aerospace and Energetics Laboratory at New York University
UPWT	Langley Unitary Plan Wind Tunnel

Methodology

Tunnels

Vought High Speed Wind Tunnel.- This facility is an atmospheric exhaust, blowdown tunnel with a test section 1.2 meters by 1.2 meters and a Mach number capability ranging from 0.5 to 5.0. Air storage is handled by six tanks capable of a maximum pressure of 4,137 kPa and a nominal temperature of 311 K.

New York University Aerospace and Energetics Laboratory.- This laboratory facility contains a blowdown tunnel having a test section of dimensions 0.261 meters by 0.203 meters.

Langley Unitary Plan Wind Tunnel.- This facility is a variable-density, continuous-flow tunnel that houses two test sections of dimension 1.2 meters by 1.2 meters. The tests were conducted in the section for lower Mach numbers with a capability ranging from 1.5 to 2.9.

Wind Tunnel Models and Instrumentation

A strain-gage balance housed within the missile model and attached to a string support system was used to obtain the force and moment measurements. The balance used for the UPWT test had a normal-force capacity of 1,779 Newtons. The balance used for the HSWT test had a normal-force capacity of 8,896 Newtons.

The pressure data was obtained through the use of 208 pressure orifices located circumferentially around the body. The most densely instrumented region was the windward wing-body interaction area so as to more effectively capture the data from the large pressure gradients that occur there. Electrical transducers connected to a pressure scanning system were used to measure pressure data. Precision mercury manometers were used to independently measure the tunnel free stream pressures.

Computational Grid

The grid was created around a database generated by a Computer Aided Design (CAD) system. It was constructed such that each computational unit of the database corresponds to one centimeter of the missiles actual size. The computational grid was generated by the GRIDGEN version 12 software from Pointwise on a Silicon Graphics Indigo 2 Workstation. A structured grid was chosen to increase the precision of the data obtained. (A similar study was conducted by another researcher using an unstructured grid.) Accelerated training in the use of GRIDGEN was undertaken by the researchers to ensure a thorough understanding of the software to increase the quality of the final flow solution.

The grid was composed of ten distinct zones or three-dimensional regions of computational space. These zones were formed from sixty-four domains (two-dimensional regions of computational space) which were created from 101 separate connectors. Only one side of the missile was gridded because of the symmetric geometry of the body. Such a configuration allowed the data from one side of the solution to be mirrored onto the other side, thereby eliminating the need to grid both halves of the missile. Zone One (see

figure 9) covered the missile's nose. Zone Two fit between the nose and the fins of the missile. Zone Five was constructed behind the fins up to the rear of the missile and contained the grid's exit plane. No portion of the grid covered areas behind the missile because the flow solution was entirely supersonic which eliminated any chance of backflow. Zones Six and Seven were built between each pair of fins. Zones Three and Four were constructed on top of Zones Six and Seven. Zones Eight, Nine, and Ten were positioned as projections off the fin tips.

Rigid spacing requirements were enforced in the dimensioning of the grid to ensure continuity throughout and maximize the accuracy of the data obtained. The grid point spacing along critical areas (such as the nose and fins) was set to 0.005 grid units. (These areas area considered critical because the gradients of momentum are high in these regions. Therefore, an increased number of grid points is needed in order to capture these large gradient changes.) Spacing along the nose grew geometrically from the tip. Spacing along the leading and trailing edges of the fins was tightly packed on the edges and grew inward. All connectors emanating radially from the body were given a spacing of 0.0005 grid units. This spacing grew geometrically from the body to the outer edges of the grid. The remaining connectors were given an equal spacing of no more that 0.5 grid units.

Cells (the three-dimensional building blocks of zones) perform the same function of measuring data as do the pressure taps in the wind tunnel experiment. Thus, it was critical to ensure that a sufficient number of grid points were used so as to produce a solution of equal of greater precision than that obtained from the wind tunnel. Critical areas such as the nose and fins were contained by far more cells since they were dimensioned with more grid points due to the complexity of the data in these regions. Zone One (see figure 9) was comprised of 168,000 cells and 177,327 grid points. Zone Two was constructed from 60,480 cells and 66,063 grid points. Zones Three and Four each contained 5,280 cells and 6,417 grid points. Zone Five was comprised of 33,600 cells and 38,247 grid points. Zones Six and Seven each contained 8,160 cells and 9,765 grid points. Zone Nine was constructed from 352 cells and 575 grid points. Zones Eight and Ten each contained 528 cells and 805 grid points. The entire grid contained a total of 316,186 grid points and 290,368 cells. Of these cells, 99.99724% had positive area, 0.00276% were positive skew, and 0% were negative or negative skew. The absence of negative cells in a grid is required to produce a converged solution in the computational solver and increases the overall accuracy of the experimental results. Thus, the grid constructed for this experiment was acceptable according to these standards.

Computational Flow Analysis Software

The flow solution on the structured grid was run using the GASP version 3 software by Aerosoft, Inc. (GASP stands for The General Aerodynamic Simulation Program.) Due to the numerous computations required to solve the Navier-Stokes equations utilized by GASP, the solution was processed

by the CRAY supercomputer in Georgia over a period of weeks. The solution was initially run inviscid and the grid was sequenced (made more coarse) to decrease its complexity. Once GASP began to converge the solution, the settings were modified to account for viscosity and the solution was allowed to run to full convergence. The grid was still sequenced for the final solution used in this study.

Test Conditions

The flow solutions were run at a Mach number of 2.70 with a roll angle $\phi = 0°$ and angle of attack $\alpha = 0°$. The wind tunnel tests were conducted under the same conditions. The values inputted into the computational simulation software for the initial and freestream conditions of the flowfield were as follows: density = 0.0981417 kg/m^3, pressure = 3,887 N/m^2, temperature = 138. 000 K, and sound speed = 235.475 m/s.

All wind tunnel tests at HSWT and UPWT were conducted with natural boundary-layer transition.

Post-Solution Processing and Data Extraction

The intermediate solutions from GASP were converted into restart files and loaded into FIELDVIEW version 5.5 for preliminary analysis. Even with partially converged solutions, errors in the grid construction can become readily apparent from scalar FIELDVIEW displays. This allows the experimenter to correct any potential grid errors and imperfections before the flow solution is fully converged. This prevents having to run an entire flow solution multiple times. When grid errors were no longer indicated by the analysis in FIELDVIEW, the flow solution was run to full convergence.

Final solution post-processing was performed using Tecplot version 7 software by Amtec Engineering, Inc. All surfaces in the missile's symmetry plane along with the airflow exit plane were exported from GASP and loaded into Tecplot as a group of two-dimensional surfaces. Y-Z planar cross-sections were taken from the missile body at various axial distances corresponding to those examined in the wind tunnel tests (see figure 2). Each planar extraction was loaded into a data file and merged with the corresponding wind tunnel data from the same cross-section. Formulas were inputted into Tecplot to calculate Cp and θ from computational x y z coordinates. The computational values were then plotted against the wind tunnel data and were examined for agreement and/or differences in terms of the results obtained.

Results

Pressure Analysis

Shown in figure 10 is the contour shaded picture of Cp along the symmetry plane of the missile. The display indicates that all significant airflow phenomena that would be expected to be observed in actual flight have been captured by the flow solver. The regions of the highest gradient changes (as indicated by

the number of contour lines in a given area) are the nose and cruciform wings which agrees with the initial predictions made when creating the grid. The nose and the upward slope of the fins are also the regions of highest pressure because they are the initial points at which the missile collides with the surrounding air and are thus subjected to the most force per unit area. The size and shape of the shock wave is consistent with airflow around flying bodies traveling at an identical supersonic speed. This is illustrated by the schlieren photographs obtained in the wind tunnel testing conducted prior to this experiment {2} (see figure 3). All of the shock wave is contained within the borders of the grid which indicates it was built to acceptable size specifications. The presence and location of the vortices originating from each wing tip are also in agreement with the schlieren photographs and are well defined by the structured grid. The pressure changes along the surface of each fin is consistent with real-world occurrences. The leading edge of each fin exhibits higher pressures than the trailing edge according to figure 10. This is in agreement with the behavior of air colliding with a body traveling at a supersonic mach number. When the air contacts the leading edge of the fin, the flow streamlines are deflected upward. This change in flow direction crosses a shock wave which causes the mach number to decrease and the pressure to increase. As the airflow approaches the trailing edge of the fin, the flow streamlines are deflected downward. The change in flow now crosses an expansion wave which causes the opposite effect. The mach number increases and the pressure decreases.

The data indicate relatively small pressure changes along the missile body at axial cross-sections that do not contain the missile's fins. At 0° angle of attack, the pressure measurements are fairly uniform around the body at a given axial distance and exhibit few drastic jumps from one radial position to another. This is reasonable and expected because the smooth, cylindrical shape of the body should not cause any drastic changes in the air flow. (This does not necessarily apply to critical regions such as the nose and fins where large gradients are quite common). Thus, the missile's flight should be very stable and controlled for the conditions in which the experiment was performed.

Though the contour shading appears to be fairly accurate in its modeling of the airflow around the missile, there still exist some possible sources of error that could affect the solution. Improper passing of information between zones is a very common difficulty in CFD. Flow solvers such as GASP must be instructed as to the nature of each zonal boundary so as to interpret the information correctly. If these boundaries are improperly specified or do not function as expected, a discontinuity will occur between two zones. One such discontinuity can be observed between Zones 1 and 2 (see figures 8 and 10). The shading on one side of the boundary is not perfectly matched to the other side which indicates a flaw in the passing of information. Various attempts were made to eliminate this problem such as changing the zonal boundary specifications and altering the shape of the grid along the missile's nose. These methods helped to minimize the discontinuity but could not nullify it completely. This was the only boundary that displayed evidence of a discontinuity and its effect on the data is most likely small.

Another more obvious source of error is the manner in which the flow solution was run. While GASP was instructed to account for viscous forces, the grid was sequenced so as to make it more coarse. This was done to decrease the overall complexity of the solution and allow it to converge faster. For this purpose, it was effective. However, sequencing also decreases the accuracy of the solution because it reduces the number of cells in the grid which collect data. Thus, the final flow solution has less definition than it would for a less coarse, unsequenced grid. Despite this, the results obtained from the grid can still be considered reliable because the amount of sequencing performed was not that extreme.

CFD / Wind Tunnel Data Comparison

Shown in figures 4 - 7 are the values obtained from the wind tunnel tests along with the data extractions from the CFD solution. The CFD data extractions were taken along the body at various axial distances (see figure 2 for the locations on the missile's geometry). Included in this report are the graphs of the extracted data for X/D = 4.000, 7.333, 10.000, and 12.000. The data (as seen in the graphs and at other axial locations) reveal an overall agreement between the CFD predictions and the values obtained in the wind tunnels. In figures 4 - 6, nearly identical trends can be observed from the matching curvatures of the Cp plots for both sets of data. This indicates the effectiveness of CFD in modeling the missile's aerodynamic behavior. The included figures 4 - 6 show a slight displacement between the two sets of data. This does not indicate, however, that the obtained results are contradictory. For both wind tunnel testing and CFD simulation, there is always a certain amount of error to be expected in the results. The observed differences in the graphs are small compared to the data values and are well within acceptable tolerances. It is for this reason that the overall shape and curvature of the graph is far more significant than the magnitude of the values.

Figure 7 illustrates a portion of data in which there is little agreement between the two methods of experimentation. The wind tunnel test indicates a large increase in Cp which peaks around T = 136° which is located along the underside of the missile (see figure 2). At the same angular location, the CFD predicts a decrease in Cp (the exact opposite trend). In addition, the wind tunnel data indicates much larger changes in Cp around the body than the CFD results which tend to be less erratic. Analysis of the data at additional axial locations reveals the following trends: Both sets of data exhibit very similar predictions in the intervals 0° to 165° and 195° to 359°. However, the data show large dissimilarities along the underside of the missile (angular interval of 165° to 195°) for most of the axial locations examined. The wind tunnel tests show large pressure changes around T = 180° while the CFD reveals no such trend. This deviation must be accounted for and explained in order to validate the results obtained.

Since CFD is the newer, less established method of experimentation, it is more likely that it is the source of error and the wind tunnel data is correct. However, there is more experimental evidence to

indicate that this is not the case. As explained earlier, the smaller changes in pressure as predicted by CFD (see figure 7) are very reasonable given the flight conditions to which the missile was subjected. At 0° angle of attack, large variations of Cp on the underside of the missile are unlikely, contrary to the results from the wind tunnel data.

Moreover, the CFD solution has the advantage of continuous data which increases its fidelity. The wind tunnel test used between four and twelve pressure sensors at each axial location which reduced the number of data points obtained. This caused the graph of T verses Cp to be more angular and less accurate for the wind tunnel results. In contrast, the CFD used a planar extraction technique which enabled the creation of a plot of continuous Cp data at each axial position. This enhanced the smoothness and continuity of the graphs, making them a closer approximation of real-world behavior.

Finally, the symmetry of the data can provide insight into which experiment was more accurate. The CFD data, as detailed earlier, is symmetric by design. This is acceptable since the missile itself has bilateral symmetry. The wind tunnel data, however, does not display nearly the amount of symmetry expected, given the geometry of the missile (see figure 8). The differences between the values for Cp on the left and right sides of the missile are much too large to be attributed solely to ordinary experimental error. One source of this asymmetry could be the test model used in the wind tunnel. In most cases, to simplify testing, a small model of the flying body is used in place of the body itself. If the model used was asymmetrical, it would produce asymmetrical data that would not coincide with real-world performance. Another possibility is that the wind tunnel probes were somehow calibrated or positioned improperly or the model was not precisely oriented with the indicated conditions which could account for the observed asymmetry. Regardless of the source of these numerical differences, the presence of asymmetrical wind tunnel data from a symmetrical body casts serious doubt as to the overall accuracy of the documented results. It is for this reason that the CFD data may actually be considered more reliable for this experiment.

Conclusion

An experimental investigation has been conducted to determine the effectiveness of Computational Fluid Dynamics in predicting the flight performance of a cruciform wing-body at Mach 2.70 with an angle of attack and roll angle of 0°. The results of wind tunnel testing on the same missile were obtained and used as the standard of comparison for the CFD data. Results from this experiment indicate that CFD is, in most cases, capable of producing the same results as those obtained in a wind tunnel test under the conditions previously mentioned. Circumstances under which the wind tunnel results disagreed with those from CFD do not conclusively show CFD to be incorrect in its predictions. Further investigation as to the accuracy of both the CFD and wind tunnel data is required to determine this definitively.

Possible future research which would further add to this study includes repeating the experiment for different orientations and flight conditions to determine the limits of CFD prediction capabilities. Other

areas to be examined could include experimenting with various flow solvers other than GASP to determine which are the most accurate and reliable in their predictions. Such software could also be analyzed in terms of the computational time it requires and the ease with which an experimenter can learn to use it effectively.

References

1. Hankey, W. L. : Introduction to Computational Aerodynamics. Computational Aerodynamics Group - Aeromechanics Division, Jan. - Jul. 1981, pp. 1-2.
2. Stallings, Robert L. , Jr. ; Lamb, Milton ; and Watson, Carolyn B. : Effect of Reynolds Number on Stability Characteristics of a Cruciform Wing-Body at Supersonic Speeds. NASA, 1980.

Figure 1. - Body pressure listings from wind tunnel test at $\phi = 0°$; M = 2.70; $\alpha = 0°$; Pt = 90.3 kPa

θ	X/D	Cp	θ	X/D	Cp
0.0	2.667	-0.0225	45.0	8.667	0.0242
90.0	2.667	-0.0193	135.0	8.667	0.0070
180.0	2.667	-0.0313	202.5	8.667	0.0123
270.0	2.667	-0.0215	225.0	8.667	0.0081
0.0	4.000	-0.0170	247.5	8.667	0.0196
10.0	4.000	-0.0163	315.0	8.667	0.0235
20.0	4.000	-0.0164	45.0	9.333	0.0295
30.0	4.000	-0.0169	135.0	9.333	0.0098
40.0	4.000	-0.0173	202.5	9.333	0.0103
50.0	4.000	-0.0176	225.0	9.333	0.0122
60.0	4.000	-0.0180	247.5	9.333	0.0154
70.0	4.000	-0.0182	315.0	9.333	0.0279
80.0	4.000	-0.0186	45.0	10.000	-0.0075
90.0	4.000	-0.0185	135.0	10.000	-0.0193
180.0	4.000	-0.0306	202.5	10.000	-0.0139
270.0	4.000	-0.0188	225.0	10.000	-0.0127
0.0	5.333	-0.0097	247.5	10.000	-0.0088
90.0	5.333	-0.0114	315.0	10.000	-0.0124
180.0	5.333	-0.0240	0.0	10.667	0.0129
270.0	5.333	-0.0115	45.0	10.667	-0.0302
0.0	6.200	-0.0076	90.0	10.667	0.0117
10.0	6.200	-0.0071	135.0	10.667	-0.0290
20.0	6.200	-0.0065	180.0	10.667	0.0085
30.0	6.200	-0.0063	225.0	10.667	-0.0332
40.0	6.200	-0.0062	270.0	10.667	0.0209
50.0	6.200	-0.0062	315.0	10.667	-0.0377
60.0	6.200	-0.0068	0.0	11.330	-0.0040
70.0	6.200	-0.0068	45.0	11.330	-0.0302
80.0	6.200	-0.0085	90.0	11.330	0.0004
90.0	6.200	-0.0077	135.0	11.330	-0.0071
135.0	6.200	-0.0100	180.0	11.330	-0.0037
180.0	6.200	-0.0208	225.0	11.330	-0.0176
225.0	6.200	-0.0203	270.0	11.330	0.0058
270.0	6.200	-0.0099	315.0	11.330	-0.0097
315.0	6.200	-0.0081	0.0	12.000	-0.0091
0.0	7.333	-0.0021	45.0	12.000	-0.0027
45.0	7.333	-0.0026	90.0	12.000	-0.0051
90.0	7.333	-0.0012	135.0	12.000	0.0015
135.0	7.333	-0.0014	180.0	12.000	-0.0113
180.0	7.333	-0.0110	225.0	12.000	-0.0087
202.5	7.333	-0.0110	270.0	12.000	-0.0065
225.0	7.333	-0.0117	315.0	12.000	-0.0009
247.5	7.333	-0.0008	0.0	13.333	-0.0090
270.0	7.333	0.0001	45.0	13.333	-0.0010
315.0	7.333	-0.0007	90.0	13.333	0.0020
202.5	7.667	-0.0017	135.0	13.333	0.0051
225.0	7.667	-0.0020	180.0	13.333	-0.0056
247.5	7.667	0.0085	225.0	13.333	-0.0100
45.0	8.000	0.0178	270.0	13.333	0.0036
135.0	8.000	-0.0007	315.0	13.333	-0.0002
202.5	8.000	0.0044	0.0	14.400	0.0052
225.0	8.000	0.0049	90.0	14.400	0.0038
247.5	8.000	0.0138	180.0	14.400	-0.0037
315.0	8.000	0.0173	270.0	14.400	0.0033

Figure 2. - Basic dimensions and locations of body pressure tubes.
All linear dimensions are in centimeters.

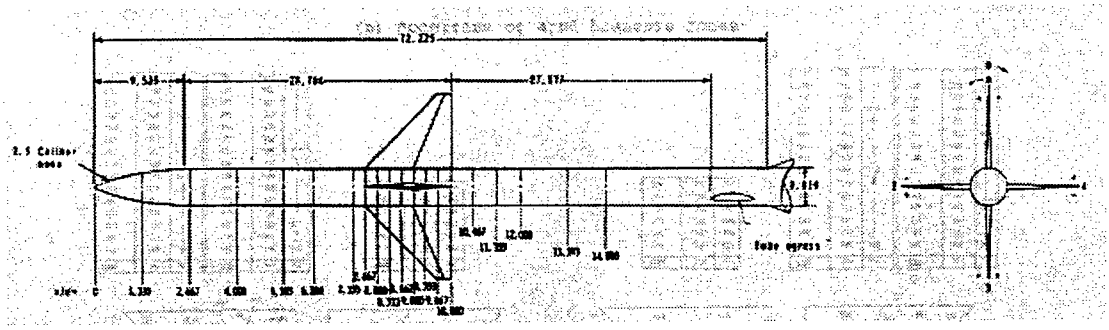

Figure 3. - Schlieren photograph from wind tunnel test at
$\phi = 0°$; M = 2.70; $\alpha = 0°$

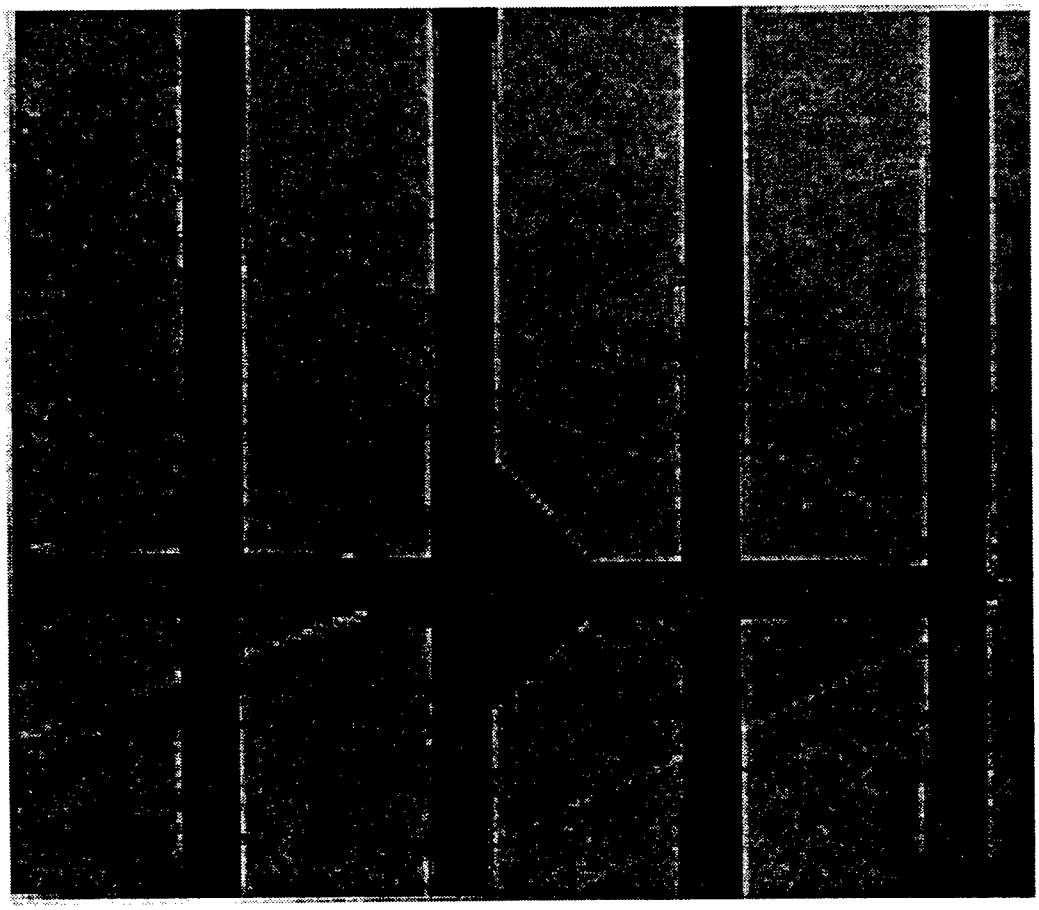

Figure 4. - Graphical comparison of pressure measurements at x/d = 4.000

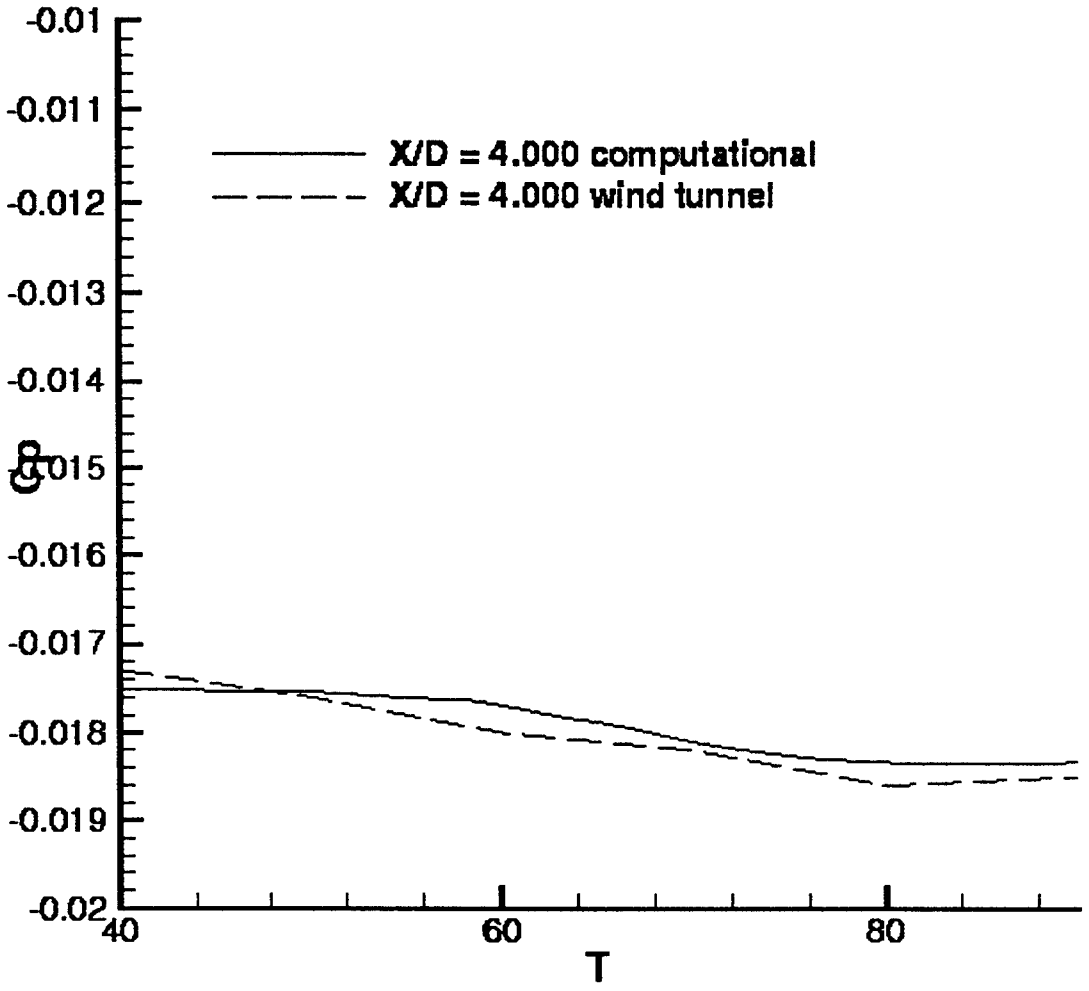

Figure 5. - Graphical comparison of pressure measurements at x/d = 7.333

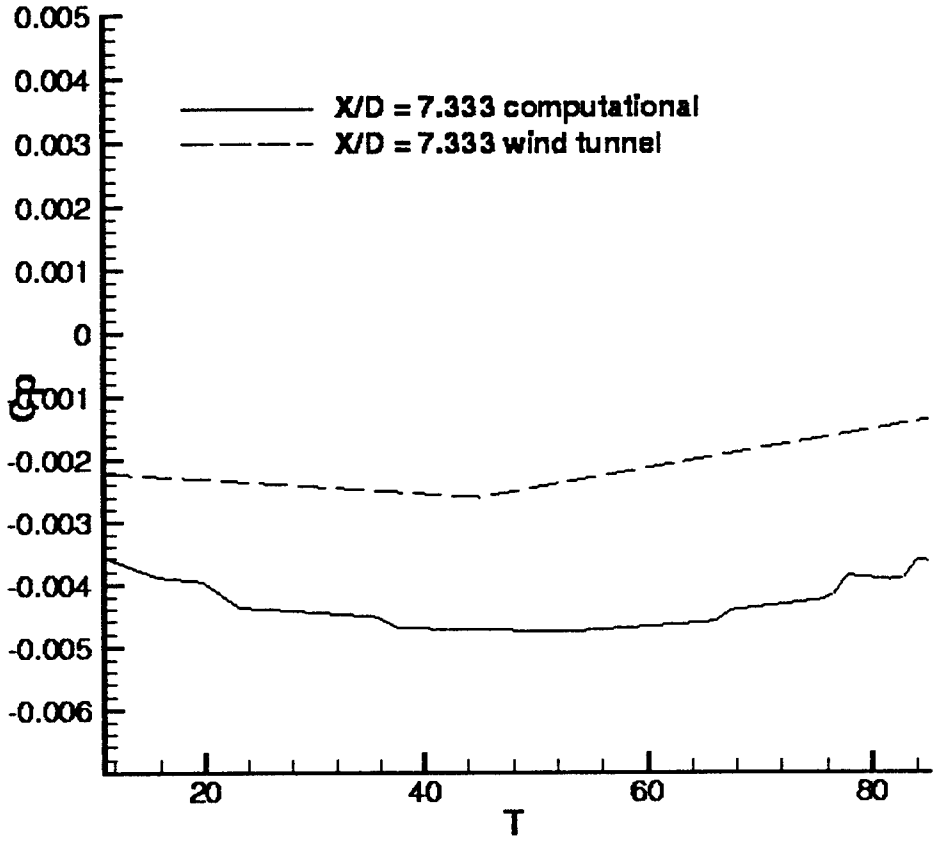

Figure 6. - Graphical comparison of pressure measurements at x/d = 10.000

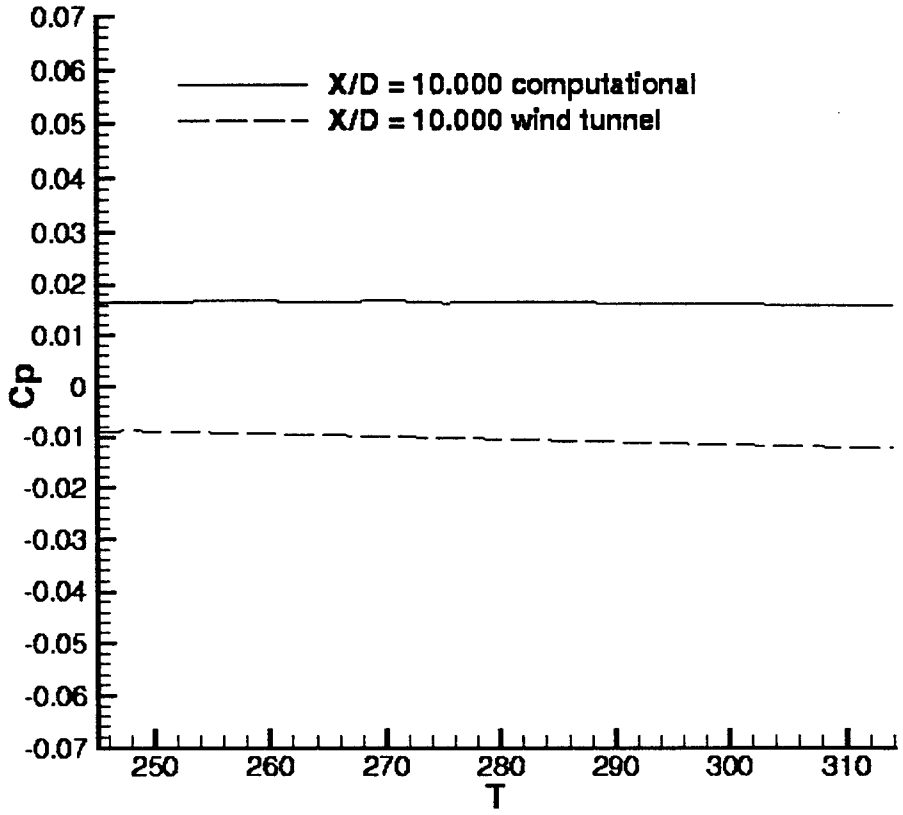

Figure 7. - Graphical comparison of pressure measurements at x/d = 12.000

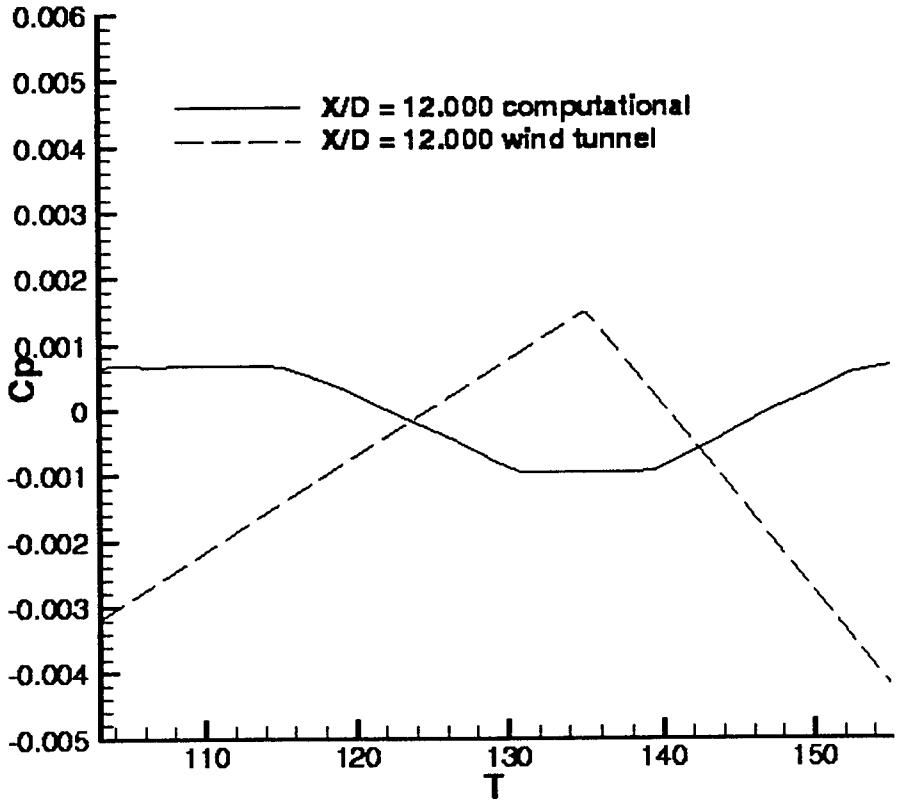

Figure 8. - Computer generated missile geometry, displayed solid

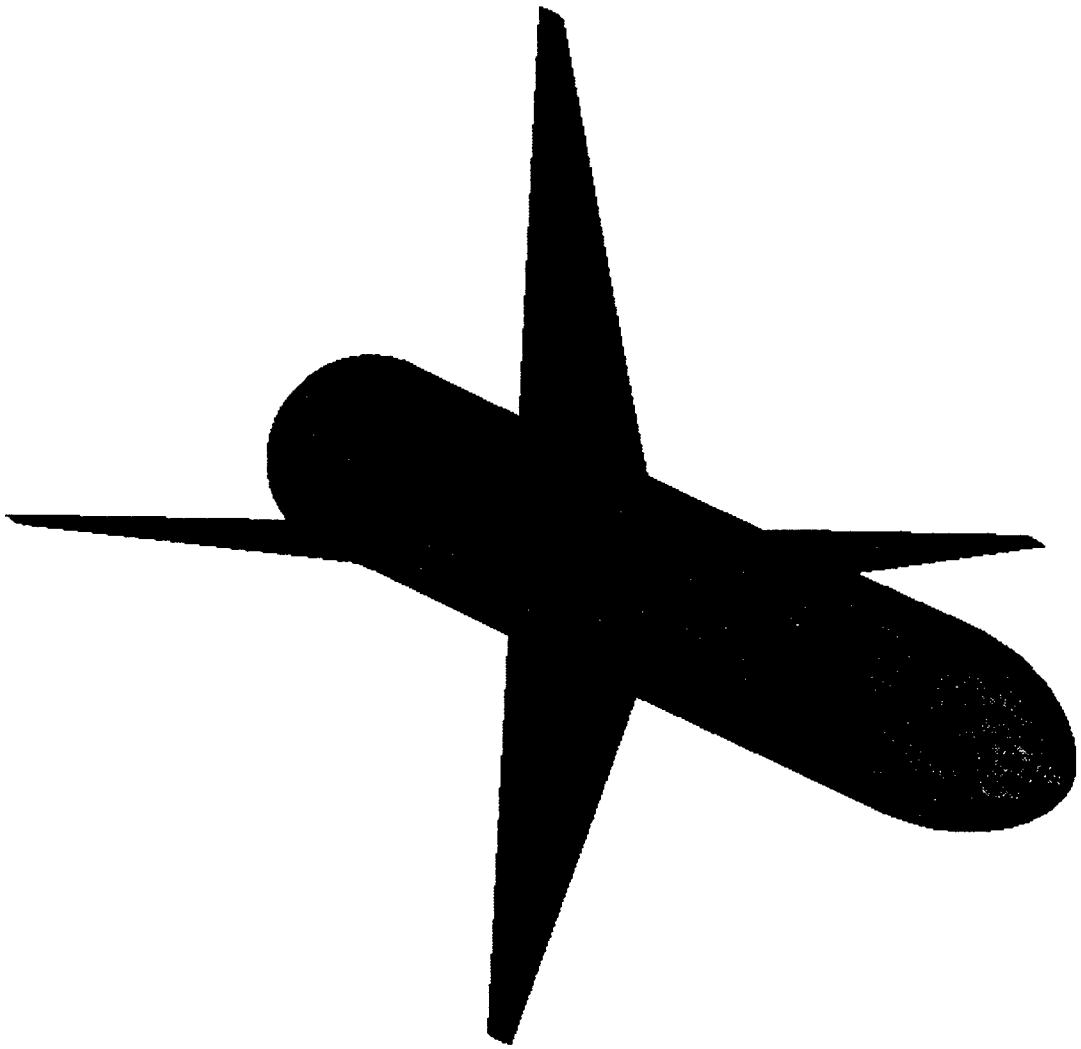

Figure 9. - Structured grid with zone numbers

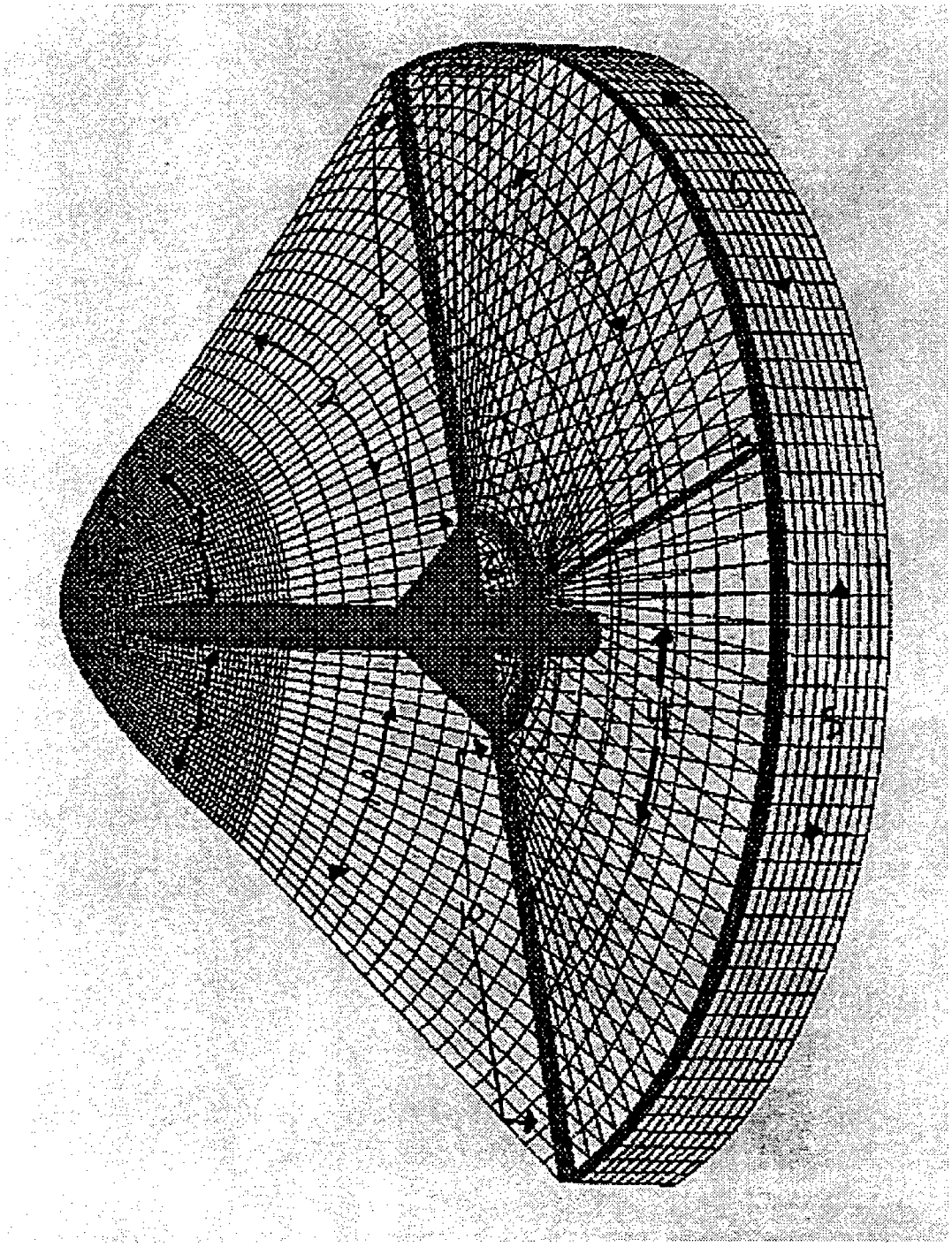

Figure 10. - Contour shaded CFD solution

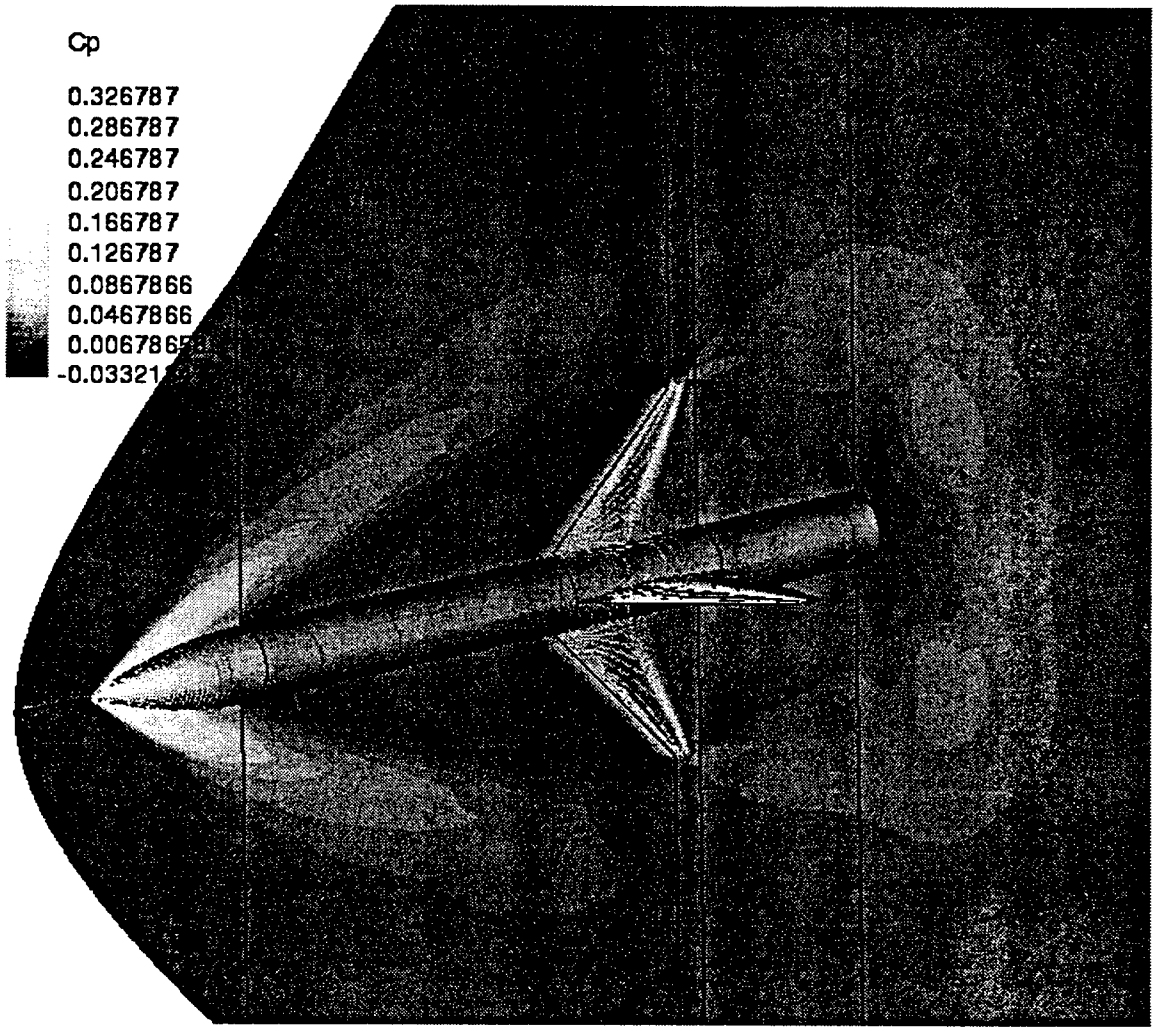

DEVELOPMENT AND APPLICATION OF MATERIALS CHARACTERIZATION WEB SITE

Nicole L. Speelman

Walter E. Stebbins High School
1800 Harshman Road
Riverside, OH 45424

Final Report for:
High School Apprenticeship Program
Wright Laboratory Materials Directorate
Wright-Patterson Air Force Base

Sponsored by:
Air Force Office of Scientific Research
Bolling Air Force Base, DC

and

Wright Laboratory Materials Directorate
Wright-Patterson Air Force Base

September 1997

DEVELOPMENT AND APPLICATION OF MATERIALS CHARACTERIZATION WEB SITE

Nicole L. Speelman
Walter E. Stebbins High School

Abstract

The Internet has proven to be a valuable tool not only for research purposes but also as a way to obtain everyday information. Having access to the Internet is one of the quickest ways to acquire facts about a vast number of topics. Because of this, a materials characterization Web site was designed for those scientists and students and others interested in understanding the different techniques of materials characterization. At the Materials Lab, the need for a designated site to bring together all knowledge at hand on this topic was vital. This Web site utilized many of the Web pages already available on those subjects dealing with materials characterization. The site was established by applying the fundamental concepts of hypertext markup language and used a Web browser to actually show the layout of those pages.

DEVELOPMENT AND APPLICATION OF MATERIALS CHARACTERIZATION WEB SITE

Nicole L. Speelman

Introduction

This project involved creating a materials characterization Web site. The first section describes the history of the Internet, how it came about, and its importance as a research tool. The next section explains Hypertext Markup Language (HTML) which is the basic computer language for building Web pages. Finally, materials characterization techniques are explained the significance of having a materials characterization Web site is also discussed.

History of the Internet

Many people today know about the Internet and purposes that it serves, but not everybody understands the true reason for why the Internet was created. Almost thirty years ago, the RAND corporation was faced with designing some sort of communication network that would be able to be maintained if a nuclear war ensued {1}. They constructed a system with no central authority and that which could be operated from the beginning while in complete disorder. The network itself would be operative from each node with its own figure of authority to pass and receive messages. The path that the information took through this system was unimportant, only the final results actually mattered {1}.

In 1969, the first such node was installed in UCLA and later that year four more nodes were put on the network known as ARPANET. These computers could transfer data at high speeds and even be programmed remotely from the other nodes{1}. ARPANET benefited many scientists and researchers by making it available to share each others computer facilities over long

distances.

As time went on though, the computer system became the center of communication, with personal addresses and the beginnings of electronic mail. ARPANET started a broadcasting technique to send the same messages to many users. Successful through the seventies, the network continued growing from these new advances {1}.

The need for quicker transmission from node to node was prevalent. The original standard for ARPA was NCP (Network Control Protocol) but this was overrun by TCP/IP. TCP (Transmission Control Protocol) converted messages into streams of packets at the source, then reassembled them back into messages at the target. IP (Internet Protocol) controlled the addressing of information and seeing to it that the packets were transferred across multiple nodes, networks, and standards.

As the development of ARPANET continued into the nineties, many different social groups had numerous powerful computers in their possession. Easily linked to networks upon networks, computers started becoming public domain and branched off in various directions. Thus, from the almost anarchic nature of the system and its easy access, the Internet was found.

The growth of the Internet is almost unbelievable in the 1990's. Now that the Internet is moving out of its primary place in the military, high schools and elementary schools along with other commercial facilities are obtaining Internet privileges. Making the Internet belong to nobody and everybody at the same time.

One of the most important scientific instruments of the twentieth century, the Internet is especially popular among scientists. Not only does it provide specialized data, but it also has sped up the pace of scientific research tremendously due to the personal communication abilities. This

gives way to using the Internet as a helpful resource.

Hypertext Markup Language

Hypertext Markup Language, or HTML, is a fairly simple markup language {4} and derives from the Standard Generalized Markup Language (SGML). SGML is not application or machine dependent and does not insert specific formatting codes into the text of a document {3}. However, SGML tagging identifies the different parts of that document for later processing. HTML is a reduced version of the SGML tagging system. Used on the World Wide Web since 1990, Hypertext Markup Language formats data to create documents that can be transferred from one platform to another {7}. Markup is merely symbols and markings on written drafts of publications. They are basic instructions for paragraph breaks, bold, and where titles or headings are. Providing information, markup says something about the structure or appearance of text {5}. Several authoring tools have come forth that permit WSIWYG (what you see is what you get) in order for the editor to jump rapidly between seeing it with the markup tag placement and the formatted text as seen in various Web browsers {7}.

The concept of hypertext was proposed by Vannevar Bush in 1945 {4}. He wanted to create a device, Memex, that books, records, and communications could occur quickly and with much flexibility. His major focus was establishing links between different areas on Memex for the full perspective on a given topic {4}.

To design the materials characterization Web site, HTML was employed. By utilizing the preformatted text tag, it enabled the viewing of the text as it would actually appear on the Web page. At the top of the pages, a hypertext target allowed for linking a word at the top of the page

to the designated target. This helps the user to not have to scroll down the page if they are looking for something specific. Also, throughout the Web pages, links were created to jump to related Web sites giving information on the same subject. Beneficial, this allows the users to get all the resources possible but not by having to search all over the Internet for those sites. For an example of an HTML document and corresponding Web page from the Materials Characterization Web site, go to Appendix A.

Materials Characterization

Materials Characterization thoroughly characterizes and classifies the microstructure of a material. By better understanding a material's composition physical matter in a solid state, that which occurs naturally or is manufactured, particular characteristics and can be achieved. Classification is done in two ways: nature of the material or the applications of a substance {6}. When the nature of a specimen is studied, scientists look at it on an atomic and molecular level because on such a distinct level of analysis what influences the physical and mechanical properties of that specimen can be determined. Also, the intermolecular forces and the configurations of molecules govern the way that substance interacts with other materials. Thus, elemental composition, phase identification, chemical state information, and structure determination are some of the most basic properties identified {2}.

Most analytical techniques involve photons, electrons, or ions as a probe beam striking the material being analyzed. Interacting with the substance in some way, the beam induces a change and then those changes are monitored after the interaction; thus, from the observation of these changes, analytical information is derived. Several other techniques take the information from electrons, photons, or ions that are ejected from the specimen under probe beam stimulation {2}.

However, the best results are ascertained when more than one technique is applied {6}. In this way, what one method does not observe, another one will.

The following techniques discussed are some of the more common ones used for materials characterization, but are not necessarily better than any other technique. All of these methods are displayed on the Web pages created for this project.

Auger Electron Spectroscopy is an instrumental method for determining the chemical composition of a material's surface by bombardment with an electron beam to produce Auger electrons whose energy spectra are characteristic of their parent atoms.

In *Angle-Resolved Ultraviolet Photoelectron Spectroscopy*, the electron energy analyzer used for UPS is gimble-mounted and free to rotate on one or two axes around the point where radiation strikes the sample. It determines the direction from which the electrons are emitted, enabling the mapping of k-space.

The *Atom Probe* is a combination of the field ion microscope and time-of-flight mass analyzer. Individual atoms are passed through an aperture in the channel plates by first acquiring the tip image on the channel plates. The desired atom is chosen and the tip is angled so the atom is placed directly over the hole. Then, the field is pulsed; the mass-to-charge ratio of the evaporated ion is taken.

Cathodoluminescence is when a specimen is excited by an incident beam of electrons and light is emitted. This occurs when an excited electron returns to its normal state, releasing some energy as light.

Energy Dispersive X-Ray Spectroscopy is a microanalytical technique that is based on the characteristic X-ray peaks that are generated when the high energy beam of the electron

microscope interacts with the specimen. Each element yields a characteristic spectral fingerprint that may be used to identify the presence of that element within the sample. The relative intensities of the spectral peaks may be used to determine the relative concentrations of each element in the specimen. The X-ray signal is detected by a solid-state silicon-lithium detector and the construction and efficiency of this detector sets a lower limit on the atomic number that may be detected.

Electron Energy Loss Spectroscopy analyses the inelastically scattered electrons present in the beam after it has been transmitted through the sample. An EEL spectrum typically consists of a monoatomically decreasing background on which are superimposed a number of peaks. Each peak is characteristic of the scattering process that has occurred in the sample. The peaks can be used to obtain information about the chemical composition and electronic structure of the sample.

Electron Probe X-Ray Microanalysis is the qualitative and quantitative use of x-rays excited by a microprobe of electrons. Available with scanning electron microscope and transmission electron microscope. This sustains the ability when electrons interact with a bulk specimen to detect and quantify characteristic emitted x-rays. It is a diagnostic system of determining chemical composition.

Fourier Transform Infrared Spectroscopy enables imaging and chemical analysis of extremely small specimens. The spatial resolution, determined by the apertures, is defined by the ability to measure an object without stray radiation. Particularly suitable for obtaining subsurface information from semiconductor devices, FTIR is also a powerful instrument for the characterization of polymeric materials and composites.

High Order Laue Zone lines in electron diffraction are equivalent to Kossel lines in x-ray diffraction. HOLZ lines usually appear in convergent beam diffraction when produced by large

unit cell metals and alloy phases, especially carbides, nitrides, and borides. Local crystal lattice constants can be derived by the position of the HOLZ lines.

Ion Scattering Spectrometry allows monoenergetic, low energy He+ ions to collide with the surface, where they lose discrete quantities of kinetic energy according to the laws of momentum conservation. The exact energy loss depends on the atomic mass of the surface atoms that are struck. ISS shows the effects of pretreatment on the top atomic layers of the sample, for example, in wafer cleaning.

A *Kossel* pattern is one which has been produced when Bragg Diffraction is satisfied and a divergent beam produces an x-ray diffraction pattern. Providing orientation data, the pattern is independent from the incident electron beam and is related directly to the specimen. Kossel patterns also help to find a crystallographic description of the microstructure.

Laser Microprobe Mass Analysis combines the principles and properties of a solid laser, the optical laser microscope, and optical emission spectroscopy. It mainly offers qualitative data but sometimes semiquantitative analysis.

In *Molecular Beam Epitaxy*, atoms are delivered to a substrate through an UHV atmosphere. This atmosphere allows the atoms to arrive on the substrate without colliding with other atoms or molecules, thus keeping the growth free of other contaminants. The heated substrate surface allows the arriving atoms to distribute themselves evenly across the surface forming an almost perfect crystal structure.

Having no charge, neutrons can penetrate quite far into a substance because they do not interact with any other subatomic particles. Therefore, a monochromatic beam of neutrons incident on a material will be diffracted by the atoms. *Neutron Diffraction* allows for the

identification of phases, lattice parameter measurement, the determination of residual stress, and the detection of preferred orientation.

Nondestructive Evaluation is a development of analysis and measurement techniques for quantitative materials characterization, tissues and structures without damaging the specimen being studied.

Nuclear Magnetic Resonance is a technique where a magnetic field is imposed on a material and the nuclei (or some of them) are caused to precess (wobble). The precessing nuclei emit electromagnetic radiation, usually at radio frequencies, of a frequency uniquely characteristic to each type of nucleus for a given magnetic field strength.

Optical Microscopy is one the most useful and easily applied method for establishing the microstructure of many different materials. However, the information depends critically upon the specimen. A range of specimens from a body must be taken in order to achieve the desired result.

In *Photoacoustic Microscopy*, an incident light pulse from a laser is focused onto the substance surface where it is partly reflected and absorbed producing heat which locally expands the surface layer. The expansion displaces the material upwards and an associated downward movement. The image results from the incident spot size, the duration of the laser pulse, and the thermal conductivity of the material.

Particle Induced X-Ray Emission obtains chemical analysis by bombarding a material with charged particles and detecting the x-rays emitted. This is ideally suited for the analysis of thin elements or thin layers of powders containing up to twenty different elements.

Because ions when penetrating the specimen surface lose energy due to inelastic collisions, some ions may be elastically scattered from the surface while the ions that have lost

energy are scattered by atoms in the bulk. *Rutherford Backscattering Spectroscopy* measures the energy and intensity of the backscattered ions; therefore, it can identify the position and concentration of the impurity atoms.

In *Reflection High Energy Electron Diffraction*, electrons strike the target at a low grazing angle. RHEED patterns for good surfaces appear as streaks on the fluorescent screen. The large primary electron energy creates a large energy difference between elastically and inelastically scattered (background) electrons. The physical arrangement of the RHEED components (in which nothing obscures the sample surface) and the technique's sensitivity to surface morphology make it ideal for studying MBE deposition of semiconductors or surface corrosion in metals.

Small-Angle X-Ray Scattering is particularly designed for studying protein structure, as well as changes in structure that may accompany food processing or engineered alterations in food proteins. Providing a substantial number of significant parameters, this method is consistent with crystallographic results and can indicate tertiary structural changes occurring under varying conditions.

Scanning Electron Microscopy is performed by scanning a focused probe across the surface of the sample to be studied. Secondary electrons emitted from the sample are typically detected by a photomultiplier system, the output of which is used to modulate the brightness of a TV monitor that is rastered in synchronization with the with the electron beam scan. The more electrons a particular region emits, the brighter the image at that point. SEM images typically contain a good deal of topographical detail.

Raman spectroscopy is used to measure the vibrational spectra of solid and liquid

materials. Surface Enhanced Raman Spectroscopy is a two photon inelastic light scattering phenomenon and is most easily understood as an energy-loss spectroscopy in which the energy of the Raman scattered radiation is equal to that of the incident photon minus that of a vibration in the sample.

Secondary Ion Mass Spectrometry uses nominally monoenergetic, high mass or reactive ions to bombard a sample. Primary ion beams of Cs+, Ga+, Ar+, O+ and O2+ have been used. Characteristic secondary ions (and ion clusters) leave the surface and are analyzed by a mass spectrometer.

In *Scanning Transmission Electron Microscopy*, the electron beam is rastered across the surface of a sample in a similar manner to SEM, however, the sample is a thin TEM section and the diffraction contrast image is collected on a solid-state detector.

In *Scanning Tunneling Microscopy* (a branch of scanning probe microscopy) an extremely fine-pointed tungsten or platinum/iridium conductor is brought infinitely close to a conductive sample surface. Since its value is a measure of the probability that an electron is in a particular location, the STM probe follows the contours of the `outer electron shells' surrounding every atom.

Transmission Electron Microscopy enables the fine scale microstructure to be examined in sufficiently thin specimens to facilitate transmission of a beam of electrons. The higher the electron energy, the better transmission. This method produces a high vacuum environment and uses ion pumps to minimize specimen contamination.

Ultrahigh Vacuum is used for many materials characterization techniques: LEED, XPS, AES, SIMS, SNMS, and FIM. The purpose of UHV is create an environment with the residual partial pressures being primarily comprised of inert gases and with the lowest possible pressure.

For Ultraviolet Photoelectron Spectroscopy the sample is bombarded with photons from a UV source. The lower photon energy (compared to XPS) interacts with electrons in the valence `shells' or conduction band. UPS, therefore, provides information about the electronic band structure of semiconductors and metals. It is widely used in studying catalysts and in `fingerprinting' polymeric materials.

In *X-Ray Photoelectron Spectroscopy* (also known as Electron Spectroscopy for Chemical Analysis or ESCA), radiation from an X-ray source strikes the sample. Atoms in the bulk are excited and both core and valence band electrons are ejected with characteristic energies, depending on the atom's chemical state.

X-Ray Diffraction uses a crystal to diffract an x-ray beam passing through it to produce beams at specific angles depending on the x-ray wavelength, the crystal orientation, and the structure of the crystal. X-rays are predominantly diffracted by electron density and analysis of the diffraction angles produces an electron density map of the crystal.

X-ray Fluorescence is the result of ionization of atoms which then rearrange emitting a photon. The most frequent occurrence of this is when the surface is stimulated by electron bombardment.

Z (atomic number) A (absorption) F (fluorescence) is a correction pattern and combination of factors used in quantitative x-ray composition analysis.

Conclusion

As stated before, these are only a few of the over two hundred materials characterization techniques in use today. Infinite amounts of information can be found on such methods, especially

on the Internet. Thus, there was a tremendous need for a Web site to tie all that information together. From the materials characterization Web site, the user can learn all there is to know about the different techniques but without having to search all over the Internet. This Web page is now a starting point for research on materials characterization.

Appendix A

Example Hypertext Markup Language (HTML) document and Web page

The following pages show what Hypertext Markup Language actually looks like for formatting a document. The coinciding Web pages are also included to display how the computer reads HTML to give the final product.

```
<HTML>
<HEAD><H3><CENTER>Click on desired topic: <A HREF="#BILE">[BILE]</A> <A
HREF="#BLE">[BLE]</A>
<A HREF="#BSE">[BSE]</A></CENTER></H3><HR WIDTH=100% ALIGN=center
SIZE=10>
<TITLE><H2><CENTER><A NAME="BILE">Beam-Induced Light
Emission</A></CENTER></H2></TITLE>
</HEAD>
<BODY>
<PRE>Visit <A
HREF="http://www1.cern.ch/ALICE/TECH_PROPOSAL/chap8/node8.html">BILE</A> Web
site for information.</PRE>
<P><HR><P>
<H2><CENTER><A NAME="BLE">Bombardment-Induced Light
Emission</A></CENTER></H2>
<P>
<PRE>D. G. Armour, J. J. Jimenez-Rodriguez, C. H. Barber, K. Snowdon,
and P. Hedbavny, "An ion beam system for ion scattering, bombardment induced
light emission and secondary ion mass spectrometry," Vacuum <STRONG>34</STRONG>(1-2),
(1984)
217-221.</PRE>
<P><HR><P>
<H2><CENTER><A NAME="BSE">Backscattered Electrons</A></CENTER></H2>
<P>
<PRE><STRONG>  Backscattered electrons are produced by an incident electron colliding with
the
nucleus of an atom in the specimen. The incident electron is then scattered back-
ward
about 180 degrees with no appreciable loss of energy, an elastic collision.</STRONG>

D. L. Barr and W. L. Brown, "A channel plate detector for electron backscatter
diffraction," Rev. Sci. Instrum. <STRONG>66</STRONG>(6), (1995) 3480-3482.</PRE>
<BR><HR>
Go to <A HREF="matechar.htm"> [HOME]</A> page.
</BODY></HTML>
```

Click on desired topic: [BILE] [BLE] [BSE]

Beam-Induced Light Emission

Visit BILE Web site for information.

Bombardment-Induced Light Emission

D. G. Armour, J. J. Jimenez-Rodriguez, C. H. Barber, K. Snowdon, and P. Hedbavny, "An ion beam system for ion scattering, bombardment induced light emission and secondary ion mass spectrometry," Vacuum **34**(1-2), (1984) 217-221.

Backscattered Electrons

Backscattered electrons are produced by an incident electron colliding with the nucleus of an atom in the specimen. The incident electron is then scattered backward about 180 degrees with no appreciable loss of energy, an elastic collision.

D. L. Barr and W. L. Brown, "A channel plate detector for electron backscatter diffraction," Rev. Sci. Instrum. **66**(6), (1995) 3480-3482.

Go to [HOME] page.

References

1. Bruce Sterling, "Internet," www.lysator.liu.se/etexts/the_internet.html.

2. C. Richard Brundle, Charles A. Evans, Jr., and Shaun Wilson, Encyclopedia of Materials Characterization, Butterworth-Heinemann, Boston, 1992.

3. George Charlesbois, "Standard Generalized Markup Language(SGML): Overview and New Developments," www.nlc-bnc.ca/pubs/netnotes/notes3.html.

4. Jakob Nielsen, Multimedia and Hypertext The Internet and Beyond, Academic Press, Boston, 1995.

5. James K. Tauber, "What is Markup?," www.uwa.edu.au/cwis/sgml/course/markup.html.

6. P. E. J. Flewitt and R. K. Wild, Physical Methods for Materials Characterisation, Institute of Physics Publishing, 1994.

7. T. Berners-Lee and D. Connolly, "Hypertext Markup Language-2.0," www.w3.org/MarkUp/html-spec/html-spec_1.html.

A STUDY OF THE EFFECTS OF THE PERFORMANCE OF POLYMER DISPERSED LIQUID CRYSTAL HOLOGRAPHIC GRATINGS WITH VARYING EXPOSURE ENERGIES

Kari D. Sutherland

Dayton Christian High School
325 Homewood Avenue
Dayton, OH 45405

Final Report for:
High School Apprentice Program
Wright Laboratories, Materials Directorate

Sponsored by:
Air Force Office Of Scientific Research
Bolling Air Force Base, DC

and

Wright Laboratory

August 1997

A STUDY OF THE EFFECTS OF THE PERFORMANCE OF POLYMER DISPERSED LIQUID CRYSTAL HOLOGRAPHIC GRATINGS WITH VARYING EXPOSURE ENERGIES

Kari D. Sutherland
Dayton Christian High School

Abstract

The focus of this experiment was to study the effects of the performance of polymer dispersed liquid crystal gratings using varying exposure energies and to find if the chemical reaction continues after exposure for some time. Exposure times of 15 seconds to 3 minutes with 15 second increments were chosen. Samples were constructed and exposed for the different exposure times by an Argon Ion laser of 514 nm. After exposing, an experiment was set up using a helium neon laser at 633nm to measure the diffraction efficiency of each sample. Switching voltage was done to compare the results with the diffraction efficiency. The diffraction efficiency continued to increase until the exposure time between 75 and 90 seconds was reached. At that point it began to level off. Voltage switching began to occur with the sample of 75 second exposure time. The switching of the higher exposure times had similar results thus agreeing with the conclusion that the refractive index modulation due to the phase separation of PDLC droplets reaches a maximum between 75 and 90 seconds and remains there independent of the exposure energy.

A STUDY OF THE EFFECTS OF THE PERFORMANCE OF POLYMER DISPERSED LIQUID CRYSTAL HOLOGRAPHIC GRATINGS WITH VARYING EXPOSURE ENERGIES

Kari D. Sutherland

Introduction

In the area of holography, research of the use of polymer dispersed liquid crystal (PDLC) in preparing Bragg gratings has expanded. Previous experiments done by members of SAIC and WL/MLPJ have found that the standard exposure time of a PDLC sample is 5 minutes. However, I looked further into this area of research. When the same beam power is applied to each sample at various exposure times, different amounts of energy are incident on each sample. This being the case, I chose to focus on the effects of the performance and morphology of PDLC gratings with varying exposure energies less than 5 minutes. In doing so, I hoped to discover an exposure time less than 5 minutes that would produce the same or very close results as a PDLC sample exposed for the standard time. Another objective was to find if the chemical reaction stops after exposure or continues for some time.

Experimental

To begin the experiment, the syrup was made. The recipe included N-vinylpyrrollidone (NVP), N-phenylglycine (NPG), dipentaerythrol hydroxy penta acrylate (DPHPA), Rose Bengal (RB), and liquid crystal (E7). After combining the recipe, the syrup was sonicated to mix the ingredients thoroughly. After sonicating, two good samples-one on a glass slide and one on an ITO slide-were constructed. To prepare the samples for recording, the lights were turned off, and the glass and ITO slides were cut in half and spacers were applied to the end of each half. A pipette was used to place drops of the syrup in the

middle of each slide. The slides were squeezed and held together with binder clips. Index matching fluid was applied to each side of the sample to hold the OD filters on. The

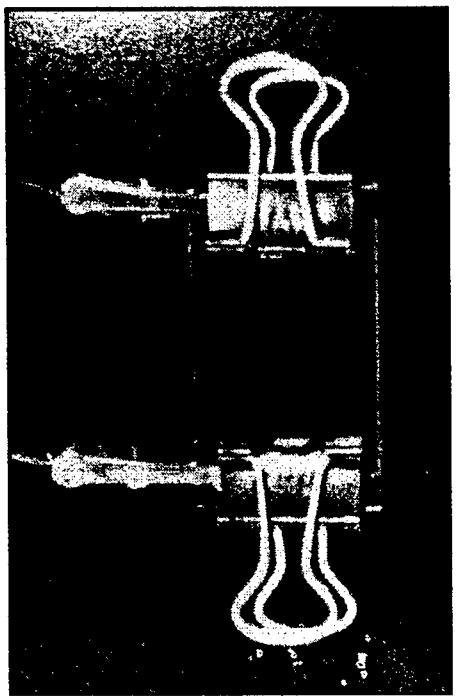

recording setup included the use of an Argon Ion laser with a wavelength of 514 nm and a power of 1 mW/cm^2 per beam. The beam was split and then recombined at an angle to create a hologram. The samples were exposed for times of 15 seconds to 3 minutes with 15 second increments. When the exposure had been completed, the OD filters were removed and the sample was placed under a postcuring lamp for a standard of 3 minutes with the clips on and 5 minutes without the clips to remove any of the rose bengal dye that might still be remaining, and to observe if the chemical reaction continues or not for some time after exposure.

Following the exposure and recording, each sample was characterized. Our setup included the red HeNe laser (633 nm). The laser beam was chopped, then beamed through a Calcite polarizer to a beam splitter to measure the incident power. The beam was then incident on the sample resulting in some of the light being transmitted and the remaining light being diffracted. The transmitted, diffracted and incident power were measured with detectors. Behind the sample the detectors were hooked up to a power meter. An ITO slide

or a glass slide (depending on whether the sample was constructed with glass or ITO) was inserted before each set of approximately 10 samples to measure the

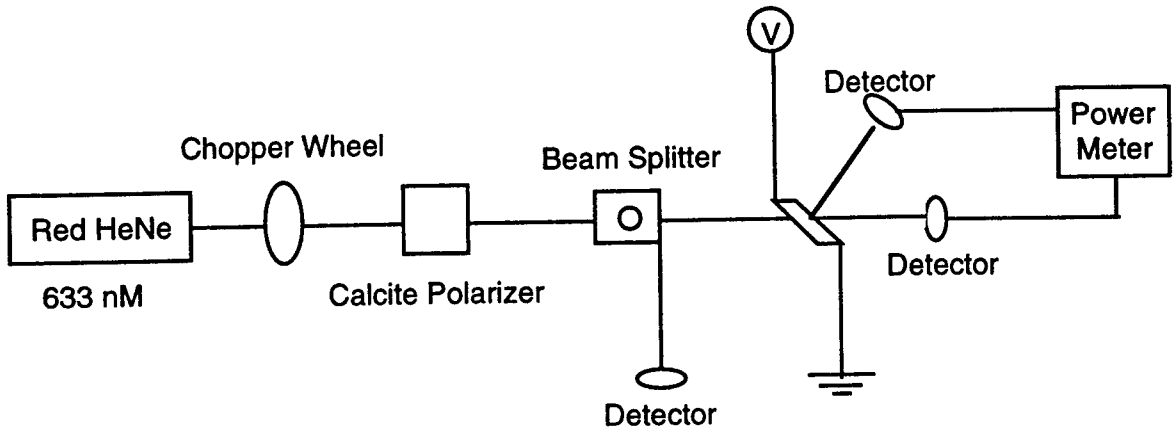

transmission and that number was used as the calibration factor. After removing the slide, each sample was placed in, measuring the highest diffracted power, the transmitted power, and the incident power using a power meter. Each sample was characterized at p polarization. After collecting the data, the numbers were calculated to find the diffraction efficiency and transmission of each sample. The diffraction efficiency (DE) was found by multiplying the diffracted power (P_d) and the incident calibration factor (y) and dividing by the incident power (P_i) multiplied by the transmission calibration factor (x). The transmission (T) was found by multiplying the transmitted power (P_t) and the incident calibration factor (y) and dividing by the incident power multiplied by the transmission calibration factor (x). These formulas are shown below.

$$\frac{(P_d)(y)}{(P_i)(x)} = DE$$

$$\frac{(P_t)(y)}{(P_i)(x)} = T$$

After characterization, a voltage was placed across each sample to measure the electrical switching.

Results and Conclusions

After the experimentation, the diffraction of the ITO samples was measured. The diffraction efficiency continued to increase until the exposure time between 75 and 90 seconds was reached. At that point the diffraction efficiency began to level off.

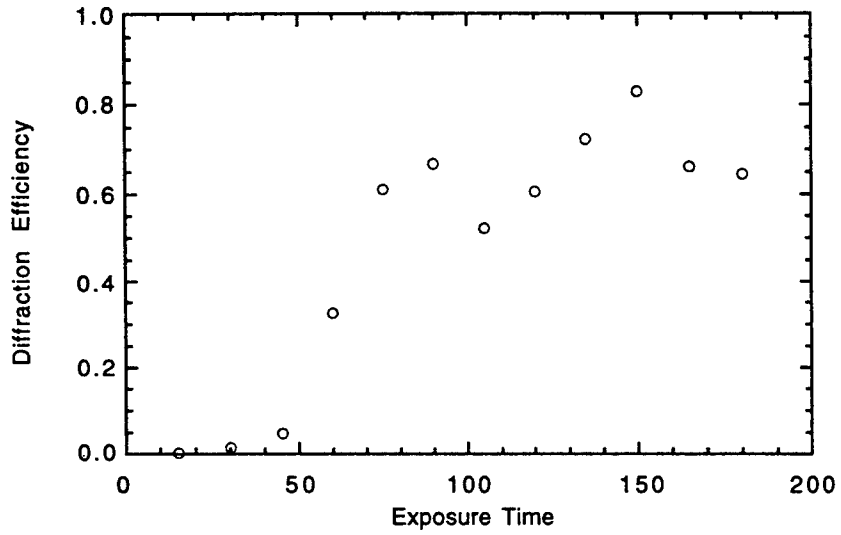

The results of the diffraction efficiency as a function of time or total energy exposure shown on the graph above appears to be extremely close to the results of a similar study recorded in a journal paper entitled "Bragg Gratings in an Acrylate Polymer Consisting of Periodic Polymer-Dispersed Liquid-Crystal Planes"(Bunnung et al.). This study recorded in the journal was done with a continuous exposure. My experiment differed only in the fact that I terminated the exposure times at increments of 15 seconds and recorded the results.

Both the graph of the results from the referenced journal article and my graph show that the diffraction efficiency of a PDLC sample continues to increase as the exposure time is

increased. However, when the exposure time reached between 75 and 90 seconds, the diffraction efficiency begins to level off and remain the same.

Therefore, from this data I conclude that the refractive index modulation due to the phase separation of PDLC droplets reaches a maximum between 75 and 90 seconds and remains there regardless of how long the exposure energy.

In my investigation of whether the chemical reaction continues after exposure, I conclude that it does not. After the exposure of each PDLC sample, the samples were left alone for approximately 10-14 days. At the end of the allotted time, the diffraction efficiency was measured. As mentioned above, the graph of the diffraction efficiency closely matched that of a similar previous study that measured the diffraction efficiency as the sample was being made. It can then be infered that no further reaction occurs in the PDLC samples after exposure.

When the diffraction efficiency measurements had been completed, voltage switching was done on each ITO sample. The voltage switching of samples with exposure times of 30, 45, and 60 seconds all appeared to decrease up to 230 volts, but no switching took place.

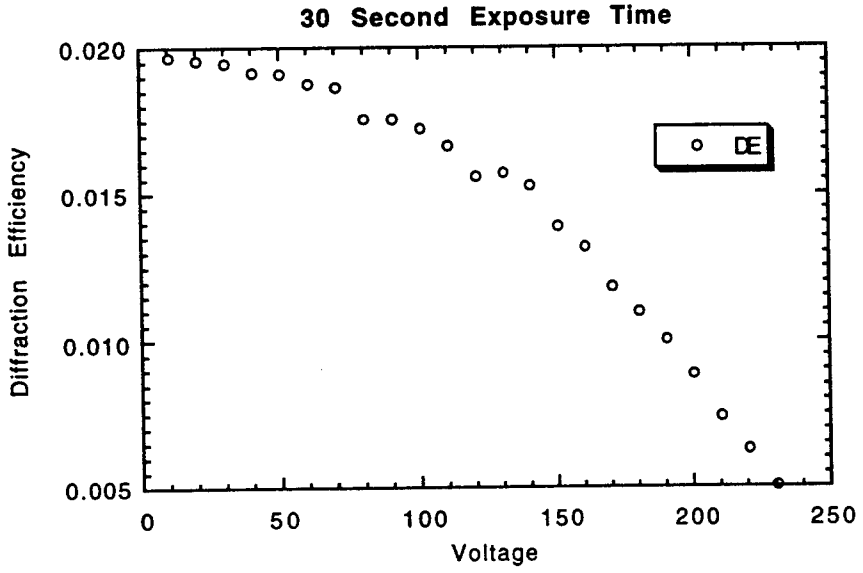

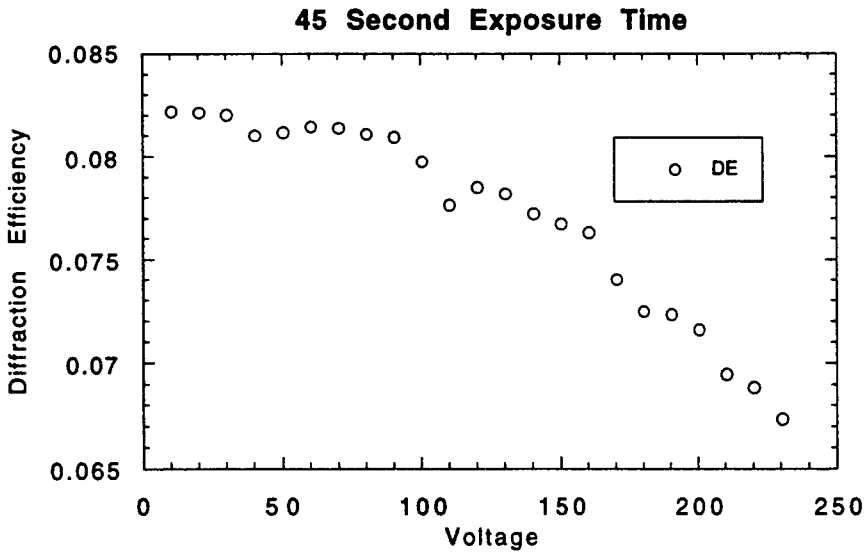
45 Second Exposure Time
0.085
0.08
0.075
0.07
0.065
Diffraction Efficiency
DE
0
50
100
150
200
250
Voltage

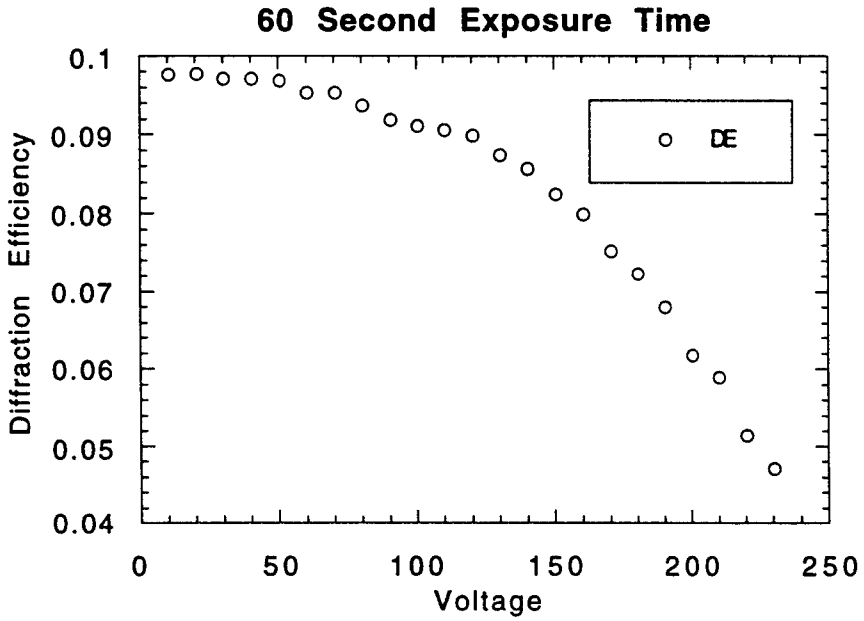
60 Second Exposure Time
0.1
0.09
0.08
0.07
0.06
0.05
0.04
Diffraction Efficiency
DE
0
50
100
150
200
250
Voltage

However, switching began to occur with the sample of 75 second exposure time. The switching of the samples with 120, 150, and 180 second exposure times closely resembled the results of the voltage switching of the 75 second exposure.

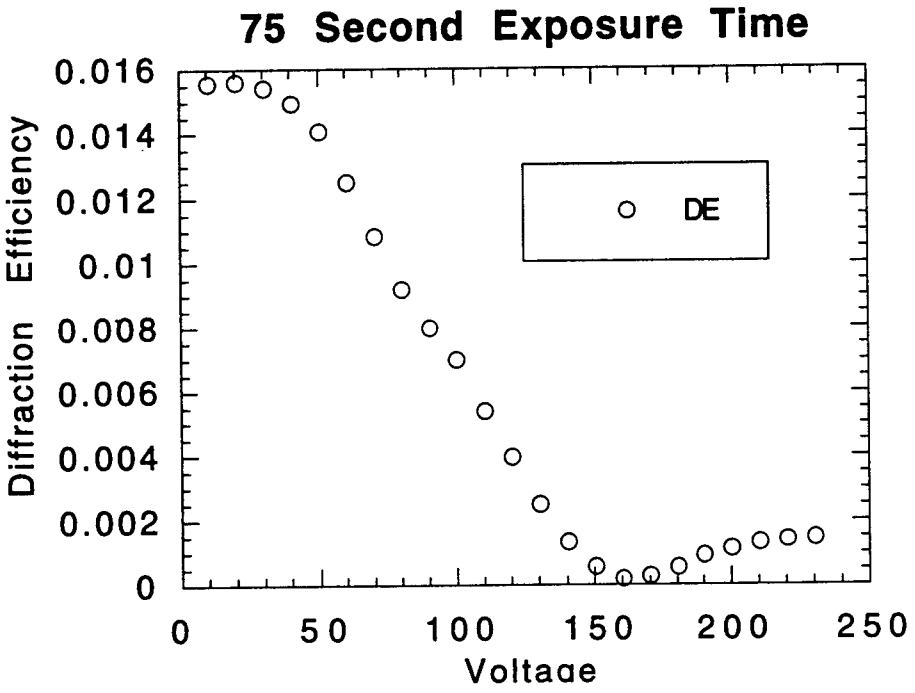

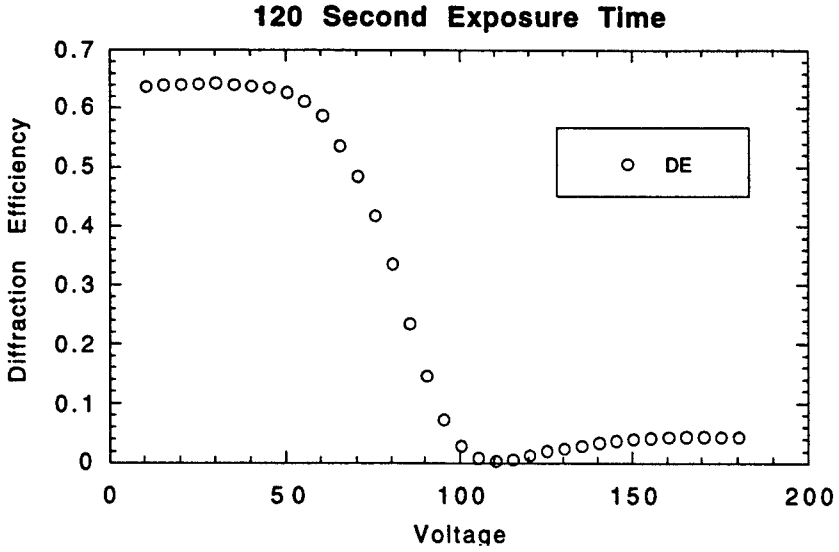
120 Second Exposure Time
Diffraction Efficiency
0.7
0.6
0.5
0.4
0.3
0.2
0.1
0
DE
0
50
100
150
200
Voltage

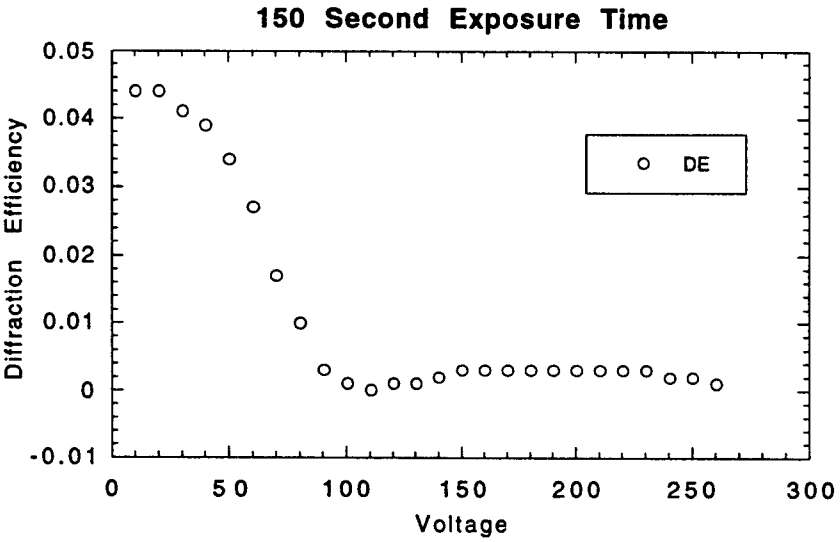
150 Second Exposure Time
Diffraction Efficiency
0.05
0.04
0.03
0.02
0.01
0
-0.01
DE
0
50
100
150
200
250
300
Voltage

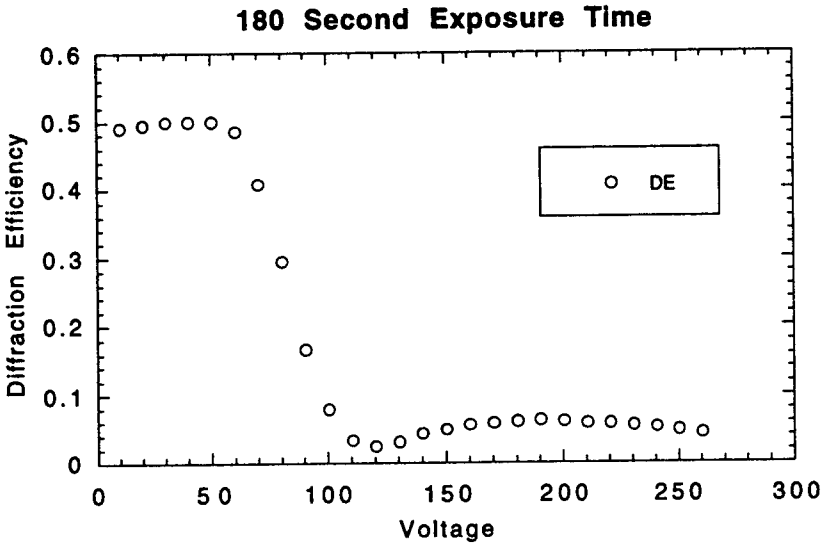

These results very closely coincide with the results of the diffraction efficiency giving more support to the conclusion that the refractive index modulation does indeed reach a maximum at about 75 seconds and remains constant independent of the exposure time.

Suggestions for Further Research

Further research into this experiment would prove very useful. I suggest that the samples be looked at under the Scanning Electron Microscope (SEM) for deeper results. I also feel that further research could be done into an interesting observation that was made.

After the voltage switching was completed, graphs were made showing the sum of the transmitted and diffracted light. The sum of the two should add up to 100%, however this did not happen. The 120 second exposure indicated a 25% loss,

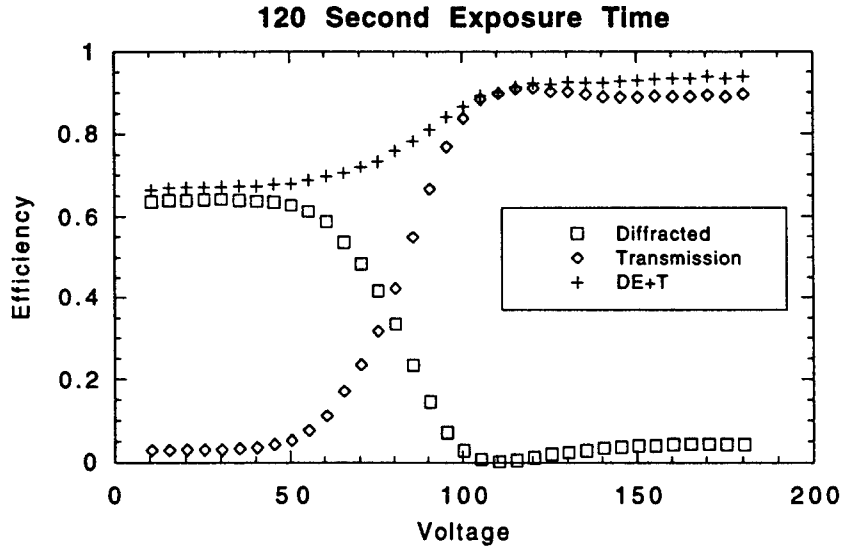

and the 180 second exposure indicated a 40% loss.

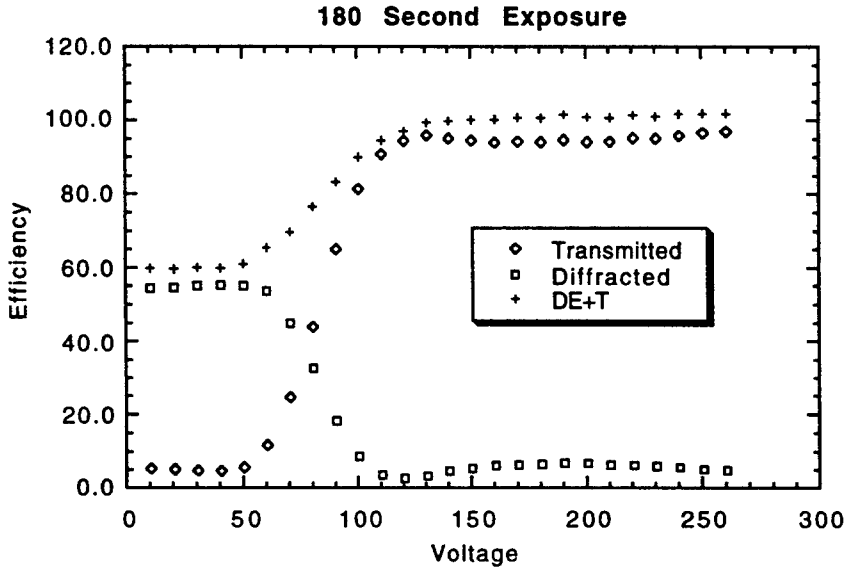

From these results, it may be concluded that there is more scattering with longer exposure times, however, there is not enough data to confirm an accurate conclusion.

One other area to investigate further into this experiment would be to find if the same results would be obtained in time if the laser power was increased rather than the time or energy.

Acknowledgments

Special thanks to Dr. L. V. Natarajan, Mark Neal, Dr. Richard Sutherland, and Vince Tondiglia for all their encouragement, guidance, and support. I also want to thank Wright Laboratories which made this experience possible.

References

Adams, W. W, T. J. Bunning, L. V. Natarajan, R. L. Sutherland, and V. P. Tondiglia. "Electrically Switchable Volume Gratings in Polymer-Dispersed Liquid Crystals." *Applied Physics Letters*, 1993: 1074-1076.

Adams, W. W, T. J. Bunning, L. V. Natarajan, R. L. Sutherland, and V. P. Tondiglia. "Volume Holographic Image Storage and Electro-Optical Readout in a Polymer-Dispersed Liquid-Crystal Film." *Optical Letters*, 1995: 1325-1327.

Adams, W. W, T. J. Bunning, L. V. Natarajan, R. L. Sutherland, VP. Tondiglia, and D. L. Vezie. "The Morphology and Performance of Holographic Transmission Gratings Recorded in Polymer Dispersed Liquid Crystal." *Polymer*, 1995: 2699-2708.

Bunning, T. J., L. V. Natarajan, R. L. Sutherland, and V. P. Tondiglia. "Bragg Gratings in an Acrylate Polymer Consisting of Periodic Polymer-Dispersed Liquid-Crystal Planes." *Chemistry of Materials*, 1993: 15331538.

David Halliday, Robert Resnick. Physics for Students of Science and Engineering. John Wiley & Sons, Inc., New York, 1965.

Associate did not participate in the program.

A STUDY OF THE CORROSION RESISTENCE OF SOL-GELS

Rebecca M. Thien

Chaminade Julienne High School
505 S. Ludlow St.
Dayton, OH 45402

Final Report for:
High School Apprentice Program
Wright Laboratory

Sponsored by:
Air Force Office of Scientific Research
Bolling Air Force Base, DC
and
Wright Laboratory

August 1997

A STUDY OF THE CORROSION RESISTENCE OF SOL-GELS

Rebecca M. Thien
Chaminade Julienne High School

Abstract

The corrosion resistance of aluminum that was previously coated with a sol-gel with and without inhibitors was studied. The two inhibitors used were sodium molybdate and sodium sebacate. The corrosion resistance of aluminum in solutions containing these inhibitors was also studied. The sol-gel was dip-coated onto 2" by 1" 2024-T3 aluminum slides. These samples were then tested using Tafel analysis and Potentiodynamic Scans. The results of the experiment showed that sol-gels could be used as corrosion prevention coatings. However, the two inhibitors, sodium molybdate and sodium sebacate, did not improve the corrosion resistance of the sol-gel when they were added.

A STUDY OF THE CORROSION RESISTENCE OF SOL-GELS

Rebecca M. Thien

Introduction

In the past few years the Air Force has made the research to find a new, safer airplane coating a priority. The current coatings contain chromate compounds to prevent corrosion. Chromate is very good in preventing corrosion , but is a carcinogen[1]. This becomes a huge problem when the coatings, topcoat, primer, and any other barrier, are stripped so that the metal surface of the plane can be inspected for spots or cracks of corrosion[2]. Commercially available surface treatments for aluminum and titanium usually require the use of toxic, corrosive chemicals, and sometimes, sophisticated electrical equipment[3].

There are environmental concerns regarding almost every aspect of preparing metal surfaces for adhesive bonding[3]. Many formulations include environmentally hazardous components, these include EPA 17, lead, etc. The coatings used now also release large amounts of Volatile Organic Compounds (VOC's). These produce smog and other air pollution.[4]

One of the Air Force's most expensive maintenance activities is the painting, stripping, repainting, and handling of the associated inspected, and repainted every 2-4 years. The cost adds up.

For these reasons the Air Force has put an emphasis on developing a coating that is less harmful to the environment and doesn't contain toxic substances[4]. It must be a low

cost coating that shows good adhesion properties on metallic substrates[5]. They also have a unique requirement of a 30-year life with the removal and reapplication of only the topcoat every eight or more years[2,6]. This would significantly reduce the cost involved.

One alternative is high-performance ceramic coatings that constitute materials and hazardous material of its planes[2]. More than 1,200 planes go through this process every year. Each plane must be stripped, combine such properties as wear-, erosion-, corrosion- and high-temperature resistance. Sol-gels are such coatings[5]. An application of the environmentally harmless sol-gel process as the surface pretreatment of aluminum alloys shows adhesion and corrosion resistance[7]. The sol-gel method is a way to produce inorganic oxide materials. It provides an alternative to traditional, energy-inefficient methods of preparing glasses and ceramics[5]. Sol-gels are created from a solution of various reactants that are undergoing hydrolysis and condensation reactions[6]. There is a continuous increase in the molecular weight of the oxide species that are produced[6]. These then start to link together in polymer chains. These normally have a diameter of 2-5 nm[6].

Most silica sol-gels use silicon alkoxide precursors. The most common are tetramethoxy orthosilicate (TMOS, $Si(OCH_3)_4$), and tetraethyl orthosilicate (TEOS, $Si(OCH_2CH_3)_4$). These reactions normally are done in ethanol. Alkoxide-based sol-gel chemistry keeps unwanted salt by-products from forming and allows more control over the final product. The balanced chemical equation for the formation of a silica gel from TMOS is:

$$Si(OCH_3)_{4\,(liq.)} + 2H_2O_{(liq.)} \rightarrow SiO_{2\,(solid)} + 4HOCH_{3\,(liq.)}$$

The balanced chemical equation for the formation of silica gels from TEOS is:

$$Si(OCH_2CH_3)_{4\ (liq.)} + 2H_2O_{(liq.)} \rightarrow SiO_{2\ (solid)} + 4HOCH_2CH_{3\ (liq.)}.$$ [6]

Other reactions that take place in the formation of sol-gel are:

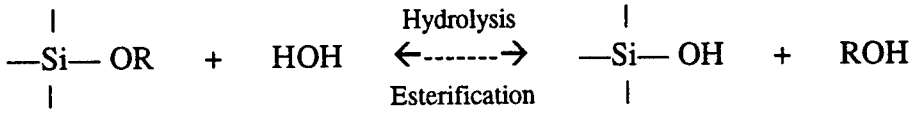

Silicon Alkoxide A Silanol

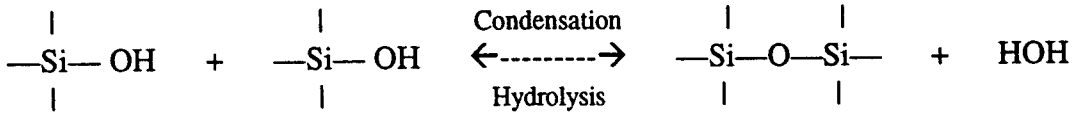

A Silanol A Silanol A Siloxane

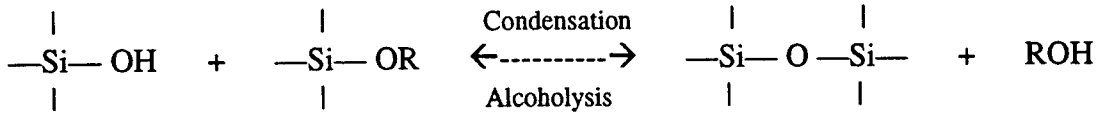

A Silanol Silicon Alkoxide A Siloxane

where R is an alkyl group (C_xH_{2x+1}). Because of these reactions there are strong hydrogen-bonding effects shown at the surface of the sol-gel.[8]

In this experiment alcohol- based sol-gels were tested. In the sol-gels TMOS was used as a source of silica, ethanol was used as a solvent, and GPTMS was used as a catalyst.

Two corrosion inhibitors, Sodium molybdate and sodium sebacate, were used in the experiment. The definition of such an inhibitor is "a chemical substance which decreases the corrosion rate when present in the corrosion system at a suitable concentration without significantly changing the concentration of any other corrosion agent[9]." In other words it helps to stop corrosion reactions.

There are three types of inhibitors: anodic, cathodic, and mixed. An anodic inhibitor effects anodic reactions, the dissolution of metal. A cathodic inhibitors effects cathodic reactions, ions in near neutral / alkali solutions reduction of oxygen to hydroxide. Mixed inhibitors help stop both anodic and cathodic reactions.[10]

The two inhibitors that were used are sodium sebacate ($NaOOC(CH_2)_8COONa$) and sodium molybdate ($Na_2MoO_4 \cdot 2H_2O$). Sebacic acid, ($HOOC(CH_2)_8COOH$), is a dibasic acid. Therefore it needs two moles of sodium hydroxide for each of its moles to neutralize. When this occurs the solution becomes a salt called sebacate. Sebacate is an anodic inhibitor. It is also an organic compound. Molybdates are non-oxidizing, anodic inhibitors. Molybdates have similar chemical properties to chromates, this is because Molybdenum is directly below chromium on the periodic table.[10]

Chromates are also corrosion inhibitors. Chromate is an anodic inhibitor. It is a very versatile inhibitor It works on many different metals and on many different types of corrosion. The major drawback is that it has biocidal, toxic, and carcinogenic properties.[10]

There are two reactions that are going on while aluminum corrodes. The balanced chemical equation for these reactions are:

$$Al \rightarrow Al^{3+} + 3e^-$$

and

$$2H_2O + O_2 + 4e^- \rightarrow 4OH^-$$

The first reaction is an oxidation reaction. It is also an anodic reaction. This reaction takes place where the pitting begins on the metal. The voltage of the metal at the start of pitting is called the pitting potential. The second reaction is a reduction reaction. All metals have a voltage when exposed to a solution. This voltage is called the corrosion

potential. The corrosion potential (E_{corr}) indicates where the sample would corrode in the solution itself. Generally the higher the potential, the more effective the sample is at resisting corrosion.

The equation to calculate the corrosion current density(i_{corr}) is:

$$i_{corr} = \frac{B}{R_p} \quad \text{where}$$

$$R_p = \frac{\Delta E}{\Delta i} \quad \text{and}$$

$$B = \frac{b_a b_c}{2.3(b_a b_c)}$$

where R_p = polarization resistance

E = potential (voltage)

B = constant for a given corrosion reaction

b_a = the slope of the anodic line on a Tafel scan

b_c = the slope of the cathodic line on a Tafel scan.[10]

Methodology

Surface Treatment

Mechanically polish 1" by 2" 2024-T3 aluminum slides with wet 600 grit sand paper. Rinse and dry. Sonicate in Brulin 815 GD (commercial detergent), diluted to 1:15 in water, for 30 minutes. Rinse with distilled water and dry. One hour before coating place samples in a warm Etching Solution for 10 minutes or until little bubbles start to appear on the metal surface. Rinse immediately in distilled water and dry.

Etching Solution

Dissolve 25g Iron II Sulfate Heptahydrate in 425 ml distilled water. Slowly stir in 75 ml Sulfuric Acid. Let the solution stir for a little while.

Sol-Gel Preparation

The basic sol-gel recipe that was used in the experiment was:

Solution 1: 14.3 ml Ethanol (ETOH)

9.6 ml Water

8.6 ml Tetramethyl Orthosilicate (TMOS)

Solution 2: 7.2 ml ETOH

11.8 ml Glycidoxypropyl Trimethoxysilane (GPTMS)

Stir the solutions separately for one hour. Pour Solution 2 into Solution 1. Stir for 24 more hours. Coat by dip-coating.

If using an inhibitor add it to the sol-gel one hour before coating and continue to stir. The inhibitors used in this experiment were 2.00g Sodium Molybdate and 1.67g Sebacic Acid neutralized with 25ml distilled water and Sodium Hydroxide.

Dip-Coating and Curing

Place two slides in each clip of the dip coater. Pour 50 ml of the sol-gel into a 50 ml teflon cell and place under the slides. Set the withdrawal speed to 10.8-11.0 cm per min. Leave in the sol-gel for two minutes before removing. Let the slides dry for a few minutes before placing the samples on a foil sheet. Put the sheet in an oven set at 60°C. Cure for at least 10 hours.

Sample Preparation for Electrochemical Analysis

Find the side of the sample that has the most consistent coating. Place the slide on a teflon disk with the best side facing up and the bare aluminum end hanging off of the

disk. With a silicone sealant, seal the edges of the sample to the disk. Take a piece of PVC pipe 3" high with a diameter of about 2". Put sealant on one of its edges. Place that side onto the disk so that it surrounds a large portion of the sample. Add extra sealant where ever it looks like there isn't a good seal. Let it sit for 20-24 hours to cure completely.

Pour 3.5% Sodium chloride into the sample. Let it set for one hour. If the sample begins to leak remove the Sodium chloride out and rinse the sample with distilled water. Apply more sealant where it had been leaking. Wait 20-24 hours before pouring more Sodium chloride solution into the sample.

Electrochemical Analysis of the Sol-Gel Samples

Connect the sample to the computer to run a Tafel analysis (see figure 1) to each of the three slides. Then run a Potentiodynamic Scan (see figure 2) on the same samples.

The parameters for the Tafel analysis and the potentiodynamic scan that were used are as follows:

	Tafel	Potentiodynamic
Initial E	-0.1	-0.05
Final E	0.1	0.6
Scan Rate (mV/s)	1	5
Sample Period (s)	2	1
Sample Area (cm^2)	1	1
Density (gm/cm^3)	7.87	7.87
Equiv. Wt.	27.92	27.92
Conditioning	Off	Off
Initial Delay	On	On
Time(s)	300	300
Stability(mV/s)	0.1	0.1
IR Comp	On	On

Inhibitor Solution Preparation

Sodium Molybdate: Dissolve 2.00g sodium molybdate in 50.0 ml Water.

Sodium Sebacate: Mix 50.0 ml water and 1.67g Sebacic Acid together in one beaker. In another beaker dissolve several grams of Sodium Hydroxide in 50.0 ml water. Add a few drops of the Sodium Hydroxide to the Sebacic Acid until the pH becomes neutral.

Sodium chloride: Dissolve 1.75g Sodium chloride in 50 ml water.

Electrochemical Analysis of the Inhibitor Solutions

Place a slide that has been surface treated in the solution. Connect to the computer for Tafel testing.

After running the test on three slides per solution, add 1.75g of Sodium chloride to the solution and run the Tafel tests again. Skip this step when using the Sodium chloride solution. Then run a Potentiodynamic Scan on all of the samples in their solutions.

Results

The Tafel analysis that was run on the samples was analyzed to find the corrosion rate, corrosion potential (E_{corr}), and the corrosion current (i_{corr}).

Of the tests run on the sol-gels, with and without an inhibitor, the sol-gel with no inhibitors (see pictures 2 & 3) had the best corrosion rate at 0.2055 thousandths of an inch (mil) per year (mpy). The sodium sebacate sol-gel (see pictures 6 & 7) was next with a corrosion rate of 2.965 mpy. The worst was the sodium molybdate sol-gel (see pictures 4 & 5) which corroded at a rate of 6.788 mpy.(see figure 3)

The sol-gel that had the best corrosion potential was also the sol-gel with no inhibitors. Its corrosion potential was -529.3mV (millivolts). It was followed by the

corrosion potential of the sodium sebacate sol-gel (-569.5mV) and the sodium molybdate sol-gel (-587.9mV), respectively.

The best corrosion current was from the sol-gel without an inhibitor with a current of 0.726 $\mu A/cm^2$. The corrosion current of the sodium sebacate sol-gel was 6.488 $\mu A/cm^2$. The sodium molybdate sol-gel had a corrosion current of 14.86 $\mu A/cm^2$.

Of the solutions, with and without sodium chloride, that were tested the sodium sebacate solution (see picture 9) had the best corrosion potential with -193.5 mV. The other solutions were not nearly as good. The sodium molybdate solution (see picture 8) had a corrosion potential of -435.8 mV. Next was the sodium molybdate solution with sodium chloride with -549.5 mV. The sebacate solution with sodium chloride added was found to be at -560.833 mV. The worst corrosion potential was from the sodium chloride solution (see picture 10) with -569.7 mV. (see figures 4 & 5)

The corrosion rate of the sodium sebacate solution was also better than the other solutions. It had a corrosion rate of .1625 mpy. The sodium molybdate solution with sodium chloride was next with a rate of 0.44 mpy. It was followed by the sodium molybdate solution (1.561 mpy) and the sodium chloride solution (3.920 mpy). The worst of the solutions was the sodium sebacate solution with sodium chloride. Its corrosion rate was 16.898 mpy. This clearly doesn't offer much, if any, protection.

The corrosion potential of the sodium sebacate solution was the best at 0.356 $\mu A/cm^2$. The second best was the molybdate solution with 4.483 $\mu A/cm^2$. The sodium chloride solution was next at 5.762 $\mu A/cm^2$. Next was the sodium molybdate solution with sodium chloride with a corrosion current of 6.392 $\mu A/cm^2$. The sodium sebacate solution with sodium chloride was worst at 36.98 $\mu A/cm^2$.

The potentiodynamic scan that was run indicated a pitting potential for the samples that wasn't good. Of the samples tested the sodium molybdate solution had the best pitting potential at -.507. The sol-gel with no inhibitor was the next best at -.515. Next was the sodium molybdate sol-gel (-.527). Following the sodium molybdate sol-gel were the sodium sebacate sol-gel, sodium sebacate solution, and sodium chloride solution with pitting potentials of -.535, -.542, and -.543, respectively.

The results of the Tafel tests was as follows :

sodium sebacate solution	best
sodium molybdate solution	
sol-gel with no inhibitor	
sodium sebacate solution with sodium chloride	
sodium molybdate solution with sodium chloride	
sodium sebacate sol-gel	
3% sodium chloride solution	
sodium molybdate sol-gel	worst

When the potentiodynamic scans were run it resulted in a slightly different order:

sodium sebacate solution with sodium chloride	best
3% sodium chloride solution	
sodium molybdate solution with sodium chloride	
sol-gel with no inhibitor	
sodium sebacate sol-gel	
sodium molybdate sol-gel	worst

Conclusion

Overall the Tafel analysis and the potentioldynamic scan showed that both the sodium sebacate and the sodium molybdate were effective corrosion inhibitors on their own. There was a significant drop off in the prevention of corrosion when 3% sodium chloride was added to the solution. The solutions with the sodium chloride were better corrosion inhibitors than the sodium chloride was on its own. The sebacate and molybdate sol-gels also didn't inhibit corrosion as well as their solutions did or as well as the sol-gel with no inhibitor. The sol-gel with no inhibitor is only a little less effective than the inhibitor solutions on their own.

In summary, sol-gels are affective coatings for preventing corrosion on aluminum. The inhibitors, sodium sebacate and sodium molybdate, should not be used in sol-gel coatings to aid in corrosion prevention.

Acknowledgments

Dr. Michael Donley for the selecting me and the use of lab space.

Dr. Carol Jeffcoate for all of her help and understanding.

Nathan Gebasch, Natasha Voevodin, and Wendy Soto for help in the lab.

Rebecca Twite and Linda Kasten for their help.

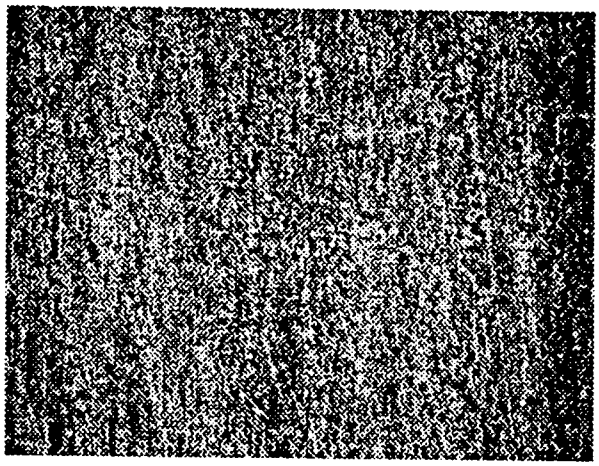

Picture 1 Bare aluminum slide after surface preparation. (100 magnification)

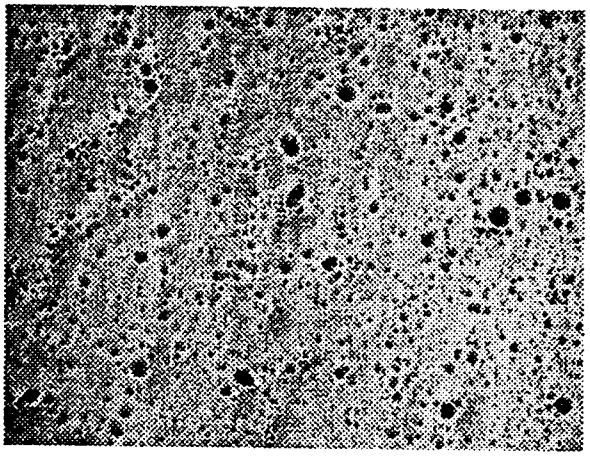

Picture 2 Surface of sol-gel without inhibitor after corrosion (50 magnification)

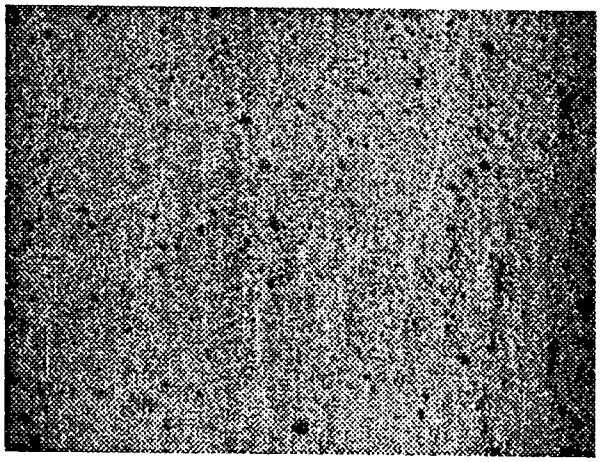

Picture 3 Surface of aluminum after corrosion through the sol-gel (50 magnification).

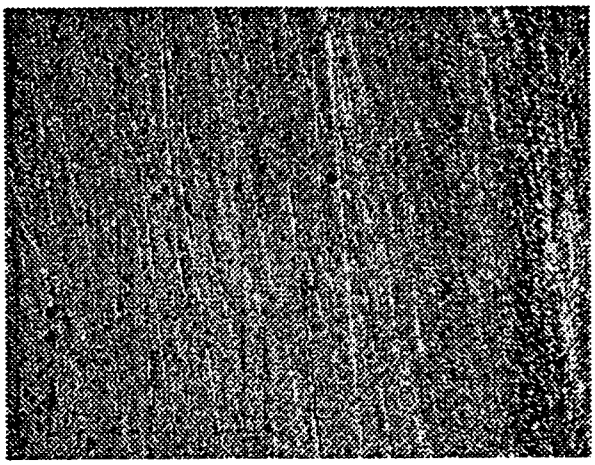

Picture 4 Uncorroded sodium molybdate sol-gel (50 magnification).

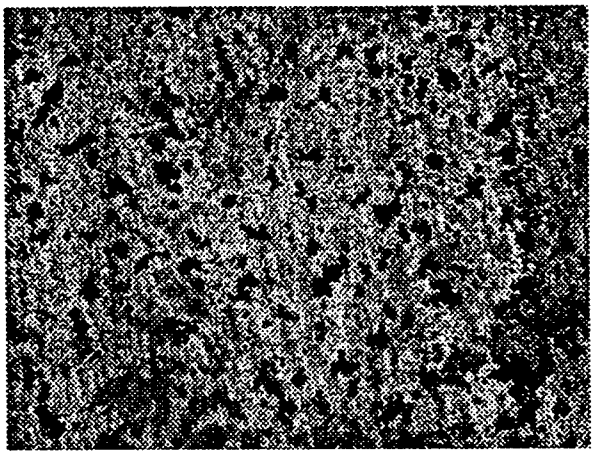

Picture 5 Corroded sodium molybdate sol-gel (50 magnification).

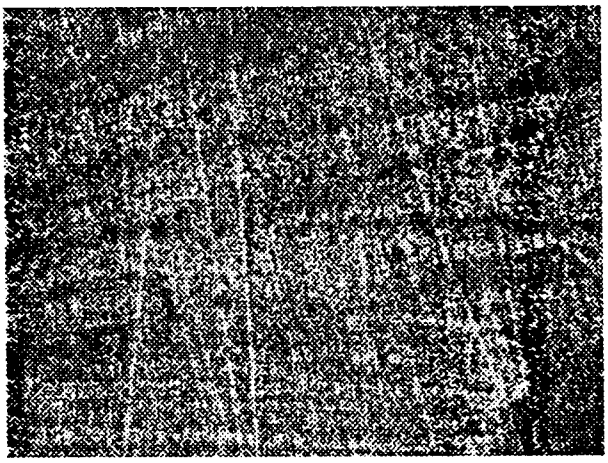

Picture 6 Uncorroded sodium sebacate sol-gel (50 magnification).

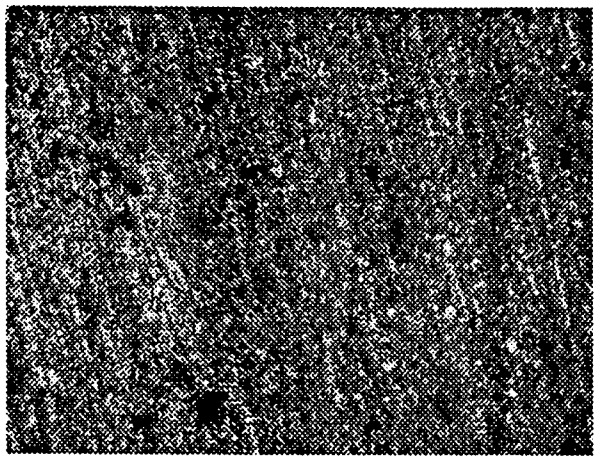

Picture 7 Corroded sodium sebacate sol-gel (50 magnification).

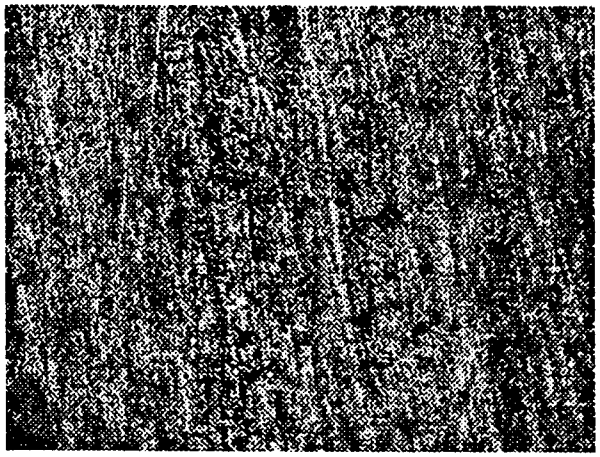

Picture 8 Sample corroded on sodium molybdate solution (50 magnification).

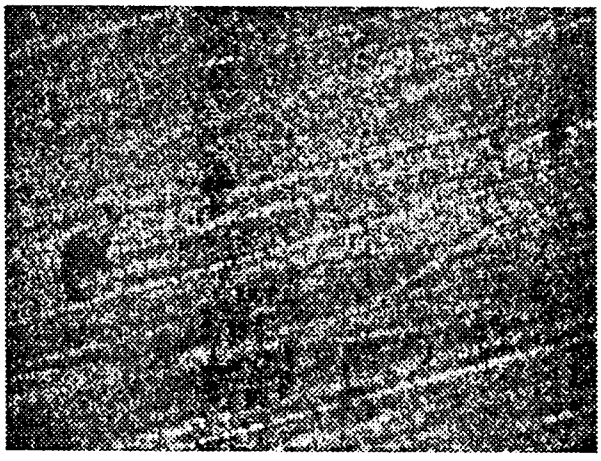

Picture 9 Sample corroded in sodium sebacate solution (50 magnification).

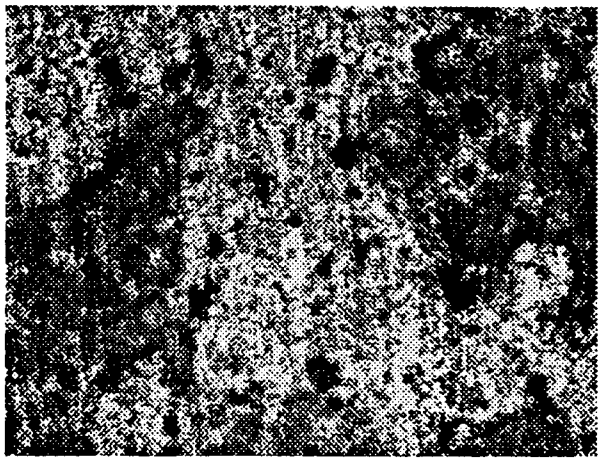

Picture 10 Sample corroded in 3% sodium chloride solution (50 magnification).

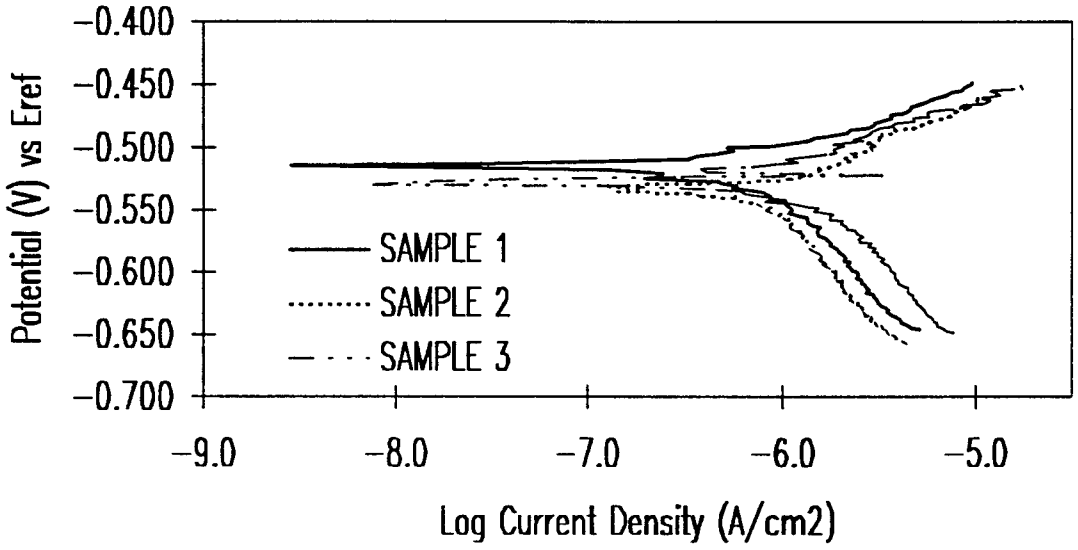

Figure 1 Tafel analysis of three sol-gel samples.

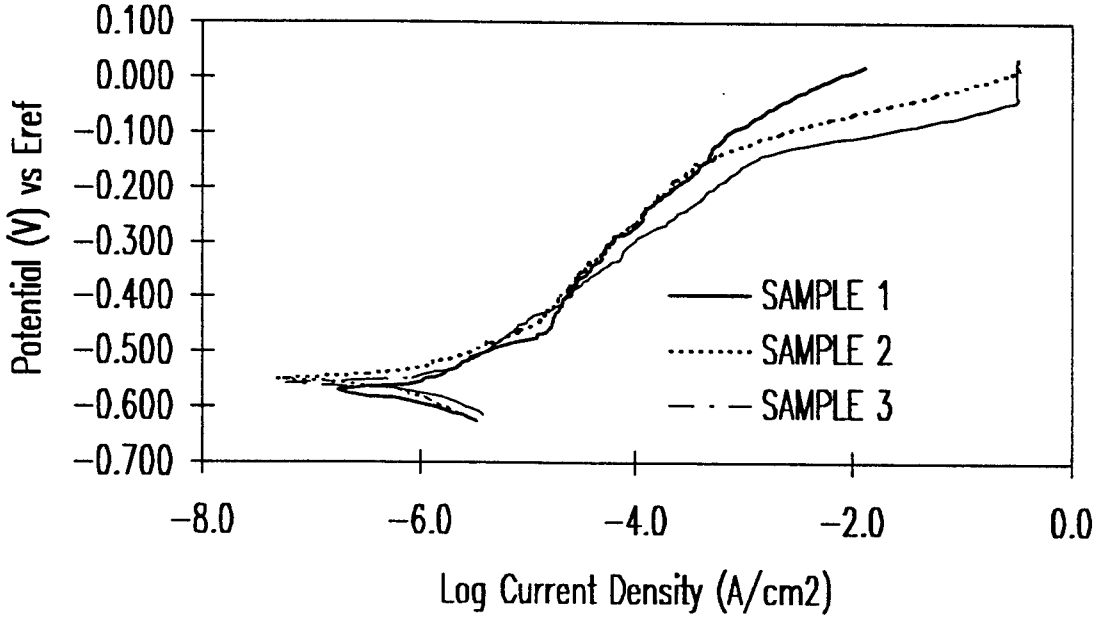

Figure 2 Potentiodynamic Scan of three sol-gel samples with no inhibitor.

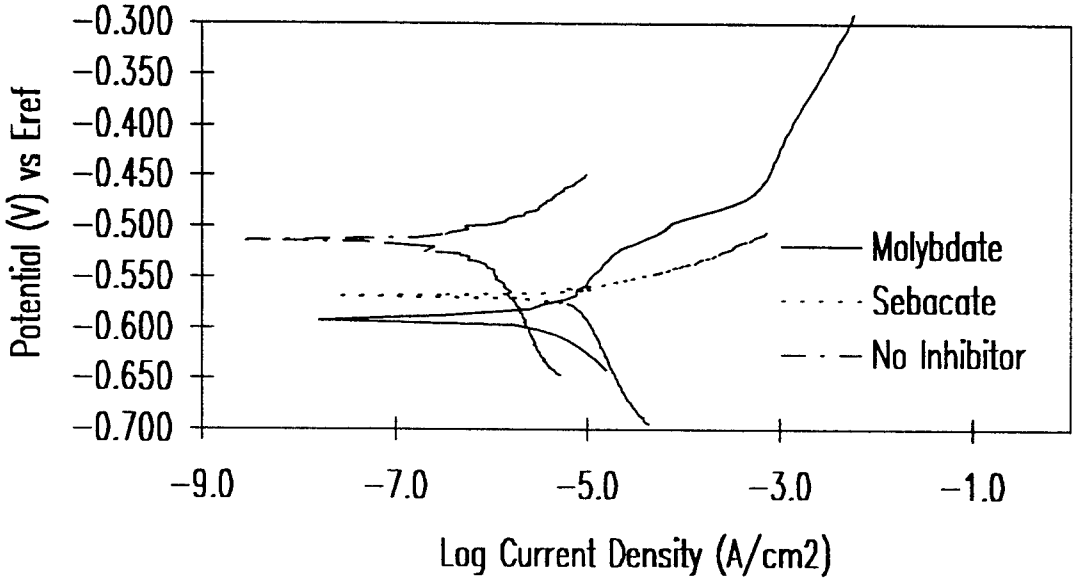

Figure 3 Tafel analysis of aluminum samples coated with sol-gels containing sodium molybdate, sodium sebacate, and no inhibitors.

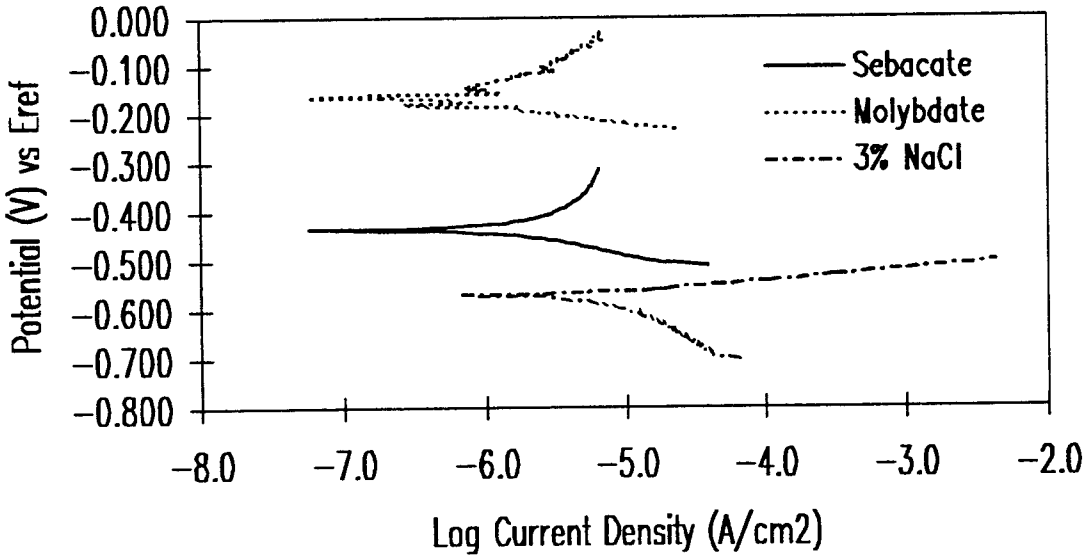

Figure 4 Tafel analysis of aluminum samples in sodium sebacate solution, sodium molybdate solution, and 3% sodium chloride.

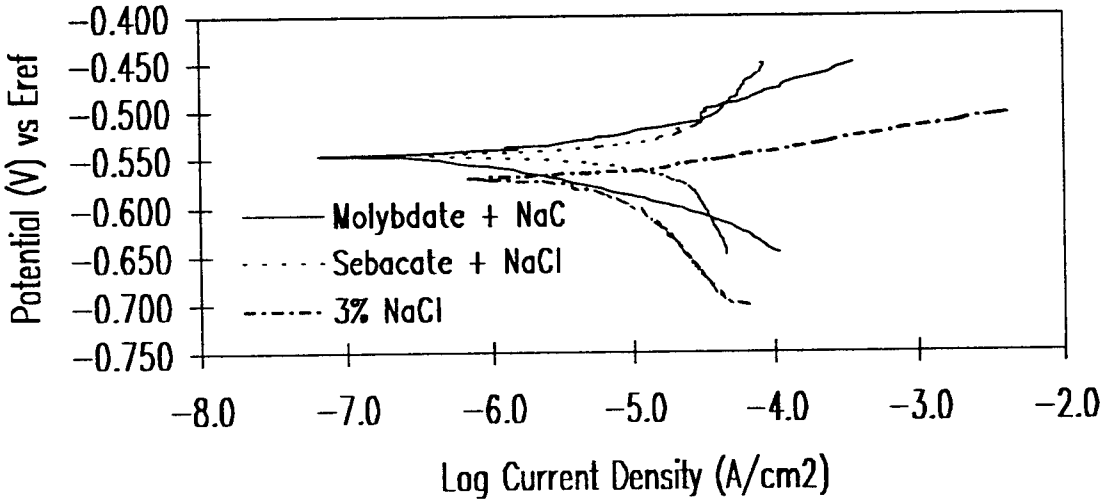

Figure 5 Tafel analysis of aluminum samples in sodium molybdate with sodium chloride, sodium sebacate solution with sodium chloride, and 3% sodium chloride.

[1] Liu, Matthew T, FY 1994 SBIR, Phase II Award Abstracts; 1994; Online; Small Business Innovation Research Program (SBIR); Internet. 2 July 1997.

[2] Donley, Michael, Advanced Aircraft Coatings Systems, Wright-Patterson AFB OH; Online; Small Business Innovation Research Program Wright Laboratory - Materials Directorate; 3 July 1997.

[3] Harrop, D., Proceedings of 'Chemical Inhibitors For Corrosion Control' Symposium, UMIST, Manchester, UK, 21-22 April 1988 Royal Society of Chemistry Special Publication, Number 71, pp 1-20.

[4] Passinault, Lt. Rob, Environmentally Compliant Aircraft Coatings, Wright-Patterson AFB OH; Online; Small Business Innovation Research Program Wright Laboratory - Materials Directorate, Wright-Patterson AFB OH; 3 July 1997.

[5] Lynntech, Inc., Environmentally Compliant Thin Oxide Films as Corrosion Inhibiting Coatings Prepared by Sol-Gel Methods; 7 Feb 1996; Online; SBIR; Internet. 2 July1997.

[6] Microstructured Material Group, "How Silica Aerogels are Made." November 1993; Online; Ernest Orlando Lawrence Berkeley National Laboratory; Internet. 2 July 1997.

[7] Zheng, Haixing, FY 1994 SBIR, Phase II Award Abstracts; 1994; Online; Small Business Innovation Research Program (SBIR); Internet. 2 July 1997.

[8] Brinker, C. Jeffrey and Scherer, George W. Sol-Gel Science. Boston: Academic Press, Inc., 1990.

[9] Harrop, D., Proceedings of 'Chemical Inhibitors For Corrosion Control' Symposium, UMIST, Manchester, UK, 21-22 April 1988 Royal Society of Chemistry Special Publication, Number 71, pp 1-20.

[10] Jeffcoate, Carol S., PhD Thesis, UMIST, Manchester, UK, 1994, pp 8-13, 35

DATA REDUCTION FOR BLAST ARENA LETHALITY ENHANCEMENT

Jonathan D. Tidwell

Rocky Bayou Christian School
2101 N. Partin Drive
Niceville, FL 32578

Final Report for:
High School Apprenticeship Program
Wright Laboratory

Sponsored by:
Air Force Office of Scientific Research
Bolling Air Force Base, DC

and

Wright Laboratory

August 1997

DATA REDUCTION FOR BLAST ARENA LETHALITY ENHANCEMENT

Jonathan D. Tidwell

Rocky Bayou Christian School

Abstract

Data from blast arena testing of three high explosive (HE) formulations was reduced. The three formulations tested were APET-257e3, AFX-757, and PBXN-111 with the purpose of determining the blast performance of these specific formulations in a 1000 lb. MK-83 warhead. Data from the shots will be compared to data from previous blast arena testing conducted by the Air Force and the Navy on the BLU-110 (MK-83 with a PBXN-109 fill). The objective of the testing is to determine the performance gains realized by replacing the standard fill with current generation explosive technology. The overall goal of the program is to achieve 75 percent of the blast performance of the MK-84 (2000 lb. warhead).

DATA REDUCTION FOR BLAST ARENA

LETHALITY ENHANCEMENT

Jonathan D. Tidwell

Introduction

Recently, the Air Force has taken an interest in increasing the lethality of its bombs. The goal was to get a MK-83 to perform as well as a MK-84. The MK-83 is a 1000 lb. warhead having a Net Explosive Weight (NEW) of 385 lb. The length of the bomb is 74.1" while its outside diameter is 14.2". The MK-84 is a 2000 lb. warhead that contains 945 lb of Tritonal. It is 98.8" long and has an outside diameter of 18.2". Scientists at the High Explosives Research and Development (HERD) facility have developed two high explosive formulations to fulfill this desire. The first, AFX-757, is composed of 20% Class 5 RDX, 5% RDX ground to 4 micron (from Fluid Energy Mill (FEM)), 30% Ammonium Perchlorate (AP), 12% Hydroxy Terminated PolyButyldiene (HTPB), and 33% Aluminum (Al). The RDX is the high explosive, the AP serves as the oxygen supplier, the HTPB is the inert binder, and the Al serves as the fuel. The second formulation, APET-257e3, is composed of 20% RDX; 30% AP; 15% TriMethylolEthane TriNitrate (TMETN), a liquid explosive; 5% Poly Caprolactone poLyone (PCL); and 30% Al. The Navy developed a third formulation called PBXN-111 which is composed of 20% RDX, 43 % AP, 12% HTPB, and 25% Al. PBXW-129, which is composed of 48.9% AP, 11.3% TMETN, 1.7% PCL, and 38.1% Al, was also developed by the Navy. Table 1 shows the compositions and theoretical maximum densities (TMD) of the explosives.

Table 1: Candidate Compositions

	Baseline	Air Force		Navy	
INGREDIENT	PBXN-109	AFX-757	APET-257e3	PBXN-111	PBXW-129
RDX	64	20	20	20	
RDX, FEM		5			
AP		30	30	43	48.9
TMETN			15		11.3
HTPB	16	12		12	
PCL			5		1.7
Al	20	33	30	25	38.1
TMD (g/cc)	1.674	1.846	1.903	1.818	2.064

It is supposed that these compositions will increase the energy, and thus, the effectiveness of the bomb. To get a 1000 lb. bomb to perform as well as a 2000 lb. will require a HE formulation that will produce a substantially increased energy. Certain compounds release a great amount of energy when they decompose. Each formulation was tested twice with the exception of the PBXW-129 that failed to propagate a detonation wave during its first test. Figure 1 shows a relative size comparison of the MK-83 and MK-84.

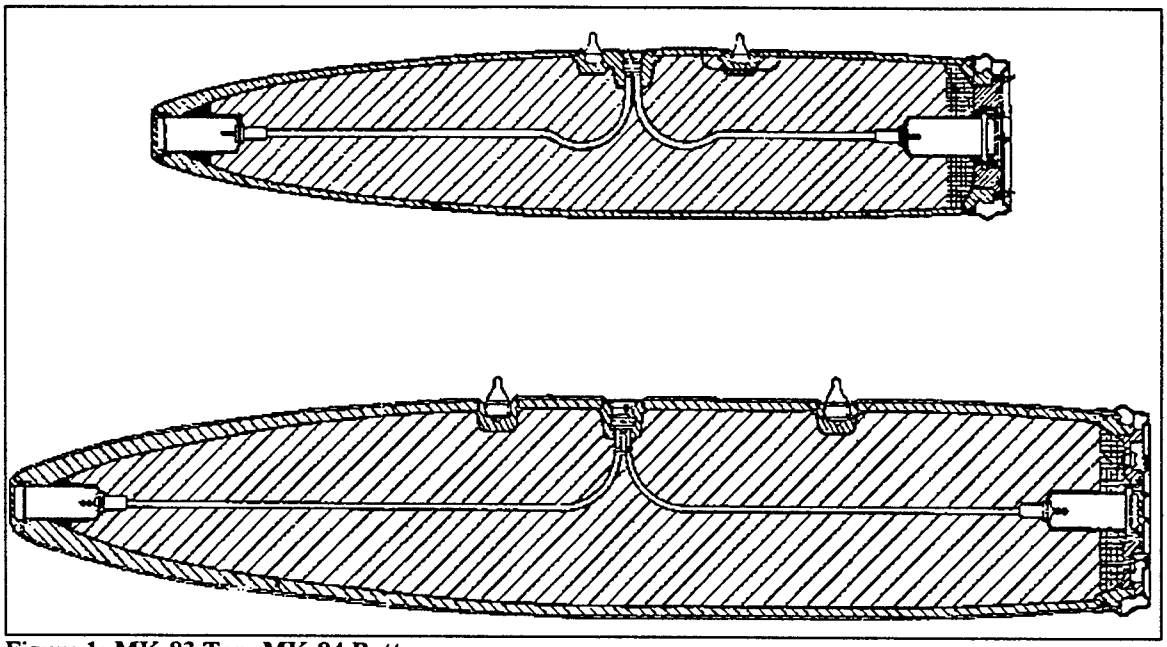

Figure 1: MK-83 Top, MK-84 Bottom

Methodology

The data that was sought from the blast arena tests was data that would show the energy and force of the explosive. To determine the force and energy of the explosive, pressure and impulse data was needed. Impulse is the strength of the wave defined as pressure multiplied by time. The methods for collecting the blast data are shown in the arena setup section. Figure 2 shows the test setup used for the blast arena testing conducted at Test Area C-80C. The testing days were June 10 through June 13, June 17, and June 25.

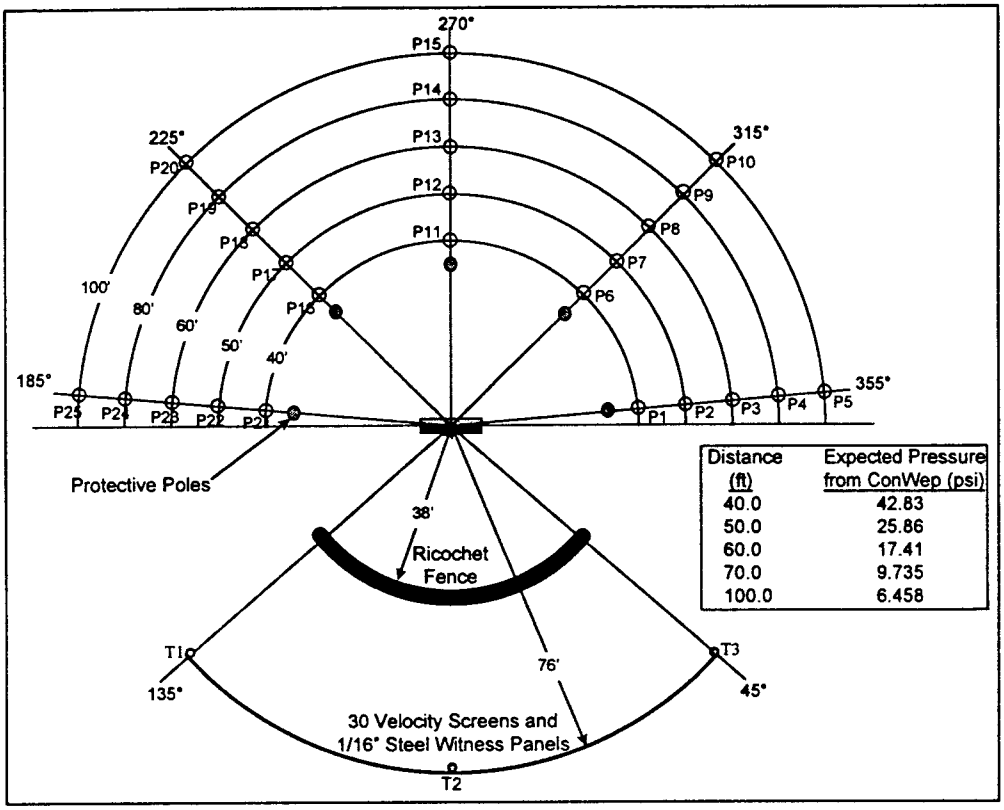

Figure 2: MK-83 BLAST ARENA SETUP

The arena was setup following the guidelines set forth in the Joint Munitions Effectiveness Manual (JMEM) *Testing and Data Reduction Procedures for High-Explosive Munitions.* Chapter 4 requires that a minimum of three static overpressure gauge lines be used to cover 90-, 0-, and 180-degree polar angles (plus or minus 20 degrees) for horizontal arena tests. Each line should have at least five gauges, with additional gauges if possible, to cover the pressure range from 1 to 100 pounds/inch^2 (psi).[1] To meet these recommendations, gauge lines were placed at polar angles of 185°, 225°, 270°, 315°, and 355° with five gauges at distances of 40, 50, 60, 80, and 100 ft. The 185-degree and 355-degree lines were offset 5° from 0° and 180° to protect them from the jetting which forms from the nose and tail of the warhead. This jetting can easily destroy an entire line of gauges upon detonation. Protective poles were also placed in front of each line to protect the gauges from smaller fragment hits. In addition to the pressure gauges, thirty velocity screens and witness panels were placed from 45° to 135° at 76 ft from the

bomb in order to collect fragment velocities and number of fragment hits. This allowed for a rough look at the fragmentation performance of each new formulation.

An ideal blast wave exhibits an instantaneous rise in pressure at a certain time, called time of arrival (t_a), after the explosion. This instantaneous rise to a peak pressure (P_{so}) is then followed by an exponential decay in pressure until the pressure returns to ambient pressure. The pressure continues to decrease below ambient due to a partial vacuum created behind the shock wave. Eventually the pressure returns to pressure as equilibrium is sought with the surrounding area. The time during which the pressure is above ambient pressure is called the positive phase duration (t_o). The area under this part of the curve is called the positive specific impulse (i_s). The area under the negative phase duration of the curve is the negative specific impulse.

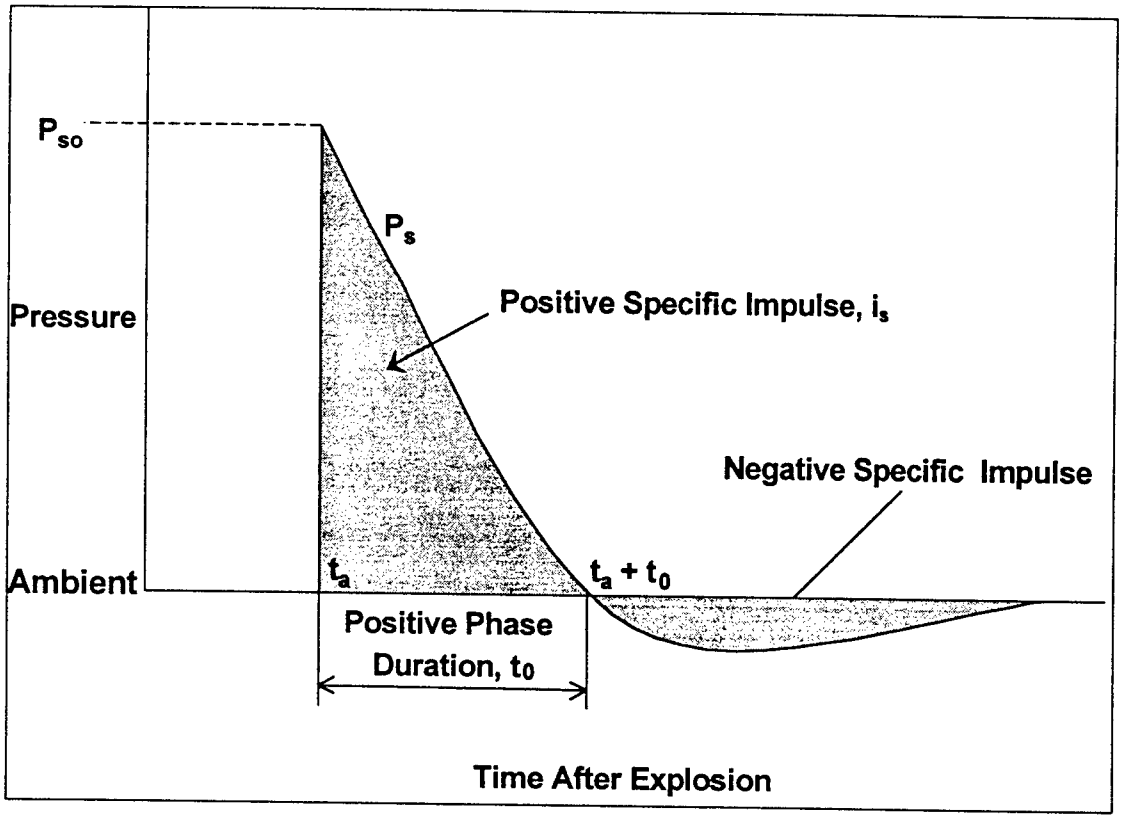

Figure 3: Ideal Pressure Wave

After the shots, the range personnel reduced the data from each gauge by removing any data not included in the positive phase duration. Graphs of the pressure trace from each gauge were digitized in ASCII format and given to the HERD. Figures 4 and 5 show two representative graphs which were sent from the range to the HERD. Figure 4 shows a pressure gauge that responded ideally to the blast pressure wave. That data plot exhibited an instantaneous rise in pressure with a gradual smooth decrease in the pressure until the pressure returned to ambient. Figure 5 shows non-ideal behavior indicating that the pressure gauge responded to anomalies in the pressure field such as fragment hits or line pulls. This is what accounts for the large spikes seen in the middle of the curve. Curve fits were applied to the pressure profiles using Freidlander's equation for exponential decay (Equation 1).

$$P(t) = P_0\left[1 - \frac{(t - t_a)}{t_0}\right]e^{\frac{t_a - t}{\theta}} \tag{1}$$

Curve fits were necessary to ascertain the peak pressure and the impulse of the shock wave. Without a fit, a graph might have a peak pressure differing significantly from the actual peak. The curve fits also smoothed out the graph in order to get more accurate impulse values. To curve fit a bad data plot, the spikes were discarded and the fit was applied to the remaining "good" data points. To determine the impulse of the curve, an integral applied to the equation generated from the curve fit (Equation 2).

$$I = \int_{t_a}^{t_a + t_0} P(t)dt \tag{2}$$

Peak pressure and impulse were based on the measured t_{oa}. Figures 4 and 5 have fits applied to the pressure data plots after the removal of the bad data points. The x intercept value of the curve fit was then recorded to observe the duration of the impulse. When Freidlander's equation is applied to the curve to get a curve fit, parameters a (P_o), b (t_a), and c (θ) are altered until the best curve fit is found. This was accomplished using TableCurve 2D software.

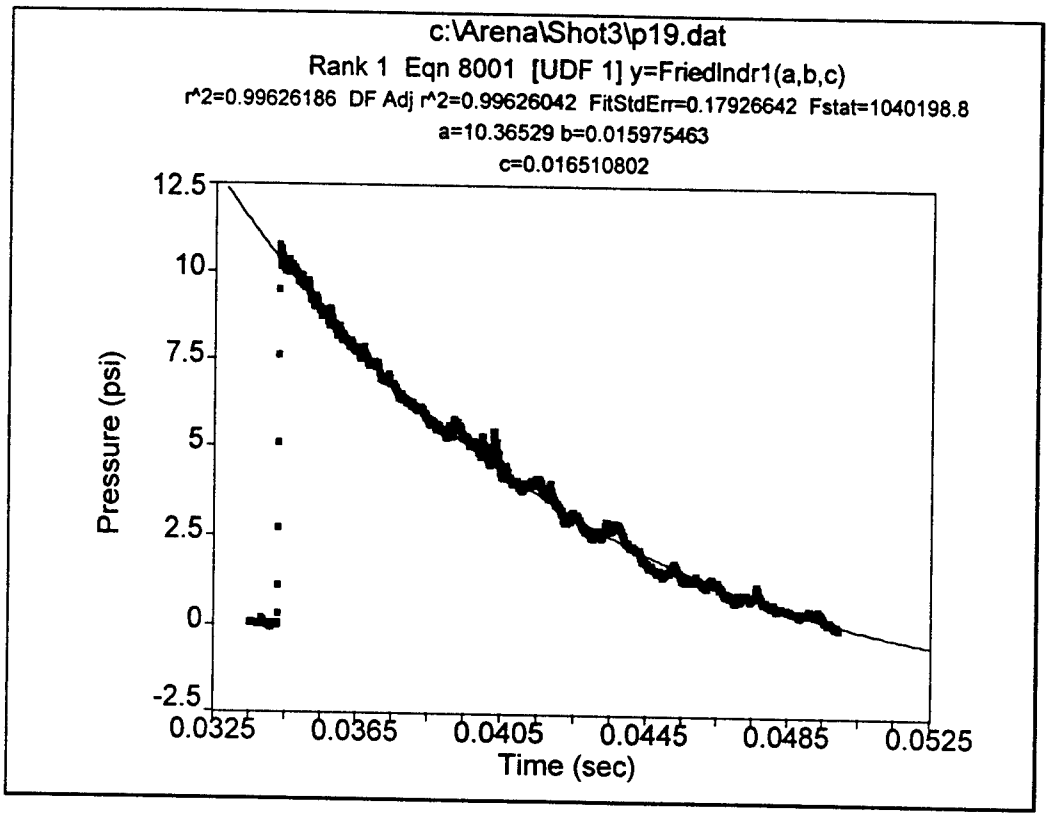

Figure 4: Example of good data

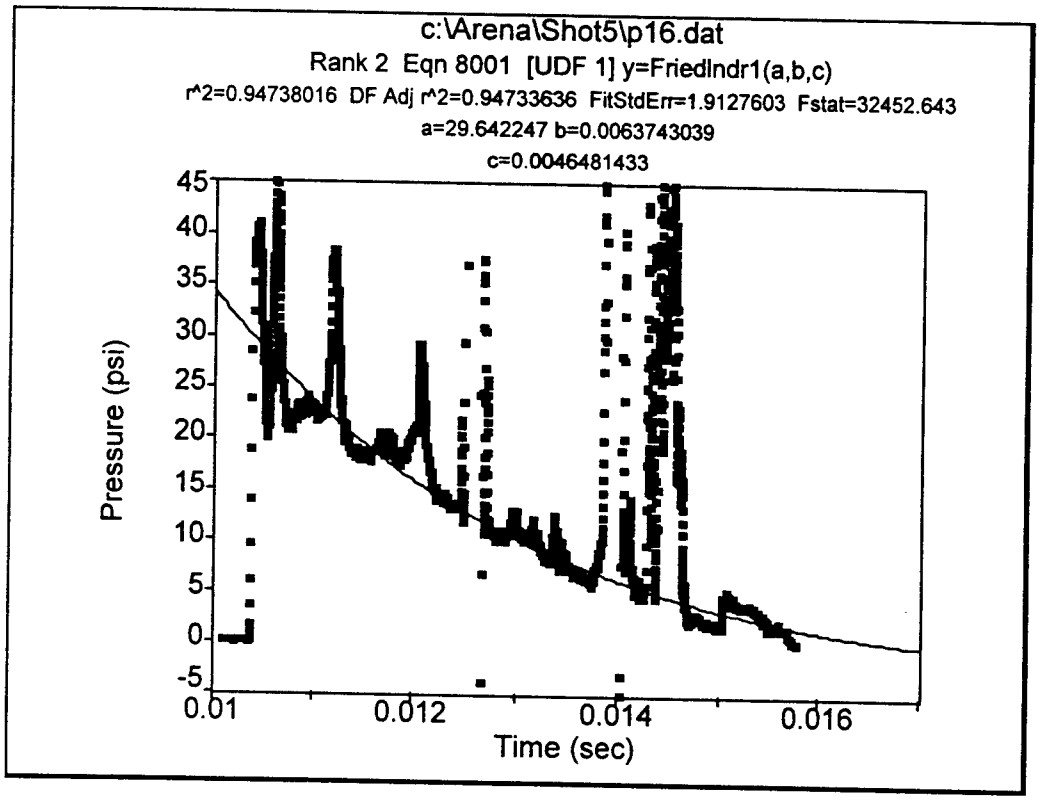

Figure 5: Example of bad data

The peak pressures, the impulses, and the times of arrival were adjusted for standard atmosphere at sea level (STP) for each of the shots. Standard pressure at sea level is 14.7 psi and standard temperature is 288.16 K.

$$S_p = P_z / P_o$$

$$S_t = \left(P_o / P_z\right)^{1/3} \cdot \left(T_o / T_z\right)^{1/2}$$

$$S_I = \left(P_z / P_o\right)^{2/3} \cdot \left(T_o / T_z\right)^{1/2}$$

From these adjusted values, the TNT equivalency was determined for the peak pressures, impulses, and times of arrival for each gauge location. TNT equivalency is the amount of TNT needed to produce the same results as a certain amount of another explosive. For instance, if PBXN-111 has a TNT equivalency of 1.5 then 1 lb of PBXN-111 would perform the same as 1.5 lbs. of TNT. Charts are shown of measured and fit data for all three formulations. Gauges six through twenty provide the best representation of an ideal blast wave. The area covered by these gauges is also the same area covered in previous testing, and can thus be compared to those systems.

Figures 6-8 show comparisons of fit to measured impulse recorded by each gauge averaged over the two shots of each formulation. A pressure wave gradually loses pressure and impulse as it radiates from its source. The gauges closest to the warhead should have the greatest pressure readings while the gauges farthest from the warhead should have the lowest readings. On each pressure gauge line, a pattern from high to low pressure or impulse should be evident. With the measured pressure and impulse data, however, this high to low pattern was not evident. Though the measured values were very erratic, the fit data adjusted the impulse values to form a high to low pattern.

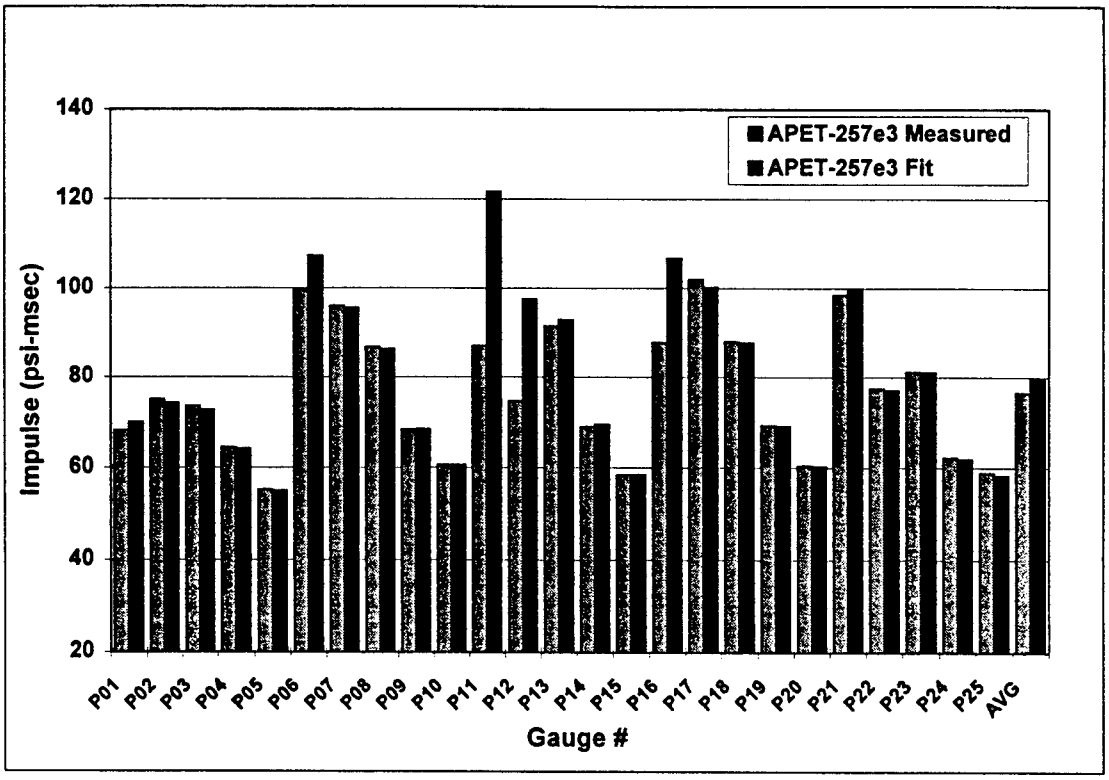

Figure 6: APET-257e3 Impulse Comparison

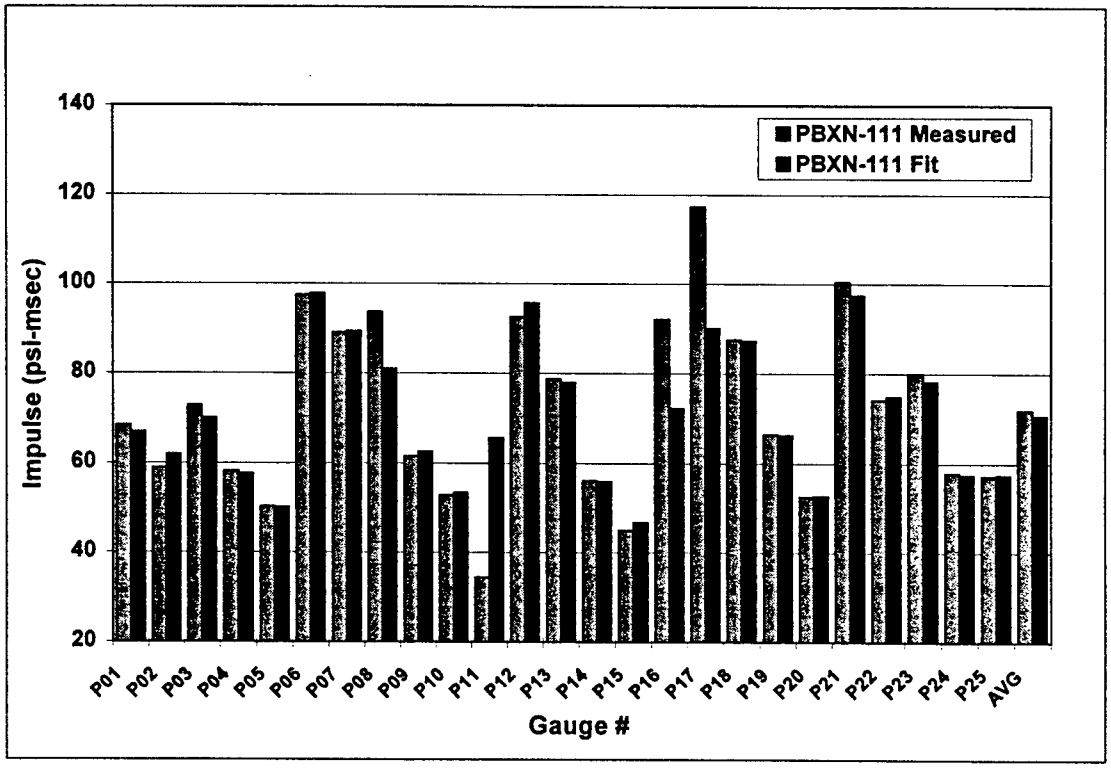

Figure 7: PBXN-111 Impulse Comparison

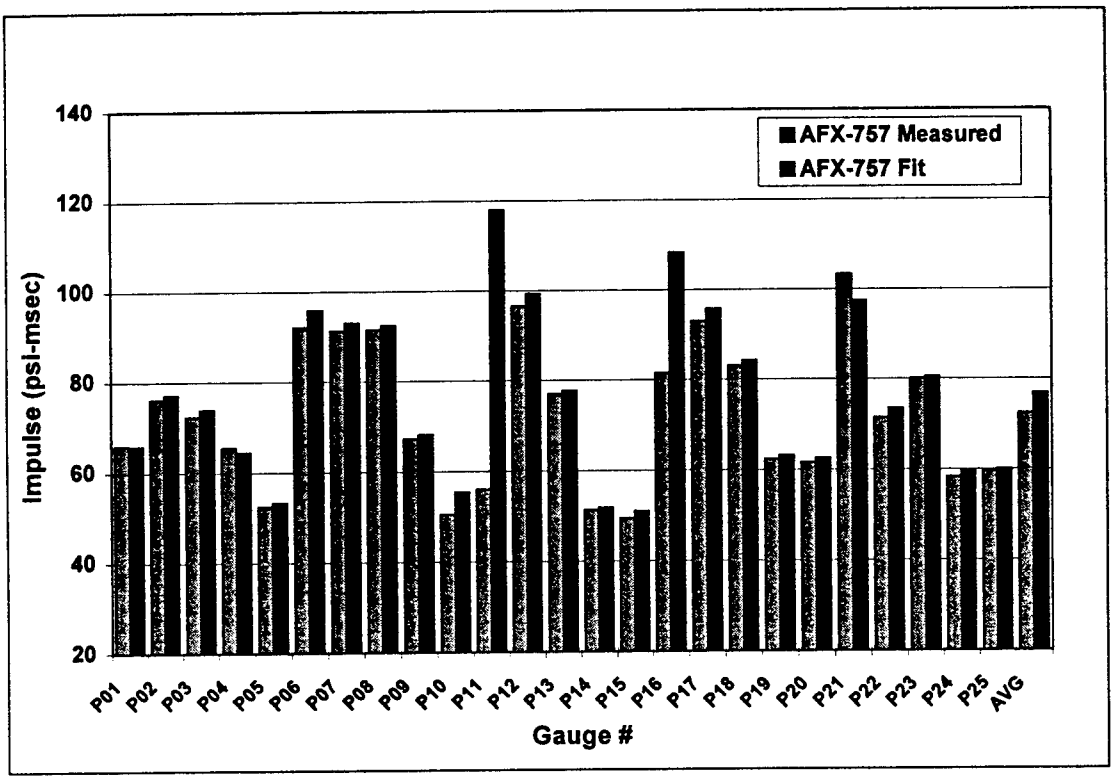

Figure 8: AFX-757 Impulse Comparison

Fragment data was collected from each shot. The number of fragment penetrations in each witness panel was counted at TA C-80C after each shot, and the computer counted the number of fragment hits and the velocities of those hits. To reduce this fragment data, any hit having a time in contact with the witness panel of less than 0.001 msec was discarded. The remaining data was then fit to distribution curves.

Figure 9 shows the number of fragments per panel averaged over the two shots of each formulation. The highest number of fragment penetrations was recorded at the 80-degree angle. This is in line with estimations due to the geometry and initiation of our warhead. The polar angles 45° through 135° along the x axis are the polar angle representations of the thirty witness panels.

The same effect can be seen in the fragment velocity comparison shown in Figure 10.

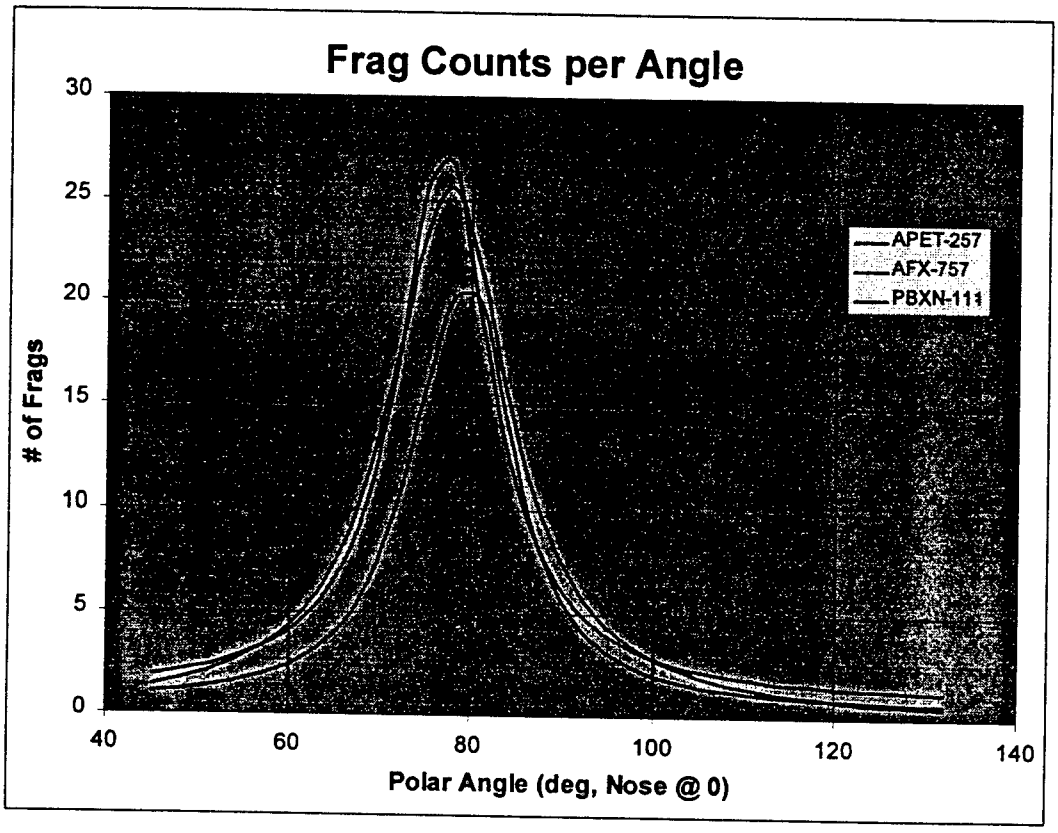

Figure 9: Average Fragment Hits per Panel

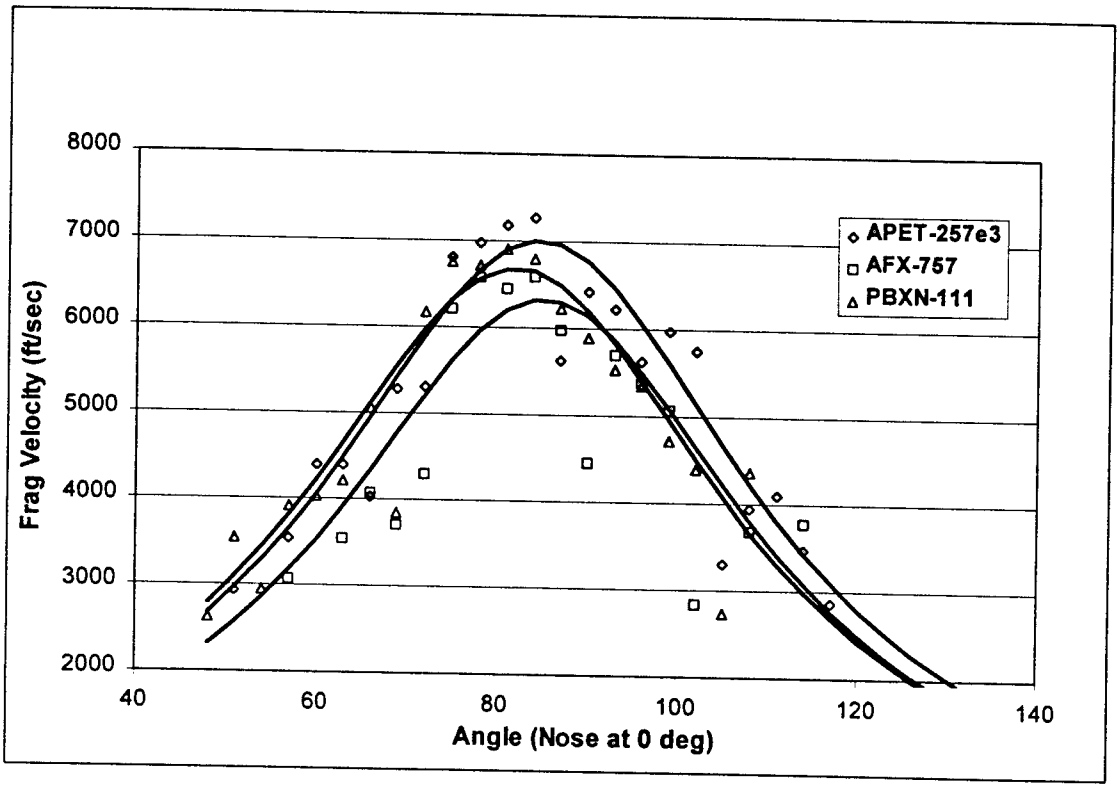

Figure 10: Fastest Fragment Velocities per Panel

Figure 10 shows the average of the two fasted fragments of each panel averaged over the two shots of each formulation. As in the previous graph, the x axis shows the panel number at degrees from 45 to 135. The fastest velocities were seen at eighty degrees. Apet-257e3 had the fastest fragments at around 7300 ft/sec while the fastest fragments of AFX-757 were around 6600 ft/sec. The highest fragment velocities of PBXN-111 were about 6900 ft/sec.

Conclusion

From the reduced data, a clear distinction could be made between the performance of the different formulations. APET-257e3 provided the greatest enhancement based on time of arrival, pressure, impulse, and fragment velocity. Because the databases to which this data could be compared were poor, two BLU-110's are scheduled to be shot in the near future. Those tests should produce a good usable baseline to which the present test data can be compared.

References

1. *Testing and Data Reduction Procedures for High-Explosive Munitions*, Joint Munitions Effectiveness Manual, 61A1-3-7, 8 May 1989. (UNCLASSIFIED)

THE CHARACTERIZATION OF A SCUD FRAGMENT

Robert L Todd

Carroll High School
4524 Linden Avenue
Dayton, Ohio 45432

Final Report for:
High School Apprentice Program
Wright Laboratory

Sponsored by:
Air Force Office of Scientific Research
Bolling Air Force Base, Washington, DC

And

Wright Laboratory

August 1997

THE CHARACTERIZATION OF A SCUD FRAGMENT

Robert L. Todd
Carroll High School

Abstract

The characterization of the metal used to fabricate a scud missile was determined. Samples of the scud fragment were cut, polished, magnified under an optical microscope and a scanning electron microscope, and tested for a chemical analysis. The results of the obersvation determined that there was a weld in the scud fragment. The microstructure of the weld looks like ferrite. The microstruction of the base metal looks like that of a duplex stainless steel. The chemistry of the scud fragment is typically that of a duplex stainless steel. The scud fragment was magnetic indicating the presence of ferrite, but because the specimen did not etch easily there is also a presence of austenite. The results proved that the scud fragment's metal was composed of a duplex stainless steel.

THE CHARACTERIZATION OF A SCUD FRAGMENT

Robert L. Todd

Introduction

The scud missile was used by the Iraqis in the Gulf War. The scud was first deployed by the Soviets in the mid-1960s as a nuclear or conventional warhead. The Iraqis modified the scud for a greater range. By the time of the Gulf War, the Iraqis had four versions of the scud, making them a potential threat to not only Israel but to the rest of the world. The scud fragment that was researched was shot down in the Gulf War by a patriot missile.

Different types of stainless steels have been manufactured. Martinsitic stainless steels fall into two different groups: low-carbon and high-carbon. The low-carbon content has a low chromium content and the high-carbon content has a chromium content as high as 18%. They have a crystal like structure that is body-centered tetragonal, making it brittle only at a low temperature of -300°F. Ferritic stainless steels are mostly ferrite, body-centered cubic, and magnetic. They do not have a high strength and are low in ductility. As the chromium content is increased, corrosion resistance is increased. A large grain size occurs when welding it, causing it to lose ductility. Austenitic stainless steels are much like ferritic stainless steels, but austenitic steels are much more ductile. Austenitic-ferritic stainless steels, also called duplex stainless steels, contains 5 to 40% ferrite. The ferrite increases its weldability and mechanical strength, while raising the resistance to stress-corrosion cracking.

Discussion of the Problem

The purpose of this project is to determine the characterization of the metal used to fabricate a scud missile.

Methodology

A macrophoto was taken of the unknown scud fragment to have a reference picture before cutting was made. With a diamond saw, the fragment was cut into five pieces. Three of the pieces were mounted in Konductomet I. Konductomet I makes the mounted sample conductive, so scanning electron microscopy (SEM) work can be done to the sample. The three samples were labeled 1, 2, and 3. The two nonmounted samples were set aside because they were not used until later in the project. The edges of the three mounted samples were beveled off with 60 grit paper to prevent sharp edges. The samples were then ready for the initial step of polishing. Each mounted sample was ground down using four different grit papers. The papers were 240 grit, 320 grit, 400 grit, and 600 grit. First, the samples were swiped on the 240 grit paper 15-20 times. They were then turned 90 degrees and swiped 15-20 times on the 320 grit paper. The same procedure was also used with the 400 grit paper and the 600 grit paper. The samples were then lapped, which is the second step of polishing. The lapping was done with 12 micron, 9 micron, and 3 micron diamond paste. Each sample was lapped in a figure-eight motion on an index card with each different diamond paste and a hyprez lubricate. The samples were then placed in the vibromets for the final polishing step. Each sample was first placed in the 1 micron vibromet overnight. In the morning they were cleaned and placed in the .5 micron vibromet overnight. The next morning, they were cleaned and placed in the .06 micron vibromet for three hours. The samples were removed from the vibromet and cleaned. They were examined under an optical microscope at 500x, and digital pictures were taken. Each sample was etched with I M Etch (45mL H_3PO_4, 45mL H_2O, 30mL HF, 15mL HNO_3). The samples were placed in a

100mL beaker with 50mL of I M Etch for 30 seconds. After the samples were etched, their grain structures were examined under the optical microscope. Digital pictures were taken of them at 50x, 200x, and 500x. All of the samples, including the nonmounted ones, were placed in a beaker filled with isopropanol alcohol. The beaker was placed in an ultrasonic cleaner to prepare the samples for the SEM. They were removed from the ultrasonic cleaner and placed in a vacuum oven over overnight. All of the samples were examined in the SEM in secondary electron imaging (SEI) and backscatter electron imaging (BEI). Digital pictures were taken of the samples at 200x, 500x, 1,000x, and 3,000x. The samples were also examined with an electron dispersion spectrum (EDS), for a spectrum analysis. This analysis is used to get an idea of the chemical make-up of the surface, and a little below the surface, of the scud fragment. A piece of the nonmounted scud fragment was sent to another laboratory for chemical analysis.

Results

Before the samples were cut from the scud fragment, the first test that was done was for magnetism. A magnet adhered to the fragment, representing the fragment's magnatism. This magnatism indicated that ferrite was present. A weld was found in sample 1. The weld was made-up of long-thin grains, which contained two phases: white plates and gray blocks. The white plates are austenite and the gray blocks are ferrite. The microstructure of the base metal contained small block grains, which represents a duplex stainless steel. Samples 2 and 3 had the same grain structures as the base metal of sample 1.

Since the samples were hard to etch, this would indicate a presence of austenite. From the EDS, three other elements were found to be contained in the metal: chromium, nickel, and molybdenum. The chemical analysis reported that iron was the base metal, 21.8% of the metal contained chromium, 5.8% of the metal contained nickel, and 3.1% of the metal contained molybdenum.

There were small traces of other elements found, but they were less than 0.5% of each element contained in the metal

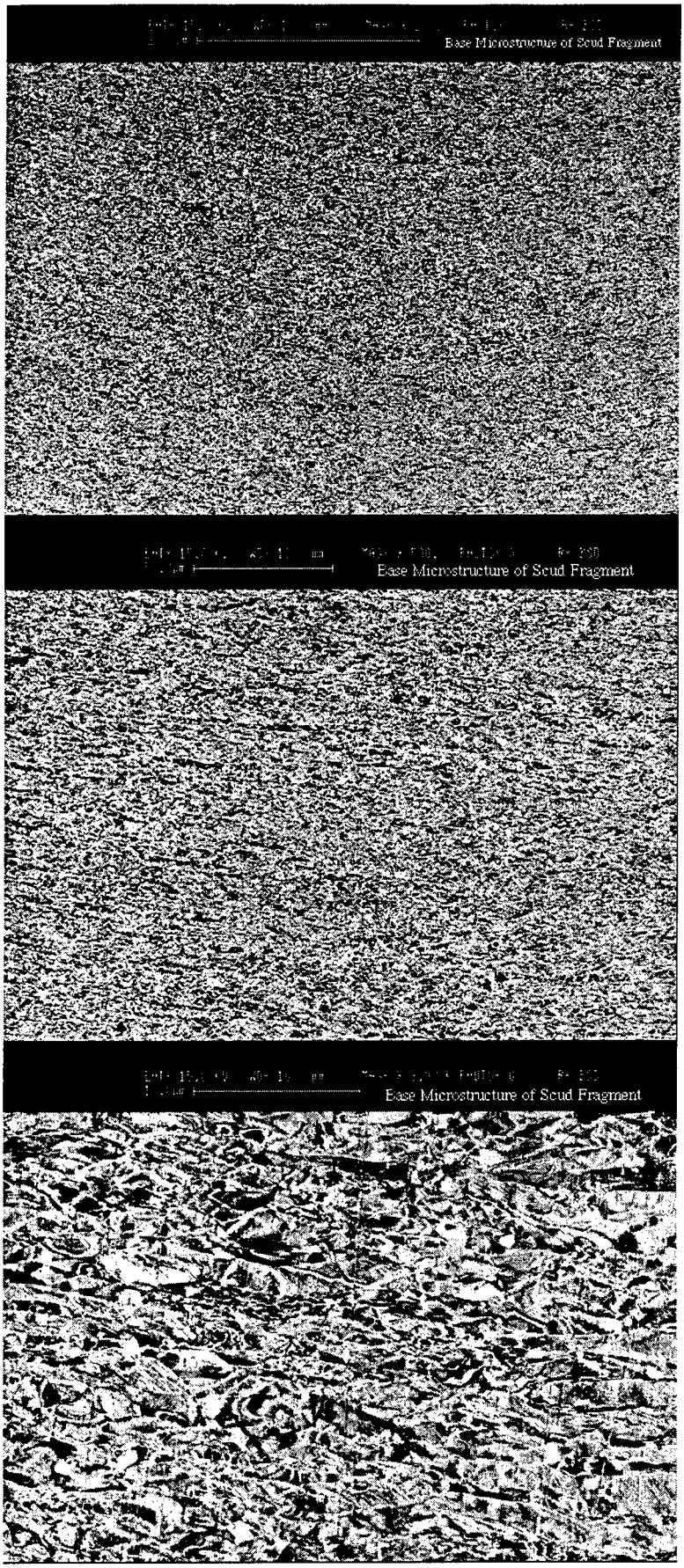
Base Microstructure of Scud Fragment
Base Microstructure of Scud Fragment
Base Microstructure of Scud Fragment

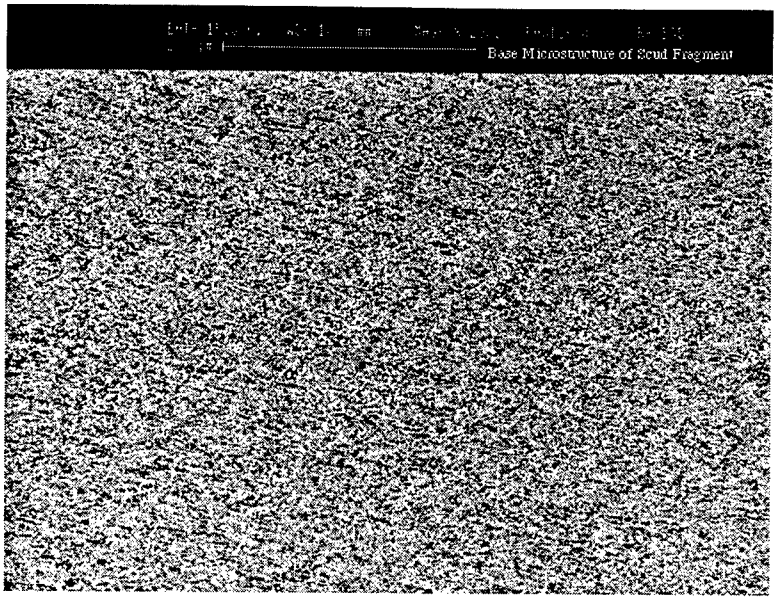
Base Microstructure of Scud Fragment

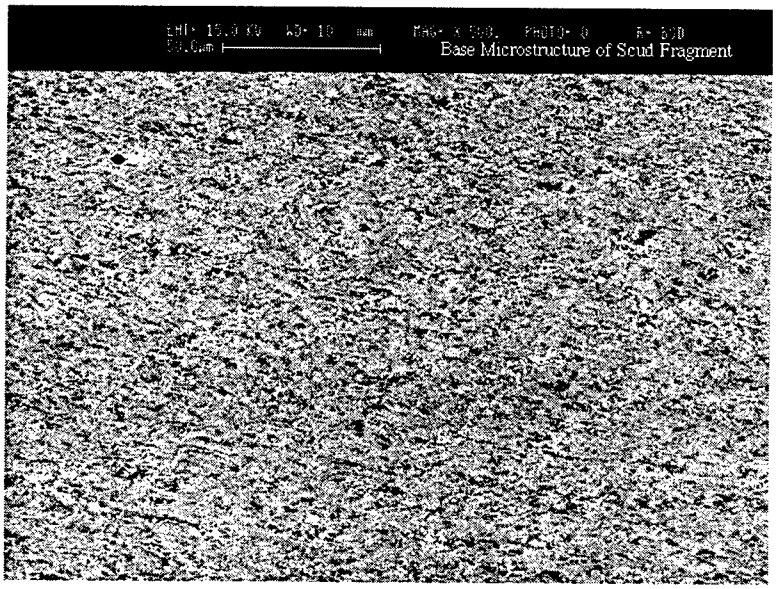
Base Microstructure of Scud Fragment


Base Microstructure of Scud Fragment

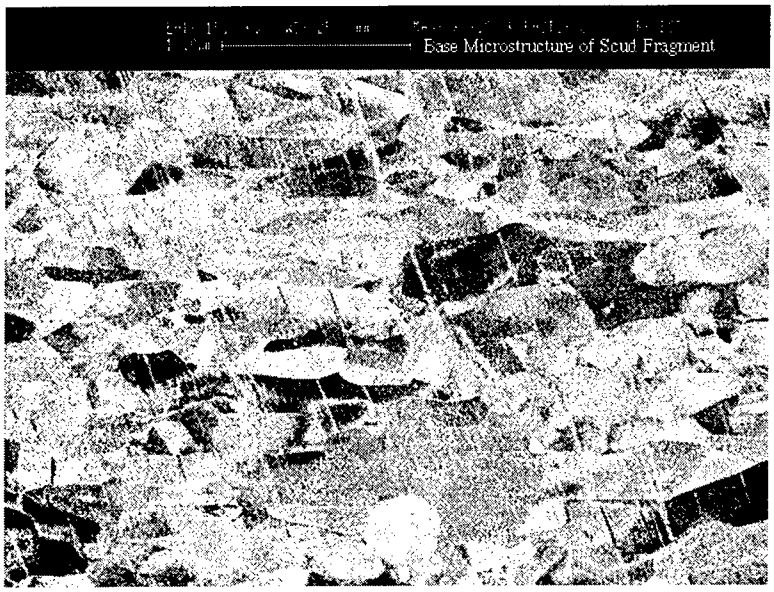
Base Microstructure of Scud Fragment


Heat Effected Microstructure of Scud Fragment

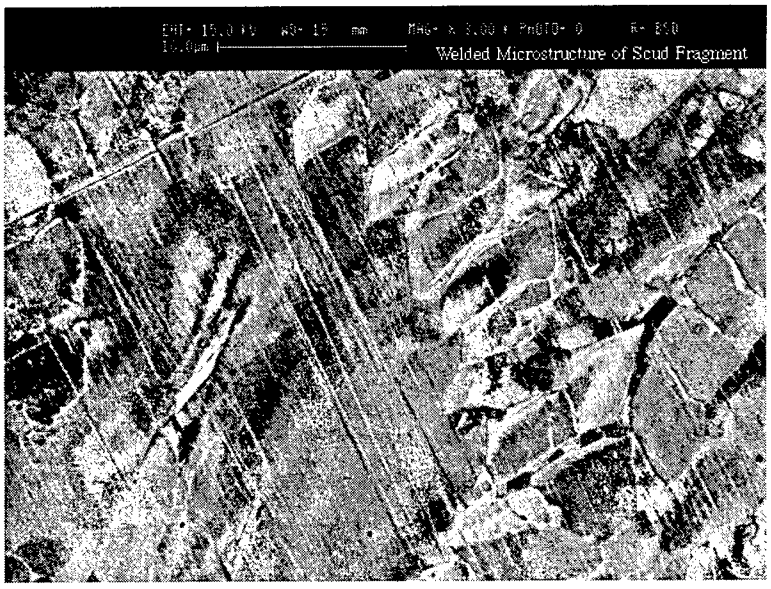
Welded Microstructure of Scud Fragment

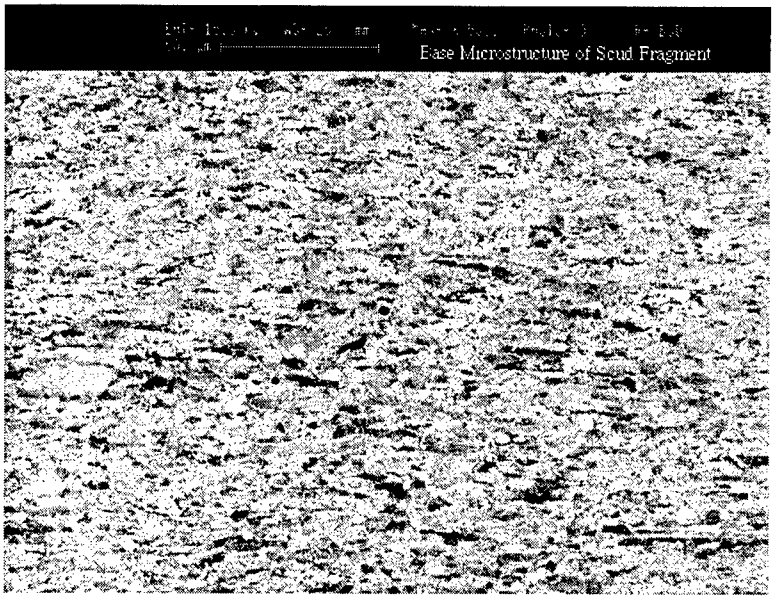
Base Microstructure of Scud Fragment

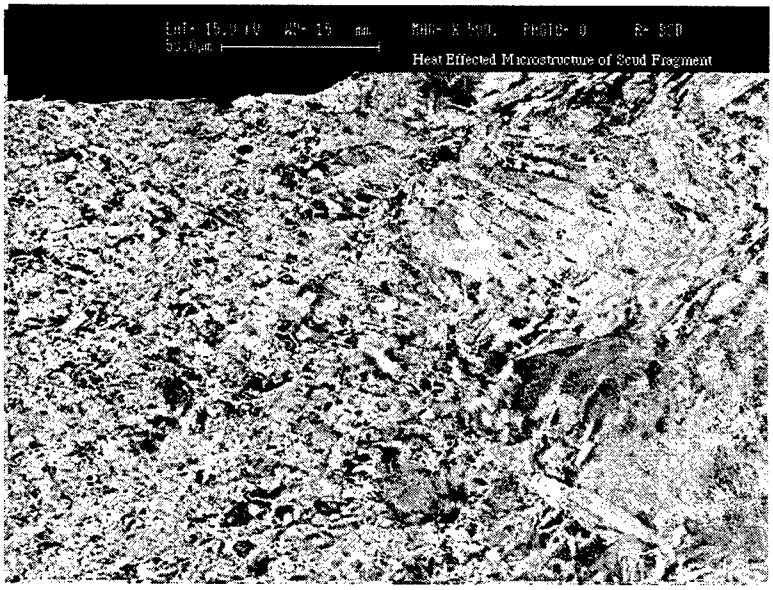
Heat Effected Microstructure of Scud Fragment

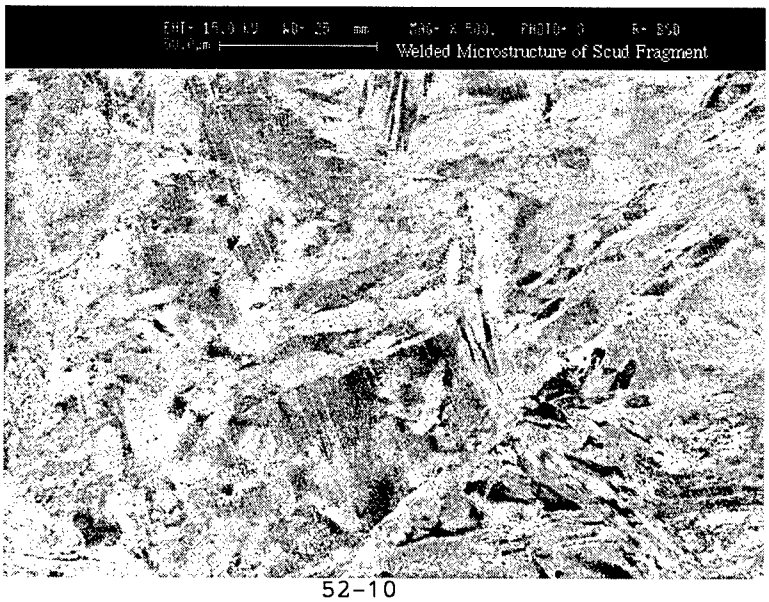
Welded Microstructure of Scud Fragment

Conclusion

In conclusion, the scud fragment is a piece of duplex stainless steel that has been welded.

References

1) An Introduction to Stainless Steels, by J. Gordon Parr and Albert Hanson, published by The American Society for Metals, 1965.

2) Desert Victory- The War for Kuwait, by Norman Friedman, published by the Naval Institute Press, 1991. The Gulf War, Frontline, www.wgbh.org, 1997.

3) Handbook of Stainless Steels, by Donald Peckner and I. M. Bernstein, published by McGraw-Hill Inc., 1977.

4) Steels: Heat Treatment and Processing Principles, by G. Krauss, published by ASM International, 1990.

CONCEPT VS. REALITY: DEVELOPING A THEORETICAL SEQUENCING PROGRAM FOR SHOCK INDUCED COMBUSTION

Elizabeth A. Walker

Niceville Senior High School
800 E John Sims Parkway
Niceville, FL 32578

Final Report for:
High School Apprentice Program
Wright Laboratory

Sponsored by:
Air Force Office of Scientific Research
Eglin Air Force Base, FL

and

Wright Laboratory

August 1997

CONCEPT VS. REALITY: DEVELOPING A THEORETICAL SEQUENCING PROGRAM FOR SHOCK INDUCED COMBUSTION

Elizabeth A. Walker
Niceville Senior High School

Abstract

Studying high-enthalpy flow conditions has significant applications in high-speed flight and missile aerodynamics. Understanding this flow is important for interpreting experimental data and designing more effective advanced vehicles and testing techniques. A mathematical sequencing program was developed for determining the variable thermodynamic coefficients for shock induced combustion given initial conditions. The program can quickly produce data by simply changing these few conditions, and a x-t diagram (including the shock front, contact surface, rarefaction head and tail, and the expansion curve), pressure curve and temperature distribution for two pressure probes, and a contour plot of p2 are all graphed.

CONCEPT VS. REALITY:
DEVELOPING A THEORETICAL SEQUENCING PROGRAM FOR SHOCK INDUCED COMBUSTION

Elizabeth A. Walker

Introduction

The development of aircraft and missiles that are able to exceed the speed of sound has sparked research in the fluid properties of gases at supersonic velocities. As shock waves pass, the temperature of the fluids in the surrounding regions increase, and at supersonic velocities, this increase can be thousands of Kelvin. Since rockets and ballistic missiles can travel at such high velocities to produce these immense temperature changes, analyzing the dynamics of gases at high-enthalpy flow is very important. Understanding this flow is vital for interpreting experimental data and designing more effective advanced vehicles and testing techniques.

Shock waves greatly impact the flight of an aircraft. The air on the streamline of the airfoil does not undergo a smooth change in velocity but rather it experiences a violent disturbance that produces a shock wave in front of the aircraft and is associated with the production of a sonic boom. If the velocity over the upper surface is greater than the total forward velocity, the flow can become supersonic when the aircraft is still subsonic. The supersonic airflow must inevitably decrease to normal subsonic flow as it leaves the airfoil, and thus a shock wave is produced (Fig. 1) [Bradley, 4]. Today the wing shape of supersonic aircraft is designed to make use of the shocks by providing the lift force once stationary shock waves become established (Fig. 2) [Bradley, 5]. A bullet is another high-speed projectile which is subjected to the build-up of shock waves (Fig. 3),

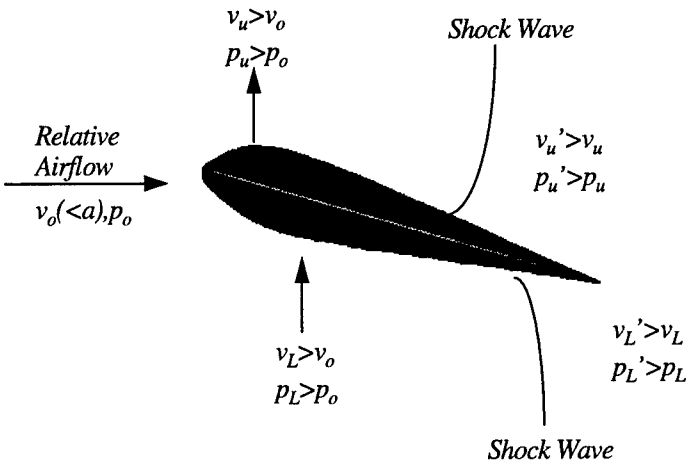

Figure 1. Pressure distribution over airfoil in supersonic flight.

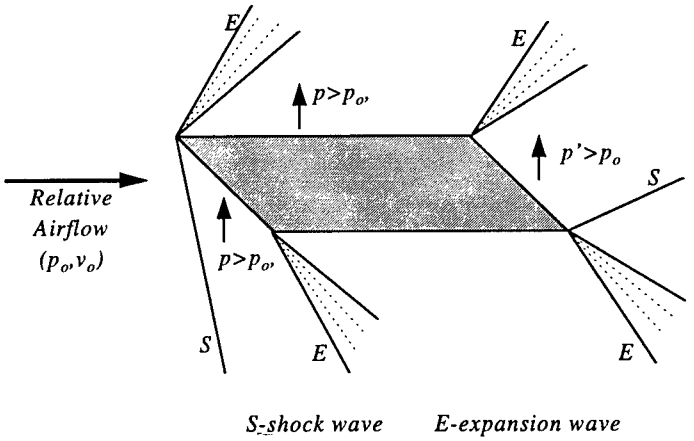

Figure 2. 'Double-wedge' airfoil used to produce lift at supersonic.

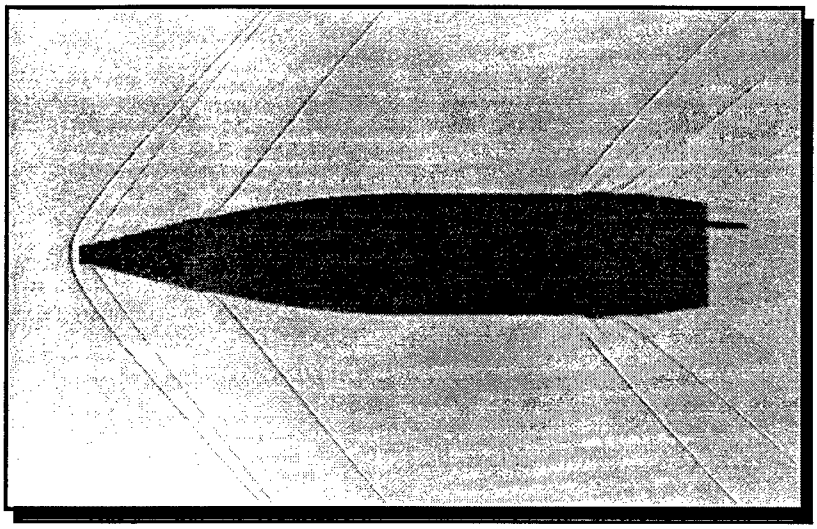

Figure 3. Shock waves produced by a bullet at supersonic velocities.

and some of their destructive power can be attributed to the traveling shock waves. A bullet is assumed to be a source of regular infinitesimal pressure disturbances, and the strength of the shock can be defined by the Mach number. Shock waves also affect missile aerodynamics and have applications in chemistry and astrophysics.

To examine the shock waves, a supersonic wind tunnel or shock tube can be used. However, the construction of a supersonic wind tunnel is extremely expensive and is restricted to a range of flow velocities which, in general, cannot produce temperatures sufficiently high enough for kinetic studies. Hence, the shock tube was developed for such studies. A shock tube is a tube closed at both ends with a thin diaphragm separating a region of high pressure gas from a region of low pressure gas (Fig. 4). The gases in two regions can be at different temperatures and have different molecular weights. When the diaphragm is ruptured, a shock wave will travel into the low pressure chamber. A rarefaction wave that is continuous in the fluid properties travels with sonic velocity in the opposite direction.

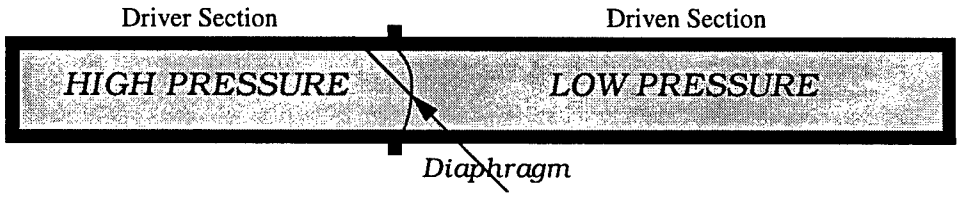

Figure 4. Pressure-driven shock tube.

The flow field in the tube after the diaphragm is burst is completely determined by the given conditions in the two regions before the diaphragm is burst. The purpose of the research is to develop a mathematical sequencing program to determine the variable thermodynamic coefficients for a shock tube given these initial conditions that is easy to use, fast, and convenient. Only the knowledge of the thermodynamic properties of the gases on either side of the diaphragm will characterize completely the properties of the resulting shock in which an x-t diagram, pressure curves, temperature distribution, experimental versus theoretical data, and a contour plot can be graphed.

Methodology

x-t Diagram

For convenience, all variable input data was put on the first half page (Fig. 5). From this, the program builds, continually calculating new equations and generating new data from the previous answers.

High Pressure Gas- Nitrogen		Low Pressure Gas - Nitrogen
$\gamma 4 := 1.404$		$\gamma 1 := 1.404$
$R4 := 297 \cdot \left(\frac{newton \cdot m}{kg \cdot K}\right)$		$R1 := 297 \cdot \left(\frac{newton \cdot m}{kg \cdot K}\right)$
$p4 := 795 \cdot psi$		$p1 := 4 \cdot psi$
$T4 := 293 \cdot K$		$T1 := 293 \cdot K$
$x4 := -0.4572 \cdot m$		$x1 := 1.158875 \cdot m$
		$d := -0.4572 \cdot m$
First Segment Length	$b := 0.33655 \cdot m$	$k := 1.7500 \cdot m$
Second Segment Length	$c := 0.727075 \cdot m$	$x := d, d + 0.01 \cdot m .. k$
# of Iterations for Curve		$n := 2000$
Time Interval from Experimental Data		$ti := 0.5 \cdot sec$
Time Conversion Factor from Experimental Data		$tcf := 1210 \cdot sec$

Figure 5. Initial input screen from Mathcad program.

The properties of the high pressure gas (driver section) are given on the left, and the low (driven) on the right. γ and R are intrinsic to the particular gas. T and p are the initial temperature and pressure values of the driver and driven sections of the shock tube. The ends of the shock tube are denoted by *x4* and *x1*. The first segment length or pressure probe one is *b*, and the second segment length or pressure probe two is *c*. The variables *d* and *k* are used only to define the domain of x for calculations and graphs. The number of iterations can also be changed as well as the time conversion factor from the experimental data. Initial pressure and temperature in the undisturbed low-pressure experimental gas are denoted with 1's ($\gamma 1$, *R1*, *p1*, *T1*, and *x1*). The region between the shock front and the contact surface is 2. The contact surface and the rarefaction fan is 3, and the initial conditions on the high-pressure side are 4's.

The physical properties of shock waves are governed by five fundamental equations - three conservation equations and two equations of state. All equations are based on three basic laws of physics - conservation of mass ($\rho_1 u_1 = \rho_2 u_2$), conservation of momentum ($p_1 + \rho_1 u_1^2 = p_2 + \rho_2 u_2^2$), and conservation of energy ($h_1 + u_1^2/2 = h_2 + u_2^2/2$). For gases under normal conditions of temperature and pressure, the behavior of the shock depends primarily on the variation of the enthalpy with temperature and pressure.

The speed of sound is first calculated by the equation $a := \sqrt{(\gamma * R * T)}$. The ratio p_4 / p_1 is the diaphragm pressure ratio. Along with the initial conditions of the driver and driven gas, this ratio determines

uniquely the strengths of the incident shock and expansion waves that are set up after the diaphragm is removed. Because the incident shock strength, p_2/p_1 is an implicit function of the diaphragm pressure ratio, the root function was used to determine p2. The temperature across the shock wave is defined as a function of the pressure ratio as follows:

$$T2 := \frac{p2}{p1}\cdot\left[\frac{\frac{\gamma 1+1}{\gamma 1-1}+\frac{p2}{p1}}{1+\left(\frac{\gamma 1+1}{\gamma 1-1}\cdot\frac{p2}{p1}\right)}\right]\cdot T1$$

In a stationary shock wave the Mach number, M_1, is the governing principle for changes across the wave, but for a moving shock wave p_2/p_1 is the major parameter regulating the changes. The wave velocity of the moving shock wave to the pressure ratio across the wave and the speed of sound of the gas into which the wave is propagating is given by:

$$W := a1\cdot\sqrt{\frac{\gamma 1+1}{2\cdot\gamma 1}\cdot\left(\frac{p2}{p1}-1\right)+1}$$

A shock wave propagating into a stagnant gas induces a mass motion with velocity u_p behind the wave. The mass-motion velocity, u_p, also depends on the pressure ratio across the wave and the speed of sound of the gas ahead of the wave.

$$up := \frac{a1}{\gamma 1}\cdot\left(\frac{p2}{p1}-1\right)\cdot\left[\frac{\frac{2\cdot\gamma 1}{\gamma 1+1}}{\left(\frac{p2}{p1}+\frac{\gamma 1-1}{\gamma 1+1}\right)}\right]^{0.5}$$

T2, W, and u_p can all be calculated for a given pressure ratio and speed of sound.

In order to create the x-t diagram, various functions had to be defined. Function 1 (f(t1)) is the shock front and is calculated from *t1:=x1/W*. Function 2, calculated by *t2:=x2/up* where *x2:=x1*, is the contact surface. Function 4 is the rarefaction head and is determined by *t4:=-x4/a4*. The third function is the rarefaction tail and took more calculations. The time is dependent upon the distance in function 4 and *M3*, defined as follows:

$$M3 := \frac{2}{\gamma 4-1}\cdot\left[\left(\frac{p2}{p1}\cdot\frac{p1}{p4}\right)^{-\left(\frac{\gamma 4-1}{2\cdot\gamma 4}\right)}-1\right]$$

The variables, *x3* and *t3*, can then be defined:

$$x3 := -x4(M3-1)\cdot\left[1+\left(\frac{\gamma4-1}{2}\right)\cdot M3\right]^{\frac{3-\gamma4}{2\cdot(\gamma4-1)}},$$

$$t3 := \frac{-x4}{a4}\cdot\left(1+\frac{\gamma4-1}{2}\cdot M3\right)^{\frac{\gamma4+1}{2\cdot(\gamma4-1)}}.$$

The equation for the rarefaction tail is then defined as a function of *t3*. The x-t diagram is now only missing the reflected rarefaction head (curve).

The curve was plotted by using the method of characteristics in which the characteristic lines and the compatibility conditions are pieced together point by point (Fig. 6) [Anderson, 234]. The slope for each line was calculated (*m1, m2, m3*, and *m4*), and *z*, the velocity interval, was defined by taking the sum of the inverses of *m4* and *m3* and dividing by the number of iterations for the curve. The first line is a simple reflection of the rarefaction head off the end wall, and its coordinates were calculated. The mass motion moves toward the right, opposite to the direction of propagation of the wave, and *u* varies linearly with *x* through a centered expansion wave. The other lines were defined using a recursion matrix (Fig. 7), and a point had to be first established for the recursion to build upon. The matrix consisted of six dependent values, *u, a, mline, mcon, x,* and *t*, where *mline* is the slope of the line from the origin to the calculated x,t coordinate and *mcon* is the slope of the line from the preceding point to x,t.

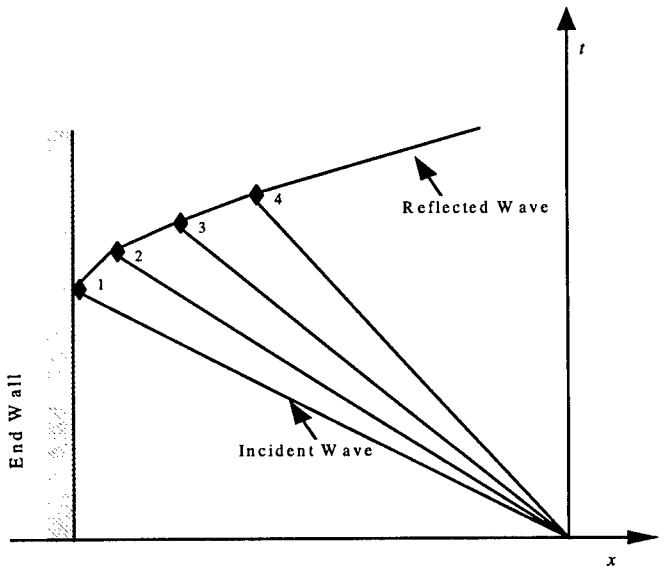

Figure 6. Reflected expansion wave on an x-t diagram.

$$\begin{bmatrix} u_{(i+1)} \\ a_{(i+1)} \\ \text{mline}_{(i+1)} \\ \text{mcon}_{(i+1)} \\ x_{(i+1)} \\ t_{(i+1)} \end{bmatrix} := \begin{bmatrix} u_2 \cdot i \\ \left(1 - \frac{\gamma 4 - 1}{2} \cdot \frac{u_2 \cdot i}{a4}\right) \cdot a4 \\ \frac{1}{\left[\frac{1}{m4} + (i+1) \cdot z\right]} \\ \left[\frac{1}{u_2 \cdot i + \left(1 - \frac{\gamma 4 - 1}{2} \cdot \frac{u_2 \cdot i}{a4}\right) \cdot a4}\right] \\ \frac{t_i - \frac{x_i}{u_2 \cdot i + \left(1 - \frac{\gamma 4 - 1}{2} \cdot \frac{u_2 \cdot i}{a4}\right) \cdot a4}}{\frac{1}{\left[\frac{1}{m4} + (i+1) \cdot z\right]} - \frac{1}{u_2 \cdot i + \left(1 - \frac{\gamma 4 - 1}{2} \cdot \frac{u_2 \cdot i}{a4}\right) \cdot a4}} \\ \frac{t_i - \frac{x_i}{u_2 \cdot i + \left(1 - \frac{\gamma 4 - 1}{2} \cdot \frac{u_2 \cdot i}{a4}\right) \cdot a4}}{\frac{1}{\left[\frac{1}{m4} + (i+1) \cdot z\right]} - \frac{1}{u_2 \cdot i + \left(1 - \frac{\gamma 4 - 1}{2} \cdot \frac{u_2 \cdot i}{a4}\right) \cdot a4}} \\ \left[\frac{1}{\frac{1}{\left[\frac{1}{m4} + (i+1) \cdot z\right]}}\right] \end{bmatrix}$$

Figure 7. Recursion matrix for expansion curve.

Appropriate equations in vector format were then defined, and the x-t diagram was plotted.

Pressure Curves

The wave pattern resulting from the diaphragm burst and the subsequent pressure distribution in the tube is shown in pressure curves. The pressure at probes one and two was calculated and graphed. The sequence began by determining the times at pressure probe one (b) -- *time3b:=b*m3*. The pressure at this point depends upon the velocity:

$$u3b := \frac{2}{\gamma 4 + 1} \cdot \left(a4 + \frac{b}{time3b}\right) \qquad pres3b := \left[1 - \frac{\gamma 4 - 1}{2} \cdot \left(\frac{u3b}{a4}\right)\right]^{\frac{2 \cdot \gamma 4}{\gamma 4 - 1}} \cdot p4$$

In order to calculate the time difference (*ttb*), it was necessary to determine which iteration of *x* was the closest approximation to *b*. By using a loop program, Mathcad was able to calculate the iteration number. The range was defined by *qb:=0,1..n2b*, where *n2b* is the number of iterations to be calculated at *b*. The time and pressure were then computed.

Program Loop

$f(x, thres) := \left| \begin{array}{l} j \leftarrow 0 \\ \text{while } x_j \leq thres \\ \quad j \leftarrow j + 1 \end{array} \right.$

Boolean Expression --

Where x = b -- $rb := f(x, b)$

Iteration Number-- $rb = 1211$

$$tb_{qb} := time3b + \frac{ttb}{n2b} \cdot qb$$

$$presb_{qb} := \left[1 - \frac{\gamma4 - 1}{2} \cdot \left[\frac{2}{\gamma4 + 1} \cdot \left(a4 + \frac{b}{tb_{qb}} \right) \right] \right]^{\frac{2 \cdot \gamma4}{\gamma4 - 1}} \cdot p4$$

Appropriate vectors were defined, and the sequences were repeated for pressure probe two. The pressure curves at both pressure curves were plotted, with the x and y axes having the same calculated values for comparing.

Temperature Distribution

The distribution of temperature that occurs in the shock tube after the diaphragm bursts can also be graphed, and this was done for pressure probes one and two. The temperature distribution was formulated similar to the pressure curves, and the temperature depended upon the previously defined pressure vector:

$$Temp3b_{qb} := T4 \cdot \left(\frac{presb_{qb}}{p4} \right)^{\frac{\gamma4 - 1}{\gamma4}}$$

Contour Plot

Another part of the Mathcad program was written in order to plot p2 on a contour plot. The range was defined by i, and p4 was written in vector format. The value given for *p2* was a guess for the root function and may be changed when appropriate. The values for *p1* were then defined explicitly. Mathcad could not run the program with the program loop for finding the root with two variables. However, the range and values may also be changed. The root function is repeated in the program eight times (the number of *p1* values). Since contour plots are drawn from matrices, the functions were defined as vectors

($V1_i:=Ua(p4)$), and the rows of the matrix were set. The contour plot was then drawn in units of atmospheres.

Results

The shock induced combustion device is shown in Figure 8. The dimensions of the shock tube were taken, and the measurements were put into the program. The diaphragm is burst by increasing the pressure, and the changes that occur in the shock tube are measured via piezoelectric transducers. The experimental data consists of four traces, from the two transducers and two within the shock tube.

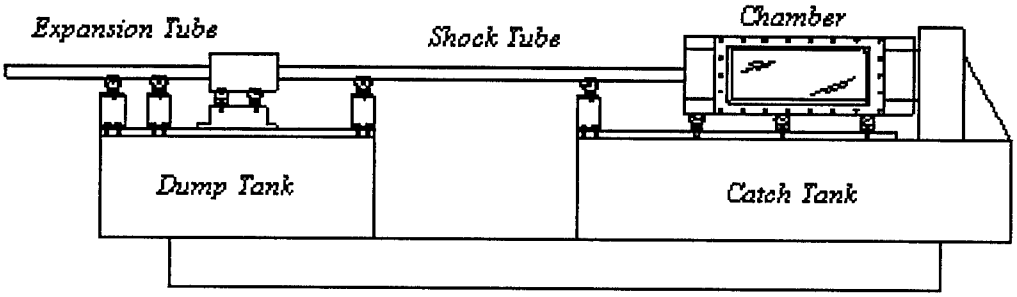

Figure 8. Shock Induced Combustion Device.

x-t Diagram

A compression wave forms in the low-pressure gas after the bursting of the diaphragm and rapidly augments to form a shock front. At the same instant, an expansion or rarefaction wave moves back into the high-pressure gas. The front of the rarefaction wave travels back with the speed of sound in the driver gas, but the pressure fall is smooth unlike the shock front. The experimental (driven) gas and the driver gas are separated at the contact surface, which advances swiftly along the tube behind the shock front. The movements of the shock front, the contact surface, and the rarefaction wave are shown in a x-t diagram, and the whole properties of both the expansion and the shock wave are specified in the x-t diagram.

The straight lines diagramming the shock front, contact surface, rarefaction tail, and the rarefaction head of the x-t diagram were fairly simple to formulate, but the reflected rarefaction head (curve) presented much more difficulties. The degree of error was also calculated, x_n-x_3 (which should be equivalent to 0), and at $n:=2000$ (the number of iterations for the curve), the error was only 0.0007292346 m for a sample case, which is negligible. Hence, the sequencing method is effective. The x-t diagrams for two cases are shown in Figures 9 and 10. The first case involves nitrogen as the low and high pressure gas, $p1 = 4$ *psi* and $p4 = 795$ *psi*. The second case consists of nitrogen as the low pressure gas ($p1 = 4$ *psi*) and helium as the high pressure gas ($p4 = 3000$ *psi*). The theoretical pressure curves from the Mathcad program for the nitrogen / nitrogen case are shown in Figures 11 and 12.

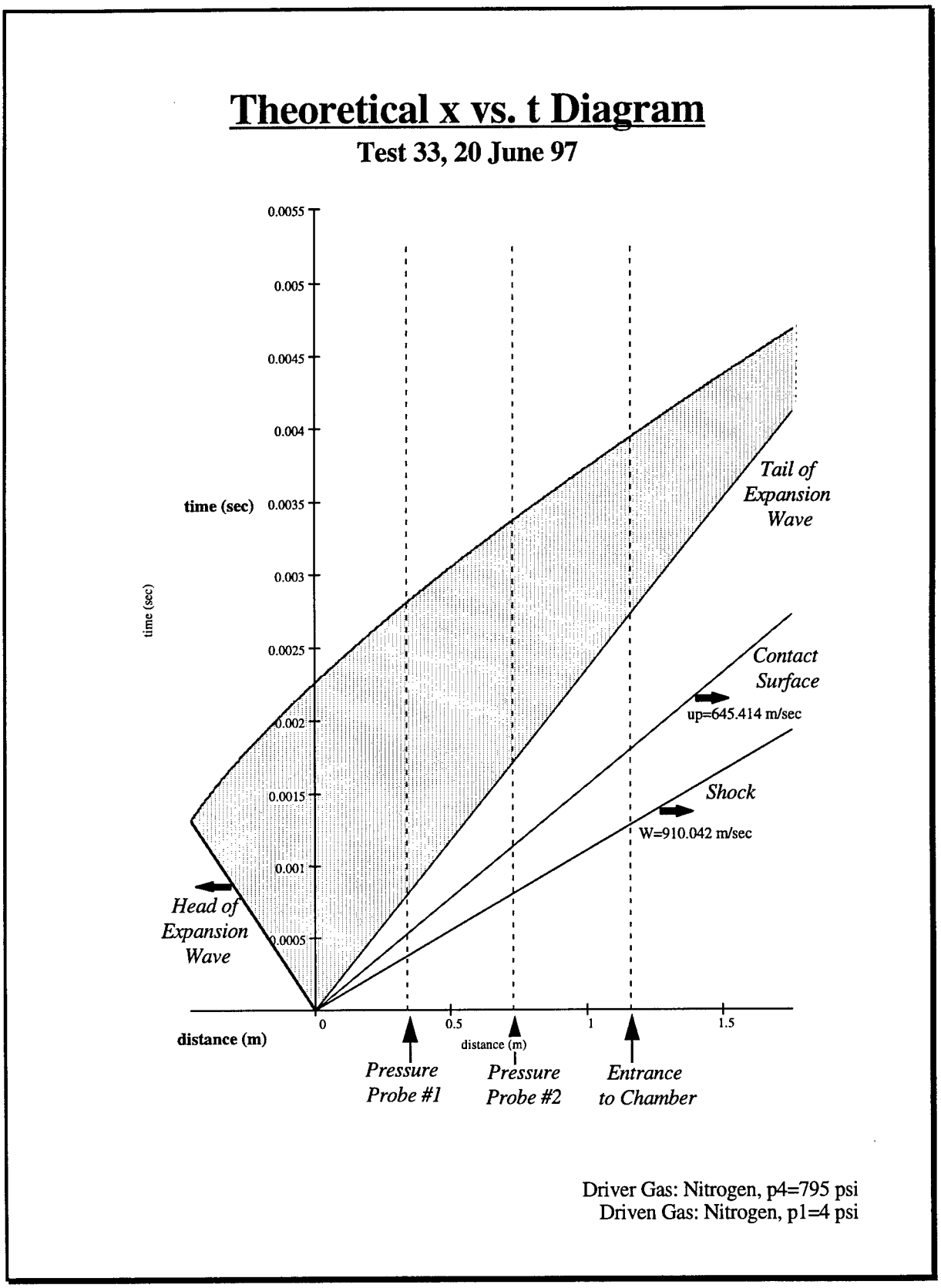

Figure 9. x-t Diagram for nitrogen / nitrogen case.

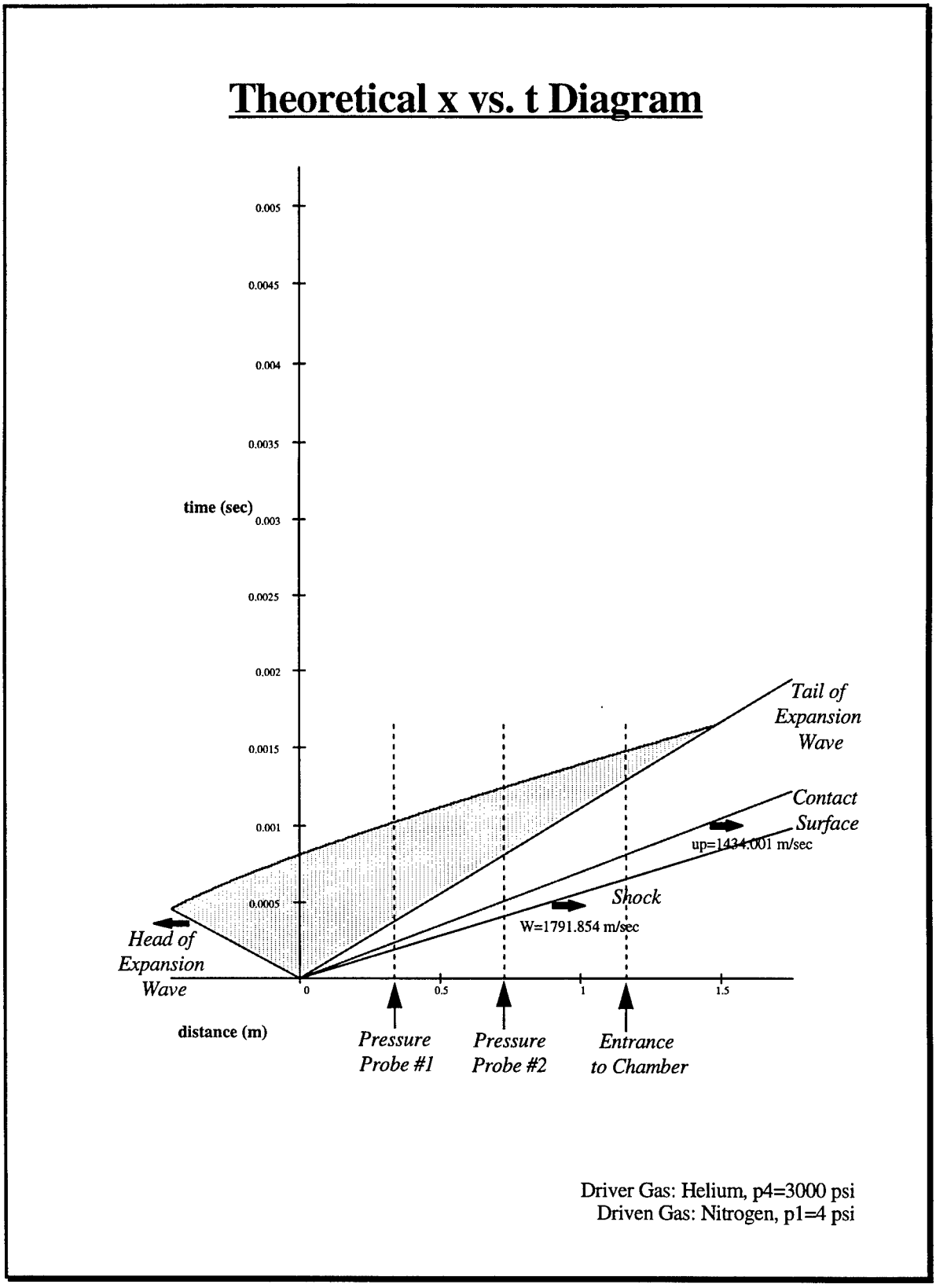

Figure 10. x-t Diagram for nitrogen / helium case.

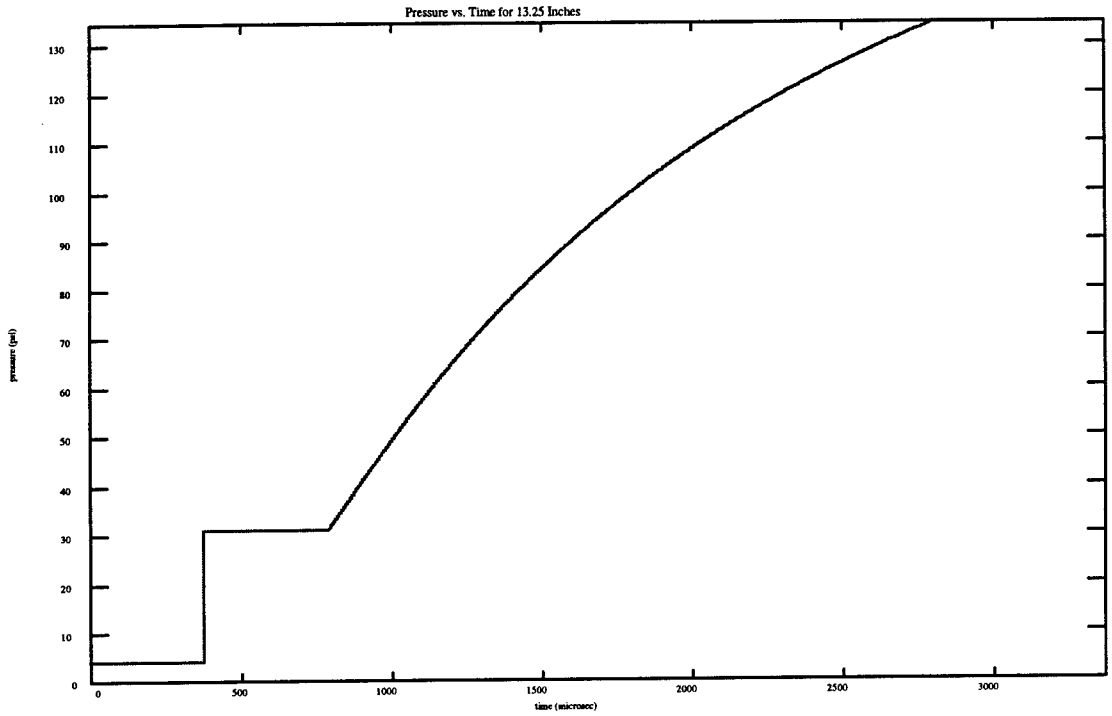

Figure 11. Pressure Curve at pressure probe one for nitrogen / nitrogen case.

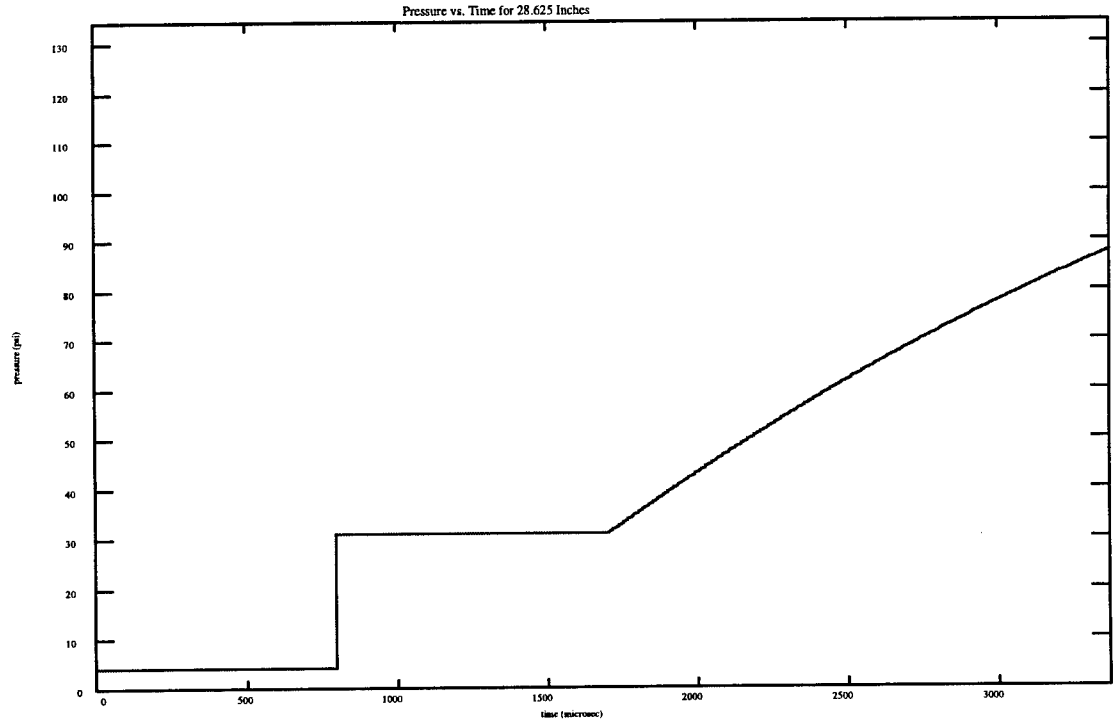

Figure 12. Pressure Curve at pressure probe two for nitrogen / nitrogen case.

Temperature Distribution

In the theoretical results, the temperature shows an abrupt rise from the initial temperature (T1) to a very high value at the shock front (T2), remains steady up to the contact surface, and then falls quickly to below the initial temperature. Then in the rarefaction fan, it rises slowly again to the initial temperature. Time2b (the time at the contact surface) is used instead of time3b (the time at the rarefaction head) as used in the pressure curves because as gas expands from the expansion fan the temperature instantaneously decreases, causing the drop in temperature after the contact surface instead of being continuous. The temperature distribution for pressure probes one and two is shown Figures 13 and 14.

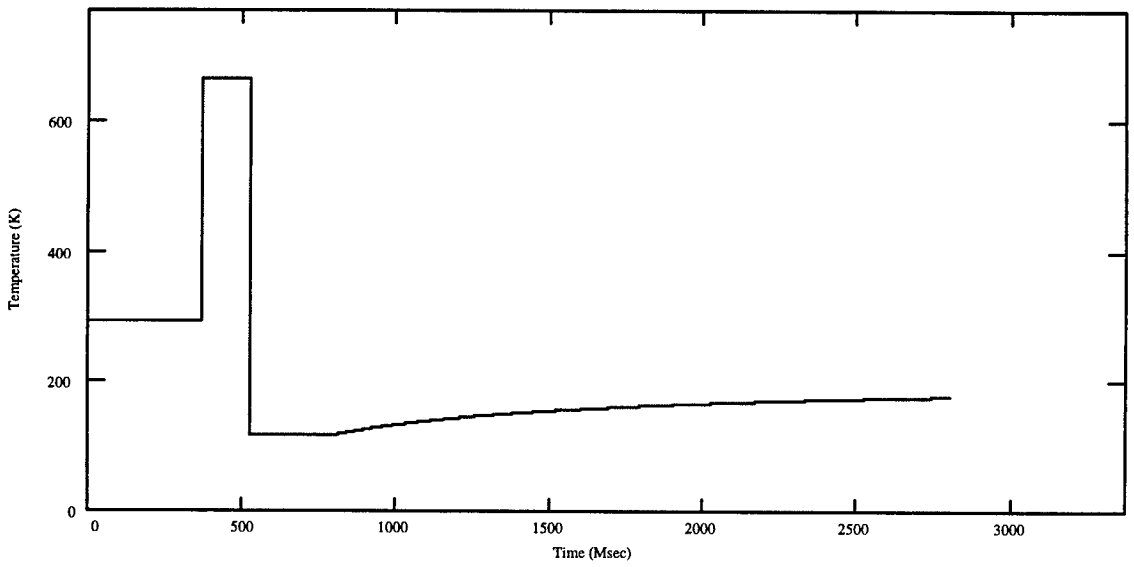

Figure 13. Temperature distribution at pressure probe one for nitrogen / nitrogen case.

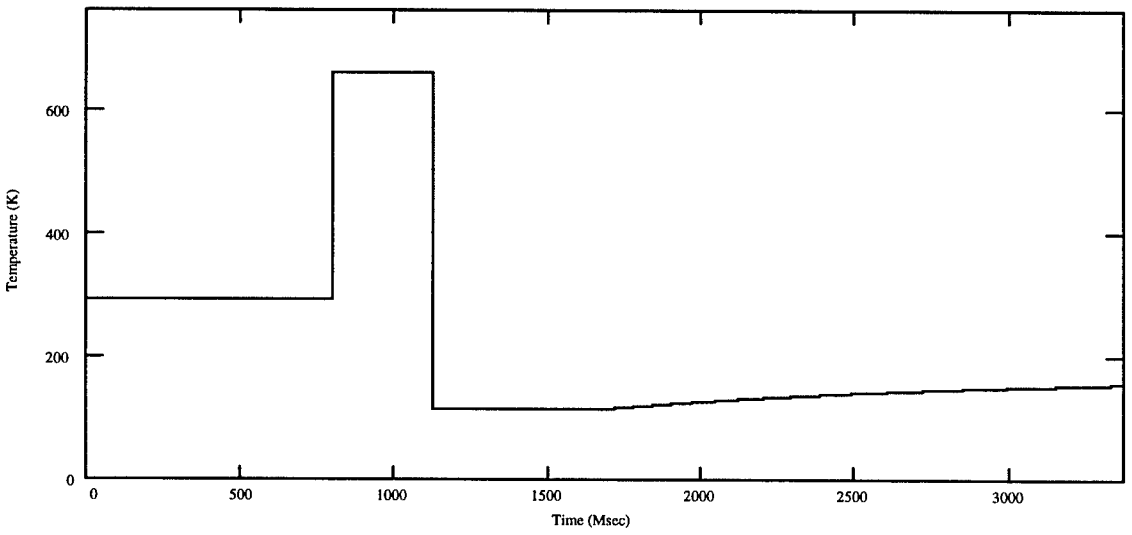

Figure 14. Temperature distribution at pressure probe two for nitrogen / nitrogen case.

Pressure Curves / Theoretical vs. Experimental Data

The experimental data has a set time interval, whereas the time interval of the theoretical data depends on the number of iterations for each pressure curve. In order to compare the theoretical data to the experimental data, additional steps had be taken. The following summarizes the procedure for comparing theoretical to experimental data:

(1) Enter data on page one of Mathcad program, and check graphs on pages 12, 19, 20, 25, and 30 to ensure program ran successfully.
(2) Import trace data off disk into Excel.
(3) Calculate time values (interval*trig point) to use as x-scale and enter value for time interval (*ti*) in Mathcad program.
(4) Adjust experimental graphs to initial pressure (*p1*).
(5) Graph experimental data. Find time conversion factor (*tcf*).
(6) Import pressure curve data (for lengths *b* and *c*) from Mathcad, adjusting for *tcf*.
(7) Graph experimental vs. theoretical data.

For step 3, it is useful to insert in column A continuous additions of one beginning with zero, and then define time in column B as equal to the *trig point* * *time interval* + *A#* (reference to the continually adding column) * *time interval*. This defines the time for specific pressures and is the x-scale. The experimental data has to be adjusted to the initial pressure (*p1*). This is done by averaging the pressure of each trace, subtracting p1 from that number, and then subtracting this number from each number in the trace. In step 5, after graphing, locate the high jump in pressure and find the time when this rapid change occurs. This is the time conversion factor (*tcf*).

For step 7, the data should be graphed in an XY Scatter plot with no data markers (With many data points, the line is no longer discrete, and the program slows down considerably.). The experimental curve can then be compared to suitable theoretical relations. Using these eight steps, gases with varying pressure and other coefficients can be easily and readily changed to produce new data for shock induced combustion. Only the first step (changing the initial inputs) is necessary to produce new theoretical data.

To compare the theoretical to the experimental data, the same time interval must exist. The theoretical time is dependent upon the number of iterations defined at the beginning of the program (*n2b*). The number of iterations was found by setting up a minimization problem in which the difference between the first and second time iterations minus the time interval should be as close as possible to 0. The following equation was used to find the closest integer solution just prior to the difference evaluation.

$$n2b := if\left(\frac{ttb}{ti} - floor\left(\frac{ttb}{ti}\right) < ceil\left(\frac{ttb}{ti}\right) - \frac{ttb}{ti}, floor\left(\frac{ttb}{ti}\right), ceil\left(\frac{ttb}{ti}\right)\right)$$

With this set up, the time interval simply has to be defined in the theoretical program. Three other related factors are calculated in the Mathcad program -- *differenceb* and *differencec*, *chartdiff*, and *conversionb* and *conversionc*. *Differenceb* and *c* represent the time interval in the sequencing program and should be equal to the time interval of the experimental data, and checks the degree of error from the time interval (which was less than 0.0001 in both cases). The next number, *chartdiff*, represents the high pressure rise in the experimental data minus the high rise in the theoretical data. Thus, *chartdiff:=tcf-time1b*10^6*. *Conversion b* and *c* are then calculated by adding this difference to the first iteration of the time at the pressure point (in μsec). The pressure at pressure probe one is equal to *p1* until the time conversion factor (*tcf*) is reached. Then the pressure jumps to *p2* and stays at *p2* until *conversionb*, when the curve data from Mathcad is imported and placed. For pressure probe two, the pressure is equal to *p1* until *tcf2*, when it jumps to *p2*. This is constant prior to reaching *conversionc*, when the imported data is positioned.

For step 7, the data should be graphed in an XY Scatter plot with no data markers (With many data points, the line is no longer discrete, and the program slows down considerably.). The experimental curve can then be compared to suitable theoretical relations. Using these eight steps, gases with varying pressure and other coefficients can be easily and readily changed to produce new data for shock induced combustion. Only the first step (changing the initial inputs) is necessary to produce new theoretical data.

With nitrogen as the driver and driven gas (p4 = 795 psi, p1 = 4 psi), the steps were followed. The experimental versus theoretical data was graphed (Fig. 15), and the results were compared. Both showed a steep rise in pressure and then a continually increasing pressure curve.

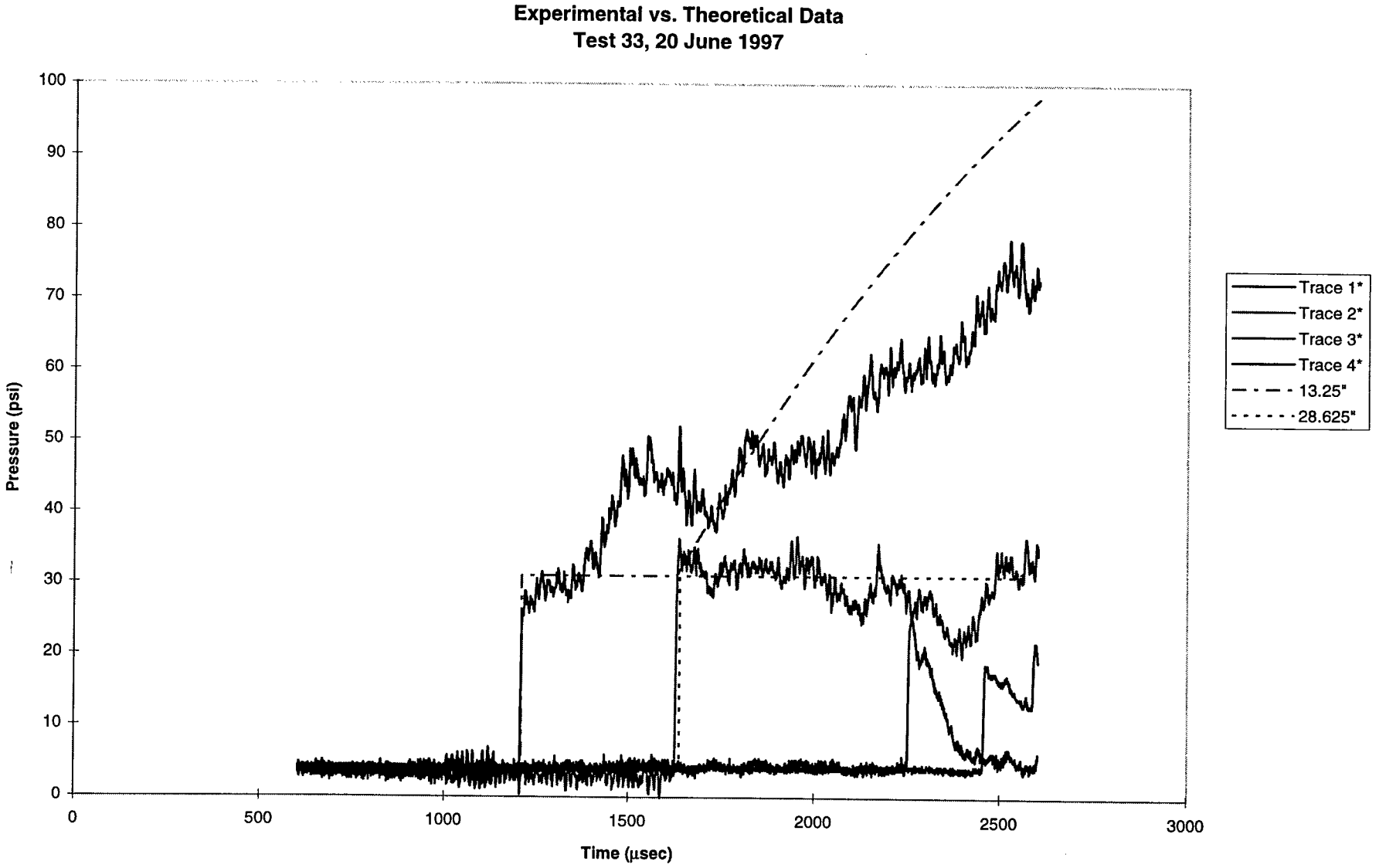

Figure 15. Experimental vs. Theoretical Data, Nitrogen / Nitrogen Case.

Driver Gas: Nitrogen, p4=795 psi,
Driven Gas: Nitrogen, p1=4 psi

Contour Plot

For a given diaphragm pressure ratio, *p4/p1*, the incident shock strength, *p2/p1*, will be made stronger as *a1/a4* is made smaller. The speed of sound in a light gas is faster than in a heavy gas. Thus, if the incident shock strength for a given *p4/p1* is to be maximized, the driver gas should be a low-molecular-weight gas at high temperature (resulting in a high *a4*), and furthermore, the driven gas should be a high-molecular-weight gas at low temperature (low *a1*). Due to this, many shock tubes use H_2 or He for the driver gas. The contour plot (Fig. 16) shows the pressure at the contact surface, *p2*. The x-axis is p4, and the y-axis is p1. From this graph, a p2 contour shows which p1 and p4 can be used to obtain a certain value of p2.

$$\frac{M}{atm} = \begin{bmatrix} 3.016 & 3.361 & 3.616 & 3.818 & 3.986 & 4.13 & 4.256 & 4.367 & 4.468 \\ 4.342 & 4.881 & 5.282 & 5.602 & 5.87 & 6.099 & 6.301 & 6.481 & 6.643 \\ 5.485 & 6.204 & 6.741 & 7.172 & 7.532 & 7.843 & 8.117 & 8.361 & 8.582 \\ 6.51 & 7.397 & 8.062 & 8.598 & 9.048 & 9.436 & 9.778 & 10.084 & 10.361 \\ 7.449 & 8.495 & 9.283 & 9.919 & 10.454 & 10.917 & 11.325 & 11.691 & 12.022 \\ 8.321 & 9.519 & 10.425 & 11.157 & 11.775 & 12.31 & 12.782 & 13.205 & 13.589 \\ 9.14 & 10.484 & 11.502 & 12.328 & 13.025 & 13.63 & 14.165 & 14.644 & 15.08 \end{bmatrix}$$

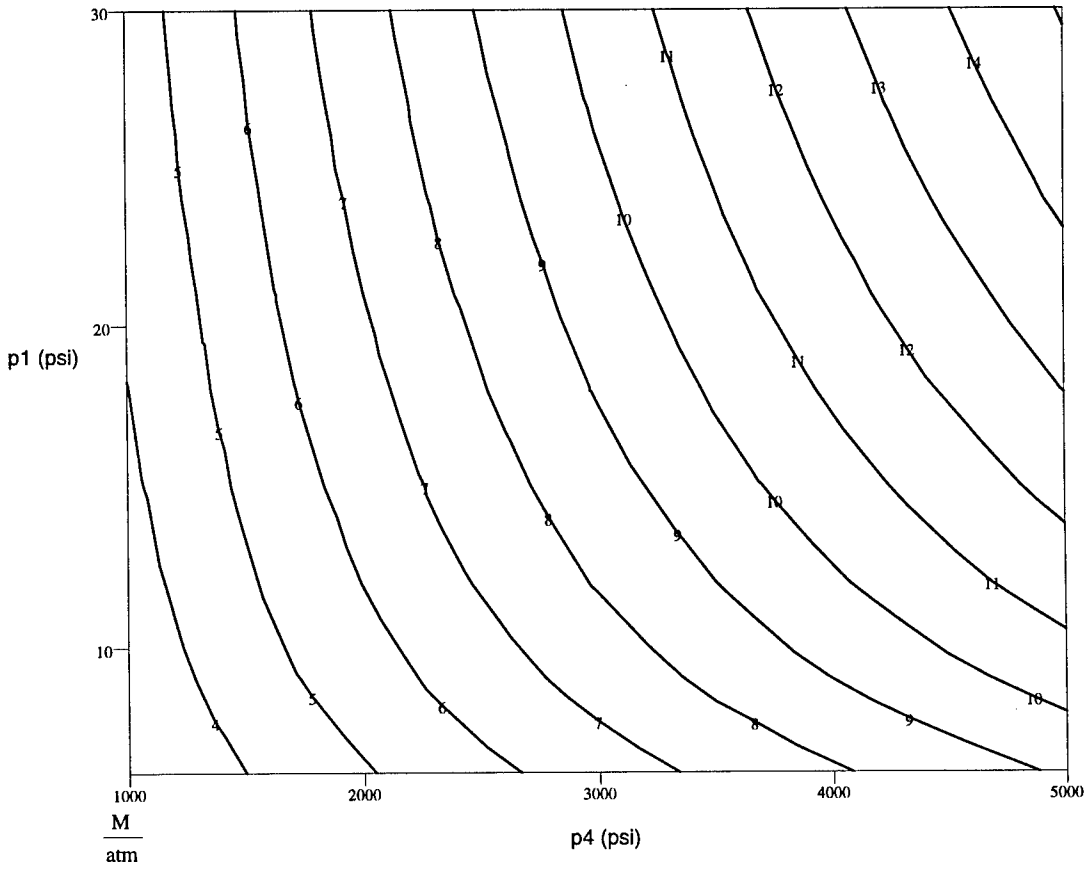

Figure 16. Contour plot of p2 and matrix values for nitrogen / nitrogen case.

Conclusion

A mathematical sequencing program was developed for determining the variable thermodynamic coefficients for shock induced combustion. The program can quickly produce data by simply changing a few initial conditions, and a x-t diagram, pressure curves and temperature distributions for two pressure probes, and a contour plot of p2 are all graphed. With more steps, the results of the theoretical program can be compared to experimental data. With a 5000-mile ballistic vehicle requiring a Mach number of 20, the air temperature behind the normal shock wave for a blunt body during the re-entry into the earth's atmosphere can be as high as 6000 K, which can no longer be considered a simple mixture of inert nitrogen and oxygen molecules. Conventional experimental tools for obtaining aerodynamic data, such as supersonic and hypersonic wind tunnels, become inadequate for investigating the real gas effects for flow around bodies at high speeds. Shock tubes are capable of stimulating the Mach number and high stagnation temperatures encountered by the long-range ballistic vehicles. The shock tube also presents a considerable saving in expense in view of the enormous energy requirements of supersonic wind tunnels. It also permits a variety of gases to be used without difficulty and enables wide and precisely defined ranges of temperature and density to be obtained. The reflection, refraction and diffraction properties can now be examined theoretically under varying conditions, reducing extensive experimental results.

References

[1] Anderson, John D. *Fundamentals of Aerodynamics*. New York: McGraw-Hill, 1984.

[2] Anderson, John D. *Modern Compressible Flow*. New York: McGraw-Hill, 1990.

[3] Bradley, John N. *Shock Waves in Chemistry and Physics*. New York: John Wiley & Sons, 1962.

[4] Gaydon, A.G. and I.R. Hurle. *The Shock Tube in High-Temperature Chemical Physics*. New York: Reinhold, 1963.

[5] Ferri, A. (Editor) *Fundamental Data Obtained from Shock-Tube Experiments*. New York: Pergamon Press, 1961.

[6] Nielsen, Jack N. *Missile Aerodynamics*. New York: McGraw-Hill, 1960.

A STUDY OF THE TENSION AND SHEAR STRENGTH OF BIDIRECTIONAL EPOXY-RESIN COMPOSITES

Darren C. Wells

Bellbrook High School
3737 Upper Bellbrook Road
Bellbrook, OH 45305

Final Report for:
High School Apprentice Program
Wright Laboratory

Sponsored by:
Air Force Office of Scientific Research
Bolling Air Force Base, Washington, DC

And

Wright Laboratory

August 1997

A STUDY OF THE TENSION AND SHEAR STRENGTH OF BIDIRECTIONAL E-GLASS EPOXY-RESIN COMPOSITES

Darren Wells
Bellbrook High School

Abstract

The tensile strength, shear strength, and water absorption of bidirectional E-glass epoxy-resin composites was studied. To undertake this study, 8"x8" squares of bi-directional E-glass fabric were used with various lay-up procedures, epoxy-resins, and curing procedures to produce a variety of composites roughly 7.5"x7.5" square. These composites were then cut into specimen seven inches long and of various width and thickness, depending on the testing. These specimens were tested in a Sintech materials testing machine to determine the composite's tensile and shear strength. This data allowed for the analysis of trends in the various composites commercially available.

A STUDY OF THE TENSION AND SHEAR STRENGTH OF BIDIRECTIONAL E-GLASS EPOXY-RESIN COMPOSITES

Darren Wells

Introduction

Within the last few decades, composites have taken on a more demanding role in the materials industry. A combination of carbon or fiberglass fibers hardened in an epoxy-resin or plastic, composites can be fashioned to have best qualities of plastics, metals, and ceramics all in one unique material. High strength, very low weight, and resistance to a large variety of chemicals are just a few of the properties of composites. A large number of industries ranging from the cutting edge in aerospace technology, the X-33 project, to car and boat manufacturers have taken advantage of this versatile material. The composites which I worked with were fiberglass composites which are used to make small commercial aircraft bodies, boat bodies, and various car parts. There are a number of resins and techniques used for making these fiberglass composites, yet the capability and strength of composites composed of various combinations of commercial products is not exactly known or readily available. An experimental analysis of the strength of these composites would be beneficial to both professionals and amateurs in determining the composite with the optimal properties for their task.

Materials

The fabric used in this study was bi-directional E-glass woven in a four horse-satin configuration and having an average weight of nine oz./sq. yd. Two types of commercial resin were used in this study, Pro-Set #125 resin and #229 hardener which is used in a 10:3 ratio respectively and Aeropoxy resin and hardener which is used in a 100:28 ratio respectively.

Methodology

Composite Lay-up Procedure

In this study I used two different methods for making the fiberglass composites. The first method is the wet lay-up procedure in which four 8"x8" fiberglass fabric squares are cut out (the tension test composites used fabric in which the fibers are oriented at 0 while the shear test composites used fabric in which the fibers are oriented at 45 angles with the first layer being +45, the second being -45, the third +45, and the fourth -45). The resin and hardener are then measured, mixed, and stirred together in a small disposable cup. The first layer of fabric is then laid on a caul plate which has a layer of nonporous peel ply on its top surface. Then enough resin to saturate the layer is pored on and a squeegee is used to even out the resin. The second layer of fabric is then placed on top of the first and the squeegee is used to smooth out the fabric, push out the air bubbles, and pull up excess resin. More resin is then pored on and smoothed even, and the process is repeated for the third and fourth layers. Once the fourth layer is placed on and saturated with resin a layer of porous peel ply large enough to cover the four layers is placed on top and smoothed out. The caul plate and curing composite is then placed in a hood to vent the gases which are released from the curing reaction.

The second process used in this experiment was the vacuum bagging technique. It is exactly as described above with a few extra steps. Before putting the first layer on, a blue putty-like tape is used to make a border at the edge of the caul plate. The same procedure for the wet lay-up is then done in the exact same order. After the porous peel-ply is placed on, an absorbent bleeder/breather ply is placed on this. A small square of breather ply big enough to cover the vacuum nozzle is then placed on the spot where the vacuum nozzle will be placed so as to provide extra protection from the resin. The vacuum nozzle is then hooked to a vacuum pump on one end and then sealed into a slit on a vacuum bag. The flat end of the vacuum nozzle is then placed on the extra padding and the vacuum bagging material is sealed to the tape so as to minimize the amount of air contained inside. The vacuum pump is then turned on to suck out all of the remaining air. The purpose of this technique is to apply constant and even pressure on the top of the curing composite so that the excess resin is squeezed out and absorbed in the bleeder/breather layer.

After a composite was cured for a day after its lay-up, it was then either placed in a post-curing oven set at 60 C for a day or let to cure out at room temperature for fifteen days.

Water Absorption Testing Procedure

To test the water absorption rate of the composites five 1" x 1" or 0.75" x 0.75" squares were cut out of the composite panels after they were fully cured. These squares were then put in a vacuum chamber for one week to completely dehydrate the specimens. Then their weight was measured on a digital scale capable of measuring to the nearest ten thousandths of a gram and recorded. The specimens were then placed in a glass jar filled with enough water to completely cover all of the specimens. The jar was then sealed and placed in an oven at 70 C so as to speed up the water absorption. The weights of all the specimens was then recorded at 4, 8, 24, 32, 48, 72, and 96 hours after first being placed in the oven so as to set up water absorption rate curves. The weights of the best four of five samples from each composite were averaged together to give a general absorption rate curve for the composite.

Tensile Testing Procedure

To test the tensile strength of each composite ten specimens of length 7" and width 0.5" (error is +-1%) were cut from each composite. These specimens were then put a process called "dog-boning" in which the mid-section of a specimen is steadily cut away in a convex fashion so as to focus the break in a certain location, preferably the very middle. In this study the specimens were dog-boned to a width of 0.275"+-1%. Then five specimens from each composite were placed in a vacuum chamber for one week so as to dehydrate them. The other five were placed in a sealed container filled with enough water to cover the specimens and put in an oven set at 70 C for 96 hours so as to saturate the specimens with water. Once the specimens were dehydrated or saturated, they were loaded in a computerized Sintech material testing machine which pulled the specimen length wise in opposite directions at a rate of 0.2 in./min. until the specimen suffered a break or failure. From this information the computer was able to calculate the tensile strength, strain, and modulus of each composite. The data of the best four of five samples was averaged together for analysis and comparison.

Shear Testing Procedure

To test the shear strength of composites two +-45 panels of each type of composite were made so as to have enough test specimens. After the panels were fully cured, they were tabbed with a composite tabbing material on both the top and bottom leaving a gage length of 5" and a total length of 7". Five specimens of total length 7" and width 0.75"+-1% were then cut out of each panel, making ten total specimens for each type of composite. Five of these test specimens were placed in the vacuum chamber for a week, and the other five were sealed in a container and placed in an oven at 70 C for 96 hours. These samples were then tested in the Sintech machine in the same manner as the tensile tests. From this information the computer was able to calculate the shear strength, strain, and modulus of the +-45 composites. The data of the best four of five samples was then averaged together for analysis and comparison.

Calculations

Tensile and Shear Strength

To calculate the tensile and shear strength of the composites, the maximum load (in pounds-force) which the specimens took before failure is divided by the cross-sectional area, or width multiplied by depth, (in sq. inches) of a test specimen.

$$S=L/(w*d)$$

(S=tensile or shear strength, L=maximum load, w=width of specimen, d=depth of specimen)

To calculate the % strain at break or % elongation at break of a composite, the extension (in inches) of the specimen directly before break is divided by the original gage length (in inches) and multiplied by 100%.

$$S=(E/G)*100\%$$

(S=% strain, E=extension, G=original gage length)

To calculate the modulus of a composite the linear portion of the tensile or shear testing graph is extended. The value of the slope of this line is the modulus value (in pounds-force).

To calculate % water absorption the difference of the final specimen weight and the original specimen weight is divided by the original specimen weight and then multiplied by 100%.

$$A=(Wf-Wo)/Wo*100\%$$

(A=% water absorption, Wf=final weight, Wo=original weight)

The standard deviation of the four recorded specimens for each test type was also taken. This was calculated by the standard equation for standard deviation as follows:

$$s=[(X2-n*Xa2)/(n-1)]$$

(s=standard deviation, X=value for a single specimen, n=number of specimens,

Xa=mean of all specimen values)

Results

The first part is the resulting data in a basic spreadsheet format. This raw data includes averages for tensile or shear strength, % strain, modulus, % loss of strength between dehydrated and water saturated composites, and the total % of water absorption. Following the raw data are three bar graphs which show tensile or shear strength, % strain, and modulus for all composites. The second part is the graphs of the water absorption rates of the composites. The third part is the standard deviation values.

The code used for identifying a composite is as follows:

(tension or shear composite)/(resin type)/(lay-up type)/(post-lay-up curing procedure)

T=tension composite

S=shear composite

P=Pro-Set resin

A=Aeropoxy resin

V=vacuum bagging lay-up procedure

W=wet lay-up procedure

O=70 C post-cure

R=15 day room-temperature cure

For example: T/P/V/R means that this composite is for tensile testing, has the Pro-Set resin, was made using the vacuum bagging technique, and was cured for 15 days at room-temperature after the lay-up.

			Part One				
			Bidirectional Tension Tests				
code number	code identity	dehydrated or water saturated	tensile strength (psi)	% strain	modulus (mpsi)	% loss of strength of dry/wet	% of water absorbtion
1	T/P/V/O	d	47530.86	5.775	0.825	38.63636	2.115061
2		w	29166.67	3.925	0.74		
3	T/P/V/R	d	48173.17	5.75	0.84	43.94616	2.486047
4		w	27002.91	3.875	0.705		
5	T/P/W/R	d	36870.76	5.775	0.6475	39.07086	1.669036
6		w	22465.03	3.9	0.575		
7	T/A/V/O	d	53221.06	5.825	0.9225	47.83957	2.368434
8		w	27760.33	3.475	0.8075		
9	T/A/W/O	d	36570.74	5.775	0.825	41.65296	1.427227
10		w	21337.95	3.4	0.63		
11	T/P/W/O	d	36342.74	6	0.6125	40.68478	2.559794
12		w	21556.78	4.2	0.515		
13	T/A/V/R	d	49546.56	5.625	0.895	36.55966	2.225608
14		w	31432.51	3.75	0.8525		
15	T/A/W/R	d	35005.16	5.85	0.6	47.51911	1.451267
16		w	18371.02	3.3	0.5525		

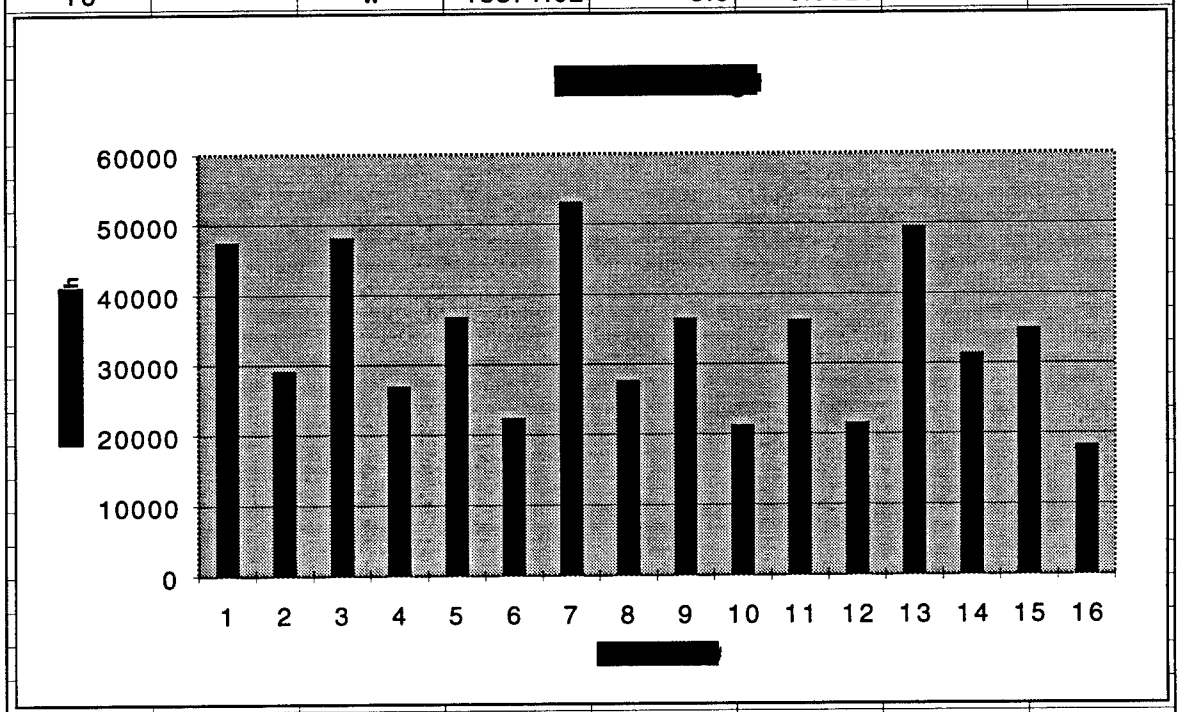

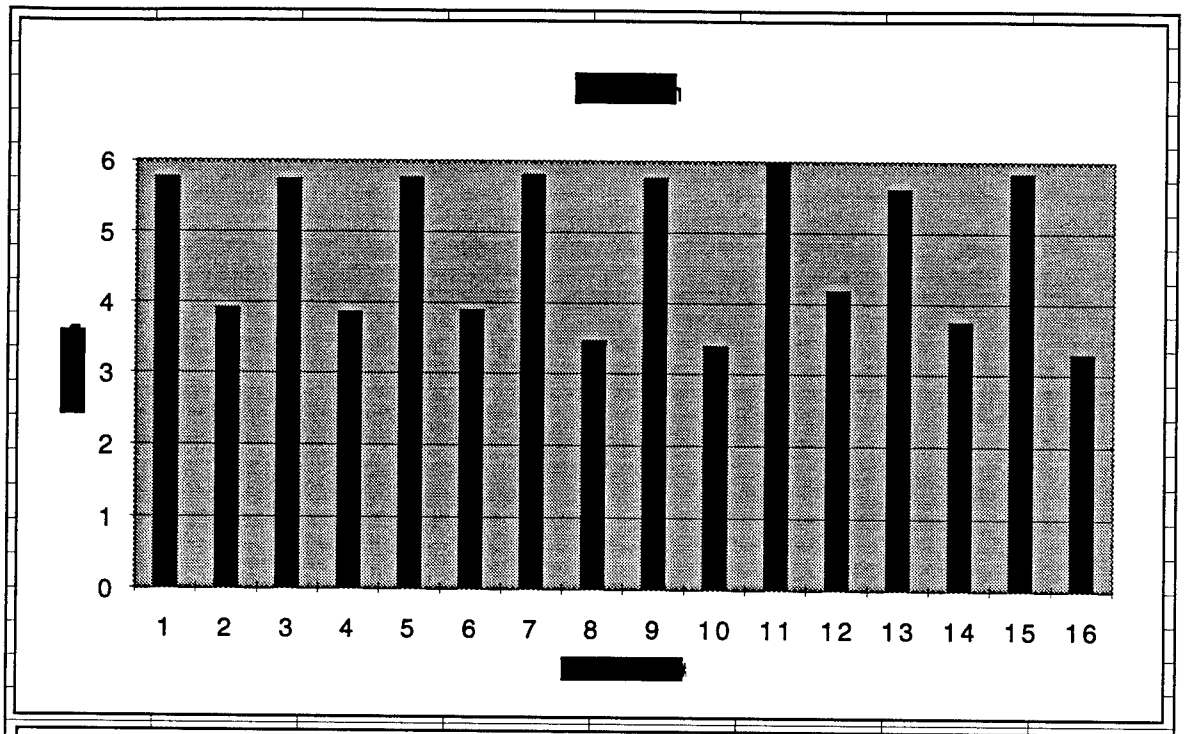
6
5
4
3
2
1
0
1 2 3 4 5 6 7 8 9 10 11 12 13 14 15 16

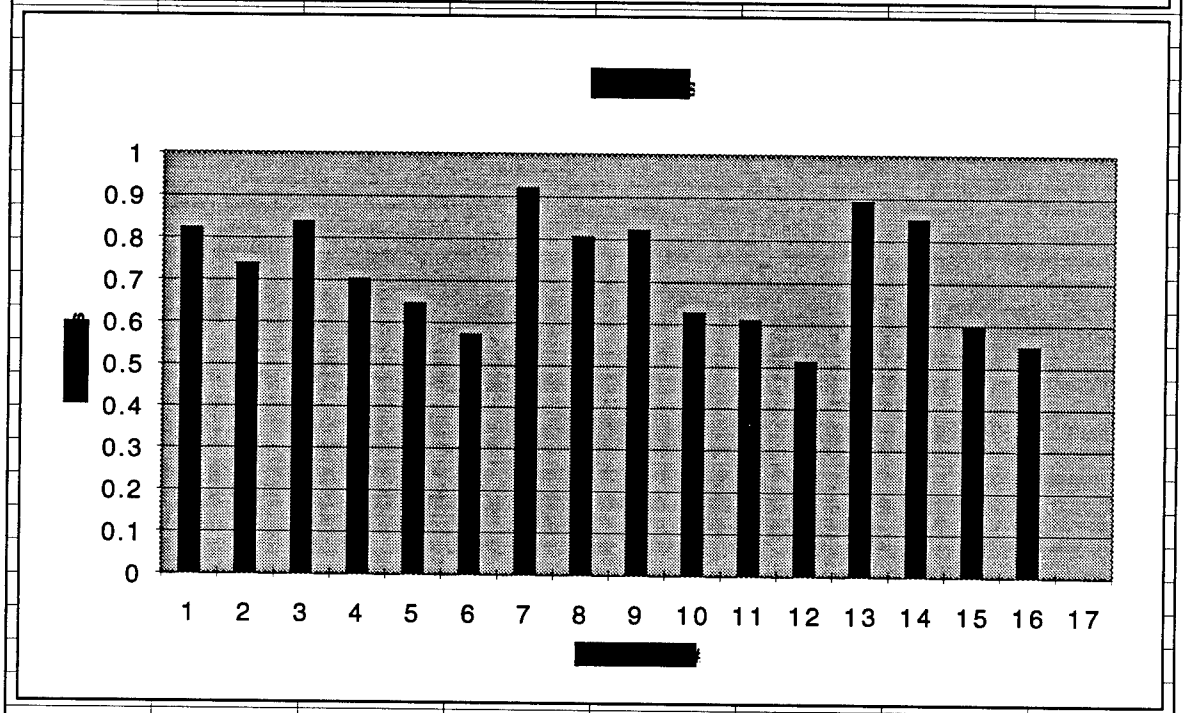
1
0.9
0.8
0.7
0.6
0.5
0.4
0.3
0.2
0.1
0
1 2 3 4 5 6 7 8 9 10 11 12 13 14 15 16 17

			Bidirectional Shear Tests				
code number	code identity	dehydrated or water saturated	tensile strength (psi)	% strain	modulus (mpsi)	% loss of strength of dry/wet	% of water absorbtion
17	S/P/W/R	d	17153.33	20.6	0.225	48.62301	1.303989
18		w	8812.865	18.575	0.125		
19	S/A/W/R	d	13202.38	23.8	0.18	15.99311	1.092467
20		w	11090.91	14.175	0.135		
21	S/P/W/O	d	19732.03	22.175	0.2125	47.36138	1.455761
22		w	10386.67	15.1	0.15		
23	S/A/V/O	d	16481.48	16.075	0.24	21.91011	1.282492
24		w	12870.37	11	0.2225		
25	S/A/W/O	d	16406.06	24.55	0.175	26.81867	0.846926
26		w	12006.17	16.05	0.1525		
27	S/P/V/O	d	18666.67	15.35	0.2525	51.49614	1.237242
28		w	9054.054	12	0.185		
29	S/P/V/R	d	19252.25	17.825	0.275	52.48271	1.216279
30		w	9148.148	13.75	0.195		
31	S/A/V/R	d	14761.9	14.35	0.235	28.3871	1.231453
32		w	10571.43	12.3	0.185		

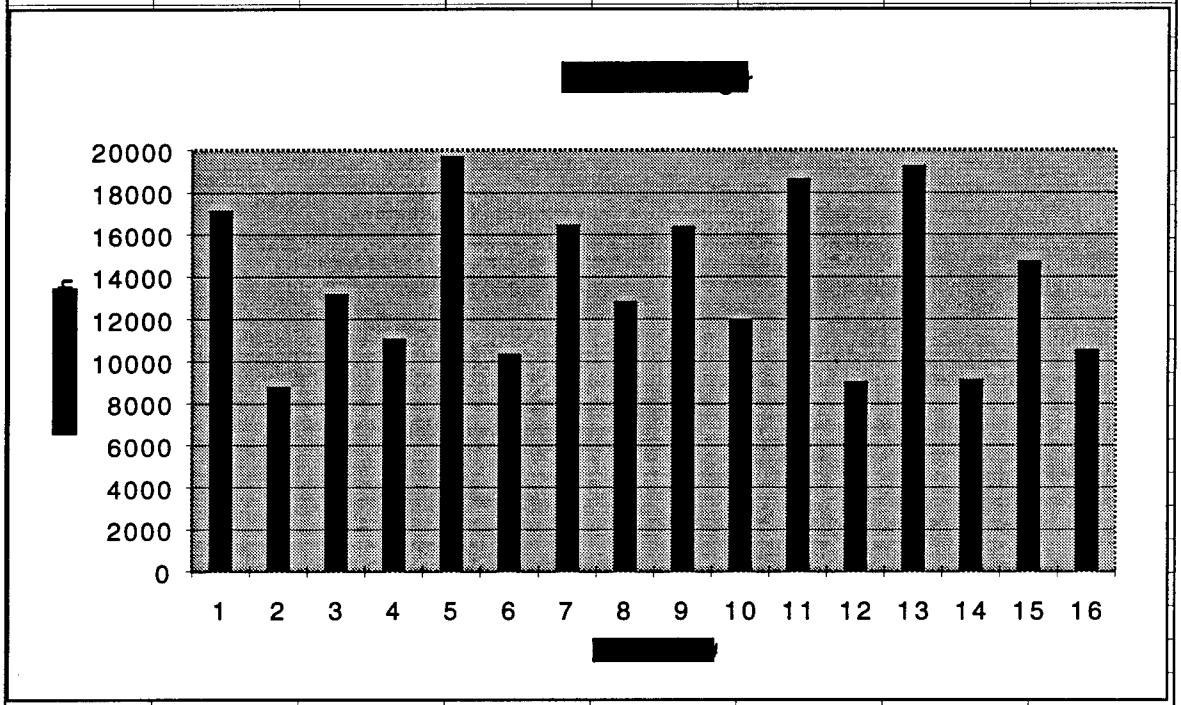

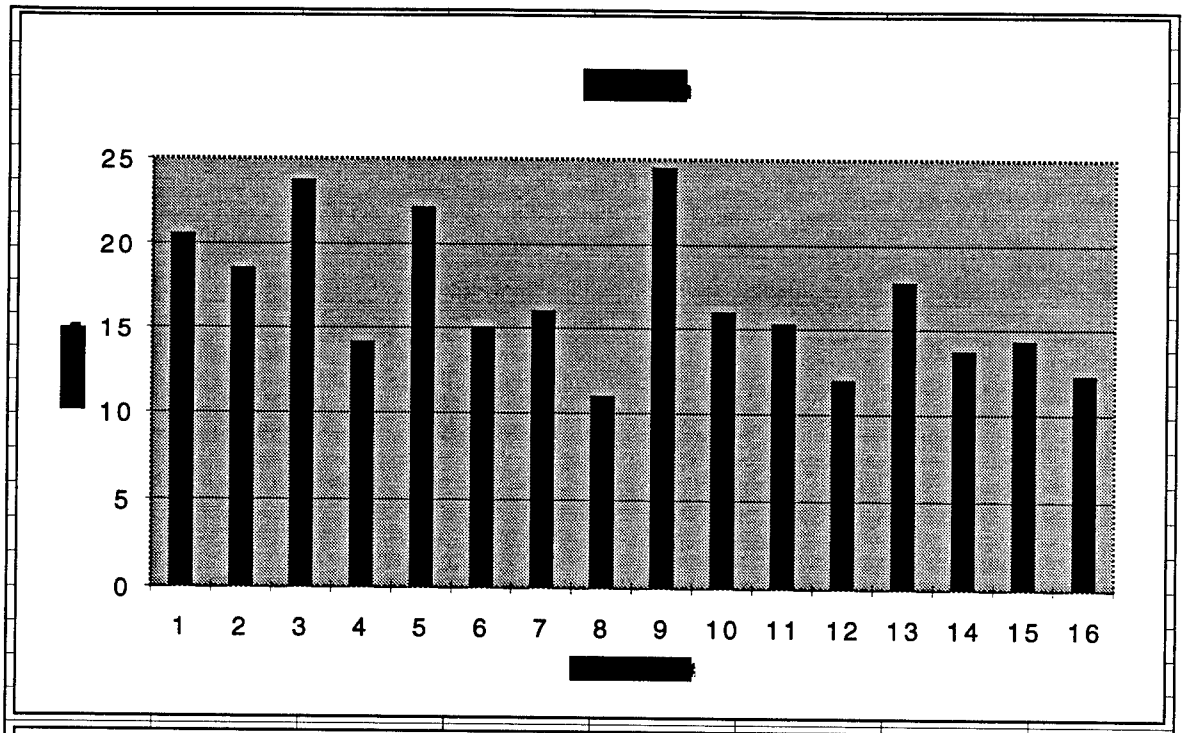
25
20
15
10
5
0
1 2 3 4 5 6 7 8 9 10 11 12 13 14 15 16

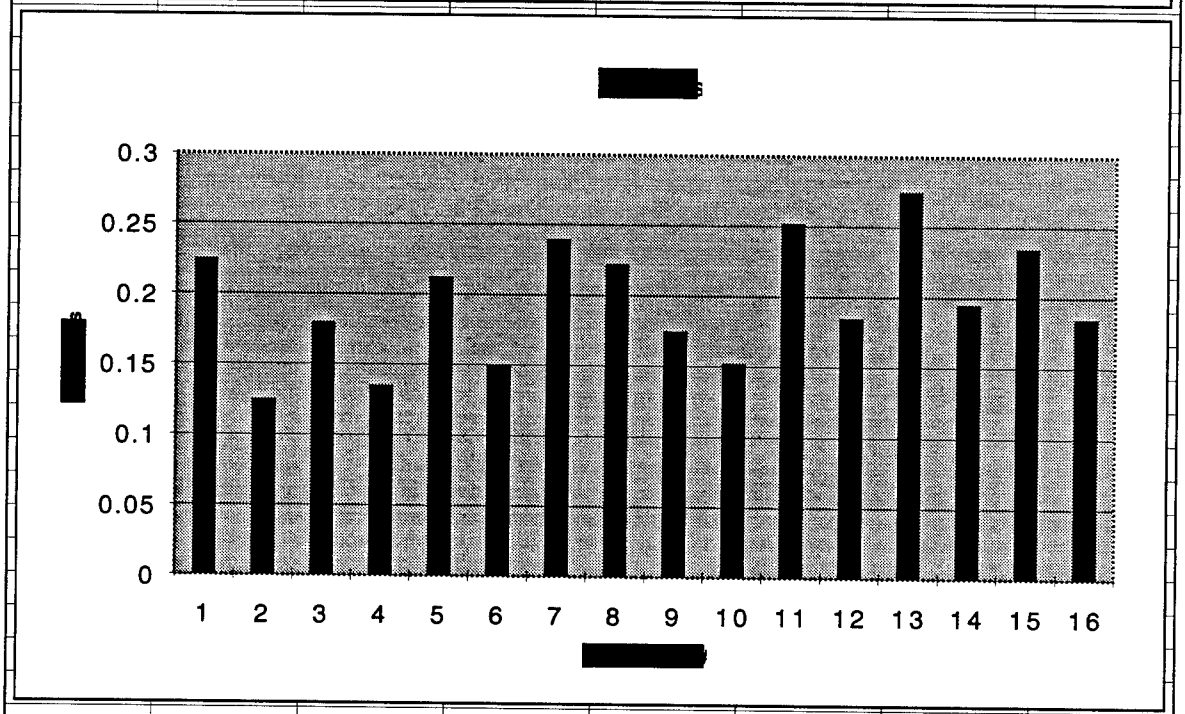
0.3
0.25
0.2
0.15
0.1
0.05
0
1 2 3 4 5 6 7 8 9 10 11 12 13 14 15 16

Part Two

The number of hours is on the x-axis.

The % water absorbtion is on the y-axis.

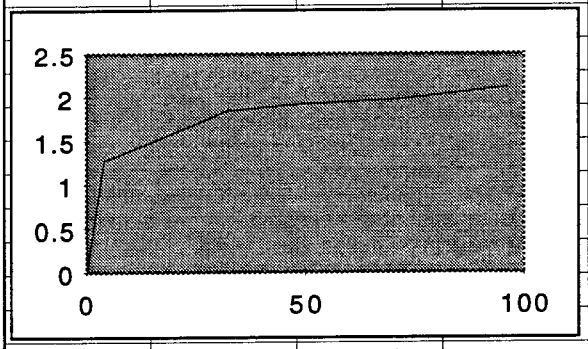

composite: T/P/V/O

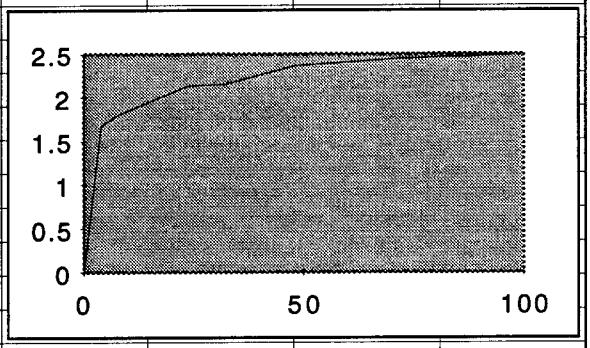

composite: T/P/V/R

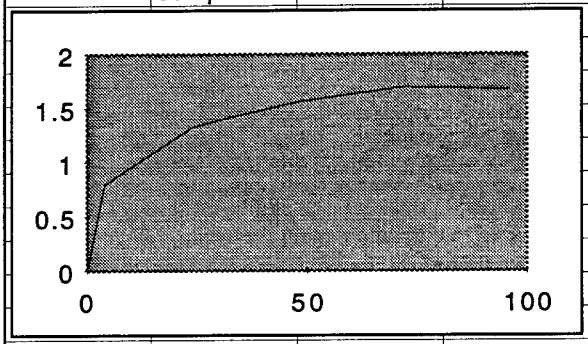

composite: T/P/W/R

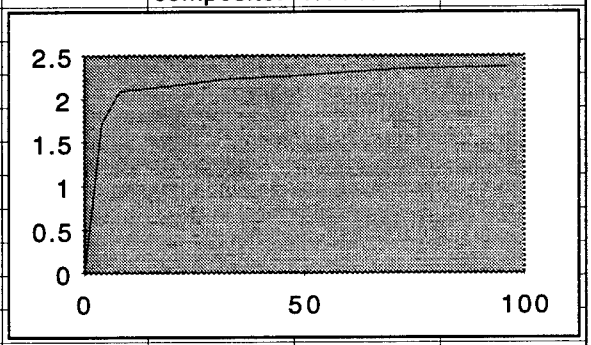

composite: T/A/V/O

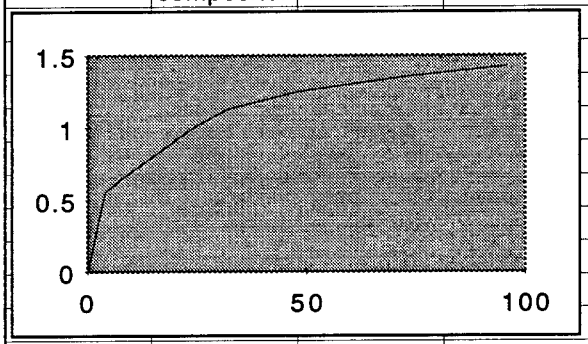

composite: T/A/W/O

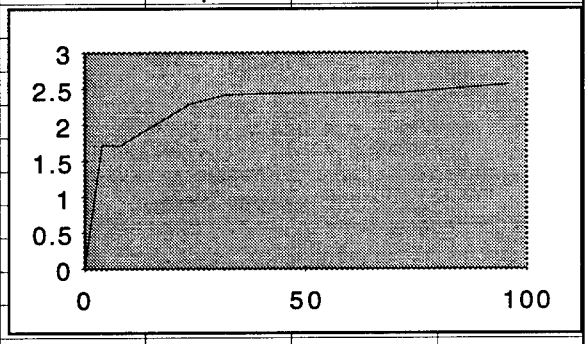

composite: T/P/W/O

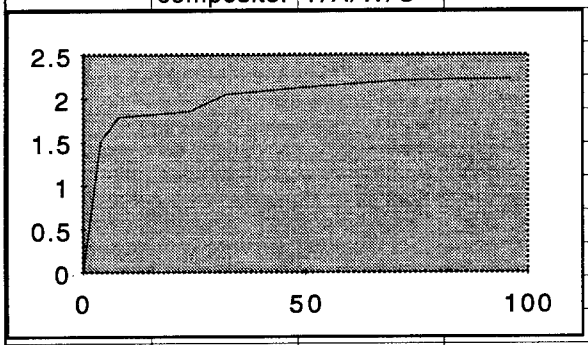

composite: T/A/V/R

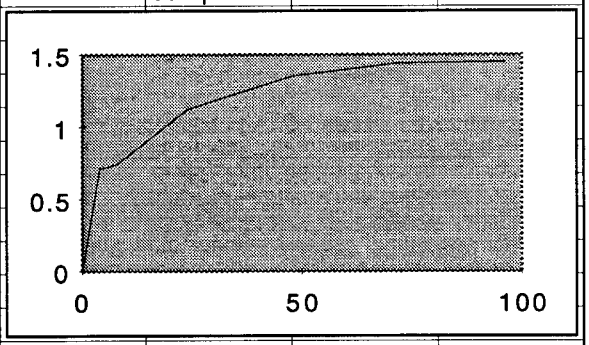

composite: T/A/W/R

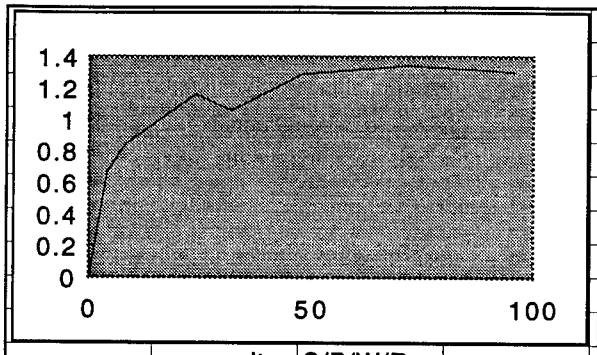

composite: S/P/W/R

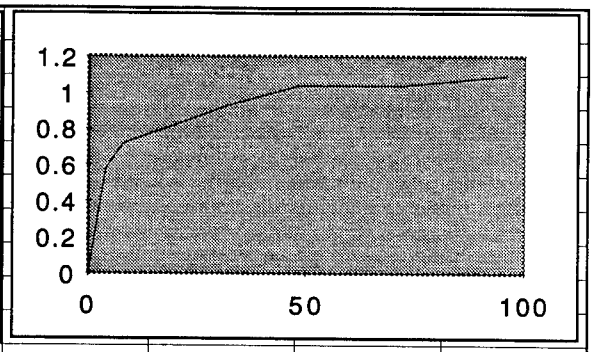

composite: S/A/W/R

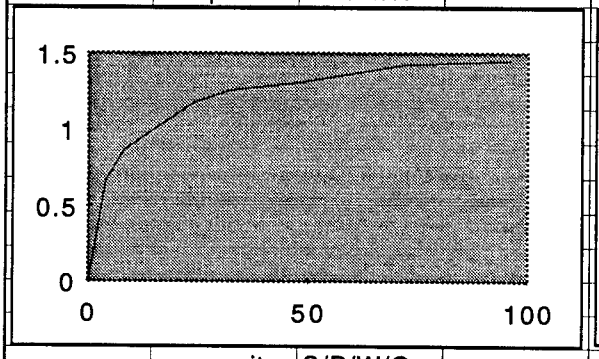

composite: S/P/W/O

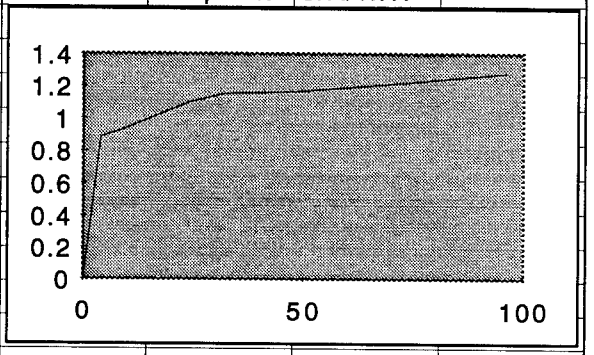

composite: S/A/V/O

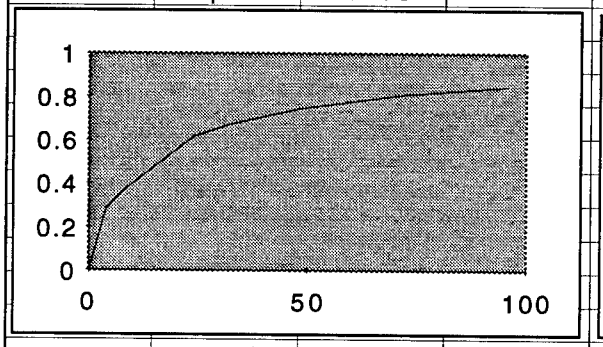

composite: S/A/W/O

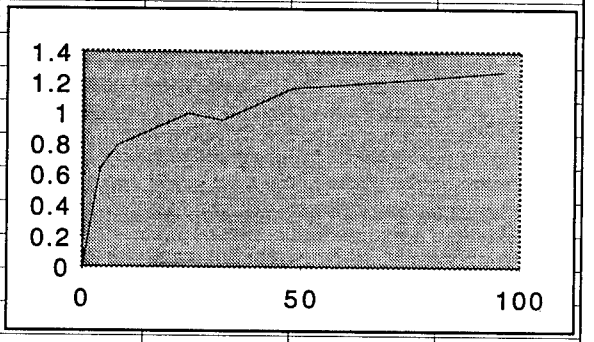

composite: S/P/V/O

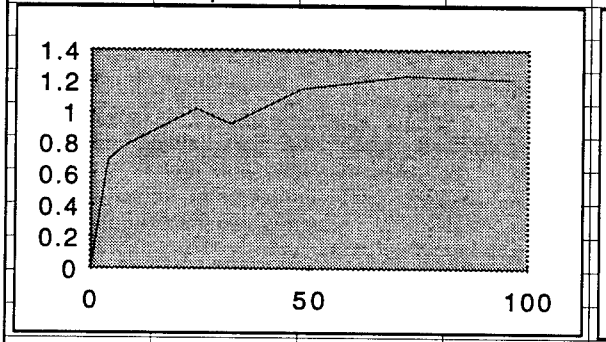

composite: S/P/V/R

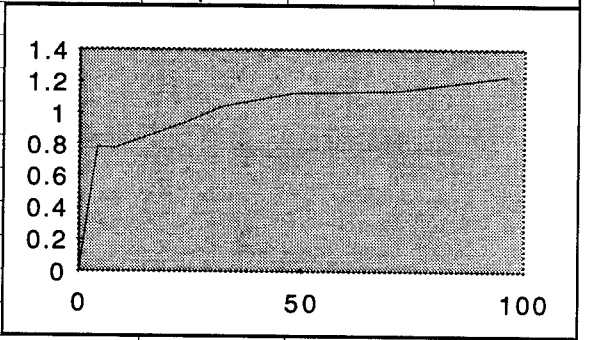

composite: S/A/V/R

			Part Three				
			Standard Deviation				
composite:	1		composite:	2		composite:	3
tensile	900.8179		tensile	380.3339		tensile	1869.801
% strain	0.095743		% strain	0.095743		% strain	0.264575
modulus	0.01291		modulus	0.011547		modulus	0.018257
composite:	4		composite:	5		composite:	6
tensile	320.8087		tensile	3117.548		tensile	1979.054
% strain	0.05		% strain	0.722842		% strain	0.294392
modulus	0.01291		modulus	0.029861		modulus	0.017321
composite:	7		composite:	8		composite:	9
tensile	2730.719		tensile	685.6181		tensile	441.8631
% strain	0.287228		% strain	0.05		% strain	0.095743
modulus	0.038622		modulus	0.005		modulus	0.01291
composite:	10		composite:	11		composite:	12
tensile	1102.729		tensile	1304.741		tensile	881.9146
% strain	0.11547		% strain	0.182574		% strain	0
modulus	0.014142		modulus	0.009574		modulus	0.017321
composite:	13		composite:	14		composite:	15
tensile	1416.307		tensile	1211.704		tensile	1463.445
% strain	0.206155		% strain	0.1		% strain	0.264575
modulus	0.01		modulus	0.030957		modulus	0.008165
composite:	16						
tensile	721.0285						
% strain	0.08165						
modulus	0.012583						

composite:	17		composite:	18		composite:	19
tensile	638.2847		tensile	344.5168		tensile	884.5914
% strain	1.169045		% strain	2.790908		% strain	2.61916
modulus	0.01291		modulus	0.005774		modulus	0.008165
composite:	20		composite:	21		composite:	22
tensile	137.8483		tensile	191.3742		tensile	51.06278
% strain	1.400893		% strain	1.973787		% strain	0.454606
modulus	0.023805		modulus	0.009574		modulus	0.008165
composite:	23		composite:	24		composite:	25
tensile	1025.063		tensile	374.6664		tensile	243.5328
% strain	1.588238		% strain	0.761577		% strain	1.709776
modulus	0.018257		modulus	0.017078		modulus	0.01
composite:	26		composite:	27		composite:	28
tensile	707.1607		tensile	626.9304		tensile	447.5583
% strain	1.144552		% strain	2.25758		% strain	1.626858
modulus	0.009574		modulus	0.005		modulus	0.005774
composite:	29		composite:	30		composite:	31
tensile	549.1802		tensile	314.2697		tensile	540.9881
% strain	0.974252		% strain	0.341565		% strain	1.310216
modulus	0.017321		modulus	0.005774		modulus	0.045092
composite:	32						
tensile	294.2636						
% strain	1.169045						
modulus	0.005774						

Conclusion

Tensile Strength Conclusions

In the area of general trends for tensile strength, vacuum bagging was much better than wet lay-ups by a decisive margin. On average Aeropoxy is somewhat stronger for dehydrated composites and Pro-Set is somewhat stronger for water saturated composites. No conclusive evidence could be drawn about post-curing vs. room temperature cure. Dehydrated samples were much stronger than saturated samples for every composite.

For specific composites, composite T/A/V/O was stronger dehydrated than any other composite, yet it had the highest % loss of strength when saturated. Composite T/A/V/R was the second strongest dehydrated and the highest when water saturated, therefore making it the best transition composite.

Shear Strength Conclusions

In the area of general trends for shear strength, vacuum bagging was slightly better for dehydrated composites, but wet lay-up composites were slightly better for water saturated samples. As for resin comparison though, Pro-Set is significantly stronger for dehydrated composites, and Aeropoxy is significantly stronger for saturated composites. On average, post-cured composites were stronger than room temperature cured ones for both dehydrated and saturated. Again, dehydrated samples were much stronger for all composites than water saturated samples.

For specific composites, S/P/W/O was the strongest for dehydrated samples. S/A/V/O had the highest shear strength for saturated samples and the fourth highest dehydrated strength making it the best overall transition composite.

Acknowledgements

I would like to thank Mr. David Curliss and Mr. Ron Esterline from Wright Laboratories Building 654 for thier instruction and advice.

Works Cited

Annual Book of ASTM Standards, 1982 Ed. Part 35. Test Method D 638-82.

Annual Book of ASTM Standards, 1976 Ed. Part 36. Test Method D 3039-76.

Annual Book of ASTM Standards, 1982 Ed. Part 35. Test Method D 570-81.

Associate did not participate in the program.

THERMAL CHARACTERIZATION OF THE 1,3,3-TRINITROAZETIDINE (TNAZ)/*N*-ACETTK-3,3-DINITROAZETIDINE (ADNAZ) BINARY MIXTURE

Tuan P. Yang

Choctawhatchee High School
110 Racetrack Road
Fort Walton Beach, FL 32547

Final Report for:
High School Apprentice Program
Wright Laboratory

Sponsored by:
Air Force Office of Scientific Research
Bolling Air Force Base, Washington, DC

And

Wright Laboratory

August 1997

THERMAL CHARACTERIZATION OF THE 1,3,3-TRINITROAZETIDINE (TNAZ)/ *N*-ACETYL-3,3-DINITROAZETIDINE (ADNAZ) BINARY MIXTURE

Tuan P. Yang

ABSTRACT

The binary phase diagram for the 1,3,3-trinitroazetidine (**TNAZ**)/*N*-Acetyl-3,3-dinitroazetidine (**ADNAZ**) system has been calculated computationally and determined experimentally. Initial physical mixtures of **TNAZ** and **ADNAZ** exhibit the thermal characteristics associated with a simple binary eutectic system, while remelt mixtures exhibit the characteristics associated with a simple linear solid solution system on the **ADNAZ**-rich side of the eutectic and a simple binary eutectic system on the **TNAZ** side. The calculated eutectic temperature/composition is 77.3°C/56.4 mol percent **TNAZ**. Neither **TNAZ** nor **ADNAZ** behave ideally in either type mixture.

THERMAL CHARACTERIZATION OF THE 1,3,3-TRINITROAZETIDINE (TNAZ)/ *N*-ACETYL-3,3-DINITROAZETIDINE (ADNAZ) BINARY MIXTURE

Tuan P. Yang

INTRODUCTION

1,3,3-Trinitroazetidine (**TNAZ**), was first prepared in 1990[1] by Archibald and co-workers. It is a powerful and thermally stable energetic material. However, its application to melt cast energetic formulations is hampered by high volatility and a tendency to form low-density castings at atmospheric pressure[2]. Researchers at this laboratory are attempting to improve these unacceptable characteristics by forming binary eutectic compositions with other energetic materials. This will result in mixtures with lower melting points and reduced volatility. To date, binary mixtures of **TNAZ** with pentaerythritoltetranitrate (**PETN**), 2,4,6-trinitrotoluene (**TNT**), 1,3,5-trinitrobenzene (**TNB**) and *N*-methyl-*p*-nitroaniline (**MNA**) have been characterized for explosive performance and thermal/shock sensitivity[3, 4, 5 and 6]. It was also demonstrated during a previous investigation that **TNAZ** exists in at least two polymorphic variations, one stable (**TNAZ I**) under ambient conditions and one unstable (**TNAZ II**). It is also noted that the former is more dense than the latter[7]. Crystal density increases with the spontaneous transition from **TNAZ II** to **I** resulting in a dendritic structure with characteristic macro-shrinkage cracks. These cracks are distributed irregularly throughout a neat **TNAZ** billet from a melt casting operation and are believed to be the primary cause of the measured low bulk density. The immediate objective of this effort is to determine the temperature/composition curve for the **TNAZ/ADNAZ**[8] binary eutectic system by using differential scanning calorimetry (DSC) supported by hot stage microscopy (HSM). The overall objective of this program is to establish a behavior baseline for a variety of **TNAZ**-based binary systems.

EXPERIMENTAL

Phase Diagram Calculation

A computer program in BASIC[9] was used to calculate the eutectic composition and the melting temperature for the binary mixture. The program repetitiously solves equation (1) by using component heats of fusion and melting points as input data,

$$R\ln x = \Delta H_{fus}(-1/T + 1/T_o) \qquad (1)$$

where T is the melting point (degree K) of the eutectic composition, T_o, ΔH_{fus} and x are the melting point, heat of fusion and mol fraction of component A or B, respectively, and R is the gas constant (1.987 calories K^{-1} mol^{-1}). The experimental melting points and heats of fusion, determined by DSC heating operations on mixtures of the stable polymorphs of both components, were used for comparison with their corresponding calculated values. Since the BASIC program does not provide a table of liquidus temperatures, they were computationally derived by solving equation (1) for the specific mol fraction values used during this investigation.

Thermal Characterization

a. Differential Scanning Calorimetry (DSC)

ADNAZ and selected **TNAZ/ADNAZ** mixtures were thermally characterized by using a TA Instruments Dual Differential Scanning Calorimeter, Model 912, equipped with a 2100 Thermal Analyzer Data System. **TNAZ** was previously characterized[7]. Standard aluminum sample pans and lids, TA Instruments Part Nos. 072492 and 073191, were used for all melting operations carried out by using the standard Dual Sample DSC (DSDSC) cell. Lids were inverted to minimize free volume over the sample. An upper temperature limit of 120 °C and a sample weight of 2.0 ± 0.1 mg were used throughout this investigation to minimize the chance for leakage from the sample pans.

The primary focus of the DSC is to measure energies and temperatures associated with melting and solid-state phase transition processes. These processes require energies and are called endothermic. The temperatures from the endothermic events are plotted versus mol percent TNAZ thus displaying graphically the experimental phase diagram. At least two melting operations were carried out for all mixtures at a heating rate of 1 °C/min. DSC experiments were also carried out with neat **ADNAZ** at a heating rate of 5 °C/min to search for polymorph modifications in a time-expedient manner. Cooling operations were either uncontrolled or accomplished at 5 °C/min by using ice/water as a cooling medium. Peak temperatures are reported for all endothermic processes. Mixtures were prepared by grinding weighed portions of the dry explosive materials in an agate mortar with a glass pestle to ensure homogeneity. The DSC was calibrated by using indium metal as a temperature standard.

b. Hot Stage Microscopy (HSM)

HSM experiments were carried out by using a Mettler Hot Stage, Model FP 82, equipped with a FP 80 Central Processor. All observations were made with a Leitz Orthoplan Universal Largefield microscope equipped with a polarizing condenser and high-resolution video system, Javelin Smart Camera, Model JE3762DSP, which was operated at shutter speeds of 1/250 or 1/500 s. The video system is also equipped with a FOR-A video timer, Model VTG-55. All photomicrographs were obtained through a Leitz NPL 10X 0.20P lens (150x). Heating and cooling rates were 1 °C/min or 5 °C/min except below approximately 45 °C where the cooling rate is not controlled. The temperature at which the last crystal melts is reported as the liquidus temperature. The estimated eutectic melting temperature is differentiated from that of component melting by observing change in the rate of the melting process.

Energetic Components

ADNAZ and **TNAZ** were purified by crash-precipitation from a hot ethanol solution into ice and water and dried under vacuum. Analysis by high performance liquid chromatography showed **TNAZ** to be 97.8 percent pure. No impurities were observed in the **ADNAZ** chromatogram.

RESULTS

Thermal Characterization

a. Thermal Properties of ADNAZ and TNAZ

The **ADNAZ** melting point and heat of fusion, 113.7 ± 0.06 °C and 6.130 ± 0.053 kcal/mol, respectively, (lit. mp 111-112 °C[1]) were obtained by DSC heating operations at 1 °C/min. During DSC heating operations with **ADNAZ** at 5 °C/min another polymorph was observed. The melting point and heat of fusion from a single experiment were 79.1 °C and 4.721 kcal/mol. The melting point and heat of fusion observed for **TNAZ** were 99.7 ± 0.1 °C and 6.607 ± 0.079 kcal/mol, respectively (lit. mp 101.1 °C/6.405 kcal/mol[7]). **ADNAZ** melting and recrystallization characteristics were also observed by HSM operations. Melting occurred at 114.4 °C. **TNAZ** was previously shown to exist in at least two polymorphic forms[7].

b. Calculated Phase Diagram

The calculated melting point and mol percent **TNAZ** in the eutectic composition are 77.3 °C and 56.4, respectively. **TNAZ** mol percent values and associated liquidus temperatures used to construct the phase diagram are shown in Table 1.

c. DSC Characterization of TNAZ/ADNAZ Mixtures

Initial melting operations carried out at a heating rate of 1 °C/min on twenty-one freshly ground mixtures of **TNAZ** and **ADNAZ** yielded a consistent, endothermic event at an average temperature of 75.4 ± 0.1 °C that is caused by eutectic melting. **TNAZ** liquidus temperatures from the DSC form a slightly concave-shaped curve positioned below that calculated by using equation (1).

Table 1. Mol Percent/Calculated Temperatures Used to Construct the **TNAZ/ADNAZ** Phase Diagram

Mol Percent **TNAZ**	Temperature(°C)
0	113.7
4.9	111.3
9.9	108.7
19.7	103.3
29.7	97.3
39.6	90.7
44.6	87.0
49.6	83.1
62.1	81.0
64.6	78.8
56.4	77.3
57.1	77.7
58.4	78.6
59.6	79.3
62.1	80.9
63.6	81.8
64.6	82.4
69.7	85.3
74.7	88.0
79.7	90.5
84.8	93.0
89.9	95.4
94.9	97.6
97.5	98.7
100.0	99.8

1. Eutectic composition.

ADNAZ liquidus temperatures form a curve above the calculated liquidus temperatures shown in Table 1. The data suggest the eutectic composition lies between 57.1 and 65 mol percent **TNAZ**. Data from all DSC melting operations on physical mixtures are shown in Table 2 along with both calculated and experimental heats of fusion. The calculated and experimental temperature/composition data from Tables 1 and 2 are displayed graphically in Figure 1.

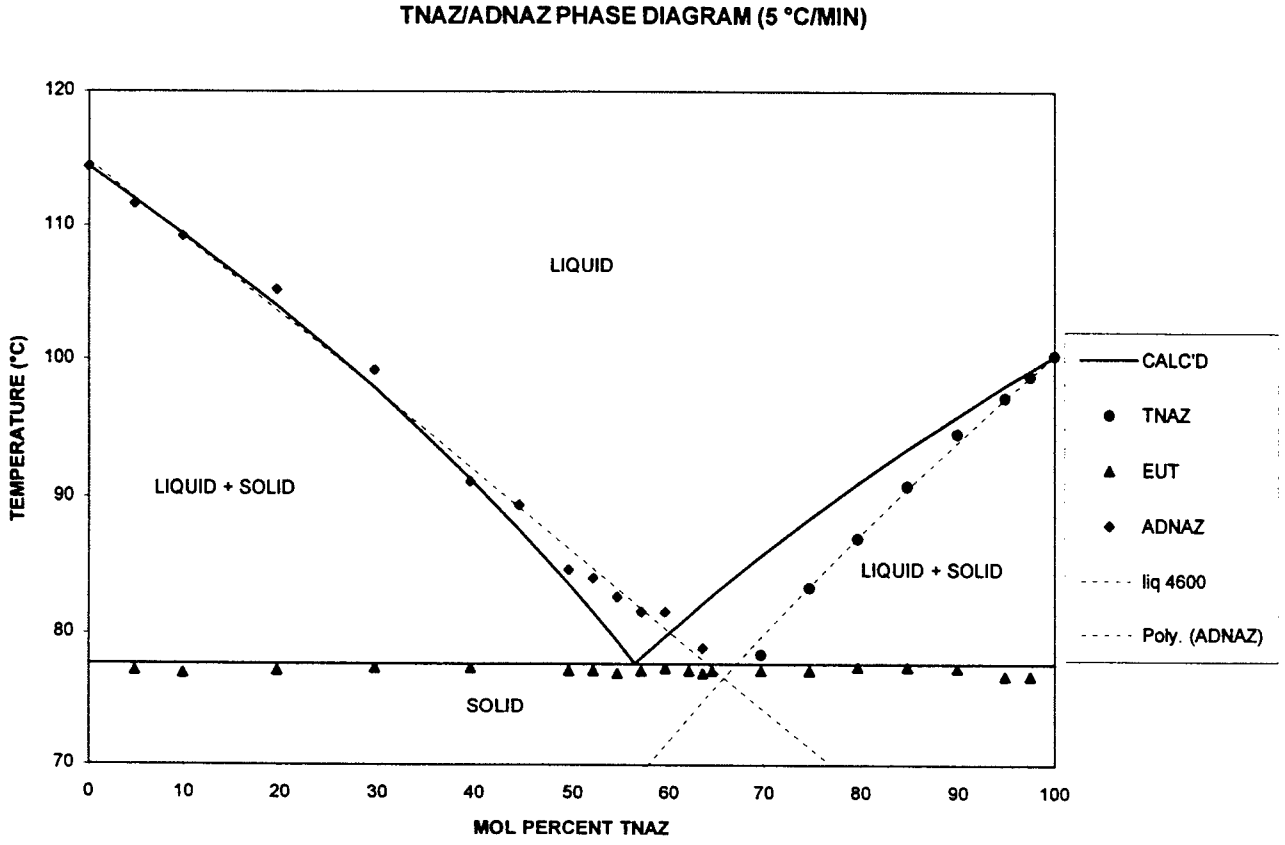
TNAZ/ADNAZ PHASE DIAGRAM (5 °C/MIN)
TEMPERATURE (°C)
120
110
100
90
80
70
LIQUID
LIQUID + SOLID
LIQUID + SOLID
SOLID
0
10
20
30
40
50
60
70
80
90
100
MOL PERCENT TNAZ
CALC'D
TNAZ
EUT
ADNAZ
liq 4600
Poly. (ADNAZ)

Figure 1

Table 2. Endothermic Peak Temperatures for Initial DSC Melting Operations with **TNAZ/ADNAZ** Mixtures (1 °C/min)

Mol Percent	Temperature (°C)			Hts of Fusion Fusion
TNAZ	Eutectic	**TNAZ**	ADNAZ	Calc'd/Exp't
0			113.7	/6130
4.9	74.2/77.4		111.2	6153/6204
9.9	75.1		108.6	6177/6360
19.7	75.6		104.2	6224/5631
29.7	75.5		95.8/99.0	6271/5199
39.6	75.4		90.4	6319/5744
44.6	75.4		86.6	6342/5265
49.6	75.4		83.6	6366/5452
52.1	75.4		NR[1]	6378/4570
54.6	75.4		NR[1]	6390/4894
57.1	75.4			6402/5340
58.4	75.4[2]			
59.6	75.6	NR[1]		6414/5296
62.1	75.4	NR[1]		6426/5400
63.6	75.4	NR[1]		6433/5515
64.6	75.6	NR[1]		6438/5377
69.7	75.6	79.5		6462/5385
74.7	75.4	82.3		6486/5074
79.7	75.6	86.4		6510/5162
84.8	75.5	89.0		6534/6137
89.9	75.4	93.4		6559/6242
94.9	75.2	96.3		6582/6327
97.5	75.0	97.6		6595/6416
100.0		99.7		/6607

1. Not resolved.
2. Calculated **ADNAZ** liquidus curve extension crosses the eutectic melting point.

Remelting operations on samples obtained by recrystallization of the melted mixtures from the initial DSC melting operations significantly changed their thermal behavior. Endothermic events associated with the melting of **ADNAZ** form two diverging convex-shaped curves. The solidus (lower) curve is continuous and extends to 59.6 mol percent **TNAZ**, while the liquidus (upper) curve remains above what was calculated by use of equation (1). **TNAZ** liquidus temperatures are generally consistent with those from initial melting operations. The average eutectic melting temperature is shifted to 74.2 $\pm$ 0.05 °C and is only observed at concentrations greater than 52.1 mol percent **TNAZ**, its intersection with the **ADNAZ** solidus curve. The eutectic composition is believed to lie between 62 and 64 mol percent **TNAZ**. The data from all DSC remelting operations, including heats of fusion from the initial melting operations, are summarized in Table 3. Temperature/composition curves are shown in Figure 2.

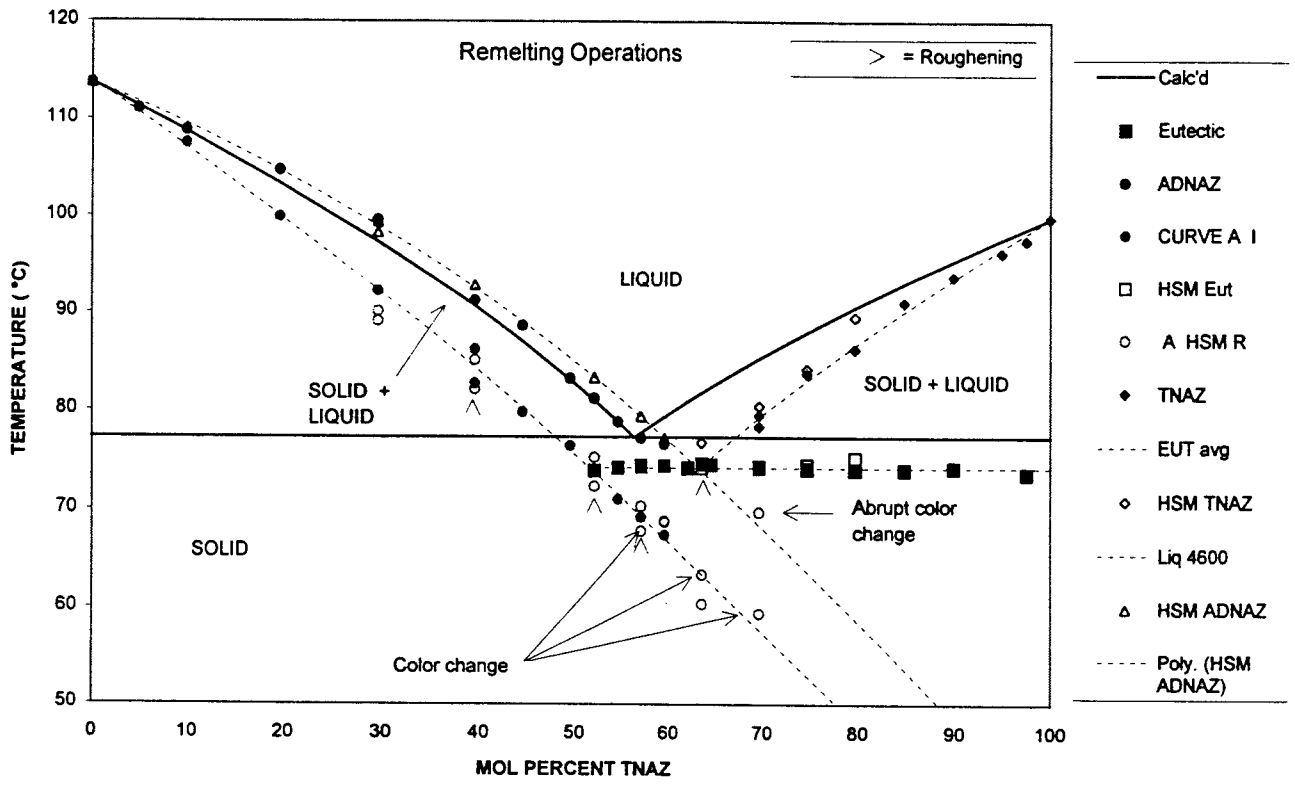
TNAZ/ADNAZ PHASE DIAGRAM (1 °C/MIN)
Remelting Operations
> = Roughening
LIQUID
SOLID + LIQUID
SOLID + LIQUID
SOLID
Abrupt color change
Color change
TEMPERATURE (°C)
MOL PERCENT TNAZ
120
110
100
90
80
70
60
50
0
10
20
30
40
50
60
70
80
90
100
Calc'd
Eutectic
ADNAZ
CURVE A I
HSM Eut
A HSM R
TNAZ
EUT avg
HSM TNAZ
Liq 4600
HSM ADNAZ
Poly. (HSM ADNAZ)

Figure 2

All molten compositions are affected by supercooling. Those closer to the eutectic composition often require special techniques, either long waiting periods or quenching in liquid nitrogen, to initiate recystallization.

Table 3. Endothermic Peak Temperatures for All DSC Remelting Operations with **TNAZ/ADNAZ** Mixtures

Mol Percent	Temperature (°C)				Hts of Fusion	
			ADNAZ			
TNAZ	Eutectic	TNAZ	Liquidus	Solidus	Initial	Remelt
0			113.7	113.7		6130
4.9			111.0		6204	6060
9.9			108.8	107.5	6123	5777
19.7			104.7	99.9	5631	5357
29.7			99.6	92.2	5199	4981
39.6			91.2	86.2/82.7	5744	5183
44.6			88.6	79.8	5265	4275
49.6			83.2	76.4	5452	4658
52.1	73.9		81.2	NR[1]	4570	4248
54.6	74.2		78.8	71.0	4897	4285
57.1	74.4		77.2	69.2	5340	4336
59.6	74.4		76.6	67.4	5296	4806
62.1	74.2				5400	4548
63.6	74.6	NR[1]			5515	5225
64.6	74.5	NR[1]			5377	4862
69.7	74.3	78.3			5385	5080
74.7	74.1	83.7			5074	5069
79.7	74.0	86.2			5162	5126
84.8	74.0	91.0			6137	5802
89.9	74.2	93.7			6242	5514
94.9	72.2	96.2			6327	5825
97.5	73.6	97.5			6416	5735
100.0		99.7			6607	

1. Not resolved.

d. HSM Characterization of **TNAZ/ADNAZ** Mixtures

HSM melting operations were carried out on nine mixtures that were prepared on a hot plate. The average melting temperature for the eutectic composition was 74.5 ± 0.2 °C. HSM cooling operations on

molten thin films were hampered by extreme supercooling, especially in proximity to the eutectic composition. All melting temperatures from HSM operations are shown in Table 4.

Table 4. **TNAZ/ADNAZ** Data from All HSM Operations

Mol Percent	Temperature (°C)				
			ADNAZ		
TNAZ	Eutectic	TNAZ	LIQUIDUS	SOLIDUS	MISC
29.7			98.3/99.4	89.1/90.1	
39.6			92.8	82.1/85.1	
52.1			83.3	72.3/75.2	
57.1	74.3		79.4	70.3/67.8	
63.3	74.2	76.7		60.4/63.4	
69.7	74.2	80.4		59.4	69.7[1]
74.7	74.5	84.2			
79.7	75.2	89.5			

1. Abrupt color change.

As with DSC remelt operations, the **ADNAZ** solidus curve is continuous (without inflection) and extends through the final eutectic melting temperature to 69.7 mol percent **TNAZ**.

DISCUSSION

Evidence of polymorphism was observed during multiple DSC heating operations at 5 °C/min on a single sample of neat **ADNAZ**. A lone endothermic event at 79.1 °C occurred during experiment number four of seven. The average melting point observed during all of the other experiments was 114.3 °C. This lower melting polymorph was never observed during DSC melting operations on neat **ADNAZ** or on mixtures at 1 °C/min or during any HSM operations. It was previously demonstated[7] that **TNAZ** exists in at least two polymorphic modifications, one stable (**TNAZ I**) at ambient conditions and one unstable (**TNAZ II**). The transition from **TNAZ II** to **TNAZ I** was observed only during HSM recrystallization operations.

ADNAZ liquidus temperatures from DSC heating operations on freshly ground mixtures was not consistent (non-ideal) with those predicted by use of equation (1). They were positioned above those predicted. TNAZ liquidus temperatures also behaves non-ideally in that they form a continuous, slightly concave curve that is positioned below that calculated by using equation (1).

The average eutectic melting temperature, 75.4 °C, is 1.9 °C below that calculated, 77.3 °C. This deviation from the predicted eutectic melting temperature appears to be caused solely by the non-ideal behavior of the **TNAZ** component. The eutectic composition lies at 65 mol percent **TNAZ**, which represents the point of intersection of the **ADNAZ** and **TNAZ** liquidus trendlines.

Remelting operations did not appreciably affect the **TNAZ** liquidus temperatures. The **ADNAZ**-rich side of the temperature/composition diagram was converted from that associated with a simple binary eutectic system to one that describes a simple linear solid solution system. The convex shaped **ADNAZ** solidus curve is continuous to a final detectable concentration of 69.7 mol percent **TNAZ** suggesting that these measurements were probably not made under equilibrium conditions. The solidus data points were observed as endothermic events by DSC operation and by HSM operation as color changes/melting at concentrations less than 52 mol percent **TNAZ** and as color changes only at concentrations greater than 52 mol percent **TNAZ**. The **ADNAZ** experimental liquidus curve is consistent with that calculated by using equation (1). Eutectic melting was confirmed only at **TNAZ** concentrations greater than 52.1 mol percent. Those endotherms attributed to eutectic melting were shifted from an average value of 75.4 °C (initial melting operations) to 74.2 °C. The eutectic composition is believed to lie between 62 to 64 mol percent **TNAZ**.

CONCLUSIONS

A temperature/composition diagram for the **TNAZ/ADNAZ** binary system has been calculated computationally by using measured heats of fusion and melting points obtained from the neat components. Experimentally, temperature/composition diagrams has been determined for physical mixtures of **TNAZ**

and **ADNAZ**. Initial Physical mixtures of **TNAZ** and **ADNAZ** exhibit the thermal characteristics associated with a simple binary eutectic system. Remelt mixtures exhibit the characteristics associated with a simple linear solid solution system on the **ADNAZ**-rich side of a simple binary eutectic system on the **TNAZ**-rich side. **TNAZ** and **ADNAZ** do not behave ideally in either type mixture.

REFERENCES

1. Archibald, T.G.; Gilardi, R.; Baum, K. and George, C., *J. Org. Chem.*, 1990, 55,2920.

2. Unpublished work at the Armament Directorate, Energetic Materials Branch, Eglin AFB, Florida.

3. Aubert, S.A., Characterization of a **TNAZ/PETN** Composite Explosive, WL-TR-96-7012, Wright Laboratory/Armament Directorate, Eglin AFB, Florida, 30 April 1996.

4. Aubert, S.A. and Sprague, C.T., Characterization of a **TNAZ/TNT** Composite Explosive, WL-TR-96 7044, Wright Laboratory/Armament Directorate, Eglin AFB, Florida, 30 July 1996.

5. Aubert, S.A.; Sprague, C.T. and Russell, T.P., Characterization of a **TNAZ/TNB** Composite Explosive, WL-TR-96-7013, Wright Laboratory/Armament Directorate, Eglin AFB, Florida, 30 May 1996.

6. Reich, R.F.; Aubert, S.A. and Sprague, C.T., Evaluation of the Characterization of a **TNAZ/MNA** (*N*-Methyl-*p*-nitroaniline) Composite Explosive, WL-TR-1997-7022, WL/Armament Directorate, Eglin AFB, Florida, 30 June 1997.

7. McKenney, R.L., Jr.; Floyd, T.G.; Stevens, W.E.; Marchand, A.P.; Sharma, G.V.M.; Bott, S.G. and Archibald, T.G., Synthesis and Thermal Properties of 1,3-Dinitro-3-(1',3'-dinitroazetidin-3'-yl)azetidine (**TNDAZ**) and Its Admixtures with **TNAZ**, *J. Energetic Materials,* accepted for publication.

8. Dave, P.R., *J. Org. Chem.* 1996, 61, 5453-5455.

9. In-house computer program written by Dr. Paul R. Bolduc.